Synthesis, characterisation, and properties of powder metallurgy transition metal-based high entropy alloys for electrocatalytic application

A thesis

submitted in fulfilment

of the requirements for the degree

of

Doctor of Philosophy in Engineering

at

The University of Waikato

by

Ashok Kumar

THE UNIVERSITY OF
WAIKATO
Te Whare Wānanga o Waikato

2023

Abstract

Water electrolysis is an eco-friendly route for hydrogen production when compared to other routes such as steam reforming, coal gasification, biomass gasification etc, however only 4% of hydrogen is being produced through water electrolysis. Water electrolysis proceeds via two half-cell reactions namely oxygen evolution reaction (OER) and hydrogen evolution reaction (HER). HER is a two-electron transfer process while OER is a four electron/proton transfer process. Hence OER is energy intensive and affects the overall efficiency of water electrolysis. To improve the efficiency of water electrolysis, it is necessary to develop an efficient electrocatalyst for OER process. Ir and Ru based oxides are the state-of-the-art electrocatalysts for OER, however their natural abundance is minuscule, hence they are expensive. Transition metal based electrocatalysts are emerging materials for OER applications due to their high natural abundance and low cost. However, these materials exhibit poor conductivity and consequently poor catalytic activity. Hence to overcome the shortcomings of conventional electrocatalysts a new class of multi component alloys termed as high entropy alloys (HEAs) are getting popular for electrocatalytic applications. However, most of the HEAs for OER are not self-supporting and being synthesised in powder form are often coated onto conductive substrates such as Ni foam and carbon fibre. Hence this powder based electrocatalysts are not suitable for industrial scale hydrogen production. In addition, most synthesised HEAs consist of Co which is an inherently expensive material. To overcome these current drawbacks in this field, this thesis considered three Co free self-supporting HEA combinations namely NiMnFeCu, NiMnFeCrCu and NiMnFeCr which were successfully synthesized. Among the synthesized HEAs examined, NiMnFeCr was found to exhibit an overpotential of 300 mV after it was subjected to 100 cycles of cyclic voltammetry (CV) activation. Furthermore, the NiMnFeCr HEA synthesised exhibited a compressive yield stress of 306 MPa manifesting the excellent combined properties of not only catalytic activity but also mechanical strength. The research showed that NiMnFeCr was a suitable candidate material for industrial scale water electrolysis and hence can be considered as a potential replacement for the conventional, prominently used electrocatalysts such as Raney nickel, Ir and Ru oxide- based catalysts. The excellent catalytic activity demonstrated by the HEA NiMnFeCr could also be attributed to its work function of 3.02 eV which is the lowest value of work function of other studied HEAs.

Acknowledgements

I would like to express my sincere gratitude to my PhD supervisor Associate Professor Fei Yang for his continuous support and guidance throughout the pursuit of my PhD.

I would like to offer my sincere gratitude to my co supervisors Associate Professor Leandro Bolzoni and Associate Professor Michael Mucalo for providing persistent support throughout my research.

I would like to express my sincere gratitude to Professor Dr. Yiming Li for his help with TEM samples.

I would like to acknowledge the support of technician Helen Turner and Dr. Stella Rayanova for their continuous support with XRD and SEM equipment.

I would like to thank everyone who directly or indirectly contributed to the preparation of this thesis.

Table of Contents

List of Tables

List of Figures

List of Publications

The following are publications that have resulted from this thesis.

The pages in the thesis where the work from these publications and have been duly cited in the reference section.

1. **Kumar, A**., Mucalo, M., Bolzoni, L., Li, Y., Kong, F., & Yang, F. (2022). Fabrication, microstructure, mechanical, and electrochemical properties of NiMnFeCu high entropy alloy from elemental powders. *Metals*, *12*(1), 167. **https://doi.org/10.3390/met12010167**

   ***Pages- chapter* 3: 85-95; chapter 4: 125-127; chapter 5: 156-158**

2. **Kumar, A.,** Mucalo, M., Bolzoni, L., Li, Y., Qu, Y., & Yang, F. (2023). Facile synthesis of a NiMnFeCrCu high entropy alloy for electrocatalytic oxygen evolution reactions. *Materials Today Sustainability*, *22*, 100360. https://doi.org/10.1016/j.mtsust.2023.100360

   ***Pages- chapter* 3: 95-102; chapter 4: 127-148; chapter 5: 165-173**

3. **Kumar, A.,** Mucalo, M., Bolzoni, L., Li, Y., Qu, Y., & Yang, F. (2023). Electronic structure tuning for enhanced oxygen evolution performance of a NiMnFeCr medium entropy alloy. *International Journal of Hydrogen Energy*. https://doi.org/10.1016/j.ijhydene.2023.03.203

   ***Pages- chapter* 3: 103-110; chapter 4: 142-151; chapter 5: 174-185**

Chapter 1

High entropy alloys (HEAs) for electrocatalytic application

1.1 Introduction

Increased consumption of fossil-based fuels such as coal and petroleum products are creating environmental degradation at an alarming rate. Furthermore, rapid depletion of fossil-based fuels also results in increasing demand for energy. Solar and wind-based energy are considered to be an environmentally friendly energy source. However, both of these energy sources are intermittent in nature and vary depending upon season and region. Conversion of this intermittent renewable resources into energy dense carriers is critical in effective utilization of renewable energy sources such as solar and wind. Hydrogen is an eco-friendly alternative energy carrier for fossil-based fuels. Gaseous hydrogen can be produced via steam reforming, coal gasification and water electrolysis. Furthermore, water electrolysis is an eco-friendly method for producing gaseous hydrogen compared to other methods of hydrogen production. However only limited amounts of gaseous hydrogen are being produced via water electrolysis. This low efficiency of hydrogen production in water electrolysis process is due to the sluggish chemical kinetics on the electrodes used. Hence to improve the efficiency of water electrolysis, an efficient electrocatalyst is required. Platinum based electrocatalysts and transition metal based electrocatalysts are emerging materials for electrocatalytic water splitting applications. However, due to high cost and poor activity these electrocatalysts are not suitable for large scale hydrogen production and still there is a need to develop an advanced electrocatalysts for improving the efficiency of water electrolysis. Recently multi component metallic alloys are gaining research interest for electrocatalytic water splitting applications. As a result, a number of multi component alloys are being synthesized and researched exclusively for their application to water electrolysis. This dissertation will discuss and identify the research gaps on the existing multi component alloys and will propose a new strategy in the design of multicomponent alloys for water electrolysis; furthermore, the dissertation will propose a new cost-effective synthesising route for multicomponent alloy system intended for water splitting applications.

The conventional approach of alloying involves combining one or two principal elements with a few other minor elements using the Hume-Rothery rule of mixing[1, 2] . These minor elements are added to improve desired properties such as corrosion resistance, wear resistance, mechanical strength etc. Several alloys namely stainless steel, high-speed steels, and superalloys are designed based on this approach[3]. However, there are still indications that this approach may be reaching a limit and may no longer provide alloys and properties needed for modern technological challenges[4]. The term high entropy alloy (denoted as HEAs hereinbelow) was first coined by Yeh et al., and in his work he proved that mixing five or more elements could produce a body centered cubic (BCC) or face centered cubic `1(FCC) crystal structure due to high configurational entropy[5]. His work was further confirmed by Cantor et.al. as well , when five or more elements are mixed, it resulted in the formation of a random solid solution of BCC and/or FCC crystal structure[6]. Since then, HEAs have attracted an enormous amount of attention amongst researchers and the number of publications related to HEAs have been steadily rising as shown in the Figure **1.1**.

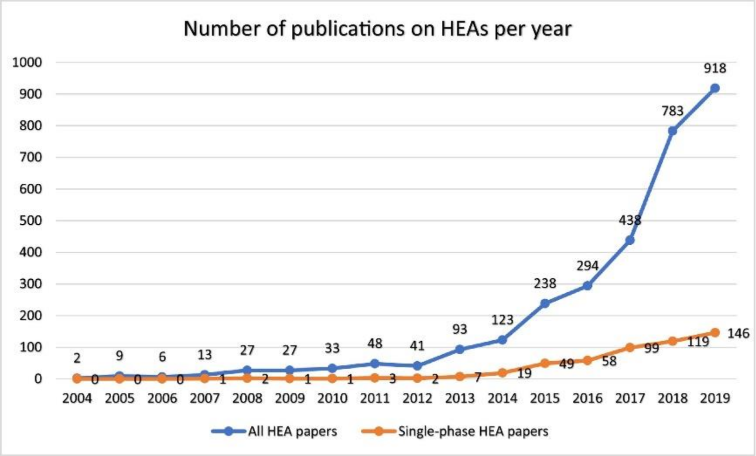

Figure 1.1 The number of publications published per year on multicomponent high entropy alloys up till 2019 as reproduced from reference [7].

1.2 Definition of high entropy alloys

HEAs are defined as multi-principal component alloys with at-least five elements, where the concentration of each component varies from (5- 35 atom %). Alternatively, HEAs can also be defined by means of a term known as the configuration entropy ΔS_{config}. HEAs are alloys for which ΔS_{config} is greater than 1.5R where R is defined as the universal gas constant. This definition can be expressed as

$$\Delta S_{config} \geq 1.5R \qquad (1.1)$$

For equi-atomic HEAs the ΔS_{config} can be expressed as

$$\Delta S_{config} = R\ln(N) \qquad (1.2)$$

Where N is the number of constituent elements. When the value of N increases the ΔS_{config} also increases. Table **1.1** represents the increase of configurational entropy as a function of N.

Table 1.1 Increase of configurational entropy as function of N (Adapted from [3]).

N	1	2	3	4	5	6	7	8	9	10	11	12	13
ΔS_{config}	0	0.69	1.1	1.39	1.61	1.79	1.95	2.08	2.2	2.3	2.4	2.49	2.57

1.3 HEA core effects

The phase formation in HEAs are governed by four core effects namely the high entropy effect, the lattice distortion effect , the sluggish diffusion effect and the cocktail effect [3]. These core effects are based on hypothesis from literatures and discussed briefly below.

1.3.1 The high entropy effect

The high entropy effect is the first significant core effect[8] and this effect is based on the fact that increased entropy of mixing will lead to the formation of random solid solutions (S) rather than intermetallic phases (I). Phase stability during alloy formation is thermodynamically governed by the Gibbs free energy of mixing ΔG_{mix}. This Gibbs free energy of mixing is further related by enthalpy of mixing, ΔH_{mix}, and the entropy of mixing ΔS_{mix}. When two or more discrete elements are mixed to form an alloy then the Gibbs free energy of mixing is given by equation 1.3

$$\Delta G_{mix} = \Delta H_{mix} - T\Delta S_{mix} \qquad (1.3)$$

Where T is the absolute temperature

Although mixing entropy (ΔS_{mix}) is composed of configurational , vibrational, electronic, and magnetic entropies, only configurational entropy is the dominant term of these entropies, hence these are often neglected and entropy of mixing can be referred to only as the configurational entropy (ΔS_{config})[5, 9]. Bearing this notion in mind for a random n constituent- containing solid solution, if the i^{th}component has a mole fraction C_i then the configurational entropy ΔS_{config} is given by equation 1.4

$$\Delta S_{\mathrm{config}} = -R\sum_{i=1}^{n} C_i \mathrm{Ln} C_i \tag{1.4}$$

where R is the universal gas constant, 8.314 J $K^{-1}mol^{-1}$[3].

HEAs are often composed of at least five elements. If the number of constituent elements increases, the configurational entropy increases as depicted in Figure **1.2**. This amplified configurational entropy increases the chance of solid solution (S) formation and inhibits the formation of intermetallic phases(I) [5]. However, a number of published works have proven that high configurational entropy, alone can be insufficient to ensure the formation of random solid solution (S). The works of Otto et al. concluded that the increased $\Delta S_{\mathrm{config}}$ could result in the formation of single-phase random solid solution(S) only in a few selected alloy systems and secondary phases such as intermetallic compounds can also be seen in alloy combinations such as CrMnFeCoNi[10]. Hence high configurational entropy alone will not guarantee the formation of a solid solution, and in fact, the role of other factors such as the valence electron concentration (VEC), atomic size misfit δ, and electronegativity are also expected to play a significant role in phase formation in HEAs [5, 11, 12].

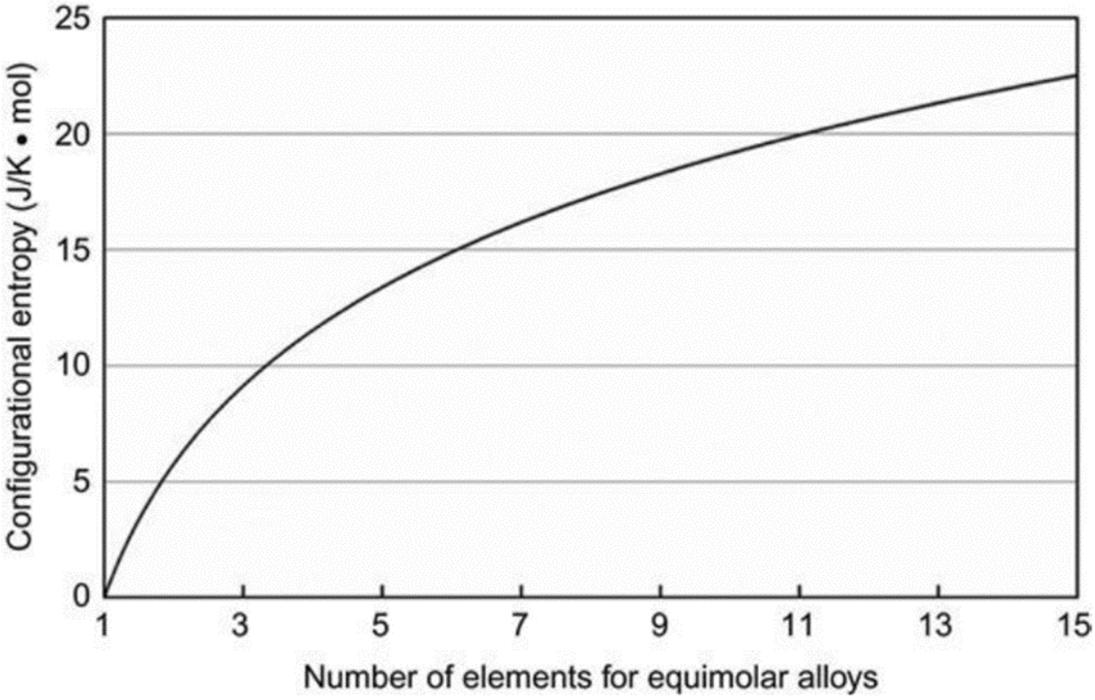

Figure 1.2 Effect of configurational entropy as function of constituent elements in HEAs(adapted from[13]).

1.3.2 The lattice distortion effect

HEAs are often composed of equi-atomic or near equi-atomic chemical compositions, as a result the solid solution in HEAs are always a whole solute matrix and no solvent matrix exists despite having FCC, BCC, HCP or other complex structures[14]. The lattices of HEAs are filled with atoms of varying atomic sizes as shown in Figure **1.3**, this creates an enormous amount of lattice strain and stress when compared to conventional alloys[3]. Hence this severe lattice distortion directly affects the properties of HEAs. For instance, lattice distortion impedes the dislocation movement and results in solid solution strengthening consequently the HEAs possess superior mechanical properties. Lattice distortion further causes enhanced scattering of electrons and phonons leading to lower thermal and electrical conductivity[15].

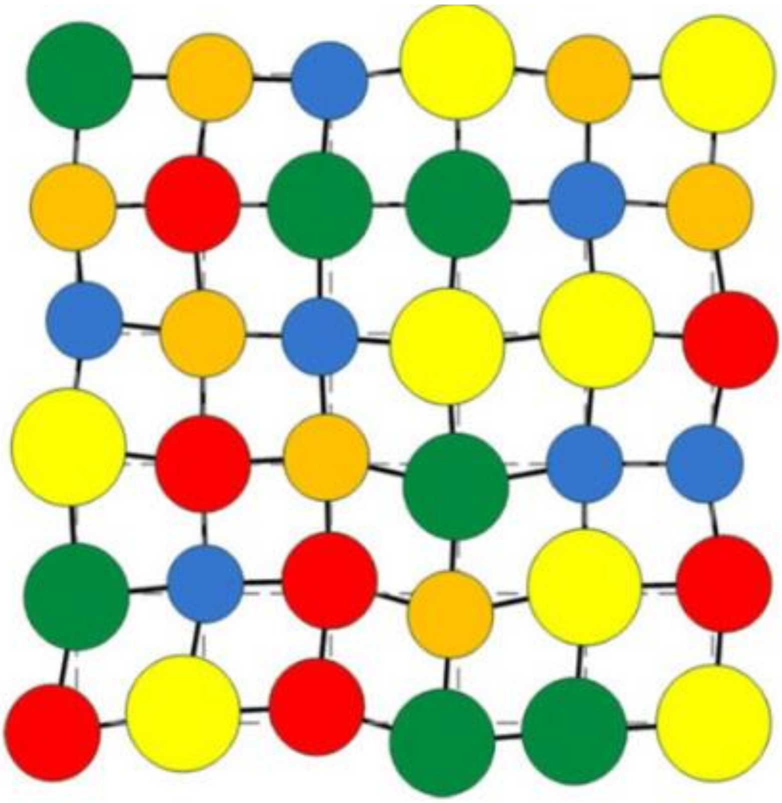

Figure 1.3 Schematic representation of the lattice distortion effect reproduced from [8].

1.3.3 The sluggish diffusion effects

Diffusion in HEAs is expected to be slower when compared to conventional metal alloys[16], with two important factors being responsible for this sluggish diffusion. Firstly, atoms occupying the neighbouring lattice points vary from each other so a difference in local atomic configuration prevails. This leads to diverse bonding and local energies for each lattice site; hence atoms are trapped in deep diffusion traps as shown in Figure **1.4**. Secondly, the diffusion rates of each element in HEAs differ from each other , some elements diffuse slowly when compared to others while other elements diffuse quickly so phase transformation is limited, because for phase transformation there should be collective and coordinated diffusion of several elements[17]. There is only limited experimental evidence on the sluggish diffusion in HEAs, Firstly Tsai et al. measured the diffusion coefficients in HEA CoCrFeMnNi alloys and found that diffusion was slower in HEA compared to that of its constituent individual elements[18]. It is worthy to note that recent reports in grain boundary diffusion kinetics in HEAs concluded that the assumption of decrease in diffusivity by increasing the number of elements in HEAs is incorrect and requires more investigation[19].

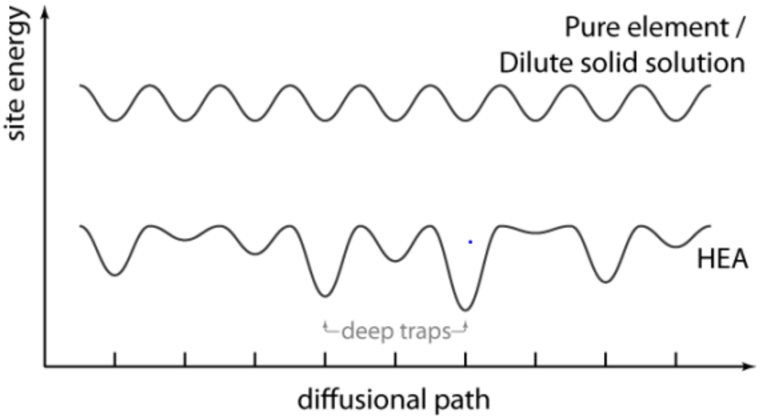

Figure 1.4 Schematic representation of the sluggish diffusion effect adopted from reference [3].

1.3.4 The cocktail effects

The term “cocktail effect” was first mentioned in the article “ Alloyed pleasures : Multi-metallic cocktail “ by Ranganathan and was not associated uniquely with HEAs , but was used to elucidate the modern trends in metallurgy [20]. The cocktail effect could be interpreted as the synergistic mixture where the end result is mostly greater than the sum of the individual elements. There is no exact definition for the cocktail effect given in the literature, but it is the widely accepted tenet that holds that the properties of HEAs depend purely on the properties of their constituent elements. Miracle et al. suggested that the cocktail effect should not be considered as a hypothesis, but an idea that is open minded to nonlinear, unexpected results that arise from the different compositional space of multi-principal elemental alloys[21].

1.4 Notation for HEAs

HEAs are synthesized in two categories either as an equi-atomic or in a near equi-atomic composition. It is important to describe how notations are given to this system of alloys.

HEAs are denoted in either as an atomic ratio or as an atomic percentage. Both systems of representations are acceptable. For example $\mathrm{CoCrCu_{0.2}Fe_{0.2}Ni}$ can also be denoted as $\mathrm{Co_{29.4}Cr_{29.4}Cu_{5.9}Fe_{5.9}Ni_{29.4}}$[3]. In most cases, elements are arranged in alphabetical order but arranging them according to atomic number is also an accepted convention.

1.5 Classification of HEAs

Based on the magnitude of entropy HEAs can be classified into three categories:

- Low entropy ($\Delta S_{\mathrm{config}}$<0.69R)
- Medium entropy (0.69R<$\Delta S_{\mathrm{config}}$<1.61R)
- High entropy alloy($\Delta S_{\mathrm{config}} > 1.61$R)[21].

1.6 Phase prediction in alloys

As discussed earlier, configuration entropy $\Delta S_{\mathrm{config}}$ has a profound effect in stabilising solid solution(S) phases, however high $\Delta S_{\mathrm{config}}$ alone cannot guarantee the formation of a solid solution phase. For example the $\mathrm{Pd_{20}Pt_{20}Cu_{20}Ni_{20}P_{20}}$ alloy system possesses a $\Delta S_{\mathrm{config}}$ value of 13.38 J $\mathrm{mol^{-1}K^{-1}}$ yet it forms an amorphous phase resulting in a metallic glass [22]. These findings were in accordance with the confusion principles established by Turnbull and Greer[3, 23, 24] which state that when more than five elements are added together to form an alloy, it will result in the formation of an amorphous phase (i.e. metallic glasses). Although the high entropy effect and the sluggish diffusion effect can ensure random mixing, greater atomic size difference between constituent elements will lead to topologically irregular phases, and this leads to the formation of amorphous phases. Thus, from the above-discussed theory, along with high entropy few other parameters should also be considered as influential in the phase formation in HEAs.

Predicting phase stability is critical in HEAs design because the properties of HEAs depend upon its constituent phases. Hence, sophisticated strategies are used in HEA design. Careful selection of constituent elements will aid in proper HEAs design and the pioneering effort on alloy design originated through Hume- Rothery (HR) rules and the Inoue empirical criterion[25, 26]. They proposed four empirical criteria for solid solution formation in 1920 [27].

i. The atomic radii of the solute and solvent should not vary by 15 % for complete solubility,
ii. The crystal structure of the mixing elements should be the similar for extended solubility,

iii. Extended solubility occurs in similar valence states.

iv. Similar electronegativity of the solute and solvent causes good solubility.

Therefore, the solid solution formation is not only limited to high entropy but also to atomic size difference, electronegativity, valence electrons, and enthalpy of mixing which all play a critical role in phase formation.

1.7 Thermodynamical Criterion for phase formation

The Hume Rothery rules furnish the necessary thermodynamical and geometrical parameters for the formation of solid solution (S) in conventional alloys. However, these rules cannot be applied to HEAs because it cannot explain how Co(HCP)-Cr(BCC)-Cu(FCC)-Fe(BCC)-Ni(FCC) alloy forms an FCC solid solution and how the addition of FCC Aluminium can change FCC type CoCrCuFeNi into a BCC structure[28]. Hence, in order to extend the work of Hume Rothery and to overcome its short comings , Zang et al.[29] established three important parameters that govern the phase formation in HEAs. These involve atomic size misfit δ , mixing enthalpy ΔH_{mix} , and entropy of mixing ΔS_{config} and which are expressed by equations 1.5-1.7

$$\delta = 100\% \sqrt{\sum_{i}^{n} C_i (1 - \frac{r_i}{\bar{r}})^2} \tag{1.5}$$

where $\bar{r} = \sum_i^n C_i r_i$ and a numerical factor of 100 is used to amplify the data for more clarity.

$$\Delta H_{mix} = 4 \sum_{i=1, i \neq j}^{n} H_{AB} C_i C_j \tag{1.6}$$

where H_{AB} is the enthalpy of mixing of the binary alloy [30]

$$\Delta S_{config} = -R \sum_{i=1}^{n} C_i Ln C_i \tag{1.7}$$

where R is the universal gas constant, 8.314 J K^{-1} mol^{-1} and C_i is the mole fraction of the i^{th} component in the HEA.

In addition, electronegativity difference $\Delta\chi$ is given by equation 1.8.

$$\Delta\chi = 100\% \sqrt{\sum_{i}^{n} C_i (\chi_i - \bar{\chi})^2} \tag{1.8}$$

where $\bar{\chi} = \sum_i^n \chi_i C_i$ and χ_i is known as the Pauling electronegativity of the i^{th} element.

Zhang et al. found from experimental data that solid solutions are formed when -15 < ΔH_{mix}<5 kJ mol^{-1} and 1 < δ < 6.6%[11].

Gou et al suggested that the valence electron concentration (VEC) can be used to predict the crystal structure[12]. VEC is given by equation 1.9.

$$\mathrm{VEC} = \sum_{i}^{n} C_i \ \mathrm{VEC}_i \qquad (1.9)$$

where VEC_i is the valence electron configuration of the i^{th} component in HEAs. To avoid confusion between VEC and e/a, (e/a is the average number of itinerant electrons per atom ratio while VEC is total electrons (including d electrons) in the valence band)[1, 31].

VEC plays very little or no role in phase stability between the amorphous phase and solid solution phase. Nevertheless, VEC is decisive in predicting the crystal structure of the HEAs. However, $\Delta\chi$ has only a limited effect in phase formation in HEAs. When VEC >8, a FCC crystal structure is formed and when VEC < 6.87 a BCC crystal structure is formed. When VEC is between 6.87 and 8 both FCC and BCC can co-exist in an HEA[12].

An additional parameter Ω which combines ΔH_{mix} and ΔS_{config} was introduced by Zang et al. and Yang et al. and it compares their relative weight by means of ratio and is represented as

$$\Omega = \frac{T_m \, \Delta S_{config}}{\Delta H_{mix}} \qquad (1.10)$$

$$T_m = \sum_{i}^{n} C_i Tm_i \qquad (1.11)$$

where T_m is the average melting temperature of the constituent elements of HEAs. It is implied from the equation (1.10) when Ω > 1.1, the entropy effect overpowers the enthalpy and tends to form a random solid solution (S) and Ω is the thermodynamic parameter and δ is the geometrical parameter which complements each other. Both parameters are considered as the guidelines for predicting phase formations in HEAs. So solid solutions (S) are formed when Ω ≥ 1.1 and δ ≤ 6.6%[11] as shown in Figure **1.5**.

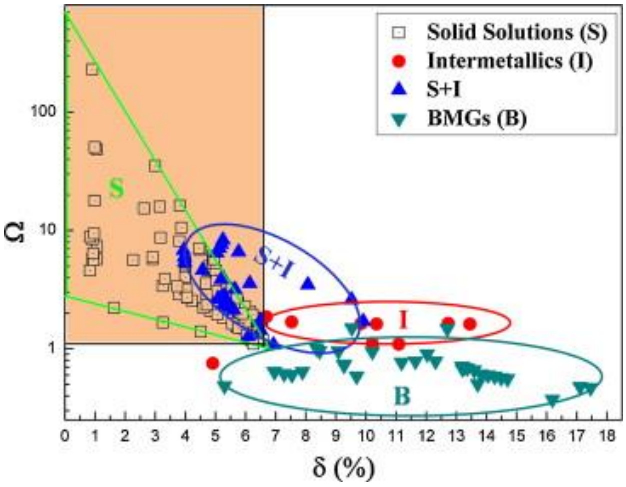

Figure 1.5 Relationship between Ω and δ for multi-component alloys displaying zones of $\Omega \geq 1.1$ and $\delta \leq 6.6$ % (figure reproduced from [32]).

1.8 σ phase formation in HEAs

It is commonly presumed that the high entropy effect always produces stable FCC or BCC solid solution phases. However, the formation of intermetallic compounds(I) is also possible in HEAs and it is reported elsewhere that when HEAs are aged at a certain intermediate temperature, 'σ ' intermetallic phases could be formed[33, 34]. Formation of a σ phase affects the mechanical properties of the HEAs because it is hard and brittle in nature, hence controlling the formation of σ phase is critical in designing HEAs to obviate any disadvantage conferred by the presence of intermetallics. The σ phase is formed between A and B elements where A is usually from the group VB or VIB element and B is usually from VIIB or VIIIB element in the periodic table[35]. σ is called as an electron compound which means its formation is closely related to the electron concentration in the outer most shell. This attribute forms the base for the theory and models which predicts the formation of the σ phase [36, 37]. This method provides valuable guidelines for predicting the σ phase in conventional alloys. However, applying this method for HEAs is complex. Hence, a simpler method is used; a parameter known as the average valence electron concentration (VEC) as a predictive tool for σ phase formation in HEA, as it is easy and straightforward to apply. Tsai et al [34] investigated the role of the VEC in determining σ phase formation in HEAs, a series of test alloys with different compositions were synthesized and the range of VEC was between 6.27 and 8.44. These as- cast test alloys were aged at 700^{o} C for 20 h to allow σ phase formation as shown in Figure **1.6**. The composition, phase, and VEC of the tested HEAs are tabulated in Table **1.2**.

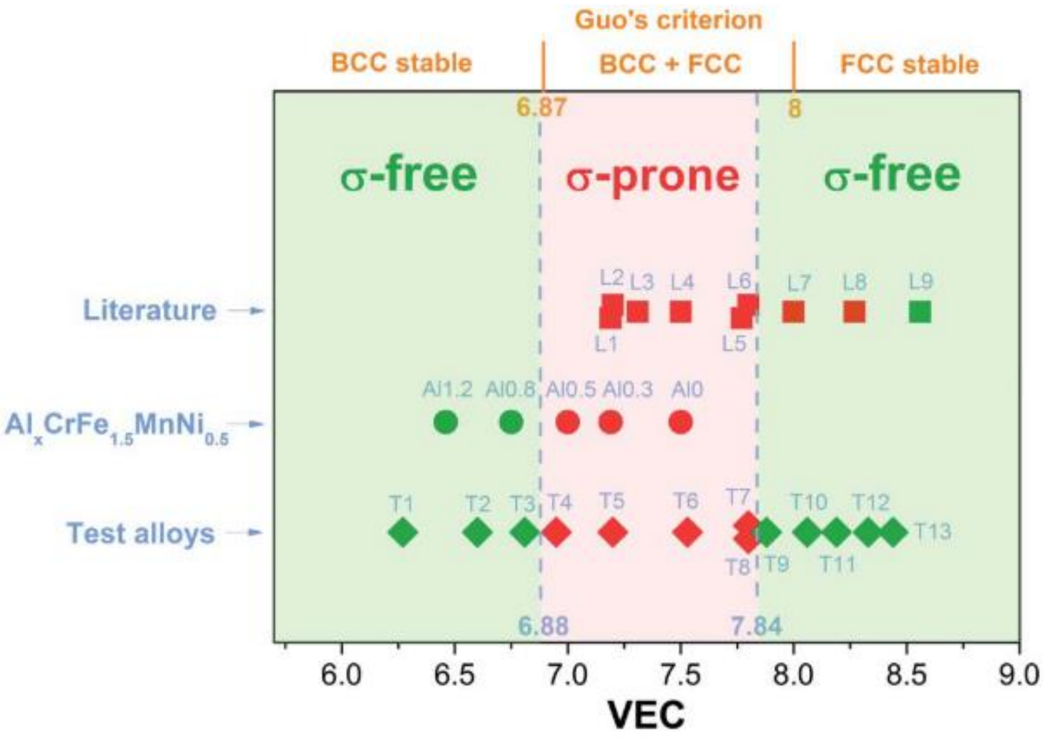

Figure 1.6 Relationship between the VEC and the presence of the σ phase after aging for a number of HEAs. Green and red icons indicate the absence and presence of the σ phase after aging respectively[34]

Table 1.2 Composition and VEC of test alloys[34].

Designation	Alloy	VEC	Phase after 700°C aging
T1	$Al_{0.5}CrFeNiTiV$	6.27	Heusler+Laves (C15)
T2	$AlCo_{0.5}Cr_{0.5}Fe_{0.5}MnNiV$	6.64	BCC
T3	$AlCo_{0.5}Cr_{0.5}Fe_{0.5}MnNiV_{0.5}$	6.8	BCC
T4	$AlCo_{1.5}Cr_2Fe_{1.5}Mn_2NiV$	6.95	σ
T5	$Al_{0.4}CoCrFeMnNiV$	7.2	σ
T6	$Al_{0.3}CoCr_2FeNi$	7.53	FCC+ σ+ FCC
T7	$Co_{0.5}CrFeMn_{1.5}Ni$	7.80	FCC + σ
T8	$CoCr_2FeNi$	7.80	FCC + σ
T9	$Al_{0.3}CoCrFeNi$	7.88	FCC
T10	$CoCr_{1.25}FeMn_{0.25}Ni$	8.06	FCC
T11	$CoCr_{0.75}FeMn_{0.75}Ni$	8.19	FCC
T12	$CoCrFe_{0.5}Mn_{0.5}Ni_{1.5}$	8.33	FCC
T13	$Co_{1.5}Cr_{0.5}FeMn_{0.5}Ni$	8.44	FCC

Based on the findings of Guo et al[12], VEC plays a crucial role in phase formation in the as-cast HEAs. It is interesting to note that the σ prone VEC range is when $6.88 < VEC < 7.84$ which is very close to the BCC +FCC range. Hence it can be understood that HEA alloys which possess dual BCC + FCC phases will, therefore, have a high probability of forming a σ phase.

1.9 Synthesis of high entropy alloys

There are several processing techniques used to synthesis HEAs. Depending upon the starting state of the elemental materials the methods of preparation are summarised in three broad categories:

i.) Liquid state: arc melting/casting, electro chemical process [38, 39] [40].
ii.) Solid state: high energy ball milling [41-43].
iii.) Gaseous state: sputtering method[44, 45].

Arc melting/casting is the most common method used for synthesizing HEAs[12, 39, 46, 47]. Repeated melting and solidification is often carried out to ensure chemical homogeneity of the synthesised alloys. Based on this technique Zhou et al. prepared HEA $AlCoCrFeNiTi_x$(where x is the molar ratio)[48] and the HEA exhibited a BCC crystal structure and excellent fracture strength and work hardenability. Wang et al.[49] also found that when the cooling rate during solidification of HEA AlCoCrFeNi is increased, the strength and plasticity is enhanced. Although melting/casting techniques offer excellent mechanical properties, the problem with this fabrication method is that the solidification process cannot be easily controlled due to the nature of rapid cooling, which thus leads to a differing microstructure from the surface to the centre of the as-cast alloy samples[50, 51]. In addition to that inevitable casting defects which includes elemental segregation, suppression of equilibrium phases, microscopic and macroscopic residual stresses, cracks, and porosities, may cause a negative impact on the mechanical properties of HEAs as well. Hence an alternative technique should be used to synthesise HEAs.

1.9.1 Powder metallurgy route for synthesizing HEAs

In the powder metallurgy(P/M) technique it is possible to produce ultra-fine chemically homogeneous microstructure, hence it can circumvent the drawbacks of the casting route of synthesizing HEAs. Using powder metallurgy, elements with different melting points and immiscible elements in the liquid state can also be produced [41-43, 52]. Mechanical alloying is the preliminary step in the P/M route. High purity elemental powders are milled in high energy ball mill for a predetermined time and intentional breaks are given to monitor the alloying process and for characterization. The various stages of the P/M route for synthesis are discussed briefly below.

1.9.2 Mechanical Alloying

Mechanical alloying (MA) is a solid-state alloying process performed by high energy ball milling and it is the preliminary step in the P/M route for synthesising HEAs. During milling the powder particles are crushed between the repeated ball to ball and ball to vial collisions as shown in Figure **1.7(a).** These repeated collisions create plastics deformation of the powder and increases the dislocation density in the powder particle as shown in Figure **1.7(b)**. The two main factors to be considered while milling is the hardness and the ductility of the powder. During milling the ductile metal powders become flattened while the brittle powder tends to fracture, and prolonged milling will lead to cold welding of the brittle metallic particles onto the surface of the ductile particles or it can make the brittle powder become trapped between the interfaces of the flattened ductile powder particles. This continuous and recurring process of fracturing and cold welding results in the formation roughly of an equilibrium state known as a saturation state[53].

During the initial stage of milling, the particles are soft, hence they have a higher tendency to cold weld. As a result, the particle size increases drastically and often gets stuck on the surface of the balls and the vial, which leads to the formation of a lamellar microstructure with layers of milled powder as shown in Figure **1.7**(b). During the final stage of milling, severely deformed powder gets strain hardened and starts to fracture. Hence there is a continuous reduction in particle size during the final stage of milling. Milling is carried out for a desired amount of time, the milling process results in the formation of a nanocrystalline and chemically homogenous mixture.

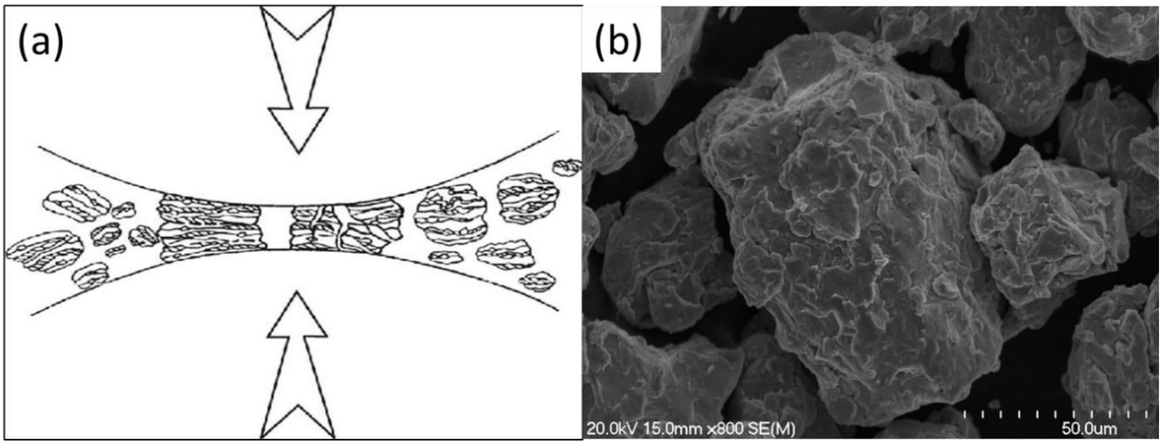

Figure 1.7 a.) Schematic representation of high energy ball milling b.) Microstructure of milled powder.

1.9.3 Milling process control variables

The milling container also known as the (vessel, vial, jar or bowl) plays a significant role in the milling process. The impact of the grinding balls on the walls of the vials will dislodge the wall material hence the possibility of wall materials contaminating the powder is high. This contamination may affect the overall chemistry of the powders. So proper precautions such as optimized milling parameters (time , speed, ball to powder ratio , process control agent etc.) are needed to compensate for the contamination[54]. The shape of the vials is also important, especially the internal design of the container with flat-ended and round-ended vials often being used and alloying takes place at a higher rate in the flat ended vials[54].

The use of high milling speeds is advantageous because it will increase the operating temperature of the vial. This will favour diffusion and dissolving of alloying elements. However, milling beyond the critical speed will result in pinning of balls down to the inner walls of the vial and does not create sufficient impact force. So milling speed should be just below the critical speed so that the ball can fall from the maximum height creating sufficient impact force[54].

Milling time is a critical parameter in high-energy ball milling. The time chosen is the saturation time between fracturing and cold welding. Milling time varies depending upon the nature of mill, the intensity of the mill, ball to powder-ratio (BPR) and the temperature of the milling. So, optimizing the milling time for a different combination is critical and prolonged milling will lead to the formation of undesired phases in the synthesised alloys[55].

The ratio of the weight of the balls to powder is termed the ball to powder ratio (BPR). A ratio of 10:1 is the most commonly used ball to powder ratio for small scale milling such as

SPEX and planetary miller. In large scale milling such as when using an attritor, a ratio of 50:1 or even 100:1 is used. The ball to powder ratio is inversely related to milling time so when a higher ratio is used, milling time is reduced[54].

Cold welding takes place especially if the particles are ductile. Real alloying will take place only if a proper balance is maintained between cold welding and fracturing. Addition of a process control agent (PCA) will minimize cold welding. PCAs can be liquids, solids or gases, and can adsorb on the surface of the particles to minimize metal to metal contact which then has the desired effect of reducing cold welding and particle agglomeration. They are used at a level of about 1-5 wt% of the total charge of the powder. A few commonly used PCAs are stearic acid, hexane, methanol, and ethanol[54].

1.9.4 Cold Compaction

High-density compacts are desirable for most applications because they ensure high green strength and minor dimensional changes during sintering. During compaction, if stress and density gradients caused by the friction on the die walls are neglected then the achieved green compact density is a function of compacting pressure. As shown in Figure **1.8** when compaction pressure increases the following process will take place in the powders. Initially, arrangement of particles occurs by the removal of clusters and cavities. Secondly, particle contact increases because of plastic deformation. Finally, oxide layer removal and agglomeration take place due to the mechanical interlocking of particles and this mechanism increases the particle strength even further. As the pressure increases, the adhesion between particles increases which consequently increases the density of the green compacts. When the compaction pressure is increased beyond the particle’s plasticity then the particles undergo fracture.

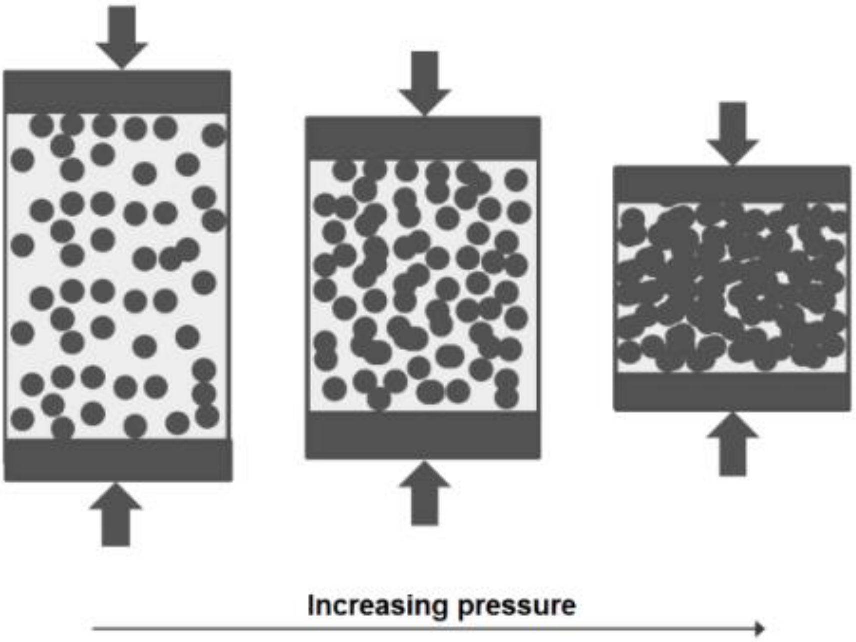

Figure 1.8 Schematic representation of the effect of compaction pressure on powder particles. Diagram reproduced from reference [56].

1.9.5 Conventional Sintering

The process which involves assembling of particles under the application of pressure by chemically bonding them into a coherent body at elevated temperature is termed sintering[56]. Densification or shrinkage tends to happen during most of the sintering operation, however sintering can happen even without dimensional changes. Temperature applied during sintering is usually lesser than the melting point of the constituent elements. In the case of high entropy alloys, the mixed rule (Vegard law) should be followed in deciding the melting temperature of the alloy. The sintering process is able to be studied in the three stages as depicted in Figure **1.9**. During the initial stage, the particle contacts are changed into sintered bridges and the powder particles remain discrete. Grain boundaries are formed between two adjacent particles in the plane of contact[56, 57]. During the intermediate stage, the size of the neck increases and the initial particles lose their identity, and a new microstructure is formed with a net of coherent pores and grain growth. Grain boundaries form between two pores and during this stage maximum shrinkage takes place. During the final stage of sintering, closure of pores takes place with relative density increasing rapidly to 90%-95% of the theoretical density. In addition to that, spherodizing of isolated pores will take place during this stage. If gases cannot diffuse, they become trapped inside the pores and no further densification is possible as the trapped gases reach equilibrium due to the surface tension.

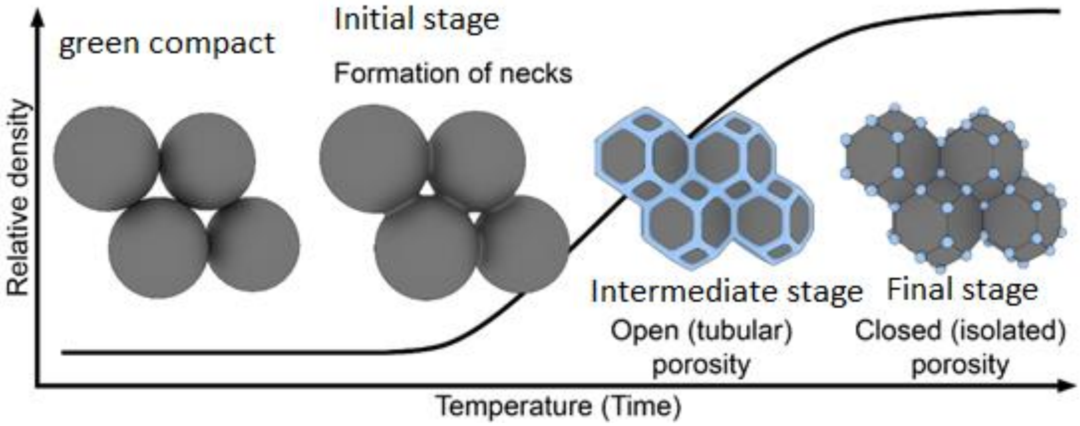

Figure 1.9 Schematic representaion of various stages of sintering processs adapted from reference [58].

1.9.6 Process variables for sintering.

The most crucial process variables in sintering are time, temperature and furnace atmosphere. The role of these parameters in the sintering operation are briefly described below. Sintering temperature is the most critical parameter during the sintering process. Increasing the temperature will significantly increase the rate and magnitude of any changes happening during the sintering operation. Mass transfer increases as a function of sintering temperature, and as a result, enhanced densification takes place at the higher sintering temperatures. Sintering time is another parameter to be considered in the consolidation process, however sintering time has a minimal effect in the sintering process when compared with the influence of temperature. The loss of driving force with the increase in time is the main reason for not achieving complete removal of porosity during the sintering operation. Finally, the sintering atmosphere should also be considered because, porous compacts are often sintered in a furnace. Hence, these compacts have a high tendency to react with the ambient atmosphere of the furnace. Therefore, the sintering atmosphere can have an influence in the sintering operation. Sintering operations are often performed in a protective gas atmosphere to prevent oxidation, H_2,NH_3, and vacuum being some commonly used sintering atmospheres.

1.10 Hydrogen production methods

Global energy demand is increasing steadily due to rapid global industrialization and the increase in the human population. 85% of the world's energy demand is currently being fulfilled by the use of fossil-based fuels. By 2050 the global energy demand is expected to rise by 30 tera Watt[59]. However, these fossil-based fuels are known to be depleting at a faster rate and are becoming less accessible. Moreover, increased consumption of fossil-based fuels is leading to massive emissions of greenhouse gases mainly CO_2, NO_x, SO_x as well as fine particles. Consequently, environmental degradation in the form of global warming and acid rain is becoming of much greater prevalence. Therefore, there is an urgent need to develop a clean energy source to reduce the adverse impact of fossil-based energy on the natural environment. Figure **1.10** depicts the global share of energy sources, electricity production and carbon emissions.

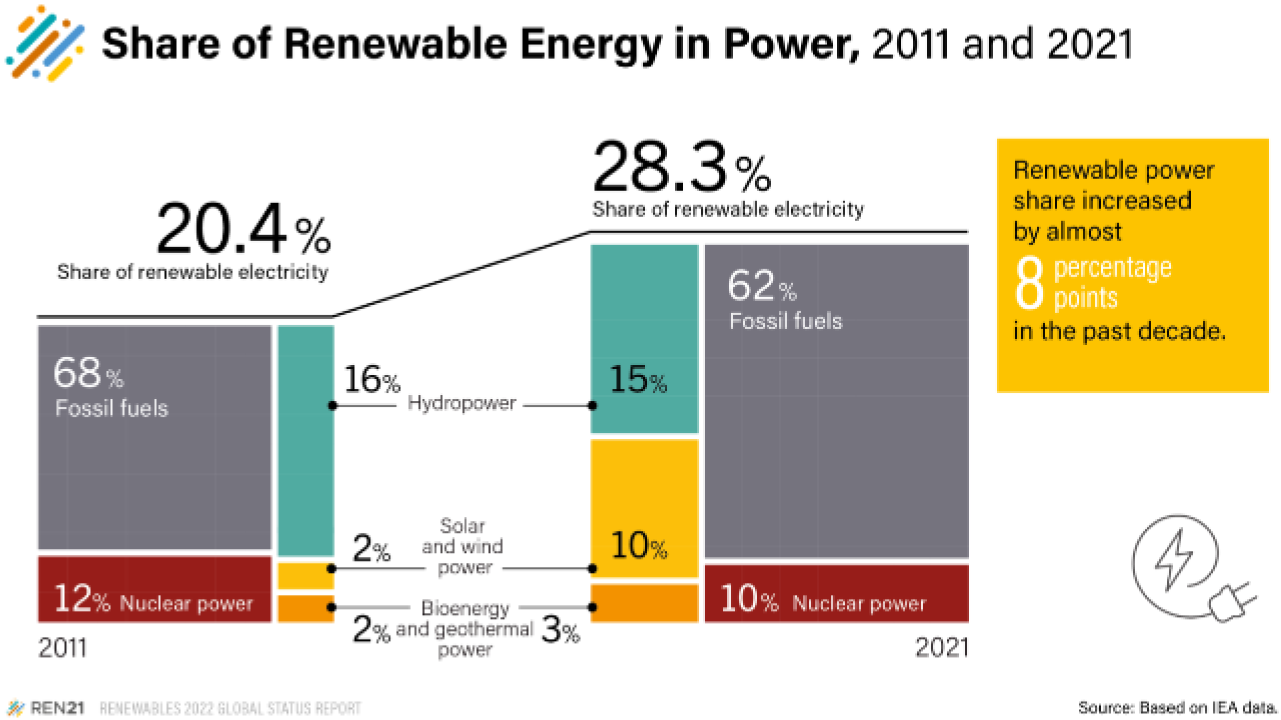

Figure 1.10 Comparison of global energy share of the year 2011 and 2021(reproduced from[60, 61].

Renewable energy sources like wind, solar and tidal energy are considered to be emissions free. However, these renewable energy sources are intermittent in nature which means the amount of energy (in the form of electricity) produced by renewable sources can vary over a sharp interval of time. For example, solar energy can be used only when there is sun. Similarly other energy sources such as wind and tidal suffer from the same problem in terms of reliability of supply in given time periods, hence it is necessary to store this energy when generated for later use. Currently batteries are widely used to store this energy. Although the efficiency of batteries are expected to be around 90%[62], the performance of the batteries degrades with time and some batteries also exhibit a large amount of energy leakage. As a result , batteries have a limited lifespan of 8.5 years with their disposal being hazardous to the environment[63].Therefore, it is necessary to find a clean energy carrier as an alternative to batteries.

Hydrogen is the tenth abundant element found in the surface of the earth. It is very scarce in the atmosphere; however it is found abundantly in several compounds such as fresh and sea water, biomass and fossil fuels. It is a promising environmentally friendly energy carrier which can replace other conventional fossil fuels like coal and hydrocarbons. Hydrogen contains high energy density of 140MJ/kg which is twice the energy density of other fuels such as methane (50.0 MJ/kg), gasoline (44.5 MJ/kg), diesel (42.5 MJ/kg) and so on. Table **1.3** lists the calorific values of the most commonly used fuels.

Table 1.3 Calorific values of the most commonly used fuels [59]

Fuel (phases it exists in)	Calorific value MJ/kg
Hydrogen (g)	141.9
Methane (g)	55.5
Ethane (g)	51.9
Gasoline (l)	47.5
Diesel (l)	44.8
Methanol (l)	20

(g) = gas, (l) = liquid

There are several methods available for hydrogen production. Based on the feedstock and processing route, hydrogen can be produced by natural gas steam reforming and coal-biomass gasification[59]. Natural gas steam reforming is the most common method for hydrogen production and 48% of hydrogen is produced by this method. Various hydrogen production methods based on the feedstocks are illustrated in Figure **1.11**. Although hydrogen is considered to be an eco-friendly energy carrier, hydrogen production routes are not absolutely environmentally friendly. Based on the feedstocks and waste production during hydrogen generation cycle, hydrogen is classified into three colour codes namely green, blue and grey. Existing production routes for hydrogen production such as steam reforming, biomass and biomass gasification primarily fall within grey and blue codes because they involve emission of $\mathrm{CO_2}$ which will again create pollution. Hence to avoid the adverse impact of hydrogen production technologies on the environment, an eco-friendly method of hydrogen production also termed “ green hydrogen” should be adopted as a future production method of this energy resource.

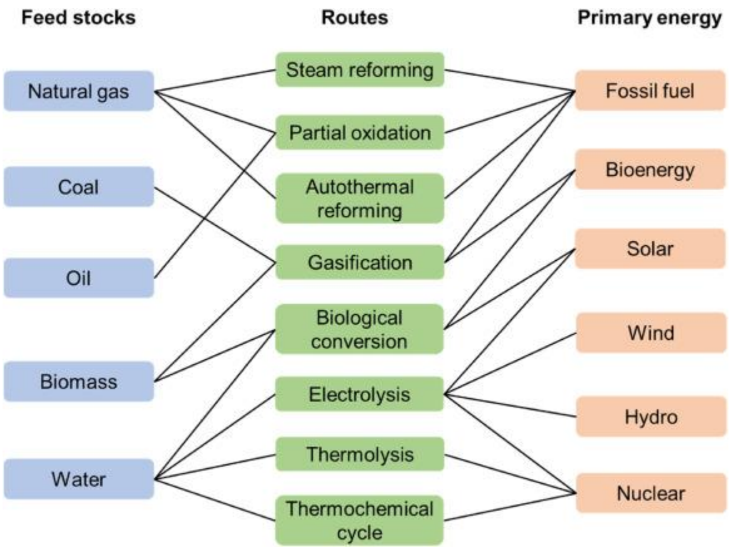

Figure 1.11 Hydrogen production methods based on feedstock and energy source adapted from [64].

Electrochemical water splitting through electrolysis is considered to be a near zero or zero end use emissions technique. Water electrolysis can be easily coupled with renewable methods of energy production (e.g. wind, solar). As a result during off peak hours in power grids, the excess load can be utilized to perform water splitting[59]. Figure **1.12** illustrates a schematic depiction of the hydrogen economy which involves production, storage, distribution and consumption.

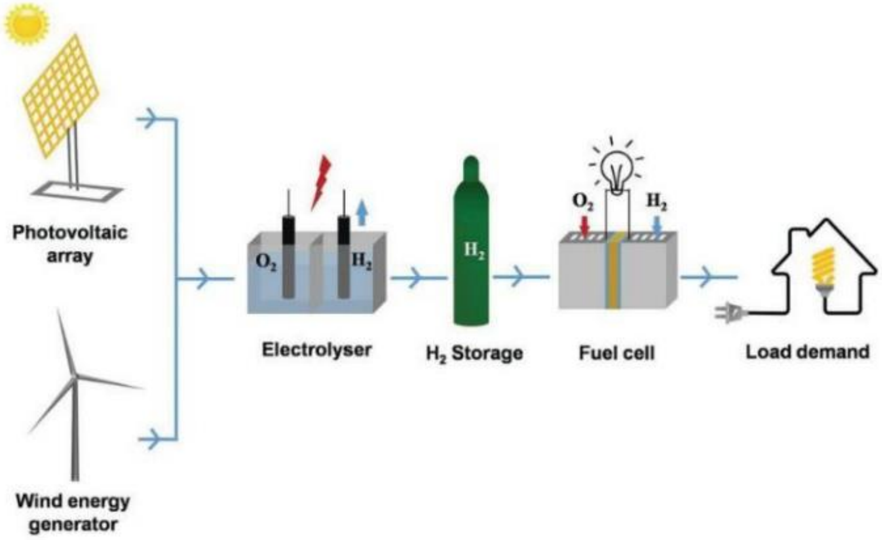

Figure 1.12 Schematic representation of the overall concept of a hydrogen economy(production , distribution and consumption) adopted from [65].

1.11 Hydrogen production by water electrolysis

Water electrolysis is an electrochemical process of splitting water into its individual elemental chemical components as shown in equation 1.12.

$$H_2O(l) \rightarrow H_2(g) + \frac{1}{2}O_2(g) \qquad (1.12)$$

The experimental setup of water electrolysis consists of two electrodes (anode, cathode) immersed in electrolyte with a diaphragm. The diaphragm separates the anode and cathode. In water electrolysis, the water molecule is converted into H_2 and O_2 by the application of external energy (potential) and this water splitting process proceeds via two half-cell reactions, namely reduction of H^+ ion at the cathode ($2H^+$ (aq) + $2e^- \rightarrow H_2$ (g)) referred to as the hydrogen evolution reaction (HER) and oxidation of water at the anode ($2H_2O(l) \rightarrow O_2(g)$ + $4H^+$(aq)+ $4e^-$) referred to as the oxygen evolution reaction (OER).

There are different types of water electrolysis technology in practice depending upon the temperature and electrolyte/pH. Low temperature water electrolysis includes alkaline water electrolysis (AWE) and proton water exchange membrane water electrolysis (PEM WE). Although PEM WE offer several advantages, such as a high energy efficiency and a higher energy production rate, its application is limited due to the high cost of electrodes and membranes. An expensive membrane is necessary to avoid mixing of H_2 and O_2. In addition, the operation cost of this kind of setup is high. AWE offers several advantages compared to other electrolysis methods as it is carried out at temperatures between 60°C and 80°C with 30% aqueous KOH solutions and produces 99.9% pure hydrogen as deduced from previous studies[66]. The AWE setup consists of a relatively simple design (Figure **1.14**). However, at first glance, alkaline water electrolysis may appear to be a simple process, in reality only 4% of hydrogen is produced by this method (Figure **1.13**). In terms of operating cost, water electrolysis requires 238 kJ of energy to produce 1 mole of H_2 while only 41 kJ of energy is required to harvest 1 mole of H_2 through a steam reformation process. This low efficiency of water electrolysis is due to the sluggish chemical kinetics of reactions taking place at the two electrodes[67].

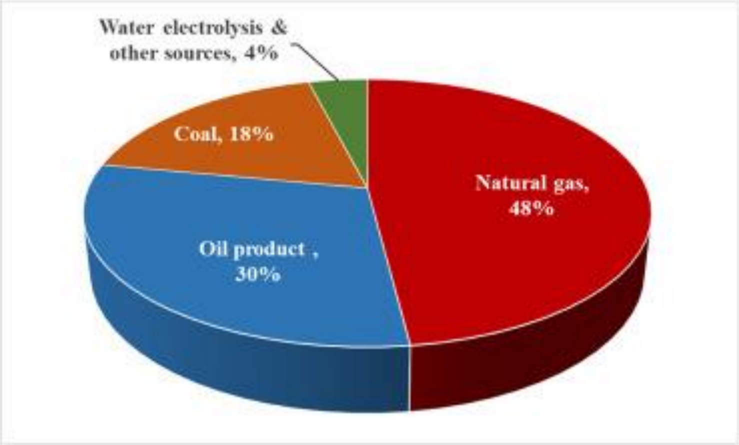

Figure 1.13 Sources of hydrogen production (feedstocks) according to reference [68].

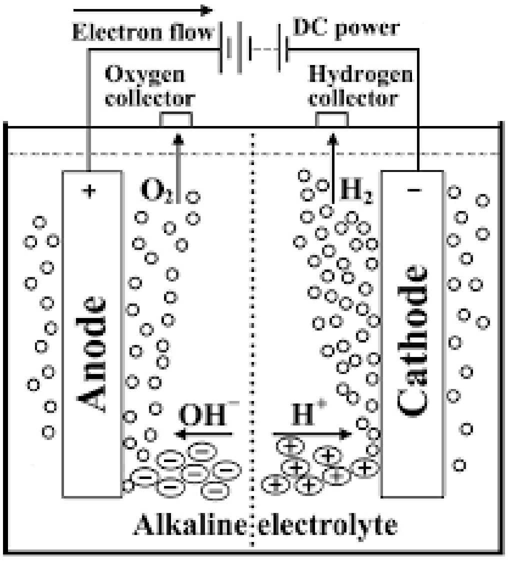

Figure 1.14 Schematic representation of water electrolysis.

1.11.1 Cathodic half-reaction (HER)

The HER is one of the half-cell reactions in water electrolysis which involves a two-electron transfer process. It takes place at the cathode and hydrogen is evolved during these reactions. The HER takes place in two pathways either in what are termed Volmer- Tafel or a Volmer-Heyrovsky step. In alkaline conditions, the catalyst firstly splits the H_2O molecule into H^+ and hydroxyl ion OH^- , and the free hydrogen ion is adsorbed on the surface of the catalyst (Volmer step), with H_2 gas then being liberated out from the surface of the catalyst by either by interaction of the H atom with a H_2O molecule (Heyrovsky step) or the combination of two H atoms (Tafel step). Figure **1.15** depicts the schematic representation of the HER mechanism. HER is a pH dependent reaction and the widely accepted reaction pathway in an alkaline environment is given by equations 1.13-1.16

The proposed mechanism for the HER in an alkaline environment is discussed by Jayabal et al. [69]

At the cathode:

$$2H_2O + 2e^- \rightarrow H_2(g) + 2\ OH^-\ (aq) \qquad (1.13)$$

Hence two electrons are involved in producing one mole of H_2

$$\text{Volmer step}: 2H_2O + 2e^- \rightarrow 2H_{ads}(g) + 2\ OH^- \qquad (1.14)$$

$$\text{Tafel step}: 2H_{ads} \rightarrow H_2 \qquad (1.15)$$

$$\text{Heyrovsky step}: H_2O + H_{ads} + e^- \rightarrow H_2 + + OH^- \qquad (1.16)$$

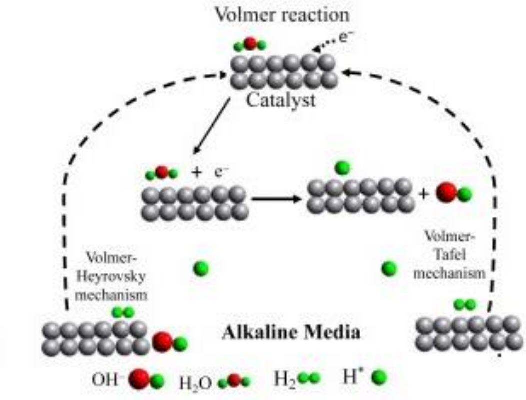

Figure 1.15 Schematic representation of mechanism of HER adapted from [70].

1.11.2 Anodic half-reaction (OER)

The OER is the other half-cell reaction involved in water electrolysis, and it takes place at the anode with oxygen being evolved during these reactions. Initially the interaction of the active catalytic site M* with a hydroxyl group will form M*OH as an intermediate. Then the interaction of M*OH with another hydroxyl group will create an intermediate species M*O.

The subsequent interaction of M*O with another hydroxyl group will generate M*OOH. Finally, interaction of M*OOH with another hydroxyl group will generate one mole of O_2. The mechanism of the OER is depicted in Figure **1.16**

In an alkaline electrolyte

At the anode

$$2H_2O(l) \rightarrow O_2(g) + 4H^+(aq) + 4e^- \tag{1.17}$$

OER is more complicated relative to HER as it involves a four-electron transfer, and it is also pH dependent.

Proposed Mechanism under alkaline conditions.

$$M^* + OH^- \rightarrow MOH + e^- \tag{1.18}$$

$$MOH + OH^- \rightarrow MO + H_2O(l) + e^- \tag{1.19}$$

$$MO + OH^- \rightarrow MOOH + e^- \tag{1.20}$$

$$MOOH + OH^- \rightarrow M + O_2(g) + H_2O(l) + e^- \tag{1.21}$$

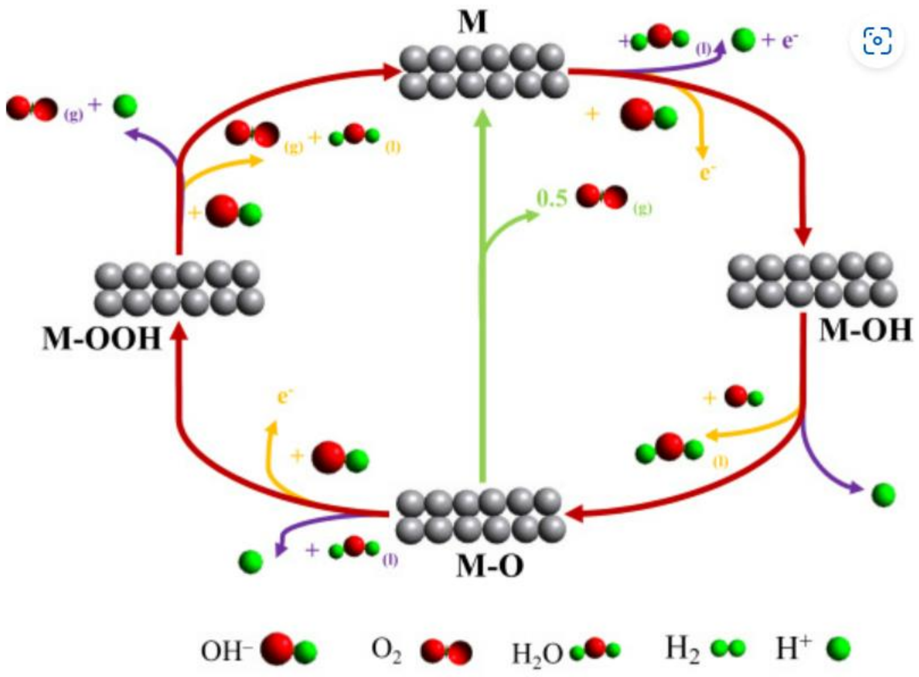

Figure 1.16 Mechanism of the OER reaction in an alkaline medium [70].

1.12 Descriptors of water electrolysis

1.12.1 Electrode and electrolyte

During electrolysis of water, oxygen and hydrogen are evolved via an electrochemical reaction. This electrochemical reaction is facilitated by an electrocatalyst which comprises the electrodes of the electrochemical cell. This electrode can be grafted onto a support material such as carbon fibre paper, nickel foam or can also exist as a whole bulk material. The function of an electrode is to adsorb the reactant from solution onto the surface as an intermediate and to facilitate charge transfer between electrode and electrolyte. A wide variety of electrodes such as glassy carbon (GC), Ni foam, precious elements like Ir and Ru based electrodes, transition metal based oxides , hydroxides, selenides, phosphides, spinel and perovskites have been studied as electrode materials for electrocatalytic OER applications. Electrolytes of both an acidic and basic nature affects the performance of the electrodes. Electrocatalysis of OER in an alkaline environment is more favourable but is poor in an acidic environment, hence most of the research is focused on developing OER electrocatalysts for use under alkaline conditions. The performance of an electrocatalyst can be evaluated through consideration of several parameters. These parameters will be discussed briefly in the following paragraphs[71].

1.12.2 Overpotential (η) and onset overpotential

Water electrolysis is a non-spontaneous process, hence in-order to initiate a redox(reduction/oxidation) reaction external energy (potential) is required. The thermodynamic potential of water electrolysis under standard conditions is 1.23 V[72]. However, in reality extra potential needs to be applied to conduct water electrolysis as shown in Figure **1.17**. This extra potential is termed the overpotential and is defined as the absolute difference between the actual applied potential and the thermodynamic potential of water splitting to kickstart the reaction. Overpotential is often measured at a specific current density and it is common practice to measure the overpotential at a current density value of 10 $\mathrm{mA\ cm^{-2}}$ which corresponds to a photo current density of 12% when undertaking efficient solar energy productions[50]. Generally, overpotential is measured in mV and represented as η. An ideal electrocatalyst should operate with as low an overpotential as possible at a higher current density. $\mathrm{E_{electrolysis}} = \mathrm{E_{reversible}} + \Delta\mathrm{E_{irreversible}} + \mathrm{iR}$, $\mathrm{E_{reversible}}$ represents the theoretical decaying voltage, iR represents the voltage drop caused by the electrolyte, wires and contact point. $\Delta\mathrm{E_{irreversible}}$ represents overpotential of OER. Based on the origins of Polarization on the electrode, the overpotential mainly includes concentration overpotential and electrochemical overpotential, which are caused by concentration Polarization and electrochemical Polarization, respectively. As for concentration Polarization, it can be reduced by vigorously stirring or raising the operating temperature to accelerate the ion diffusion. This iR drop towards OER can be eliminated by iR compensation. iR compensation can remove the effect of the resistance from the electrode and electrolyte. Furthermore, the resistance between the solution and the electrode can be reduced by placing the working electrode very close to the tip of a Luggin capillary. The onset overpotential is a point where the current density starts to increase sharply, and it is usually calculated at a current density of 1 $\mathrm{mA\ cm^{-2}}$. Linear sweep voltammetry (LSV) is used to measure the overpotential effectively and the pH of the electrolyte used often ranges from 13.8 to 14

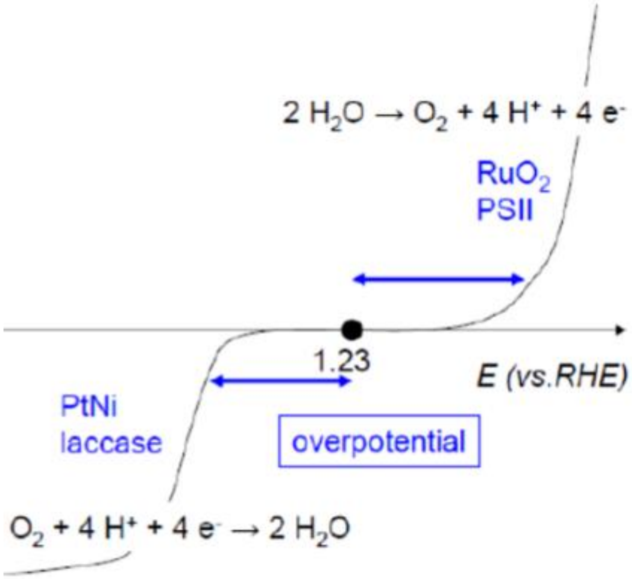

Figure 1.17 Definition of overpotential in water splitting reactions adapted from [73].

1.12.3 Exchange Current Density and Tafel slope

The relationship between exchange current density (j) and overpotential(η) can be given by the Butler Volmer reaction as shown in equation 1.22 where j_o is the exchange current density , n is the number of transferred electrons, F is the faraday's constant, R is the universal gas constant, T is the thermodynamic temperature, and α_a and α_c refer to the transfer coefficient of the anodic and cathodic reaction respectively and are usually assumed to be 0.5.

$$\mathrm{j} = \mathrm{j_o}[\exp\left(\frac{\alpha_a \mathrm{nF}\eta}{\mathrm{RT}}\right) - \exp\left(-\frac{\alpha_c \mathrm{nF}\eta}{\mathrm{RT}}\right)] \tag{1.22}$$

When the anodic overpotential is sufficiently larger (and hence dominating at the electrode relative to any cathodic current, this current can be neglected hence equation 1.22 can be rewritten as equation 1.23

$$\mathrm{j} = \mathrm{j_o}[\exp\left(\frac{\alpha_a \mathrm{nF}\eta}{\mathrm{RT}}\right)] \tag{1.23}$$

Taking the log of both sides of equation 1.23 gives equation 1.24 which is termed the Tafel equation. From this the exchange current density j_o and the Tafel slope (b) can be calculated accordingly.

$$\log\mathrm{j} = \log\mathrm{j_o} + \frac{\eta}{\mathrm{b}} \tag{1.24}$$

The Tafel slope b can be calculated from the linear region of the LSV curve, and it shows the rate of increase of the exchange current density with respect to overpotential and a smaller Tafel slope implies faster kinetics and good electrocatalytic properties. The magnitude of the exchange current density (j_o) manifests intrinsic bonding/charging interactions between the electrocatalyst and the electrolyte. A high measured exchange current density at a low overpotential is the indication of excellent electrocatalytic properties.

1.12.4 Electrochemical impedance spectrum analysis

Electrochemical impedance spectroscopy (EIS) is a technique performed to investigate the reaction kinetics of the OER process at the electrode/electrolyte interface. The charge transfer resistance ($\mathrm{R_{ct}}$) indicates the ease of charge transfer taking place between the electrolyte and electrode interface. It can be measured empirically by determining the intercept of the Bode plot on the abscissa. The solution resistance $\mathrm{R_s}$ can be measured similarly from the Bode plot as shown in Figure **1.18**. EIS measurements are often measured between the frequency range of 0.01 Hz to 10^5Hz with an AC amplitude of 1.5 V vs RHE (on the faradaic region).

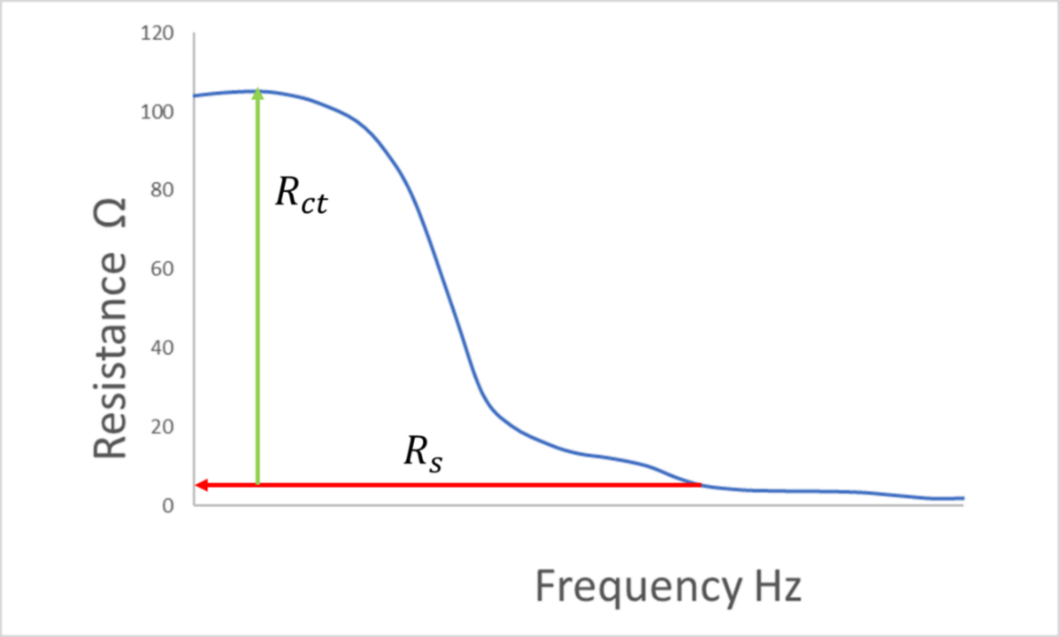

Figure 1.18 Representative Bode plot indicating charge transfer resistance $\mathrm{R_{ct}}$ and solution resistance $\mathrm{R_s}$.

1.12.5 Stability

Long term stability is one of the critical parameters in determining the merit of an electrocatalyst. It is otherwise referred to as an accelerated degradation test. In an OER catalyst, a 100 to 1000 cycles of an accelerated degradation test is carried out but it is rare to find an OER catalyst with extreme stability when subjected to over 1000 cycles of an accelerated degradation test. After the accelerated degradation test, the change in onset overpotential (η_o) and the overpotential at a defined current density of 10 mA cm^{-2} are taken as parameters for judging whether the material under investigation is a stable electrocatalyst or not. Stability under constant exposure to a fixed potential (chronoamperometry) or a fixed current density (chronopotentiometry) is examined for several minutes to hours. It is widely accepted that a stable current density (e.g., 10 mA/cm^2) for more than 10 hours by chronoamperometry or a small rise in overpotential at a current density of 10 mA/cm^2 for more than 10 hours by chronoamperometry is sufficient for an electrode material to be recognized as an efficient electrocatalyst for both the OER and HER.

1.12.6 Electrochemical active surface area

The double layer capacitance ($\mathrm{C_{dl}}$) is measured to study the electrochemical surface area (ECSA). The cyclic voltammetry technique is employed to measure the $\mathrm{C_{dl}}$. The potential window of 1- 1.06 V vs RHE can be used at scan rates of 20, 40, 60, 80 and 100 mV s^{-1}. $\mathrm{C_{dl}}$ can be determined using the plot of the difference in exchange current density ΔJ = $\mathrm{J_{anode}}$-$\mathrm{J_{cathode}}$ at 1.03 V vs RHE against the scan rate. The plot can be fitted by linear regression to estimate the $\mathrm{C_{dl}}$ which is twice the slope. The electrochemical surface area, ECSA can be determined using the formula ECSA = $\mathrm{C_{dl}}/\mathrm{C_S}$, where $\mathrm{C_S}$ is the specific capacitance which is equal to 0.040 mF cm^{-2}. A larger $\mathrm{C_{dl}}$ value indicates there are increased active sites which is highly desirable for an electrocatalyst.

1.13 Electrochemical cell

A three-electrode system is widely used in a laboratory scale water electrolysis investigation. It consists of the counter electrode (CE), the reference electrode (RE) and the working electrode (WE). The reference electrode has a constant potential with a low current density. The role of the reference electrode is to act as a reference in controlling and measuring the potential of the working electrode. The counter electrode is used to pass the current required to balance the current measured in the working electrode. No current passes through the reference electrode. The schematic arrangement of a three-electrode system is shown in the Figure **1.19**

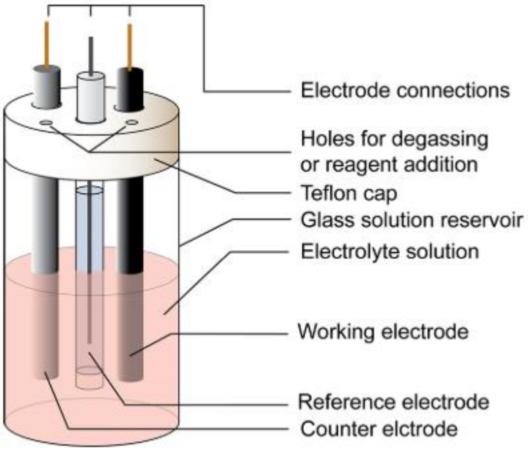

Figure 1.19 Schematic representation of the three-electrode system[74].

1.14 OER catalyst material

Water electrolysis can be represented by two half-cell reactions in which hydrogen and oxygen are evolved via the cathode and anode respectively. The HER is a two-electron transfer reaction as outlined in equations 1.13-1.16 while the OER is a four-electron transfer reaction as shown in equations 1.17-1.21. As a result, the kinetics of the OER is more sluggish because of the multistep reactions which each involve one electron transfers. Each of these steps hence require certain activation energies and therefore the accumulation of energy at these steps requires a large overpotential to operate when compared to the HER. This excessive overpotential is known to be a bottleneck in developing an efficient OER catalyst. Hence extensive research is being carried out to develop an efficient electrocatalyst for OER reactions. Currently $\mathrm{IrO_2}$ and $\mathrm{RuO_2}$ based electrocatalysts are the existing state-of-the-art catalyst for OER reactions[71]. However due to their lower natural abundance and consequently high cost, these materials are not economically viable if used for industrial scale water electrolysis. This factor is the main reason which hinders large-scale production of hydrogen by electrolysis currently.

It has been well established that (oxy)hydroxides of the first-row transition metal can be used in electrocatalytic applications for water electrolysis[67, 75]. These oxides are based on metals like Fe, Co, Ni, Cr, etc which have a greater natural abundance. These elements are consequently cheaper so they can potentially replace the scarce and expensive noble metal-based catalysts. However, these transition metal oxides possess poor electrical conductivity, low intrinsic catalytic activity, and poor durability. These oxide catalysts materials hence need to be optimized for better OER performance for implementing in large scale hydrogen production[76]. These aforementioned transition metal based electrocatalysts for OER reactions and other commonly used electrocatalyst will be discussed in detail in the following sections.

1.14.1 Precious metal-based oxides OER catalysts and mixtures

Precious metals and their oxides are the most investigated catalyst for OER electrocatalysis. The trend in OER activity of precious metal elements is given by Ru>Ir>Pd>Pt. As a result, iridium (Ir) and ruthenium (Ru) based electrocatalysts have been investigated intensively and are considered as the state of the art electrocatalysts for use in OER reactions[77]. However, it is reported elsewhere that RuO_2 is unstable at higher anodic potential and can deteriorate during OER operation, IrO_2 is more stable compared to RuO_2, although RuO_2 is comparatively more catalytically active compared to IrO_2 [77, 78] . To overcome this drawback, mixed oxide catalysts or $Ir_{0.1}Ru_{0.9}O_2$ have been investigated and the mixed oxide catalyst exhibited catalytic activity very close to RuO_2. Moreover, the stability of $Ir_{0.1}Ru_{0.9}O_2$ was better compared to that of RuO_2[79].

1.14.2 Transition metal oxides as OER catalyst

Group VIII 3d transition metal oxides are widely used for OER catalyst materials. They are cheap and abundant hence they could be considered as an alternative to the precious metal based electrocatalysts. Based on their structures, they are classified into mono metallic transition metal-based oxides, perovskite and spinel structures. Mono metallic oxides such as Ni based oxides and Co based oxides are used as electrocatalysts for OER applications[75]. When compared to IrO_2 and RuO_2 these catalysts are abundant and cheap, however they possess poor electrical conductivity and their OER activity was moreover, poor. Hence extensive work is being carried out to overcome these shortcomings by combining two or more metals oxides namely perovskites and spinel to form better electrocatalysts.

1.14.3 Materials in the perovskite family of solids as OER catalyst

Perovskites are considered to be an efficient electrocatalyst. They are easy to synthesise and their electronic structure can be tuned easily[80]. The perovskite family is represented by ABO_3 where A is an alkaline metal and B is a transition metal. Numerous reported works are available on the perovskite catalytic family, the most interesting of them being $La_{1-x}Sr_xFe_{1-y}Co_yO_3$. Matsumoto et al. investigated this electrocatalyst and found that the OER the activity increased with increasing values of x and y. They claimed that high activity is due to the d band character and high oxidation state of Co ions, proving that the OER activity is strongly related to the electrons present in the d band of the perovskite. In perovskite the oxidation state of B (transition metal site) is either 3+ or 4+ or a mixture of the two oxidation states[81]. To investigate the oxidation states, Hong et al. performed statistical studies for exploring the descriptor for OER activity on 51 perovskites and collected 101 OER activity data reports through literatures and experimental data searching. They found that these descriptors belonged to five families. Among them electron occupancy and metal oxygen covalency are the most prominent. From their work, they confirm that the d electron occupancy, optimal e_g electrons and metal oxygen covalency play a crucial role in OER activity[82]. Jin Suntivich et al. estimated the hybridization of transition metal oxide states of perovskites and found out that hybridization (mixing of 3d electrons of transition metals and 2p electrons of O) increases with an increase in d electron count in perovskites. Increased oxidation states in perovskites also increase hybridization and create reduced transition metal 3d and oxygen 2p energy differences and increased covalency[82]. Table **1.4** provides the overpotential values of a few perovskites used for OER studies.

Table 1.4 Electrocatalytic activity of perovskite based electrocatalyst for OER reactions.

Catalyst	Substrate	Electrolyte	Overpotential mV	Tafel slope mV/dec
$CaCu_3Fe_4O_{12}$	GCE*	0.1M KOH	400 @10mA cm^{-2}	51
$CaFeO_3$	GCE	0.1M KOH	390 @10mA cm^{-2}	47
$SrFeO_3$	GCE	0.1M KOH	410 @10mA cm^{-2}	63
$LaFeO_3$	GCE	0.1M KOH	500@10mA cm^{-2}	77
$La_{0.2}Sr_{0.8}FeO_3$	Self-supported	1M KOH	622@40mA cm^{-2}	58

*GCE – Glassy carbon electrode

1.14.4 Spinels as OER catalyst

Transition metal-based oxides with the spinel structure AB_2O_4 have attracted a certain amount of research interest due to their high electrical conductivity, excellent charge transfer kinetics and stability in an alkaline environment. The spinel structure can be defined by the formula AB_2O_4 where A is the transition metal with an oxidation state of +2 and occupying the tetrahedral site while B is a transition metal with an oxidation state of +3 occupying the octahedral site. The electronic structure can be adjusted by altering the metal and the number of oxygens in these A and B sites thereby enhancing the OER performance. Spinel compounds exhibit high electrical conductivity and good stability in alkaline solution. Most reported spinel oxides are Co based and Fe based with other alkaline/transition metal dopants such as (Mn, Ni, Cu, Zn and Li) being present. For example, in a ferrite system Li et al. have reported a trend of OER catalytic activity of $CoFe_2O_4$ > $CuFe_2O_4$> $NiFe_2O_4$ > $MnFe_2O_4$ for M Fe2O4 (M = Co, Ni, Cu, Mn)[71] as presented in Table **1.5**

Table 1.5 Electrocatalytic activity of spinel based electrocatalysts for OER reactions.

Catalyst	Substrate	Electrolyte	Overpotential mV	Tafel slope mV/dec
$MnFe_2O_4$	GCE	0.1M KOH	470 @10mA cm^{-2}	114
$CoFe_2O_4$	GCE	0.1M KOH	370 @10mA cm^{-2}	82
$NiFe_2O_4$	GCE	0.1M KOH	440 @10mA cm^{-2}	98
$CuFe_2O_4$	GCE	0.1M KOH	410 @10mA cm^{-2}	94
Mn_3O_4	GCE	1M KOH	>600 @ 3 mA cm^{-2}	60

1.14.5 Transition metal based oxy hydroxides as OER catalysts.

The double layered structure hydroxides (LDH) $M(OH)_2$ and oxyhydroxides MOOH on transition metals(M) have also shown excellent catalytic activity towards OER reactions. Suitable electronic structure and low cost have attracted interest among researchers and numerous works have been reported based on these materials. These electrocatalysts include $Co(OH)_2$, NiFe LDH, NiOOH and NiFeOOH. Subbaraman et al. conducted experiments on transition metal based oxy hydroxides (Ni, Co, Fe, Mn) and found that the OER activity followed the same trend (Ni > Co > Fe > Mn) as seen in perovskites. They found that the excellent catalytic activity of NiOOH is due to the optimal binding strength between active sites of Ni and OH (Sabatier principle)[83]. It was found that the presence of Fe impurity in the electrolyte to the level of 1 ppm increased the OER activity of NiOOH. It was also reported that the catalytic activity of NiOOH increased with an increase in concentration of Fe[84, 85]. Table **1.6** summarises the catalytic properties towards OER of a few common transition metal-based hydroxides.

Table 1.6 Electrocatalytic activity of transition metal hydroxide based electrocatalysts for OER reactions.

Catalyst	Substrate	Electrolyte	Overpotential mV	Tafel slope mV/dec
MnOOH	PtO	0.1 M KOH	470 @5 mA cm^{-2}	-
FeOOH	PtO	0.1 M KOH	525 @5mA cm^{-2}	-
NiOOH	PtO	0.1 M KOH	375 @5 mA cm^{-2}	-
CoOOH	PtO	0.1 M KOH	450 @5 mA cm^{-2}	-

1.14.6 Transition metal-based phosphides

In recent times transition metal phosphides have been studied for OER activity. They have high electrical conductivity when compared to transition metal oxides. However, they show poor electrochemical stability under OER conditions. Extensive studies have been conducted in-order to improve the stability of these transition metal-based phosphides such as Ni_2P and CoP. Chang et al. produced CoP nanosheets with a surface oxide layer using Co_3O_4 as precursors using phosphorization method. The synthesised electrode was used as a bifunctional catalyst. A current density of 335 mA cm^{-2} was achieved at a cell voltage of 1.8 V in 1M KOH[86] as presented in Table **1.7**.

Table 1.7 Electrocatalytic activity of transition metal phosphide based electrocatalysts for OER reactions.

Catalyst	Substrate	Electrolyte	Overpotential mV	Tafel slope mV/dec
Co_2P	GCE	1 M KOH	370 @10mA cm^{-2}	128
CoMnP	GCE	1 M KOH	330 @10mA cm^{-2}	61
Ni_2P	Nickel foam	1 M KOH	290@10mA cm^{-2}	59

1.15 Electrodes for industrial alkaline electrocatalysis

Despite the above discussed electrocatalysts for water electrolysis exhibiting promising electrocatalytic activity towards OER activity, these electrocatalysts are often not self-supported and are hence often grafted onto a conductive more mechanically robust substrate such as a glassy carbon electrode, nickel foam and carbon fibre paper. Moreover, they are deposited on to these substrates by means of binders (Figure **1.20**) and under long time scale operating conditions these binders tend to degrade so that the catalyst loses conductivity. As a result, the aforementioned catalysts are not suitable in large scale hydrogen production and their applicability in industrial scale water electrolysis is yet to be experimentally elucidated. An ideal catalyst for alkaline water electrolysis is expected to possess high catalytic activity, superior electrochemical and mechanical stability, and low manufacturing cost. Raney nickel and stainless-steel based electrodes are prominently used in industrial scale alkaline water electrolysis due to their low cost relative to precious metals based catalyst such as Ir and Ru[87]. Although Raney Nickel and stainless steel have sufficient strength to function as a self-supported electrocatalyst, their catalytic activity towards the OER reaction is unsatisfactory. As a result, these electrocatalysts are subjected to surface modification and are often used in the form of a mesh or nano porous structure to increase the availability of active sites. Furthermore, the abundance of Ni on the earth's crust is only 0.01% and so large-scale adoption of Ni as an electrode will increase the cost of water electrolysis and often the process of synthesising Raney nickel involves chemical leaching which is expensive and time consuming [88, 89]. Hence a new methodology for designing highly efficient and low cost electrocatalysts for the OER is required to make large scale hydrogen production more affordable.

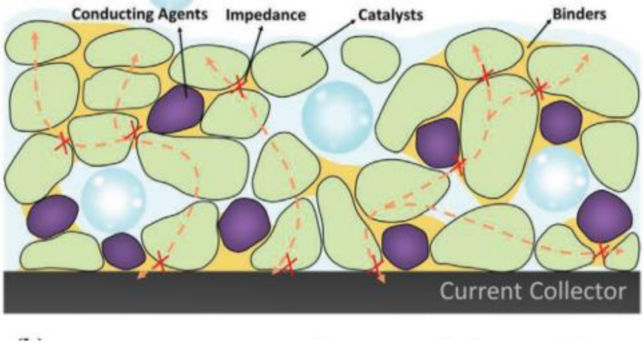

Figure 1.20 Schematic representation of coated powder based electrocatalysts reproduced from [90].

1.16 Design principles underlying the development of an efficient OER electrocatalyst

To ensure efficient operation of water electrolysis, it is indispensable to increase the density of the active sites present on the surface of the electrocatalyst. The presence of a large number of active sites can facilitate mass transfer kinetics between the electrocatalyst and the intermediates of the OER reaction such as O, OH and OOH. Several design strategies such as defect engineering[91], heteroatom doping, cyclic activation[92, 93], electronic structure tuning[94], and porosity control [95] measures have been studied in order to improve the density of the active sites and thereby improve the catalytic activity of the electrocatalyst for OER reactions. It is reported elsewhere that cyclic activation over the non-faradaic potential range will lead to formation of nano oxy/hydroxide layer and advanced in situ/operando techniques have also proven the existence of these oxide layers[96, 97]. In addition, these oxy/hydroxide layers function as active sites and improve the OER activity. The in situ formed oxide layers represent core shell structure and change the local electronic structure such as hydrophilicity, metal-oxygen covalency and co-ordination number which lead to improved OER performance[98, 99]. Several OER electrocatalysts were designed and developed based on this strategy[92, 93, 96, 97]. However, the formed oxide lacked stability and in addition to that, factor like temperature and concentration of the electrolyte were found to also play a critical role in the stability of these nano oxide layers. In industrial scale water electrolysis, the operating condition is expected to be 60°C-80°C and the concentration of the electrolyte is expected to be 30% KOH. Cyclic activation cannot be used as a technique for improving the catalytic activity in industrial scale water electrolysis. Hence it is necessary to improve the intrinsic catalytic activity of the electrocatalysts. The intrinsic catalytic activity of the electrocatalyst can be improved by two methods, one is to tune the electronic structure by altering the composition of the electrocatalyst and the other is to induce porosity on the surface of the electrocatalyst to increase the density of active sites.

The electronic structure of the electrocatalyst can be described by the following indicators: d electron count, $\mathrm{e_g}$ occupancy and metal – oxygen covalency. Among them the d electron value and $\mathrm{e_g}$ occupancy play a major role in predicting the catalytic activity, hence only these two indicators are studied in this research for predicting the catalytic activity. Shao-Horn et al. proposed a theory for predicting the OER activity through filling of $\mathrm{e_g}$ of prevoskites electrocatalysts. However, it was hard to measure this $\mathrm{e_g}$ filling experimentally and most values of these $\mathrm{e_g}$ filling were hence calculated theoretically[100].

The relationship between the catalytic activity and electronic structure also known as the d band theory was first established by Hammer and Norsok[101]. It is noted from equations 1.17-1.21 that OER is a four proton /electron transfer process. Since equation 1.18 and 1.19 are not considered as a rate determining step, the difference in Gibbs free energy of equation 1.20 and 1.21 viz $\mathrm{G_o - G_{OH}}$ can be considered as a descriptor for the OER activity. A volcanic plot can be plotted between overpotential (η) of the OER reaction vs the binding energy difference of $\mathrm{G_o - G_{OH}}$ as shown in Figure **1.21**. As per the Sabatier principle an efficient electrocatalyst should not bind the intermediates either too strongly or too weakly. The left-hand side of the volcano plot represents binding of the intermediates (OOH) while the right-hand side of the volcano plot represents the deprotonation of $\mathrm{OH^-}$. Hence the ideal electrocatalyst is expected to be present at the summit of the volcano plot.

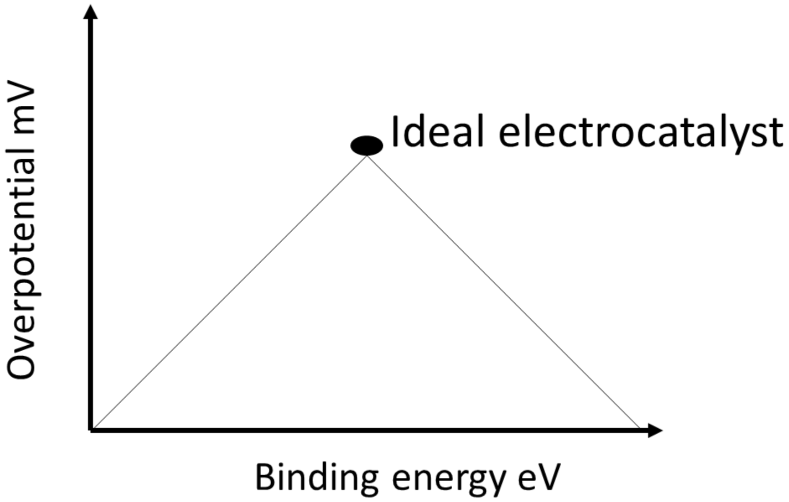

Figure 1.21 Sabatier principle for design of an electrocatalyst.

To achieve this moderate binding strength, moderate (neither too strong nor too weak) tuning of the energy level of the d band is required and the centre of gravity of the d band (d band centre) can be considered as a widely accepted descriptor for predicting the catalytic activity. In 1995, Norskov and Hammer formulated a model to describe the trends in adsorption strength of various metals based on the position of d band (energy levels)[102, 103]. This model describes the interaction between the valence states of the absorbates and the s and d states of the transition metal surface and forms the basis for prediction of catalytic activity of the catalyst in heterogenous catalysis. According to this d band model, the strength of the bond formed between the adsorbates and the transition metal surface is given by the filling of the antibonding states, and this filling is governed by the energy of the antibonding states in relation to the Fermi level. When the energy of the d states in relation with the Fermi level increases, the energy of the antibonding states increases, and consequently the bond strength between the adsorbates and the transition metal increases. This may lead to the adsorbates blocking the active sites in the catalyst, and results in poisoning of the electrocatalyst. When the energy of the d states in relation with the Fermi level decreases, the energy of the antibonding states decreases, and consequently the bond strength between the adsorbates and the transition metal decreases which as a result weakens the transition metal/absorbate bond so facilitating desorption[104]. Hence the energy of the d band relative to the Fermi level should be at an optimum level (i.e. neither too small or too large) for superior catalytic activity. The schematic representation of the d band model is given in Figure **1.22**

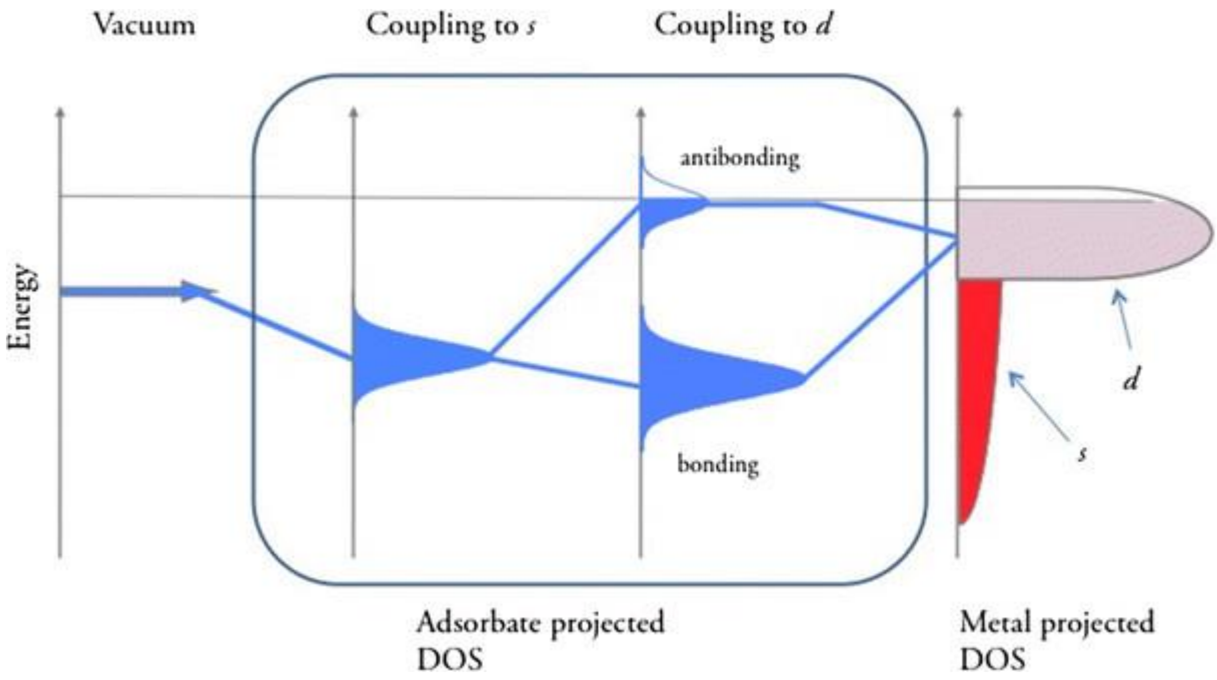

Figure 1.22 Schematic representation of d band theory[105].

The d band theory is widely accepted as the descriptor for catalytic activity, with several OER electrocatalysts being designed using this strategy[106-109]. However, all the reported works on the d band are based on theoretical calculations using density function theory, there is no reliable technique to experimentally determine the d band centre. So, an alternative method should be adopted to effectively measure the activity of the electrocatalyst. Work function is another effective descriptor for OER catalysis which can be experimentally determined. In the works of Yeong Cheon et al [110] it was established experimentally that doping heteroatom atoms like N , S and O with the mesoporous carbon electrocatalyst reduced the local work function of the electrocatalyst. The triple doped carbon exhibited superior catalytic activity when compared to double doped or mono doped electrocatalyst. From their work it was concluded that doping more atoms showed superior activity and this could be attributed to lowering of the local work function due to doping. Hence, this technique of lowering the work function by doping of heteroatoms to improve OER activity can be used for designing electrocatalysts for OER reactions.

The work function of the electrocatalyst can be determined using the valence band spectrum obtained from ultraviolet photo spectroscopy (UPS). Figure **1.23** represents the valence band spectrum of the element Au which is used to demonstrate the method for calculating the work function. The Fermi level E_f is always located at 0 eV which is represented as a step that separates the occupied and unoccupied states. The strong peaks found between 0 eV – 7eV correspond to the valence band of Au metal. The high binding energy cut off is also termed the secondary electron cut off and is located on the left side of the spectrum. Given the binding energy at the secondary electron cut off is known, it is possible to calculate the work function of the metal from the difference between the binding energy of the UV photon (He I light source) and the binding energy at the secondary electron cut off as demonstrated in equation 1.25.

$$\Phi = h\nu - E_{\text{Secondary electron cut off}} \qquad (1.25)$$

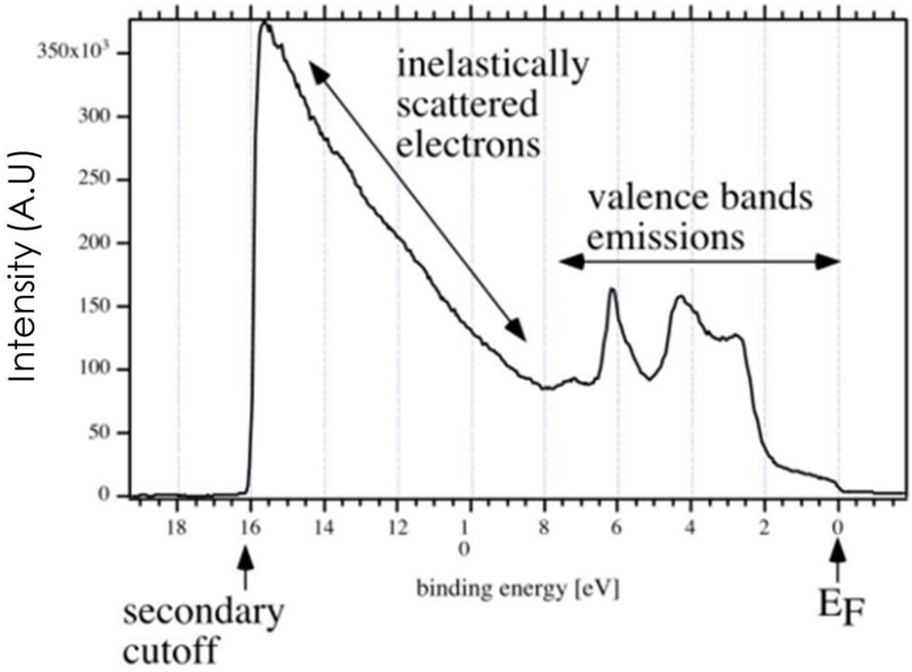

Figure 1.23 Valence band spectrum of the element Au[111],E_F – Fermi level.

To improve the intrinsic catalytic activity of the electrocatalyst, it is not only necessary to tune the chemical composition but also the structural properties (pore size, morphology) of the electrocatalyst. Several reported works on water electrolysis have proven that the presence of pores on the electrocatalyst can increase the density of active sites thereby contributing to improved catalytic activity[112, 113]. The most adopted methods to produce porous electrodes is by grafting the electrocatalyst on porous substrates such as metallic foams and carbon fibre paper[113, 114]. Although these electrocatalysts offer advantages like easy penetration of electrolyte and high gas diffusion which provides for better catalysis, they suffer from erosion of catalytic material from these substrates at larger exchange current density values (> 100 mA cm^{-2}). Another efficient method to produce porous electrocatalyst is to develop intrinsic pores in a self- supported 3-dimensional catalyst. Thermal decomposition and dealloying are the most common ways of producing intrinsic porous electrocatalysts[115]. Electrocatalysts synthesised using these routes exhibited superior catalytic properties due to the presence of porosity. Several OER electrocatalysts such as Ni based, Co based, Fe based porous electrocatalyst were synthesised using these techniques[115-117]. The mesoporous structure of these electrocatalysts offers high conductivity through easy electrolyte diffusion and the higher density of active sites facilitates better OER activity. However, these mesoporous electrocatalysts lack sufficient mechanical strength to function as a stable electrocatalyst in practical industrial water electrolysis. As a result, Ni and stainless steel are extensively used in practical industrial water electrolysis. Figure **1.24** shows the components used in industrial water electrolysis including self-supported bulk electrocatalyst(electrodes). It has been previously reported that, although Ni and stainless steel possess sufficient strength and microstructural stability under the rigorous operational stresses of practical alkaline water electrolysis, their electrocatalytic activity towards the OER is found to be unsatisfactory[87, 90]. In addition to that, the aforementioned techniques such as thermal decomposition and dealloying for synthesising electrocatalyst could not provide a sufficiently high strength and active electrocatalyst which meets the requirements of practical industrial electrocatalysis. Moreover, thermal and chemical decomposition (leaching) are expensive and time-consuming routes for manufacturing electrocatalysts. Hence to develop an electrocatalyst for industrial water electrolysis a new approach which combines strength and activity is required.

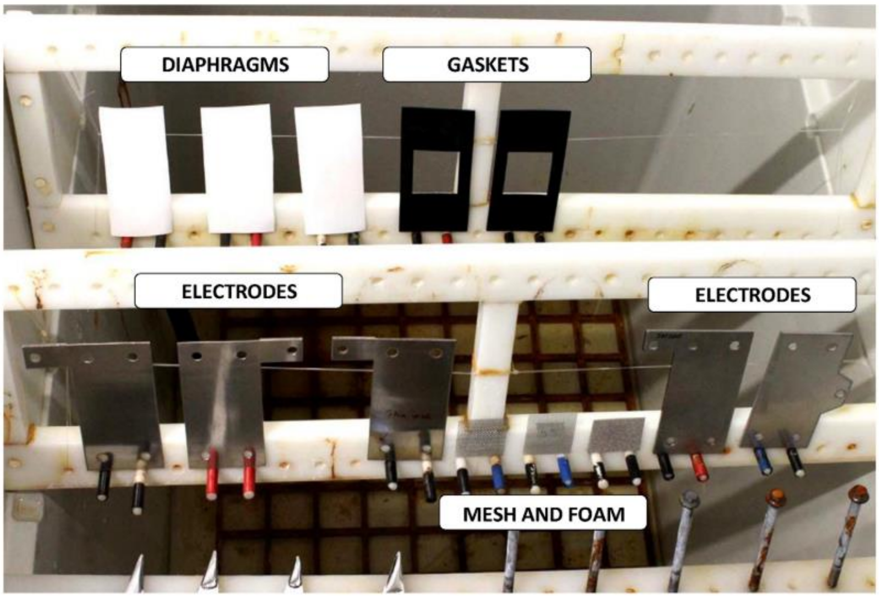

Figure 1.24 Components used in industrial water electrolysis reproduced from [118].

Powder metallurgy is an economically viable technique for producing porous materials which includes electrocatalytic materials also. Precursor materials used for synthesis of electrocatalysis are either blended or alloyed mechanically. The as- milled material is subsequently cold compacted and then sintered in a vacuum furnace. Figure **1.25** represents the proposed schematic methodology of synthesising porous electrodes intended for water electrolysis. Hence a powder metallurgy route of synthesising electrodes can provide combined high strength and a high active electrocatalyst for OER reactions. As detailed in the objectives of this PhD research, we report a unique technique which combines powder metallurgy and multi-metallic approach in designing electrocatalysts for the OER reaction which can exhibit sufficient strength and a lower work function for achieving high catalytic activity towards the OER reaction.

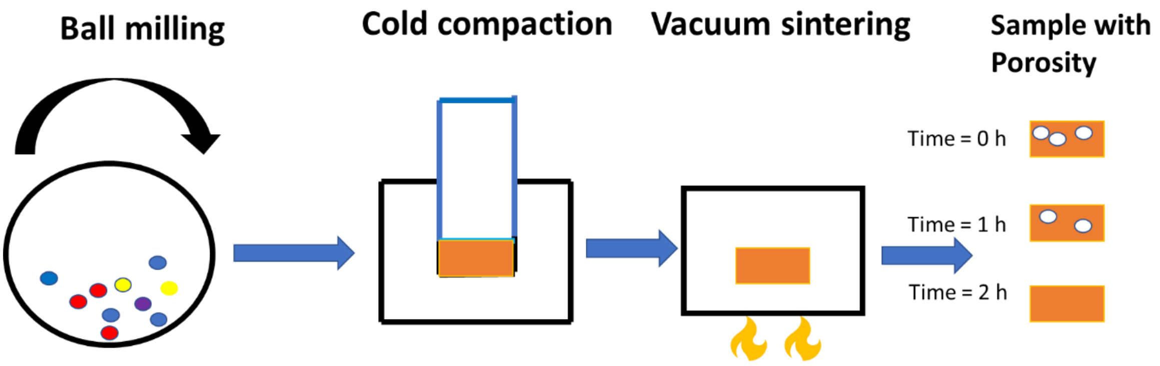

Figure 1.25 Schematic representation of synthesising of HEA based electrocatalyst for OER reaction.

1.16.1 High entropy alloys for electrocatalysis

HEAs are a multi component alloy system; so that they possess several advantages in water electrolysis applications when compared to the above discussed mono metallic or bimetallic catalytic material systems. Since HEAs constitute a complex mixture of several metallic elements arranged randomly, there are more active sites present due to this compositional randomness. This creates charge transfer (via surface adsorption/desorption process) more effectively. As a result, catalytic activity increases significantly when compared to conventional catalytic materials. It has been speculated that the synergistic effect among the constituent elements in HEAs also termed as cocktail effect also plays a crucial role in catalytic activity. Transition metals (TM) are commonly used in electrocatalytic applications due to their partially filled d orbitals. The presence of unpaired electrons in d orbitals can easily bond the ligands (OH^{-}) onto the surface of the catalyst [119]. So if these TM elements were utilized to synthesis HEAs, the synthesised HEAs are expected to have good electrocatalytic properties. The presence of a multi component system can create numerous atomic arrangements and the lattice of HEAs are distorted heavily as a result. This creates more potential energy in the HEAs, lowering the potential barrier for surface adsorption. The work function of the HEAs can be significantly lower when compared to mono metallic or bimetallic catalysts due to the vast compositional space it offers. The fine tuning of the composition of HEAs can lead to shifts in the d band centre towards the optimum values. This leads to reduction in adsorption energy between the electrode and intermediates. Hence several HEAs are specifically studied for OER activity and are briefly described below.

Dai et al.[120] synthesised HEA MnFeCoNi through mechanical alloying for water splitting (oxygen evolution reactions) applications. The as-milled HEA possessed a single-phase FCC crystal structure. Under cyclic voltammetry (CV) activation, the HEA MnFeCoNi exhibited the growth of nano-oxide sheets represented as MO_x (M = Mn, Fe, Co, Ni). As a result, the measured overpotential was 302 mV at 10 mA cm^{-2} with a Tafel slope of 83.7 mV dec^{-1} as shown in Figure **1.26**(a-b) and these overpotential values were better than as-milled HEA without CV activation and the state of the art RuO_2 based catalysts. This excellent electrocatalytic property is attributed to the formation of nano oxide sheets which resulted in a core shell structure due to CV activation. The metallic property of the HEA acted as a core while the nano oxide sheets acted as shell. This core-shell structure exposed the active sites and thereby increased the electrochemical surface area (ECSA). This core shell structure was absent in the HEA without CV activation and as a result it possessed an overpotential of 377 mV at 10 mA cm^{-2} which constituted relatively lower electrocatalytic activity when compared to an HEA with CV activation. This excellent catalytic activity was also reflected in electrochemical surface area analysis and EIS studies as depicted in Figure **1.26**(c-d)

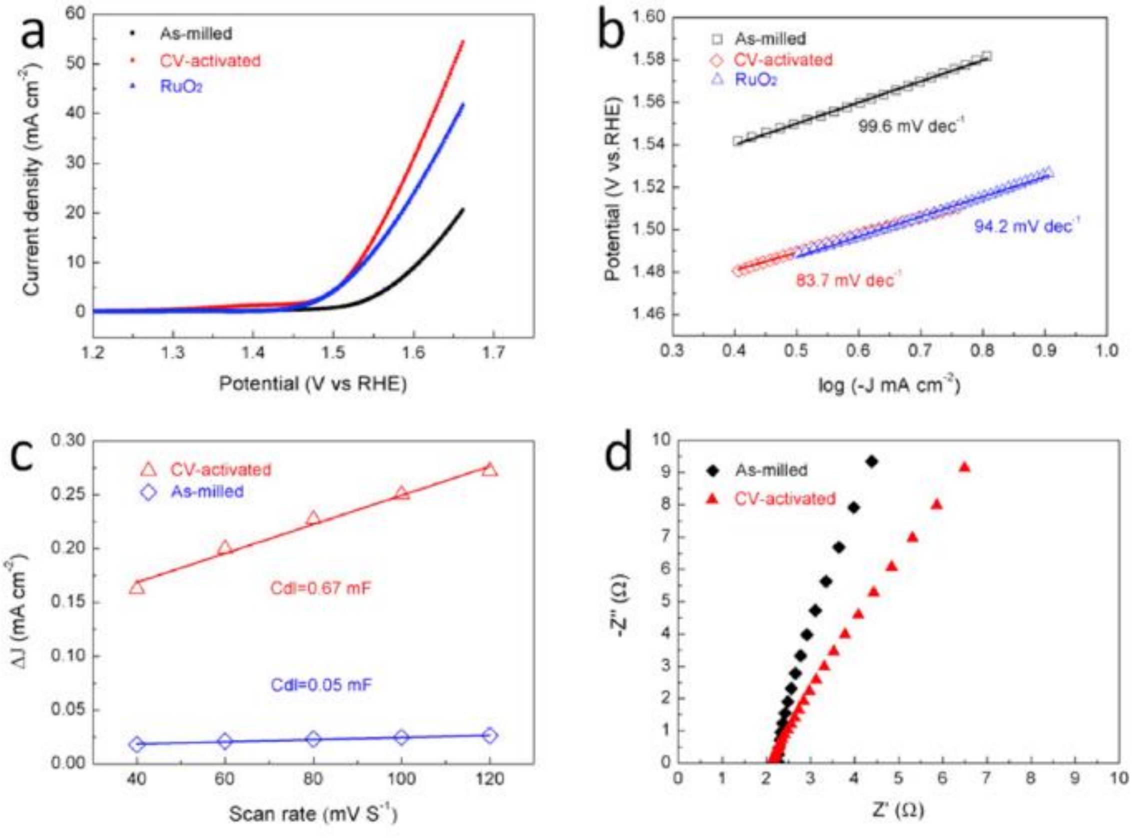

Figure 1.26 Electrocatalytic properties of HEA MnFeCoNi towards OER (a) LSV curves (b) Tafel slope (c) Double layer capacitance curve (d) EIS spectrum [120].

Tang et al. [121] synthesised HEA CoCrFeNiMo by combination of MA and microwave sintering using Mg as space holders. The sintered HEA possessed a single-phase FCC crystal structure and when the weight of the Mg space holders increased from 0 , 10 and 20 mg the catalytic activity also increased correspondingly. CoCrFeNiMo-20 mg space showed a low overpotential of 220 mV and a Tafel slope pf 59 mV/dec at the current density of 10 mA cm^{-2} while CoCrFeNiMo-0 mg exhibited a higher overpotential of 270 mV and a Tafel slope of 65 mV/dec at the same current density as depicted in Figure **1.27**(a-b). The evaluation of electrochemical impedance spectra also proved CoCrFeNiMo-20 mg exhibited the smallest semi-circle implying minimum resistance required for charge transfer and consequently faster OER kinetics. Similar results were also reflected in ECSA analysis which is shown in Figure **1.27**(c-d). The study concluded that the excellent catalytic activity is attributed to the porous structure, increase in the active sites, and to the presence of stacking faults and twin boundaries due to high energy ball milling.

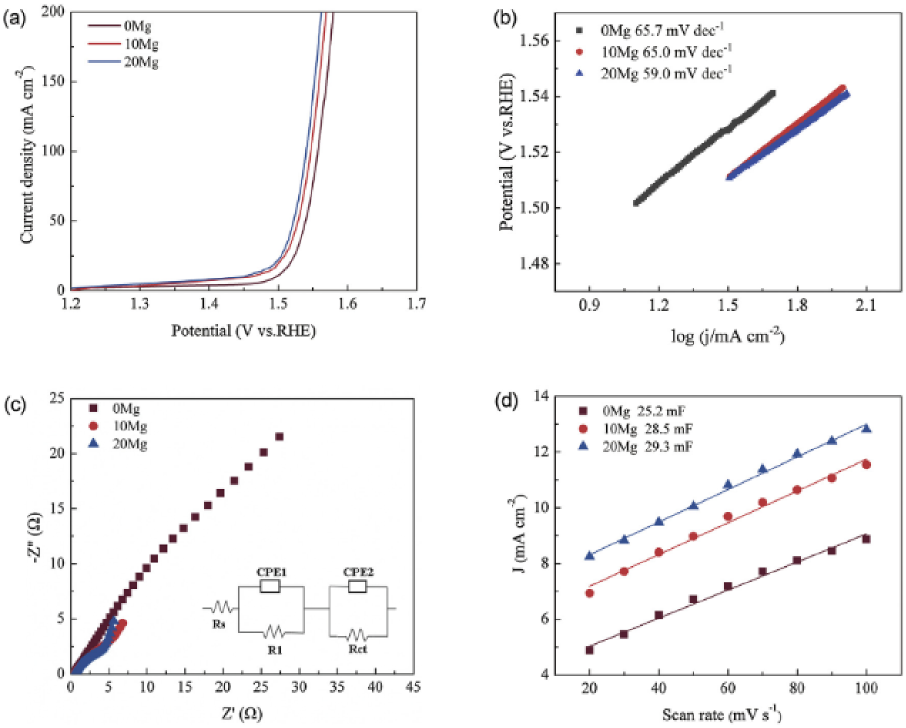

Figure 1.27 Electrocatalytic properties of HEA CoCrFeNiMo towards OER (a) LSV curves (b) Tafel slope (c) EIS spectrum (d) Double layer capacitance curve[121].

Huang et al. [122] synthesised $FeCoNiCuZn_x$ by an electrochemical reduction process of metallic oxides of the constituent elements. The synthesised HEA possessed a single-phase FCC crystal structure for values of Zn from x= 0 to 0.8. The overall catalytic activity increased as a function of Zn. The overpotential of HEA(Zn_0) and HEA ($Zn_{0.8}$) were 380mV and 340 mV and the Tafel slopes were measured to be 84mV dec^{-1} and 48 $mVdec^{-1}$ respectively as shown in Figure **1.28**(a-b). The 24 h chronoamperometry test proved the HEA($Zn_{0.8}$) showed excellent stability (Figure **1.28**(c)). The element Zn in its elemental form has no activity towards OER however, increasing the concentration of Zn increases the catalytic activity of the HEA $FeCoNiCuZn_x$. This confirms the existence of a synergy amongst the constituent elements in the given HEA[122].

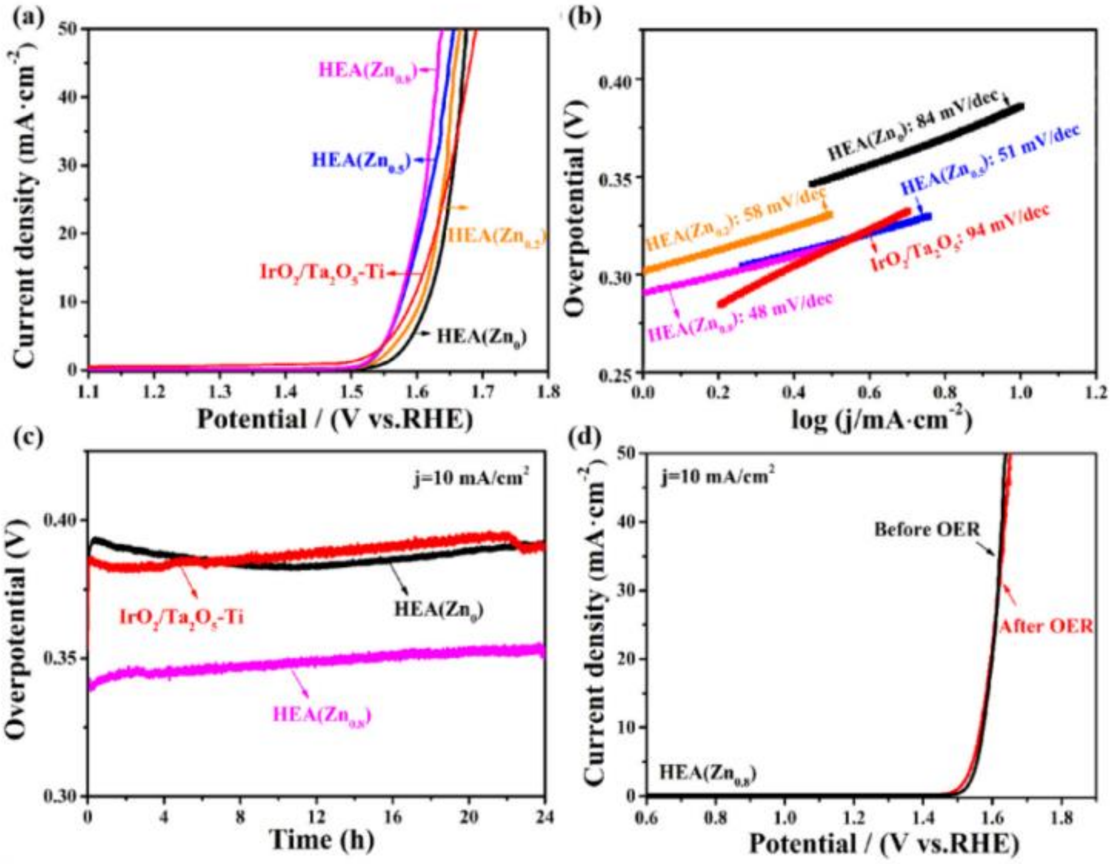

Figure 1.28 Electrocatalytic properties of HEA $FeCoNiCuZn_x$ towards OER (a) LSV curves (b) Tafel slope (c) chronoamperometry (d) Durability test[122].

Sharma et al. [108] synthesised HEA CoFeGaNiZn by cast-cum communition techniques for OER application. The synthesised HEA possessed single phase FCC crystal structure and under CV after 3000 cycles the HEA showed a low overpotential of 370 mV at the measured current density of 10 mA cm^{-2}. This excellent OER activity is due to the formation of oxide layers on the surface of the catalyst during CV. The overpotential and Tafel slopes of HEA-no cycling, HEA-3000cycles, HEA-6000cycles and RuO_2 were 370mV and 71 mV/dec , 370mV and 63mV/dec, 380mV and 63mV/dec , 430mV and 108mV/dec respectively as shown in Figure **1.29**(a-b). EIS spectra of the HEA showed smaller semi-circles for HEA so implying smaller charge transfer resistance when compared to the RuO_2 as shown in Figure **1.29**(c). The stability of the HEA was evaluated using chronoamperometry, with the HEA retaining 80% of current for the time period of 10 h, while RuO_2 retained only 15% of current as depicted in Figure **1.29**(d)

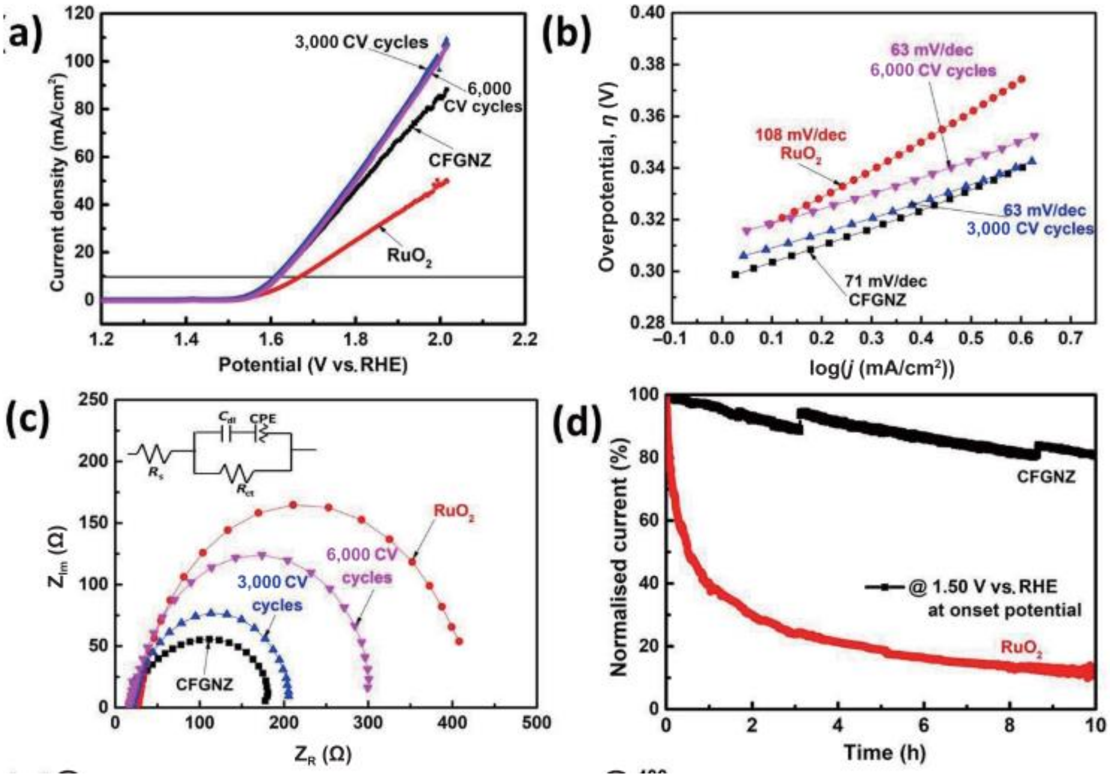

Figure 1.29 Electrocatalytic properties of HEA CoFeGaNiZn towards OER (a) LSV curves (b) Tafel slope (c) EIS spectrum (d) Chronoamperometry curve[108].

Chen et al. [123] synthesised $Fe_{50}Mn_{30}Co_{10}Cr_{10}$ high entropy alloy using a selective laser melting technique. The as-prepared HEA was treated under different sulphate containing solutions such as $CoSO_4$, $NiSO_4$ and $FeSO_4$ for 24 h, after treatment a honeycomb like nano structures were formed on the surface of the HEA. The HEA treated with $NiSO_4$ (HEA-250 Ni) solution exhibited better electrocatalytic OER properties when compared to HEA treated with other sulphate solutions. In addition to that the HEA treated with 250 mM $NiSO_4$ of exhibited exceptional OER activity with overpotentials as low as 247 mV, 313 mV and 362 mV for current densities of 10 , 50 and 100 mA cm^{-2} compared to pristine HEA and nickel foam(NF) as shown in Figure **1.30**(a). The Tafel slope of 250 mM $NiSO_4$ treated HEA was the smallest with 64 mV dec^{-1} when compared other studied materials (Figure **1.30**(b)). The C_{dl} value manifests the density of the active cites on the catalyst and 250 mM $NiSO_4$ treated HEA exhibited a C_{dl} value of 13.1 mF cm^{-2} indicating high density of active cites when compared to NF and pristine HEA as shown in Figure **1.30**(c). The EIS study indicates that the R_{ct} value of HEA-250 Ni was the lowest with 1.2 Ω compared to other studied materials as shown in Figure **1.30**(d). This further supports the superior catalytic activity of HEA-250 Ni. The CV and chronoamperometry curve shown in Figure **1.30**(e-f) illustrates that the HEA is stable under prolonged operation with negligible change in OER properties. The study proves that OER activity is increased by treating HEA with divalent Fe^{2+}, Co^{2+}, Ni^{2+}corrosive sulphate solutions.

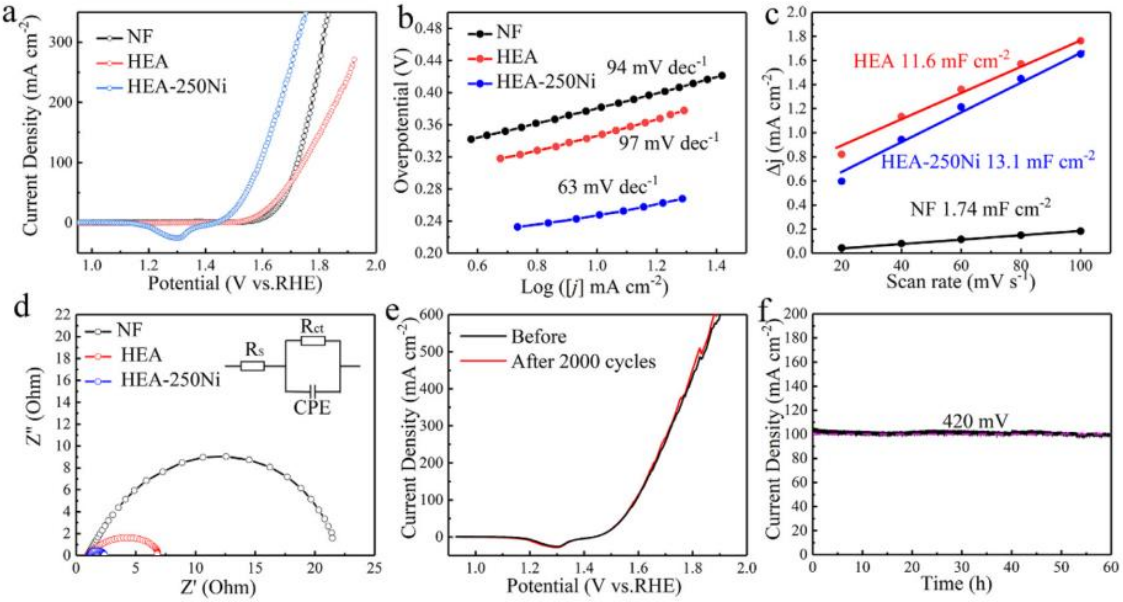

Figure 1.30 Electrocatalytic properties of HEA $Fe_{50}Mn_{30}Co_{10}Cr_{10}$ under various test conditions towards OER (a) LSV curves (b) Tafel slope (c) Double layer capacitance curve (d) EIS curve (e) LSV curve after 2000 cycles of CV (f) chronoamperometry curve[123].

Table **1.8** summarises the electrocatalytic activity of existing HEA based electrocatalysts for the OER reaction.

Table 1.8 Electrocatalytic activity of HEA based electrocatalysts for OER reactions

Catalyst	Substrate	Electrolyte	Overpotential mV	Tafel slope mV/dec
CoFeGaNiZn	GCE	1M KOH	370 @10mA cm^{-2}	71
CoCrNiFeMo	Self-supported	1M KOH	220@10mA cm^{-2}	59
MnFeCoNi	Carbon fibre paper	1M KOH	302@10mA cm^{-2}	83.7
FeCoNiCu$Zn_{0.8}$	Self -supported	1M KOH	340@10mA cm^{-2}	48
FeCoNiCu	Self -supported	1M KOH	439 @50mA cm^{-2}	50
$Fe_{50}Mn_{30}Co_{10}Cr_{10}$	Self-supported	1M KOH	247 @10mA cm^{-2}	64

1.17 Water electrolysis in sea water

The availability of highly pure water for water electrolysis especially in dry and arid regions, is a hindrance for implementing large scale water electrolysis. In addition to that , a high cost desalination unit is required to produce high purity water which will be used as a feedstock to carry out water electrolysis[124]. Hence to produce hydrogen it is necessary to rely on complicated and expensive water purification system. To avoid such dependence a readily available, low-cost feedstock is required to make water electrolysis an economically viable route for producing hydrogen. It is well known that 96.5% of the total water reserves in the world comprise seawater. Thus, direct sea water splitting can be considered as a viable process for producing hydrogen.

Since a typical water electrolysis process is a two-half-cell reaction involving release of hydrogen in the cathode (HER) and oxygen (OER) at the anode. The reaction taking place at the anode (OER) is a 4 electron/proton transfer reaction hence it is more chemically sluggish compared to HER. However, in direct seawater in addition to sluggish OER, few more challenges should also be considered. The overall salinity of sea water reaches ∼ 3.5 wt% with a pH of around 8.2[125]. In addition, the most dominant ions present in the sea water includes Na^+ and Cl^- . Hence considering the ion composition of the natural seawater, oxidation of electrochemically active Cl^- tends to compete with OER. The chlorine evolution reaction, (CER) is given by equation 1.26. Table **1.9** lists the average chemical composition of natural seawater.

$$2Cl^- \rightarrow Cl_2 + 2e^- \quad E^0 = 1.358 \text{ V vs RHE} \tag{1.26}$$

Table 1.9 Chemical composition of the natural seawater based on reference [125]

Element	Concentration range (ppm)
Cl	19,500-22000
Na	10,770-14039
Mg	1290-1490
S	905-3200
Ca	378-421
K	380-469
Br	67
C	28

The complex CER and several other reactions such as hypochlorous acid formation and the formation of hypochlorite ion are likely to happen depending upon the pH of the seawater and applied potential and these reactions are represented by means of Pourbaix diagrams in Figure **1.31**. Hence highly selective OER electrocatalysts are required to perform water splitting in natural seawater. Moreover, formation of insoluble precipitates in the solution and on the electrocatalysts surface, undesirable oxidation and reduction reactions due to metal impurities may also affect the OER process in natural sea water[126].

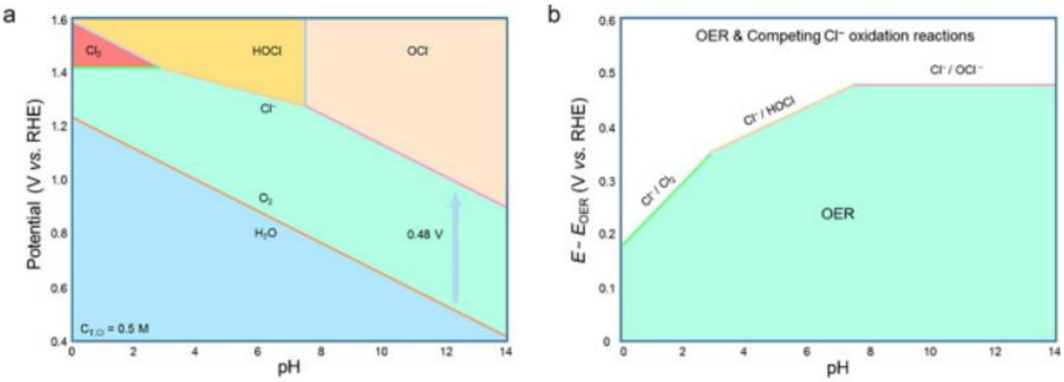

Figure 1.31 Pourbaix diagrams for saline systems.(a) Stability of 0.5 M NaCl saline electrolyte, including the H_2O/O_2 and the Cl^- /Cl^2 /HOCl/ ClO^- redox couples. (b) Maximum overpotentials (green area) allowed for an OER electrocatalyst to achieve 100% water splitting [124].

1.18 Research hypothesis and objectives

From the above discussed literature, it is evident that for efficient operation of industrial scale water splitting a highly active, cost effective and high strength electrocatalyst is required. Although transition metals (group VIII 3d) based oxides, oxyhydroxides, phosphides/sulphides are considered to be an economically viable alternative for expensive precious metal-based catalysts (IrO_2/RuO_2), they are found to suffer from severe drawbacks such as poor conductivity, mechanical stability and low activity. Moreover, these transition metal based electrocatalysts are often synthesised in powder form and coated on conductive substrates such as Ni foam, carbon fibre paper etc. Under prolonged operation, especially at high current densities, these coated electrocatalysts suffer from erosion and consequently results in loss of conductivity and activity. In addition to that, these transition metal based electrocatalysts are mono/bi/tri metallic in nature, hence offer very limited electronic structure tuning which renders and their catalytic activity at best modest. On the other hand, HEAs are multi component alloys with at least 5 elements having an atomic proportion of 5-35%, which offer a vast compositional space for effective electronic tuning. Hence, they can be considered as an alternative for mono/bi/trimetallic electrocatalysts. Several HEAs are specifically synthesised for water splitting applications using synthetic routes such as the electrochemical route, or processes involving chemical dealloying melt spin etc and these routes can incur high manufacturing costs as a result. Moreover, it is worthy to note that all the HEA combinations investigated so far contain cobalt which in itself an expensive element. As a result, the synthesised HEA itself, could still incur a high raw material cost. Hence to overcome all these research gaps this thesis will propose a cost-effective synthetic approach as a research hypothesis and step by step objectives addressing the shortcomings of the existing electrocatalysts for water splitting applications with the aim of designing/fabricating/testing a new multicomponent electrocatalyst for OER purpose.

- This thesis will investigate three Co free HEAs for electrocatalytic OER reactions namely NiMnFeCu. NiMnFeCrCu and NiMnFeCr. These investigated HEAs can potentially be a cost-effective alternative to other previously studied HEAs containing Co.
- The thesis will also explore a novel facile synthesis of HEAs which includes mechanical alloying and vacuum sintering and elucidate the role of process parameters such as sintering temperature and time on catalytic activity and mechanical strength.
- It is also the aim of the thesis to explore the role of electron spin correlated parameters such as work function among the studied HEAs on catalytic activity.
- A final aim will be to study the compatibility of the studied HEAs for water electrolysis in natural seawater media.

Chapter 2

Experimental methods

2.1 Raw materials

All the powders utilized in this work were supplied by Sigma Aldrich and were used without further purification. The details related to the purity, particle size and morphology of the precursor powders are given below.

Nickel

The particle size of the nickel powder was less than 10 μm. The morphology of the powders was spherical as shown in Figure **2.1**. The purity of the powders was greater than 99% according to energy dispersive X-ray analysis (EDS).

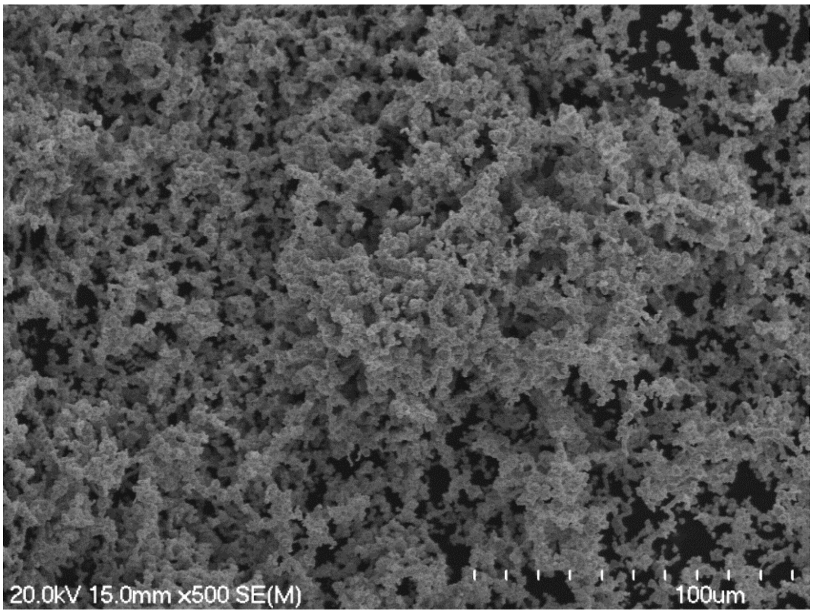

Figure 2.1 Morphology of elemental nickel powders.

Manganese

The manganese powder used in this study had a particle size of < 45μm. The chemical purity of the powder was 99.5% as confirmed by EDS analysis. The morphology of the powders was irregular as shown in Figure **2.2**

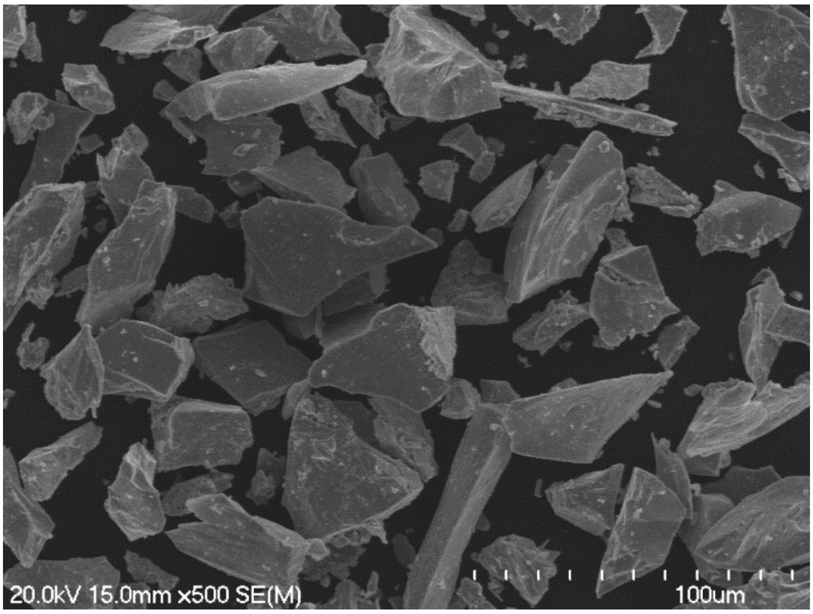

Figure 2.2 Morphology of elemental manganese powders.

Iron

The particle size of iron powder was less than 5 μm. The chemical purity of the powders was around 99.99% as measured by EDS. The morphology of the powders was spherical as shown in Figure **2.3**.

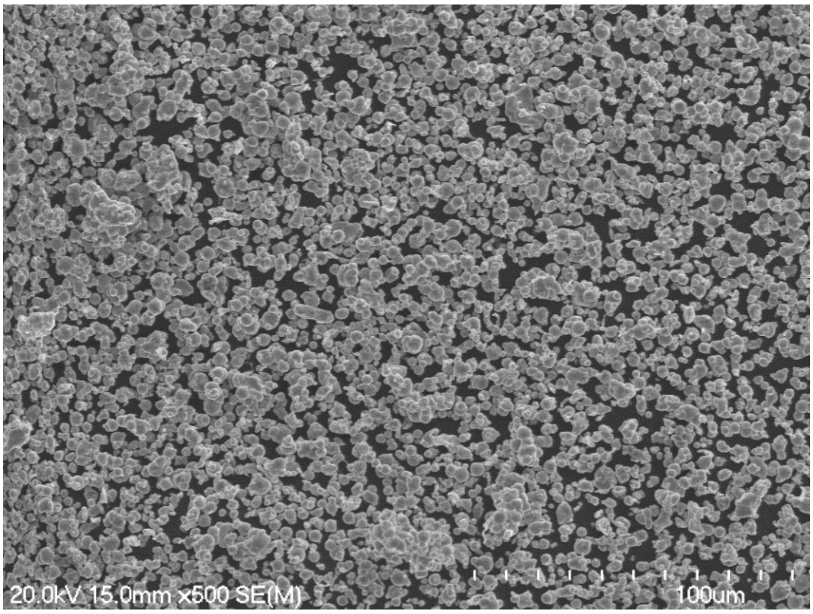

Figure 2.3 Morphology of elemental iron powders.

Copper

The morphology of the elemental copper was dendritic as shown in Figure **2.4** The purity was greater than 99% which was confirmed by EDS analysis. The particle size was around 60 μm.

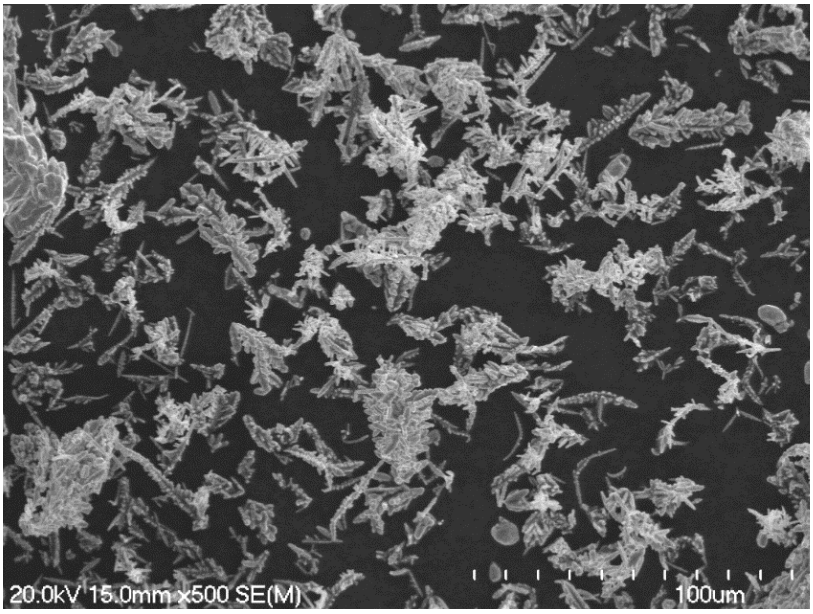

Figure 2.4 Morphology of elemental copper powder.

Chromium

The purity of chromium powder was greater than 99.5% according to EDS analysis. The particle size was around 50 to 60 μm. The morphology of chromium powders was irregular as shown in Figure **2.5**

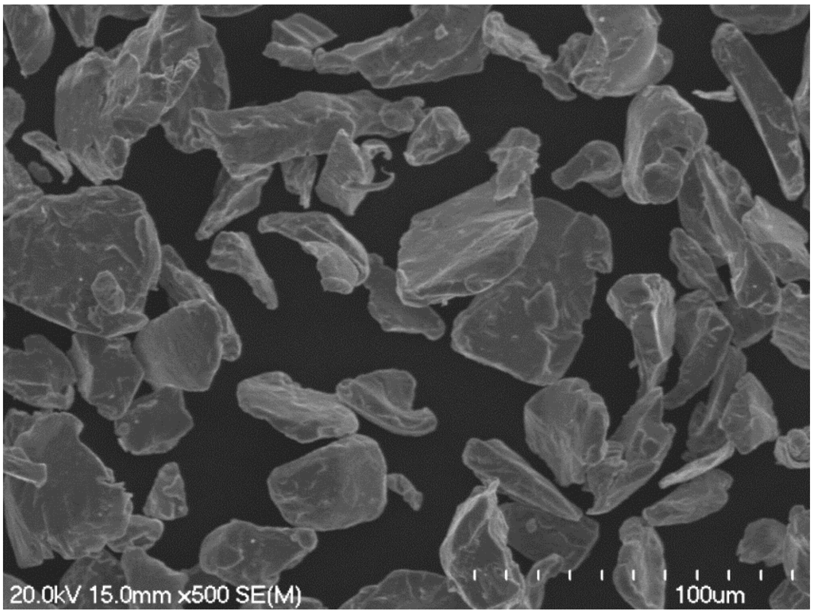

Figure 2.5 Morphology of elemental chromium powder.

The above-mentioned physical characteristics of the raw elemental powders utilized in the study are also summarised in Table **2.1**

Table 2.1 Physical characteristics of raw elemental powders.

Element	Particle size, µm	Morphology	Purity %
Ni	< 10	spherical	99
Mn	45	irregular	99.5
Fe	<5	spherical	99.9
Cr	50-60	irregular	99.5
Cu	60	dendritic	99.6

2.2 Material preparation

2.2.1 Mechanical alloying

All the metallic powders were measured out in equimolar amounts in a ratio of 1:1:1:1 (for all metals) and then placed into a stainless steel milling vial with stainless steel balls, and with a ball to powder ratio of 10:1. To avoid excessive cold welding, a process control agent (PCA, with a ratio of 3 mL ethanol (PCA) per 75 g of powder) was added to the mix. The milling vial was sealed under a protective argon gas environment. The mechanical milling was carried out using high energy ball milling equipment (Fritsch Pulverisetter-6, Oberstein, Germany) as shown in Figure **2.6,** at a speed of 350 rpm. A small amount of the milled powders was sampled from the milling vial every 5 h for analysis. The combination NiMnFeCu was utilized for optimizing the milling parameters and these optimised parameters were utilized for the other combinations namely NiMnFeCrCu and NiMnFeCr. The milling parameters utilized for various compositions used in this study are summarised in Table **2.2**

Table 2.2 Milling parameters utilized for HEAs.

Composition	Milling time h	BPR	PCA %
NiMnFeCu	20	10:1	3
NiMnFeCrCu	15	10:1	3
NiMnFeCr	15	10:1	3

Figure 2.6 Ball milling equipment Fritsch pulverisette 6 utilized in this study.

2.2.2 Cold compaction

The milled powders were cold compacted using a graphite lubricated cylindrical shaped H13 steel die under an uniaxial pressure of 700 MPa at room temperature. The density of the green compacts was measured using a mass/volume formula. The relative density was compared with the theoretical densities of each composition using the rule of mixtures (Vergad Law). The details of the green compacts of various compositions are summarised in Table **2.3**

Table 2.3 Compaction pressure and green density of the HEAs utilized in the study.

Composition	Compaction pressure MPa	Relative green density%
NiMnFeCu	700	70
NiMnFeCrCu	700	67
NiMnFeCr	700	65

2.2.3 Vacuum sintering furnace

The cold compacted green compacts were consolidated using a sintering furnace (Figure **2.7**) maintained at a vacuum of 10^{-3} Pa. The heating rate of 10 K/min was maintained. The sintering parameters were different for different compositions. Three samples on each condition were sintered to verify the repeatability of the results. The details of the sintering parameters of each combination utilized in the study are listed in the Table **2.4**

Table 2.4 Sintering parameters of HEAs utilized in the study.

Composition	Temperature °C	Time h
NiMnFeCu	1000	1
		2
	1050	1
		2
NiMnFeCrCu	1000	1
		2
	1050	1
		2
NiMnFeCr	1150	1
		2
	1200	1
		2

Figure 2.7 Vacuum sintering furnace utilized in this study.

2.3 Microstructural observation

2.3.1 Sample preparation procedure for microstructural observation

For microstructural observation of the milled powders and the sintered alloys, the samples were prepared by the following steps: (a) The powder and bulk samples were cold mounted using epoxy resin, (b) the cold mounted samples were then ground using waterproof silicon carbide papers spanning from 300 grit to 4000 grit, and (c) OP-S-brand non dry (colloidal silica) was used for the final polishing of ground samples. ImageJ was employed to carry out the microstructural analysis for evaluation of the porosity.

2.3.2 Scanning electron microscopy

Microstructural observation was carried using the scanning electron microscopy (SEM, Hitachi S4700) equipped with energy dispersive spectroscopy with an accelerating voltage of 20kV in secondary electron and back scattered electron mode. Energy dispersive X-ray (EDS) analysis was performed to investigate the chemical homogeneity.

2.3.3 Optical microscopy

Microstructural observation was carried out using the optical microscope (OM, Olympus BX 60) in bright field mode (Figure **2.8**). Image J software was used to study the pore size, morphology and pore area.

Figure 2.8 Olympus BX 60 optical microscope utilized in this study.

2.3.4 X-ray diffraction analysis

A Panalytical Empyrean X'pert (X-ray powder diffractometer, Malvern, United Kingdom) with Cu Kα (λ = 0.154157 nm) radiation was used to identify the crystal structure of the milled powders and the as-sintered samples. A step size of 0.01° was used for a regular scan while a slow scan of 0.003° step size was used to acquire higher resolution scans of the most intense peaks for the purpose of determining crystallite size and lattice strain. The Scherrer equation was used to calculate the crystallite size and Williamson Hall equation equation was used to find the lattice strain[127]. The most intense peak of each phase detected in the HEA were fitted with the Caglioti function, which was utilized for quantifying the phase composition of the HEA via the use of equation (2.1)

$$\mathrm{X_k} = \frac{\mathrm{I^{h_k k_k l_k}}}{\sum \mathrm{I_k^{h_k k_k l_k}}} \tag{2.1}$$

where $\mathrm{X_k}$is the volume fraction of $\mathrm{k^{th}}$ phase and $\mathrm{I^{h_k k_k l_k}}$ is the integrated intensity of $\mathrm{h_k k_k l_k}$ plane.

2.3.5 Transmission electron microscopy analysis

A field emission transmission electron microscope (FETEM, JEM-2100 F, 200kV, China) was utilized for further studying the microstructure of the as-sintered HEAs. Initially the sample was manually ground down to a thickness of ~60 μm using SiC papers and punched into a 3mm disc. To obtain an electron transparent region for analysis the disc was further polished using a twin jet polishing method with an electrolyte consisting of 20 vol% $\mathrm{HClO_4}$ and 80 vol% $\mathrm{C_2H_5OH}$ under a temperature of -30°C and with an applied voltage of 20V.

2.4 Physical analysis

2.4.1 Thermal analysis

Differential scanning calorimetry (DSC) analysis was carried out using a NETSCH (Netzsch Jupiter STA 449 F5) thermogravimetric instrument as shown in Figure **2.9**. 50 mg of the milled powder placed in alumina crucible was used with a heating rate of 10ºC/min under argon purging. The heating was carried out from room temperature (25°C) to 1400°C.

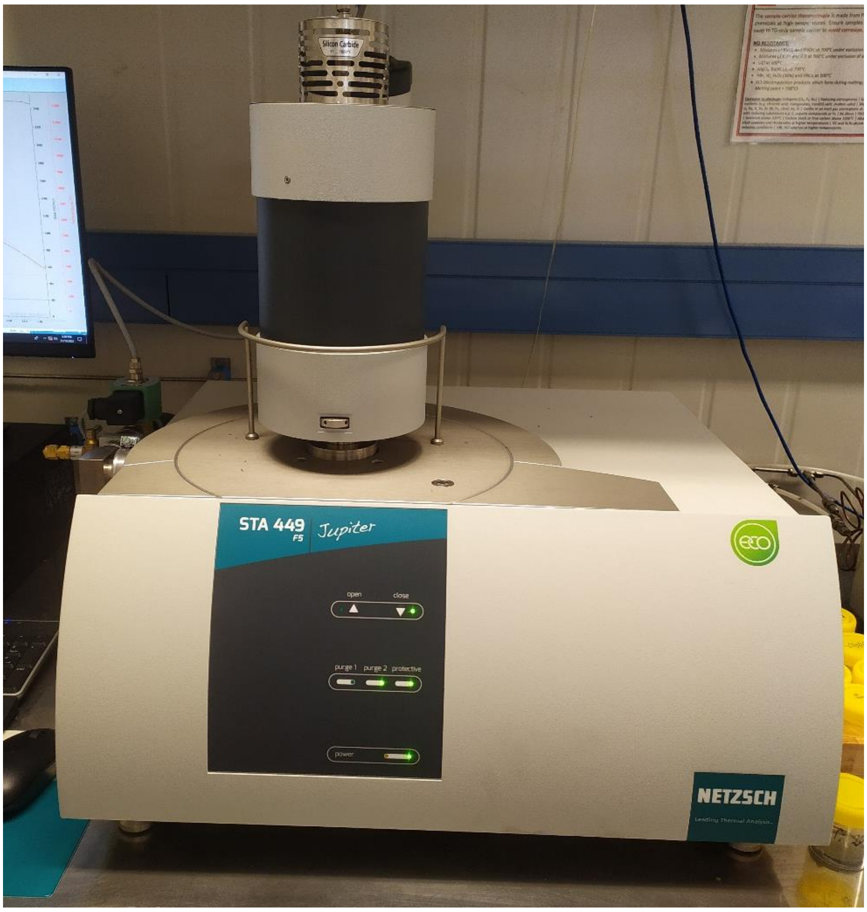

Figure 2.9 NETSCH Jupiter STA 449 F5 thermogravimetric instrument used in this study.

2.4.2 Particle size analysis

The particle size of the as-milled powders was analysed using a Mastersizer 3000 (Malvern U.K) with distilled water as dispersant and the refractive index of the distilled water was 1.33. The stirrer speed was maintained at 300 RPM. Three readings were acquired and the average values of D50 were taken as the final average particle size.

2.4.3 Density measurement

The theoretical density of the sintered samples was calculated using the formula given below.

$$\rho_{\mathrm{theoretical}} = \frac{\sum \mathrm{C_i A_i}}{\sum \frac{\mathrm{C_i A_i}}{\rho_\mathrm{i}}} \tag{2.2}$$

where $\rho_{theoretical}$ is the theoretical density of the HEA, $\mathrm{C_i}$, and $\mathrm{A_i}$ are the mole fraction and atomic mass of the constituent elements while ρ_i is the density of each constituent element.

The green density was calculated using the equation 2.3.

$$\text{Green Density} = \frac{\text{Mass of the green compact}}{\text{Volume of the green compact}} \tag{2.3}$$

The relative green density (RGD) was calculated using the equation 2.4.

$$\text{RGD} = \frac{\text{green density}}{\text{theoretical density}} \tag{2.4}$$

The relative sintered density (RSD) was calculated using a gas pycnometer and the Archimedes method using the equation 2.5.

$$\text{Relative sintered density} = \frac{\text{sintered density}}{\text{theoretical density}} \tag{2.5}$$

2.5 Mechanical testing

2.5.1 Microhardness

Vickers micro-hardness measurements were conducted using a micro-hardness tester (LM-700, Leco Ltd.) (Figure **2.10**) under a load of 1kgF (9.80 N) for 15 s. Measurements were performed on 10 different locations of the sample and the mean and standard deviation of the values were taken as the final hardness value.

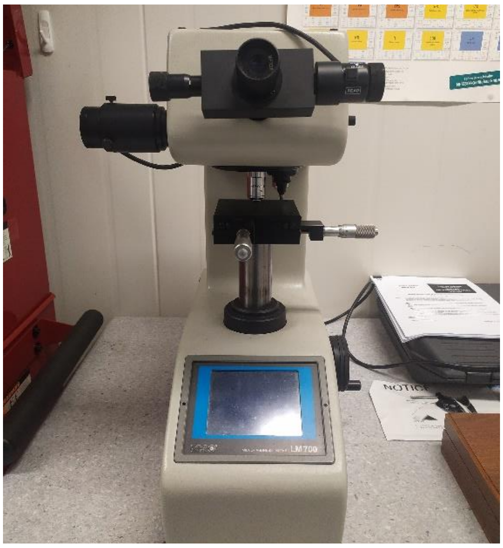

Figure 2.10 Leco LM microhardness tester utilized in this study.

2.5.2 Compression test

Cylindrical specimens (4 mm diameter, 6 mm height) were used for compression testing at room temperature using a universal testing machine (Instron 5982) with a strain rate of 10^{-3} s^{-1}. Two samples were tested, and their mean and standard deviation of compressive yield stress values were recorded.

2.6 Ultra-violet photo spectroscopy

The as-sintered HEAs were sectioned in dimensions 5x5 mm and utilized for ultraviolet photo spectroscopy. The valence band spectra of the HEAs were obtained using He I light (21.2 eV) source on a Thermo Scientific -ESCALAB X-ray photoelectron Spectrometer, China with a sample bias of -5 eV. The work function ϕ was measured by the difference of the photon energy of the He I light source with the binding energy of the secondary electron cut off.

2.7 Electrochemical measurements

Electrochemical measurements were carried out using an eDAQ e-corder 410 electrochemical potentiostat,(New South Wales , Australia) with a standard three-electrode system setup. The as-sintered HEAs (dimensions, 10 mm X 10 mm) were used as the working electrode, with a Pt wire as the counter electrode, and a standard Ag/AgCl (Radiometer red rod) as the reference electrode with experiments being conducted in 1 M KOH electrolyte solutions (Figure **2.11**). In addition to that natural seawater with a pH of 8.2 was also used as an alternative electrolyte. The potential(voltage) data were converted to reversible hydrogen electrode (RHE) reference values via to the equation E(RHE)= (E(Ag/AgCl) +0.0591pH + 0.197V), and the pH of the electrolyte was measured using an electronic pH meter with the pH being found to be approximately 13.8. The electronic pH meter was calibrated with a standard buffer solution of pH 10. Linear sweep voltammetry (LSV) was performed to measure the overpotential of the oxygen evolution reaction (OER) on samples with a scan rate of 5 mV s^{-1}. The overpotential (η) was measured using the formula η= E(RHE)-1.23V. The Tafel slopes were derived from the linear region of the LSV curves and fitted using the Tafel equation η= blogj + a (where b is the Tafel slope and j is the current density and a is an intercept related to current density). Cyclic voltammetry (CV) was carried out over the potential range 1.0-1.6 V vs RHE for 100 cycles at the scan rate of 100 mV s^{-1}. Double-layer capacitance values (C_{dl}) were determined by CV curves over a potential window of 1- 1.06 V vs RHE at scan rates of 20, 40 , 60 , 80 and 100 mV s^{-1}. C_{dl} was determined using the plot of ΔJ = J_{anode}- $J_{cathode}$ at 1.03 V vs RHE against the scan rate. The electrochemical surface area

ECSA was determined using the formula ECSA = C_{dl}/C_S , where C_S is the specific capacitance which is equal to 0.040 mF cm^{-2} [120]. Electrochemical impedance spectroscopy (EIS) was performed to measure the charge transfer resistance (R_{ct}) and solution resistance (R_s) using the Solartron 1260a between the frequency range of 0.01 - 10^5 Hz at an AC amplitude of 1.6V vs RHE.

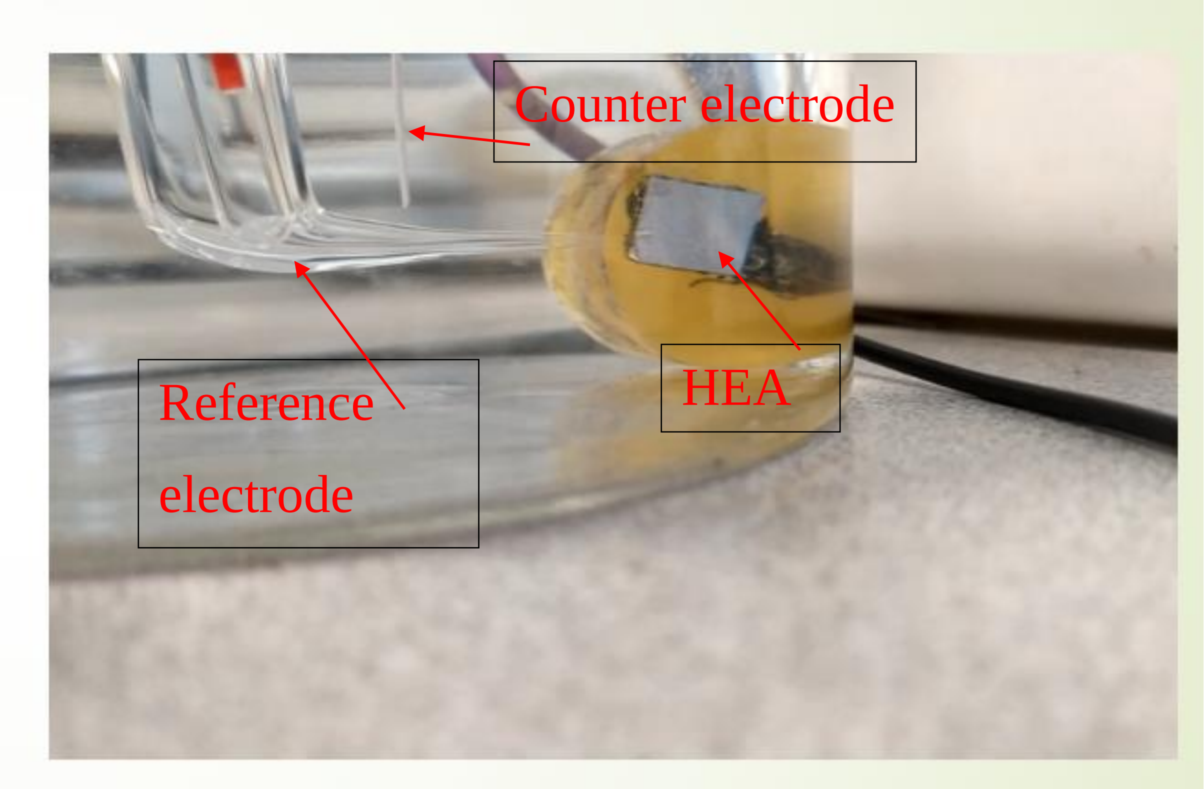

Figure 2.11 Experimental setup of the three-electrode system used in the present study.

Chapter 3 Mechanical alloying-Results & Discussion

3.1 Synthesis of HEA NiMnFeCu

3.1.1 Phase predictions in HEA NiMnFeCu

Phase prediction in HEAs is critical to attain desired structural and functional properties. As mentioned in section **1.7** phase formation in HEAs depends upon several factors like atomic size misfit δ, mixing enthalpy ΔH_{mix}, configurational entropy ΔS_{config}, valence electron concentration (VEC), and the weighted ratio Ω. These parameters are calculated using equations **1.5-1.10** and Table **3.1** presents the physico-chemical parameters and binary mixing enthalpies of the HEA NiMnFeCu. Table **3.2** summarises the calculated thermodynamic and geometric parameters for the HEA NiMnFeCu. The calculated values fall within the threshold range for solid solution formation with FCC crystal structure as described in section **1.7**, hence HEA NiMnFeCu is predicted to form a single phase random solid solution with FCC crystal structure.

Table 3.1 Physico-chemical and binary mixing enthalpies (kJ/mol) of the constituent element in HEA NiMnFeCu [21, 30].

Element	Ni	Mn	Fe	Cu
Melting point ˚C	1453	1519	1538	1083
Atomic radius(pm)	124	135	126	128
Electronegativity (Pauling)	1.8	1.55	1.8	1.9
Ni	Ni	-8	-2	4
Mn		Mn	0	4
Fe			Fe	13
Cu				Cu

Table 3.2 Calculated thermodynamic and geometric parameters for HEA NiMnFeCu.

HEA	ΔS_{config} J/K.mol	ΔH_{mix} kJ/mol	δ	VEC	Ω
NiFeMnCu	11.526	2.75	3.4	9	6.7

3.1.2 Effect of milling time on phase evolution of HEA NiMnFeCu

Figure **3.1** depicts the XRD patterns of the milled NiMnFeCu alloy powders at a time interval of 5 h of mechanical milling. After 5 h of mechanical milling, the peaks of the individual starting elemental powder disappeared completely and only the principal diffraction peaks at 2θ values 42.8˚, 49.7˚, 73.19˚, 88.6°and 94.2˚ could be seen. These peaks are indexed as (111), (200), (220), (311) and (222) and correspond to a solid solution with a single-phase FCC structure. On continuation of milling the powders for times extending to 10, 15 and 20 h, the principal diffraction peaks of FCC crystal structure remain unchanged. This implies that the NiMnFeCu HEA forms after 5 h of milling and this phenomenon is attributed to the dissolution of the starting elements and formation of the solid solution[128]. Continuous milling to extended times of 10, 15 and 20 h caused no further change in the diffractions peaks which suggests that there is no further phase change. It is reasoned that the formation of the FCC phase in the studied NiMnFeCu HEA could be due to the presence of excessive FCC forming elements, since the alloying elements could be grouped into two categories: one is the FCC forming elements such as Cu, Ni, Co, Mn; and the other is the BCC forming elements such as Al, Cr, W, Fe and V[129]. In addition, the calculated VEC of HEA NiMnFeCu was 9, as discussed in the section **1.7**, and this factor also led to the formation of the FCC structure in the studied HEA.

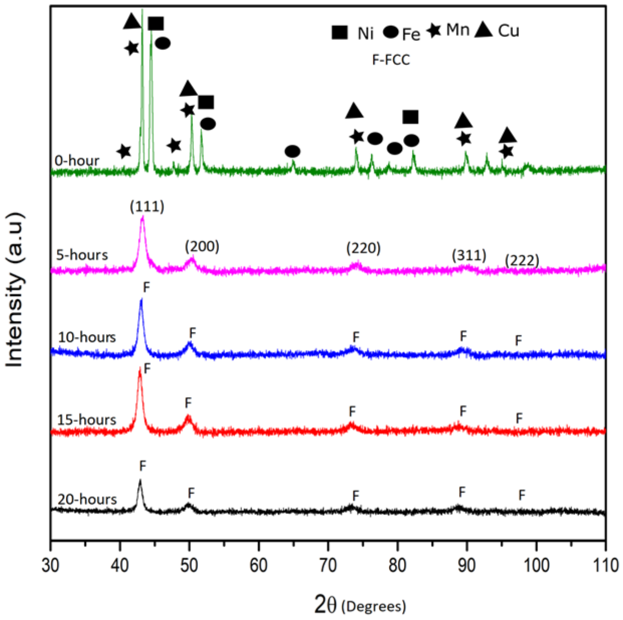

Figure 3.1 X ray diffraction patterns of the milled NiMnFeCu HEA powder as sampled after a time interval of 5 h (milling time).

3.1.3 Effect of milling time on crystallite size and lattice strain of NiMnFeCu powders

Figure **3.2** illustrates the effect of milling time on crystallite size (CS) and lattice strain (LS) of NiMnFeCu powders. It is evident that when the milling time is increased until 10 h (of milling), the crystallite size is decreased significantly, after 10 h of milling there is only a minor decrease in the crystallite size. Similarly, the lattice strain is increased significantly until 10 h of milling while there was only negligible increase in the lattice strain for milling times of 10 to 20 h. The full width at half maximum (FWHM) of the (111) peak increases continuously as a function of milling time. Table **3.3** summarises the changes in crystallite size and lattice strain as a function of milling time in NiMnFeCu powder.

A continuous increase in FWHM values resulted in a decrease in CS and an increase in LS. This could be attributed to accumulation of dislocation density owing to severe plastic deformation during high energy ball milling [130]. After 10 h of milling there is only a negligible decrease in CS and a negligible increase in LS. This negligible change of LS and CS during the final phase of milling could be attributed to a phenomenon termed "dynamic balance" in which only a minor change in CS and LS is possible in the milled HEA powders[131].

Table 3.3 Effect of milling time on crystallite size and lattice strain of NiMnFeCu powders.

Milling time h	FWHM °	Crystallite size nm	Lattice strain %
5	0.578	14.6	2.44
10	0.748	10.8	3.47
15	0.800	10.5	3.55
20	0.823	10.2	3.66

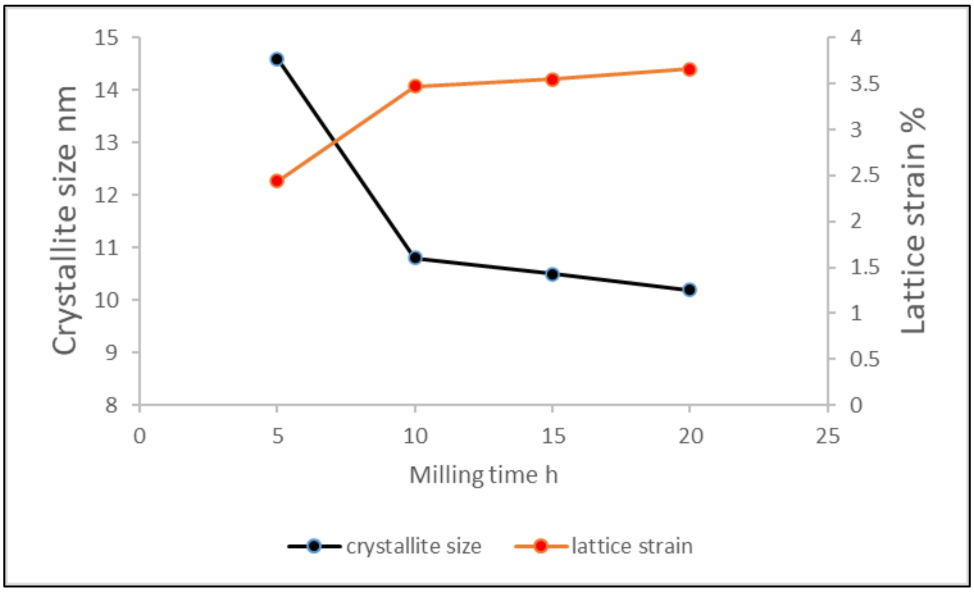

Figure 3.2 Effect of milling time on crystallite size and lattice strain of milled NiMnFeCu powders.

3.1.4 Effect of milling time on particle size and powder yield of NiMnFeCu powder

Figure **3.3**(a-d) shows the morphology of the raw elemental powder and Figure **3.3**(e-h) depict the morphology of the milled NiMnFeCu powders. It is clearly seen that the raw elemental powders have different morphologies (Mn-irregular, Fe-spherical, Cu-dendritic, Ni-spherical). The average particle indicated as D50 signifies 50% of particle volume[132]. After milling for 5 h, the morphology of the milled powders shows irregular shapes and the measured powder particle size is observed to be about 105 microns(D50). After prolonging the milling time to 10, 15, and 20 h, the morphology of the milled HEA NiMnFeCu remains unchanged, however the particle size changes dramatically. With an increase in the milling time, the particle size of the milled powders decreases continually, with a value of 99.3 microns(D50) observed for the 10 hour milled powders, 73.2 microns(D50) for the 15 h milled powders and 42 microns(D50) for the 20 h milled powders respectively. The variation of powder particle sizes for the milled powders as function of milling time is presented in Figure **3.4** (the average particle size of the starting powders was measured to be about 20 microns (D50)).

Table **3.4** summarises the effect of milling time on the powder yield of NiMnFeCu. It can be seen that the powder yield after 5 h of milling is very low, only reaching 44%. With increasing the milling time, the powder yield continually increased. The powder yield is over 90% after 15 h of milling, and after 20 h milling time the powder yield reaches 97%.

The significant increase of the milled powder particle size from 20 microns (average particle size of starting powder) to 105 microns (for 5 h milled powders) suggest that the milling is only at its initial stages within the 5 h of milling. This implies that the cold-welding effect is dominant at this stage, and this causes the particle size to be coarsened. The low powder yield also confirms that the powders were severely stuck on the balls and the vial because of the cold-welding effect as shown in Figure **3.5**(a), and that with an increase in the milling time the powder is continually deformed and work hardening effects became severe, this leads to the milled powder becoming fractured[131]. This explains the phenomenon that the milled powder particle size is slightly reduced after 10 h of milling compared to that of the powder milled after 5 h[54]. With further increase in the milling time , the fracture phenomenon of the milled powders takes on a more dominant role than the cold welding effect, and this leads to the particle size of the milled powders to continually decrease[131]. Due to the increased fracturing, during the final phases of milling the powder yield increases as a function of milling time. Hence only a negligible amount of powder was seen sticking on the balls and on the vial as shown in Figure **3.5**(b). Although a HEA solid solution phase is formed at 5 h of milling, it is nevertheless highly beneficial to mill for up to 20 h in order to guarantee a high powder yield (97%) and finer particles which will have a high driving force during the sintering process.

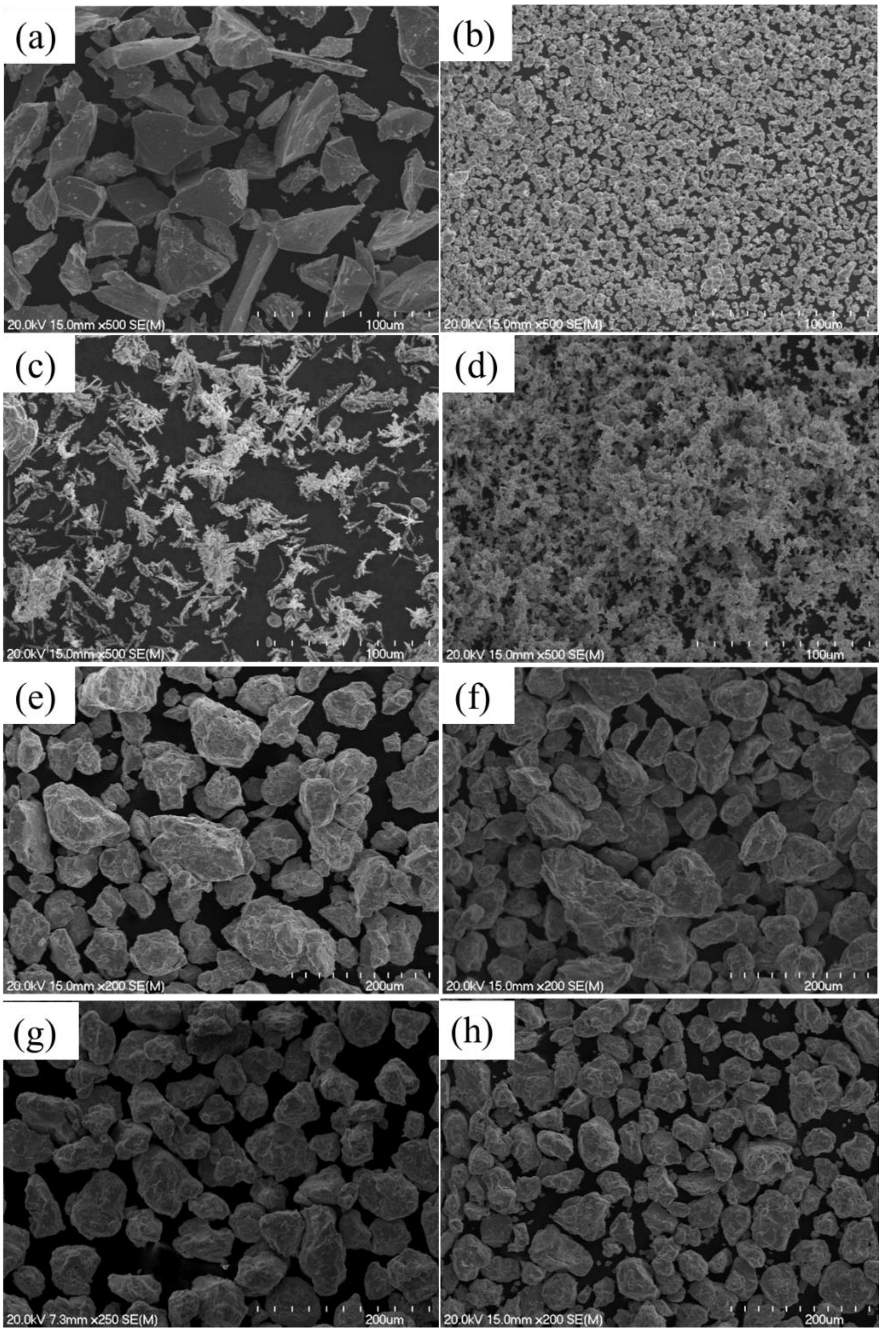

Figure 3.3 SEM images of the elemental and milled HEA powders (a) Mn (b) Fe (c) Cu (d) Ni (e) 5h (f) 10h (g) 15h h) 20h.

Table 3.4 Effect of milling time on powder yield of NiMnFeCu powders.

Milling Time Hrs	Weight of the Vial grams	Weight of the Balls	Powder Yield %
0	3123	700	-
5	3143	720	44
10	3133	715	64
15	3125	702	90
20	3124	701	97

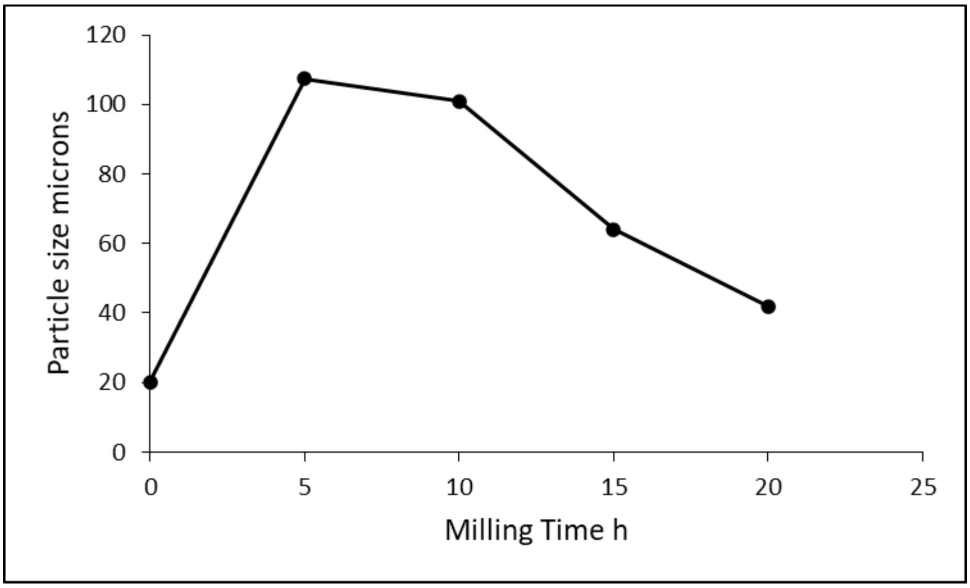

Figure 3.4 Variation of particle size as a function of milling time of NiMnFeCu powders.

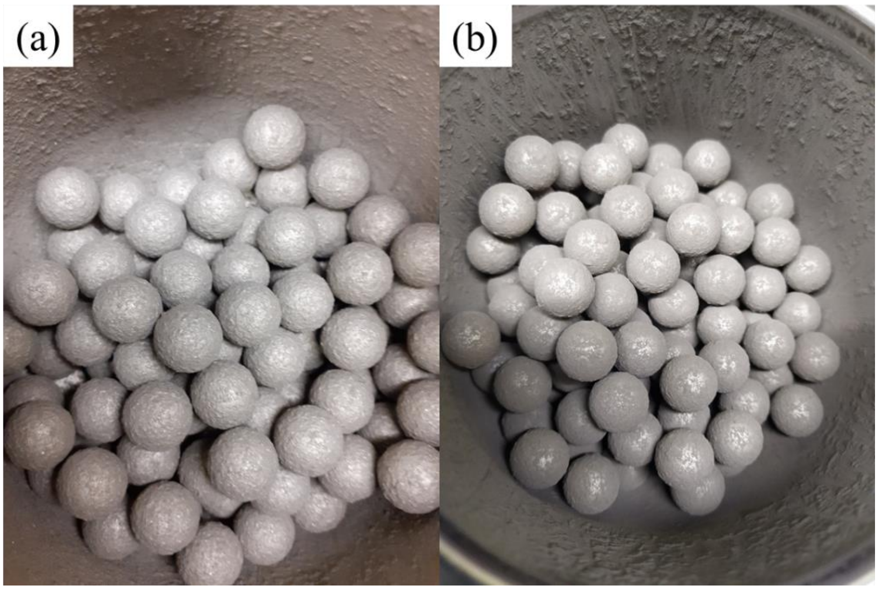

Figure 3.5 Photographs of the milling balls (a) at 5 h and (b) at 20h (of milling time).

Figure **3.6** depicts the SEM/EDS map of the milled HEA NiMnFeCu powders at various time intervals. The SEM/EDS maps reveal that the chemical homogeneity remain unchanged throughout the time period of milling. The full area scans reveal that the measured atom % of the milled HEA is very close to the nominal composition until the end of the 5 h milling time as listed in Table **3.5**. When prolonging the milling to 10 and to 15 h, there is no significant change noticed in the chemical homogeneity of the powders. At a 20 h milled state, the concentration of Fe in the powder increases significantly as shown in Table **3.5**. This increase of Fe after 20 h of milling could be attributed to erosion or dislodging of material from the milling media (balls and vial) due to the longer milling time. Hence it could be concluded that milling for more than 15 h leads to addition of impurities from the milling media, and there is a need to moderate the milling time to 15 h to minimise occurrence of this erosion.

Table 3.5 Measured elemental composition of the milled HEA NiMnFeCu powders at various milling time.

	Ni	Mn	Fe	Cu
Nominal atom % (full area scan)	25	25	25	25
5 h	25.01	22.46	25.16	25.57
10 h	24.56	24.99	24.51	23.94
15 h	24.53	26.33	26.34	22.80
20 h	22.81	26.37	29.67	20.71

.

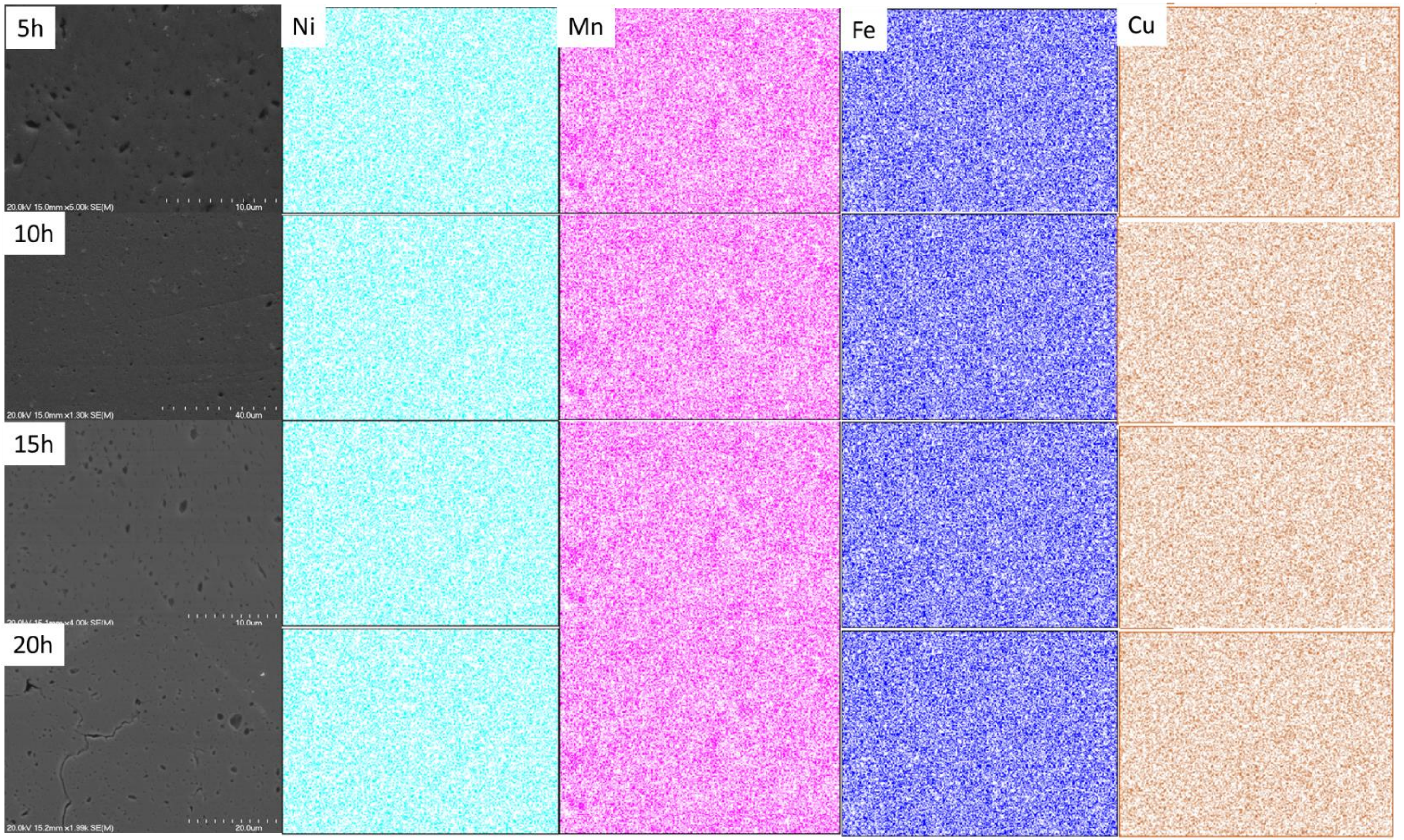

Figure 3.6 SEM/EDS map of the milled HEA NiMnFeCu powders after (a) 5h (b)10h (c)15 h (d) 20h of milling.

3.1.5 Effect of the process control agent (PCA) on powder yield and particle size of the HEAs

Figure **3.7** depicts the effect of PCA concentration on particle size distribution of the milled NiMnFeCu powders when milled for 15 h. It is clearly observed that when the PCA concentration increases, the particle size distribution curve moves towards the left indicating a decrease in the average particle size. The average particle size (D50) was 110 µm when no PCA is added. The average particle size D50 value decreases to 99 µm when 1% PCA is added. The average particle size further decreases to 62µm and 33µm for 2% and 3% of added PCA respectively.

During high energy ball milling the powder particles are trapped between the balls as a result of the repeated ball to ball and ball to vial collisions, this leads to defects (dislocations) in the particles. As a result, the milled powder particles have a high surface activity. This increases the tendency of the particles to agglomerate (cold welding) especially in ductile-ductile systems. Hence as a result of this excessive cold welding the D50 value of 0% PCA was 110 µm and the powder yield was only 40% (Figure **3.8**) due to the heavy coating of the powder particles on the milling media as shown in Figure **3.5**(a) earlier. When the PCA concentration is increased to 1% the D50 value decreases to 99. 99 µm when compared to 0% PCA and the powder yield also increased slightly to 60% (Figure **3.8**). Increase in the concentration of PCA to 2 and 3% leads to a decrease in the average particle size to 62µm and 33 µm and improves the powder yield to 80% and 97% respectively as shown in Figure **3.8**. This phenomenon could be attributed to the fact that PCAs minimize metal-to-metal contact during milling and hence mitigate the excessive cold welding[133, 134].

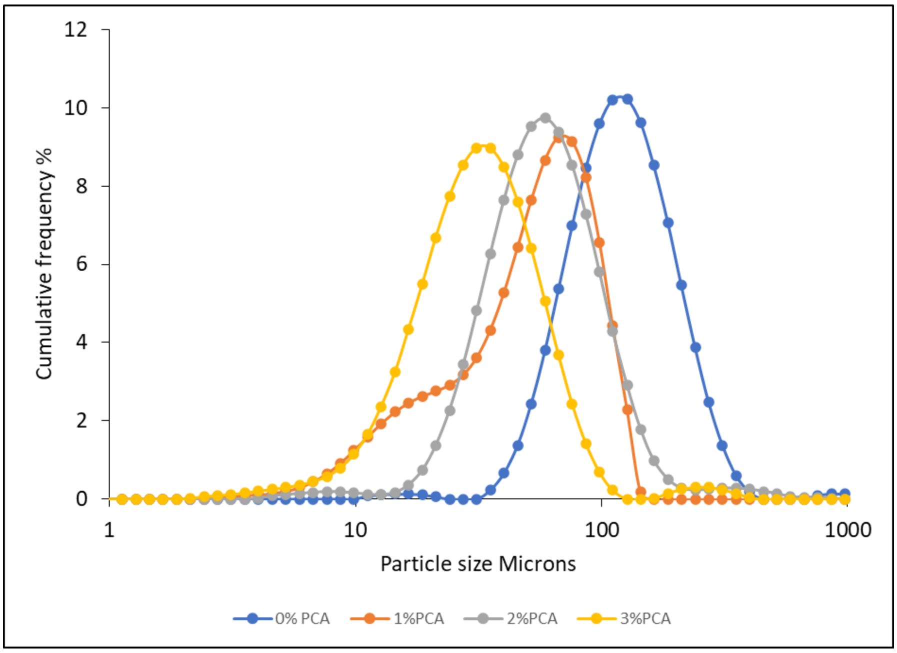

Figure 3.7 Effect of PCA concentration on particle size distributions of the milled NiMnFeCu powders after a milling time of 15 h.

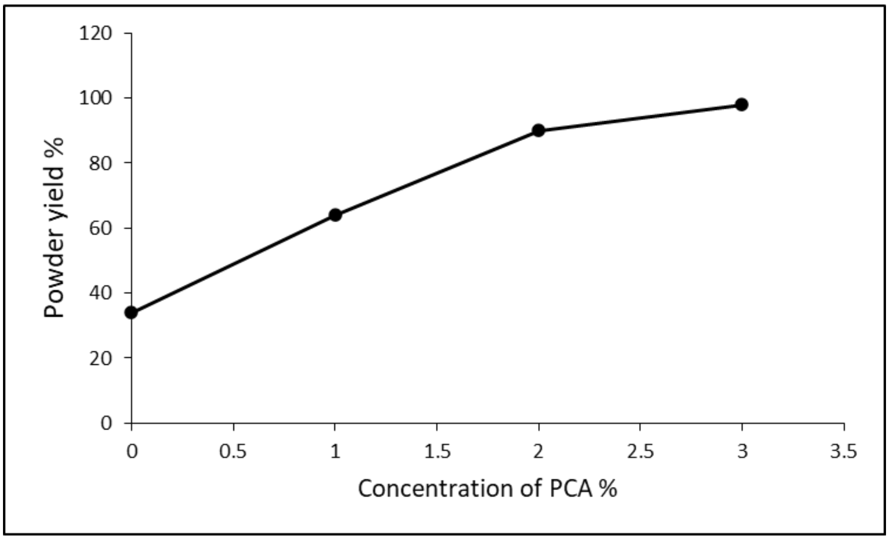

Figure 3.8 Effect of PCA concentration on the powder yield of the HEA NiMnFeCu

3.1.6 Sources of contamination during mechanical alloying

Figure **3.9** represents the concentration of Fe as a function of milling time. As the milling time increases the percentage of Fe in the milled powder also increases. After 5 h and 10 h of milling , the concentration of Fe was 25.15% and 24.96% respectively which is very close to the nominal (i.e. expected) composition (25%). However, after 15h and 20 h milling the concentration of Fe was 26.33% and 29.67% which is higher than the nominal composition. This increase in concentration of Fe is due to the increased erosion of Fe from the stainless-steel grinding media (balls and vial). At 20 h of milling, the Fe percentage increased to almost 30%, which is 5 % higher than the nominal composition. This addition of excessive Fe will lead to undesirable effects on the overall composition of the HEA powders which may be detrimental to the electrocatalytic properties, hence, to minimise the contamination of Fe, an optimized milling time should be adopted.

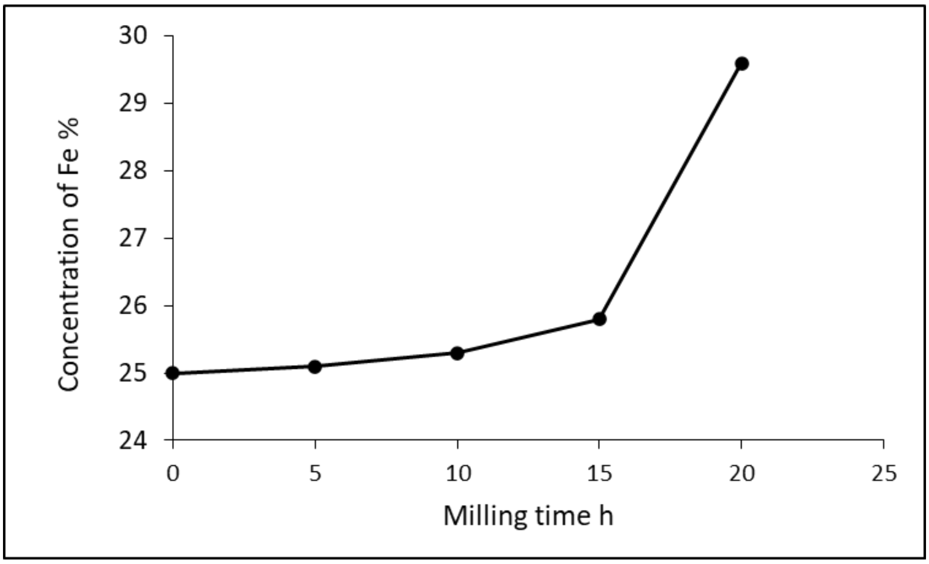

Figure 3.9 Concentration of Fe as a function of milling time.

PCA is the second source of contamination which may affect the overall chemistry of the milled powders. The PCAs used in mechanical milling are organic compounds, ethanol (C_2H_5OH) being used in the present study. During milling this PCA mixes with the alloying elements and minimizes the cold-welding effects with the ethanol evaporating due to its lower boiling point (75°C) compared to water. The oxygen, hydrogen and carbon atoms in the degraded ethanol may occupy the interstitial positions in the lattice of the alloying elements due to their smaller atomic radii when compared to the constituent elements of the HEA. Although the PCA decomposes and settles as interstitial impurities, as stated above if their concentration increases beyond the critical limit it could react with elements which have higher affinity to form oxides (e.g of Fe, Mn) or carbides (Cr) hence their concentration should be limited[54]. The purpose of adding PCA is to minimize the cold-welding effect and increase the powder yield. From Figure **3.8**, at 3% PCA almost 97% of the powders were recovered at the end of the milling process. Hence 3% PCA could be considered as the optimum to use for the milling process. Based on the above elucidated experimental aspects, optimal milling parameters were able to be established for HEA NiMnFeCu and have been tabulated in Table **3.6** . However, these milling parameters should not be regarded as absolute for all combinations as there could be minor changes needed in amounts added depending upon specific requirements.

Table 3.6 Optimized milling parameters for HEA NiMnFeCu.

Milling Parameter	Optimized parameter
Time	15 hours
Speed	350 RPM
PCA	3 %
Ball to powder ratio (BPR)	10:1

Based on these optimized parameters other HEA combinations such as NiMnFeCrCu and NiMnFeCr were synthesised in this research.

3.1.7 Thermogravimetric analysis

Figure **3.10** represents the DSC curve of the 20 h milled HEA NiMnFeCu powder. It can be seen that the powder has both exothermic and endothermic trends. There are three endothermic peaks, which occur at 77 ˚C, 1066˚C and 1220˚C.

The endothermic peak at 77˚C corresponds to the decomposition and volatilisation of the process control agent (PCA) (viz, ethanol). As the milled powders contain a large amount of internal stress, induced by work hardening and plastic deformation, the exothermic zone up to 800˚C corresponds to the relief of this internal stress during heating[135]. The broad endothermic range between 1060˚C and 1080˚C could be related to the presence of a partial liquid phase due to the rapid absorption of energy noted prior to complete melting[130] [136]. The sharp endothermic peak observed at 1220˚C suggests that the HEA powder is completely melted at this stage and that this temperature is very close to the theoretical melting point of the NiMnFeCu HEA powder (1331˚C).

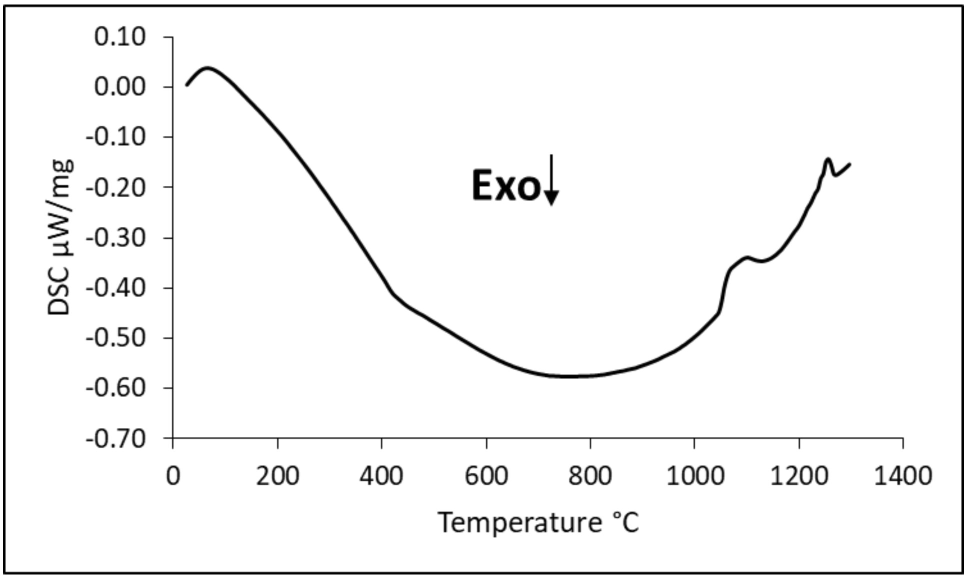

Figure 3.10 DSC curves of the milled NiMnFeCu powders after 20 h of milling.

3.2 Synthesis of HEA NiMnFeCrCu

Table **3.7** summarises the physico-chemical parameters and binary mixing enthalpy of the constituent elements of the HEA NiMnFeCrCu while Table **3.8** lists the calculated thermodynamic parameters of the HEA NiMnFeCrCu. From the calculated values it is predicted that the HEA NiMnFeCrCu will form a single phase random solid solution with a FCC crystal structure.

Table 3.7 Physico-chemical parameters and binary mixing enthalpy of the constituent elements of HEA NiMnFeCrCu [21, 30].

Element	Ni	Mn	Fe	Cu	Cr
Melting point ˚C	1453	1519	1538	1083	1890
Atomic radius(pm)	124	135	126	128	128
Electronegativity (Pauling)	1.8	1.55	1.8	1.9	1.6
Ni	Ni	-8	-2	4	-7
Mn		Mn	0	4	2
Fe			Fe	13	-1
Cu				Cu	12
Cr					Cr

Table 3.8 Calculated thermodynamic parameters for HEA NiMnFeCrCu.

HEA	$\Delta S_{\mathrm{config}}$ J/K.mol	ΔH_{mix} kJ/mol	δ	VEC	Ω
NiMnFeCrCu	13.38	2.75	3.21	8.4	9.3

3.2.1 Effect of milling time on phase evolution of NiMnFeCrCu

Figure **3.11**(a) depicts the XRD patterns of the milled HEA NiMnFeCrCu powders after the time interval of 5 h of milling. Initially upon mixing (i.e at a milling time of 0 h), the XRD peaks of the starting elemental powders are all able to be observed. After milling for 5 h, most of the XRD peaks of the individual elements had mostly disappeared, however, the elemental Mn peak is still present at a 2θ value of 47.5° (Figure **3.11**(b)). This suggests the formation of HEA is not yet completely achieved after 5h of milling. Prolonging the milling time to 10 h resulted in the complete disappearance of all elemental peaks of the starting raw powders and the formation of the principal diffraction peaks of the HEA. The principal diffraction peaks are indexed as (111), (200), (220) and (311), which correspond to the FCC crystal structure, and (110), (200) and (211), which correspond to the BCC crystal structure. This confirms the formation of HEA with major FCC and minor BCC crystal structure after 10h of milling. Furthermore, the intensity of the (110) peak (the most intense peak of the BCC phase) is decreased compared to that of 5h milled powders. Upon continuous milling up to 15 h, the principal diffraction peaks of the HEA corresponding to the FCC crystal structure remain unchanged. However, the intensity of the (110) peak is further decreased. The complete disappearance of the elemental powder peaks in the XRD patterns and formation of the principal diffraction peaks of the powders after 10 h of milling are attributed to the complete dissolution of the individual elemental powders and the formation of a high entropy random solid solution[137]. As mentioned before, alloying elements are grouped into FCC forming elements: Ni ,Mn, Cu and Co and BCC forming elements : Al , Cr , V and W [129]. In addition, chromium, has a melting point of 1907˚C which is the highest among the constituent elements in the studied HEA, so it has a relatively lower coefficient of diffusion compared to the other elements. This would favour the formation of a BCC phase (rich in Cr), to some extent for the studied NiMnFeCrCu HEA. Ren et al. and Cui et al. also synthesised NiMnFeCrCu HEAs by a casting method and confirmed that the alloy has both FCC and BCC crystal structure[129, 138]. This is different to that of the calculated thermodynamic and geometric parameters listed in Table **3.8** predicting formation of a NiMnFeCrCu HEA as a random solid solution with FCC crystal structure. It is worth noting that the thermodynamic and geometric parameters will not always predict the phases formed accurately.

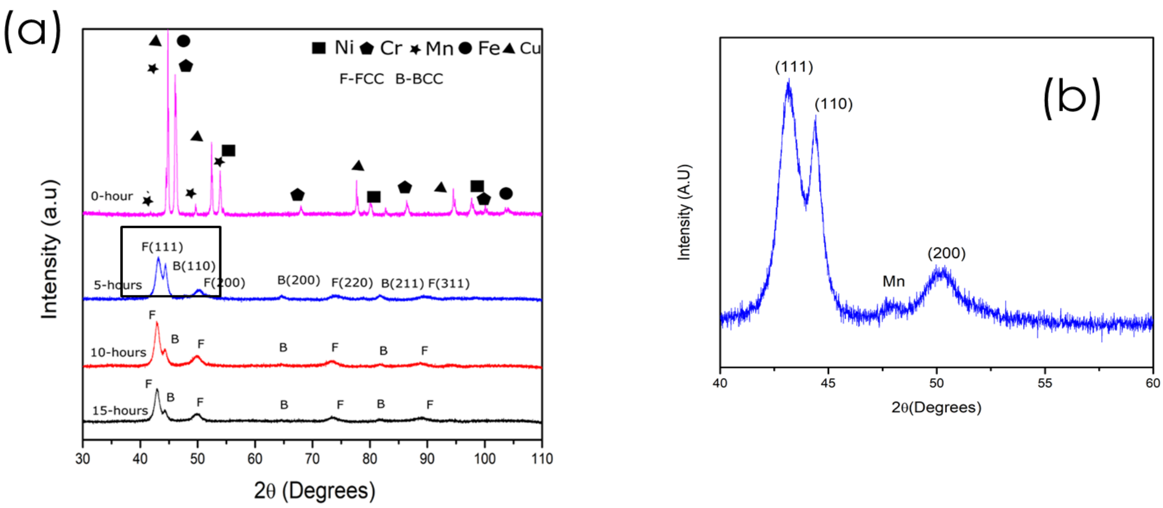

Figure 3.11 a) XRD patterns of the milled HEA NiMnFeCrCu powders at various milling times (b) XRD pattern of the milled HEA NiMnFeCrCu powders at 2θ values 40° to 60° after 5h of milling.

3.2.2 Effect of milling time on chemical homogeneity

Figure **3.12** represents the SEM/EDS map of the milled HEA NiMnFeCrCu after various time intervals. From the observations it is evident that the powders produced after 5 h of milling lack chemical homogeneity. This lack of chemical homogeneity is also demonstrated in the atom % of the elements presented in Table **3.9**. The measured atom % clearly deviated from the nominal atom% values. HEA powders produced after 10 and 15 h of milling possess excellent chemical homogeneity and the measured atom % values are very close to the nominal atom % values.

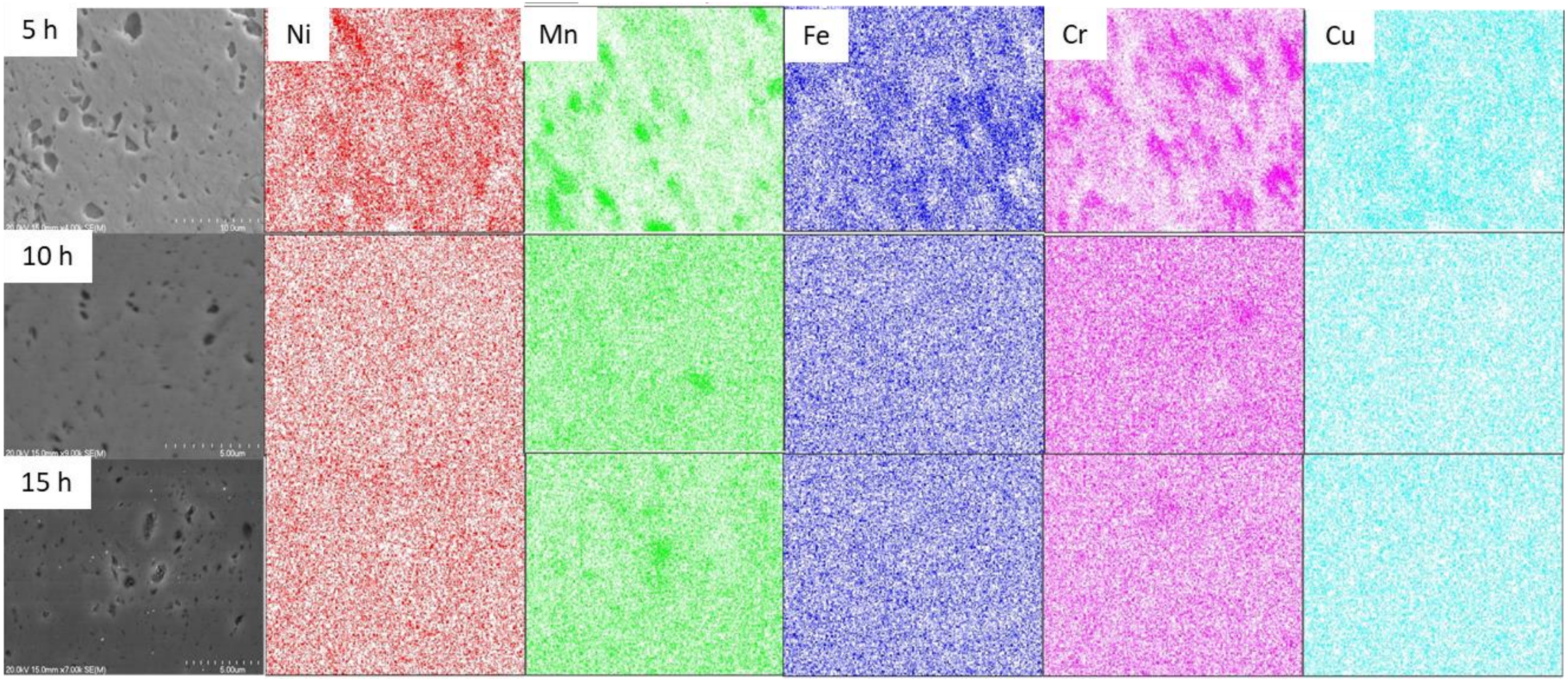

Figure 3.12 SEM EDS map of the milled HEA NiMnFeCrCu powders produced after various milling times.

Table 3.9 Measured elemental atom % of the milled HEA NiMnFeCrCu powders.

	Ni	Mn	Fe	Cu	Cr
Nominal weight % (full area scan)	20	20	20	20	20
5 h	21.9	12.87	22.11	19.88	23.15
10 h	18.49	20.96	21.82	18.24	20.49
15 h	20.17	20.96	21.82	18.93	20.73

3.2.3 Effect of milling time on phase fraction/composition, crystallite size and lattice strain of the NiMnFeCrCu HEA powder

Table **3.10** lists the effects of milling time on phase composition/fraction, crystallite size and lattice strain of the milled NiMnFeCrCu. It is evident that, for both FCC and BCC phases, the crystallite size decreases steadily as a function of milling time while the lattice strain is increased. For the FCC phase the crystallite size is decreased to 7.8 nm, 7.7 nm and 7.3 nm and the phase fraction is increased to 73%, 81% and 90% when the milling times is 5, 10 and 15 h respectively. The lattice strain is increased to 1.30%, 1.36% and 1.43% for the powders milled for 5h-, 10h- and 15 h respectively. For the BCC phase the crystallite size is decreased to 10.9 nm, 9.3 nm and 9.3 nm and the phase fraction is decreased to 27%,19% and 10% and the lattice strain is increased to 0.93%, 1.22% and 1.23% for the powders milled for 5 h, 10 h and 15 h respectively. The decrease in crystallite size and increase in lattice strain are due to the refinement of crystallites and accumulation of dislocation density owing to severe plastic deformation caused by high energy ball milling[54, 139]. The decrease in the volume fraction of the BCC phase as a function of milling time is attributed to further homogenisation of the Cr composition in the alloy which is brought about by the dissolution of the Cr rich BCC phase into the FCC phase. This transformation is facilitated by the substitution of the Cr by any of the atoms of Mn, Fe, Cu and Ni since the atomic size of Cr is similar to that of the other elements in the studied HEA[139].

Table 3.10 Effect of milling time on phase composition/fraction , crystallite size and lattice strain.

HEA samples	Milling time (hours)		Phase %	Crystallite size nm	Lattice strain %
NiMnFeCrCu	5	FCC	73	7.8	1.30
		BCC	27	10.9	0.93
	10	FCC	81	7.7	1.36
		BCC	19	9.3	1.22
	15	FCC	90	7.3	1.43
		BCC	10	9.3	1.23

3.2.4 Effect of milling time on particle size of the milled HEA NiMnFeCrCu powders

Table **3.11** and Figure **3.13** illustrates the effect of milling time on particle size of the milled HEA NiMnFeCrCu. It is clearly observed that the particle size increased as a function of milling time. After 5 h of milling the average particle size D50 is 21.2 μm, while extending the milling time to 10 h gave an increased average particle size of 25.3 μm while further milling to 15 h increased the average particle size to 28.4 μm. The shift of the particle size distribution curve from left to right affirms this increase of average particle size as observed. The increase in particle size could be ascribed to FCC to BCC transformation during mechanical alloying because FCC alloys tend to flatten during milling hence the particle size reduction will take place only after complete FCC to BCC transformation[54].

Table 3.11 Effect of particle size on milling time of the milled HEA NiMnFeCrCu powders.

Milling time (h)	D10 μm	D50 μm	D90 μm
5	7.24	21.2	64.6
10	9.36	25.3	76.8
15	12.8	28.4	70.4

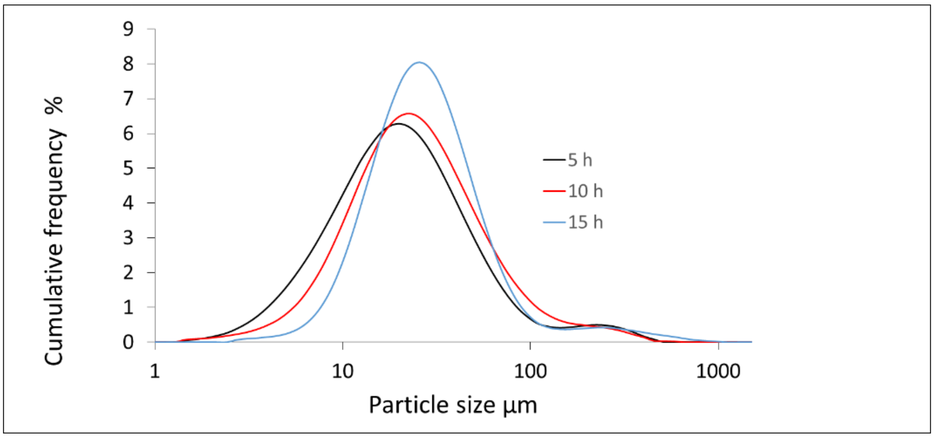

Figure 3.13 Effect of milling time on particle size distribution of the milled NiMnFeCrCu HEA powder.

3.2.5 Thermogravimetric analysis

Figure **3.14** depicts the DSC curve of the milled HEA NiMnFeCrCu powders after 15 h of milling. It is evident that the DSC curve possesses both exothermic and endothermic trends. A wide exothermic trend is seen from 30°C - 549°C. An exothermic peak is observed at 550°C. After 550°C the curve shows an endothermic trend until 1200°C. An endothermic peak is also seen at 1210°C.

The exothermic trend from 30°C - 549°C corresponds to releasing of internal stress accumulated during high energy ball milling[139]. To experimentally verify the reason for the observed exothermic peak at 550°C , the milled HEA was heat treated at 350°C and 950°C and the corresponding XRD patterns are presented in Figure **3.15**(a-b). From the patterns it is evident that at 350°C there is a major FCC phase and a minor BCC phase. However, at 950°C the major FCC split into two FCC phases and the BCC phase remain unchanged. Hence the exothermic peak at 550°C could be attributed to a phase transformation which resulted in conversion of a single FCC phase into two FCC phases[140]. This conversion of the single FCC phase into two FCC phases will be discussed later in detailed. The endothermic trend after 550°C is due to absorption of energy and the endothermic peak at 1210°C could be due to the complete melting of the HEA alloy[141].

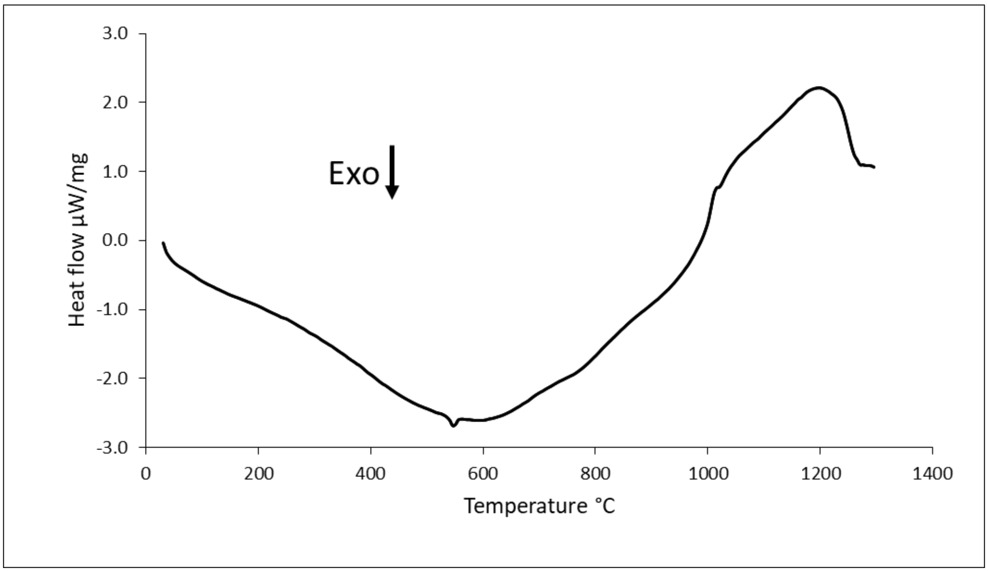

Figure 3.14 DSC curve of the milled HEA NiMnFeCrCu powders after 15 h of milling.

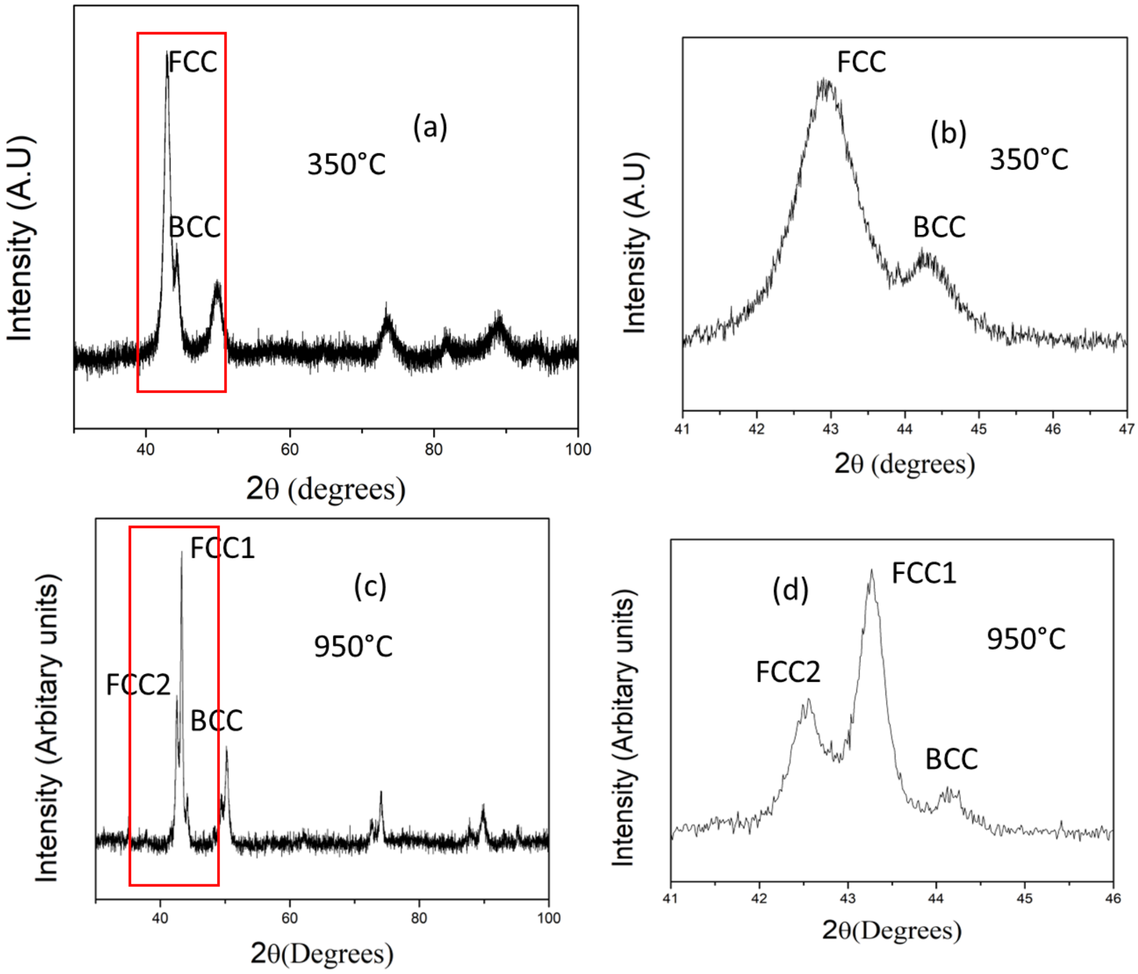

Figure 3.15 XRD patterns of the heat-treated HEA NiMnFeCrCu at temperatures (a-b) 350°C (c-d) 950°C.

3.3 Synthesis of HEA NiMnFeCr

Table **3.12** summarises the physio-chemical parameters and binary mixing enthalpy of the constituent elements of HEA NiMnFeCr. Table **3.13** lists the calculated thermodynamic parameters of the HEA NiMnFeCr. It is predicted that the HEA NiMnFeCr will form a random solid solution with FCC + BCC crystal structure.

Table 3.12 Physico-chemical parameters of the constituent elements of HEA NiMnFeCr [21, 30].

Element	Ni	Mn	Fe	Cr
Melting point ˚C	1453	1519	1538	1890
Atomic radius(pm)	124	135	126	128
Electronegativity (Pauling)	1.8	1.55	1.8	1.6
Ni	Ni	-8	-2	-7
Mn		Mn	0	2
Fe			Fe	-1
Cr				Cr

Table 3.13 Calculated thermodynamic and geometric criteria for HEA NiMnFeCr.

HEA	$\Delta S_{\mathrm{config}}$ J/K.mol	ΔH_{mix} kJ/mol	δ	VEC	Ω
NiFeMnCr	11.526	2.75	3.56	7.75	4.4

3.3.1 Effect of milling time on phase evolution of HEA NiMnFeCr

Figure **3.16** depicts the XRD patterns of the milled HEA NiMnFeCr powders after a time interval of 5 h of milling. Initially the peaks of the starting elemental powders are visible when no milling of the powders had taken place (just mixed state corresponding to 0 h of milling). After 5 h of milling, the intensity of the peaks of the starting elemental powder disappears completely and only the fundamental diffraction peaks of the HEA are observed. The peaks at 2θ values of 43.1°, 50.2°, 74.2° and 89.7° are indexed as (111), (200), (220) and (311) (FCC crystal structure) and the peaks at 2θ values of 44.2°, 64.3° and 81.5° correspond to (110), (200) and (211) reflections (characteristics of the BCC crystal structure). Hence, formation of the HEA after only 5 h of milling time is confirmed. After extending the milling time to 10 h, it is found that the intensity of the BCC peak (110) further decreased, and the intensity of the FCC peak (111) increased when compared to the results obtained after 5 h of milling. A continuation of the milling to 15 h led to the intensity of the FCC peak (111) increasing further while the intensity of the BCC peak (110) further decreased when compared to the results obtained after 10 h of milling. This complete disappearance of elemental powder peaks and formation of fundamental diffraction peaks during mechanical milling can be attributed to the dissolution of raw elemental powders and the formation of a solid solution[137].

The calculated thermodynamic parameters as listed in Table **3.13** predicts that the HEA is expected to form a dual FCC + BCC phase. As predicted, the 15 h milled HEA powder possesses a major FCC phase and a minor BCC phase. The alloying elements can be grouped into FCC stabilizers: Ni ,Mn , Cu, Co and BCC stabilizers: Cr , Al , Mo and V [129, 138]. In addition, it should be noted that chromium has the highest melting point of all the elements involved in the HEA at 1907°C, so it has the lowest coefficient of diffusion. This is the factor favouring the formation of the BCC structure for the milled NiMnFeCr HEA powders as it is richer in Cr.

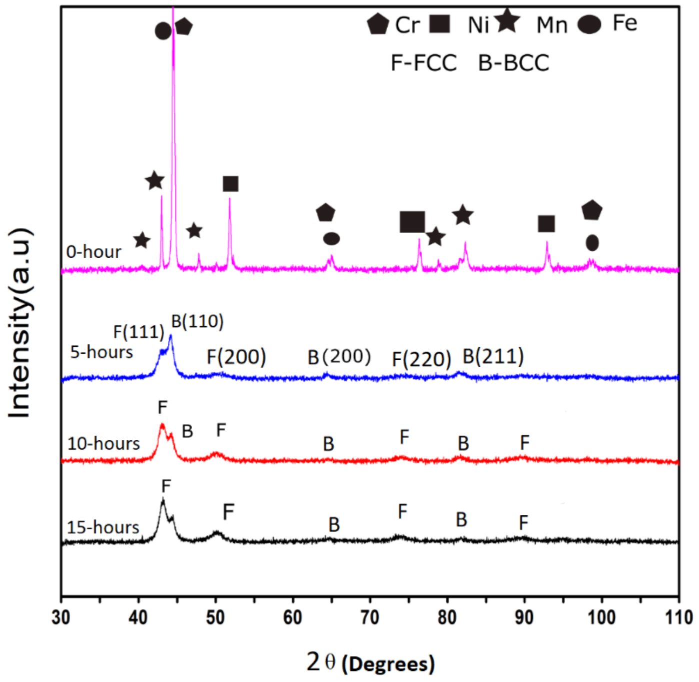

Figure 3.16 XRD patterns of the milled HEA NiMnFeCr powders after various milling times.

3.3.2 Effect of milling time on chemical homogeneity

Figure **3.17** represents the SEM/EDS map of the milled HEA NiMnFeCr powders as a function of milling time. After 5h of milling the milled HEA powders lack compositional homogeneity. This non-homogeneous nature of the powders can be attributed to imbalances developed between cold welding and fracturing during milling. However, after 10 and 15h of milling time, the compositional consistency of the milled HEA powders improved significantly due to the attainment of balance between cold welding and fracturing. This balanced state is also termed a saturation state and the particle size of the powder decreases significantly during the process of attaining the saturated state[54]. Hence, the 15 h milled HEA powder is superior and preferred over the 10h powder for further consolidation because of its better compositional consistency and smaller particle size. Table **3.14** represents the measured atom% of the milled HEA NiMnFeCr powders as a function of milling time.

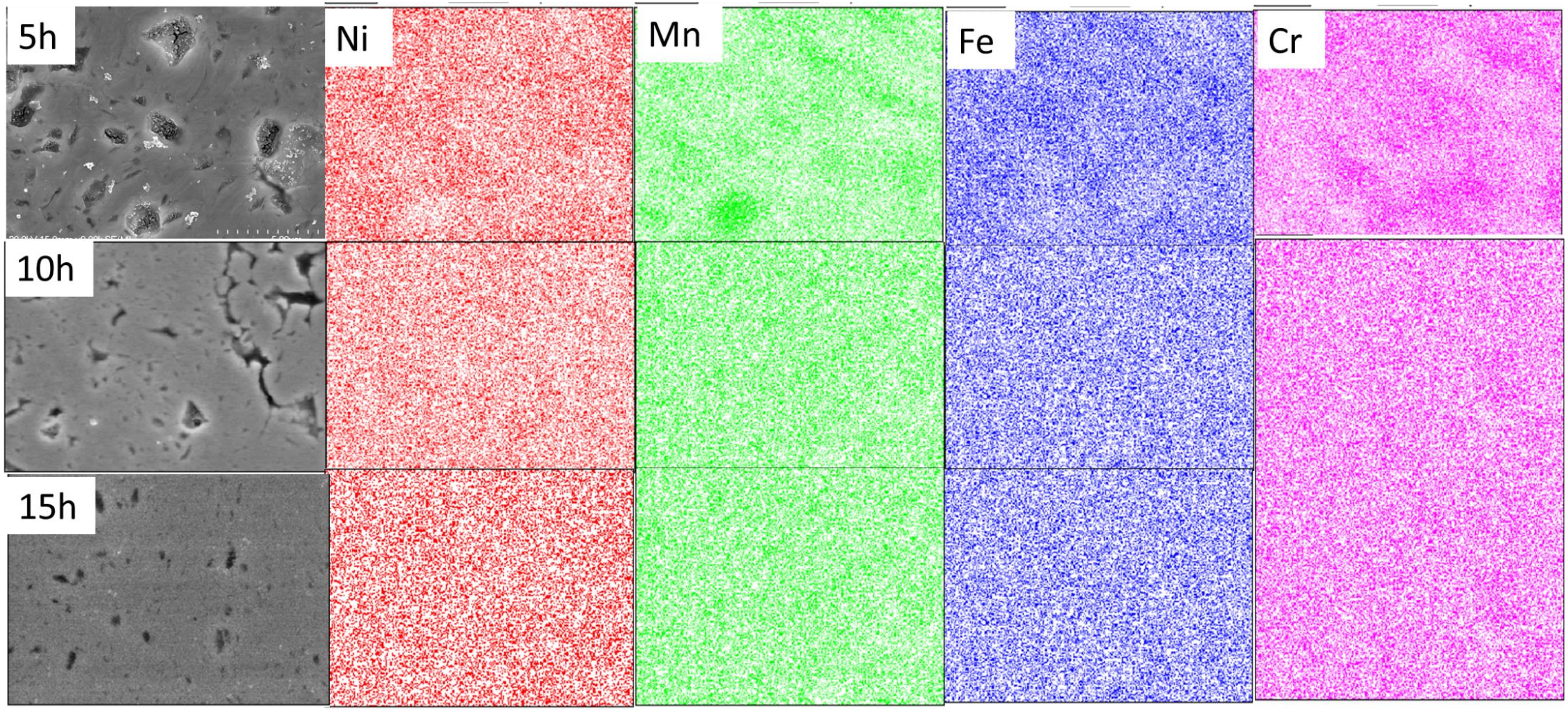

Figure 3.17 SEM EDS maps of the milled HEA NiMnFeCr powders after various milling time.

Table 3.14 Measured elemental atom % values for the milled HEA NiMnFeCr powders after various milling times.

	Ni	Mn	Fe	Cr
Nominal atom % (full area scan)	25	25	25	25
5 h	28.07	19.51	29.17	23.25
10 h	26.97	23.57	26.39	23.94
15 h	23.80	24.13	25.70	26.37

3.3.3 Effect of milling time on the particle size of the milled HEA NiMnFeCr powders

Table **3.15** and Figure **3.18** illustrate the effect of milling time on particle size for the milled HEA NiMnFeCr. It is clear from this data that the particle size increased as a function of milling time. After 5 h of milling the average particle size represented as D50 is found to be 16.97 μm , with the particle size distribution being bimodal in nature, while prolonging the milling time to 10 h increases the average particle size to 18.4 μm and further milling to 15 h increased the average particle size to 23.7 μm. The bimodal distribution of particle size is attributed to the imbalance between cold welding and fracturing[142] as referred to earlier. The particle size distribution curve is shifting left to right indicating an increase of average particle size. The increase in particle size is due to the FCC to BCC transformation during the alloying process.

Table 3.15 Effect of milling time on particle size of the milled HEA NiMnFeCr powders.

Milling time (h)	D10 (μm)	D50 (μm)	D90 (μm)
5	3.87	16.97	91.6
10	6.17	18.4	98.4
15	8.96	23.7	82.6

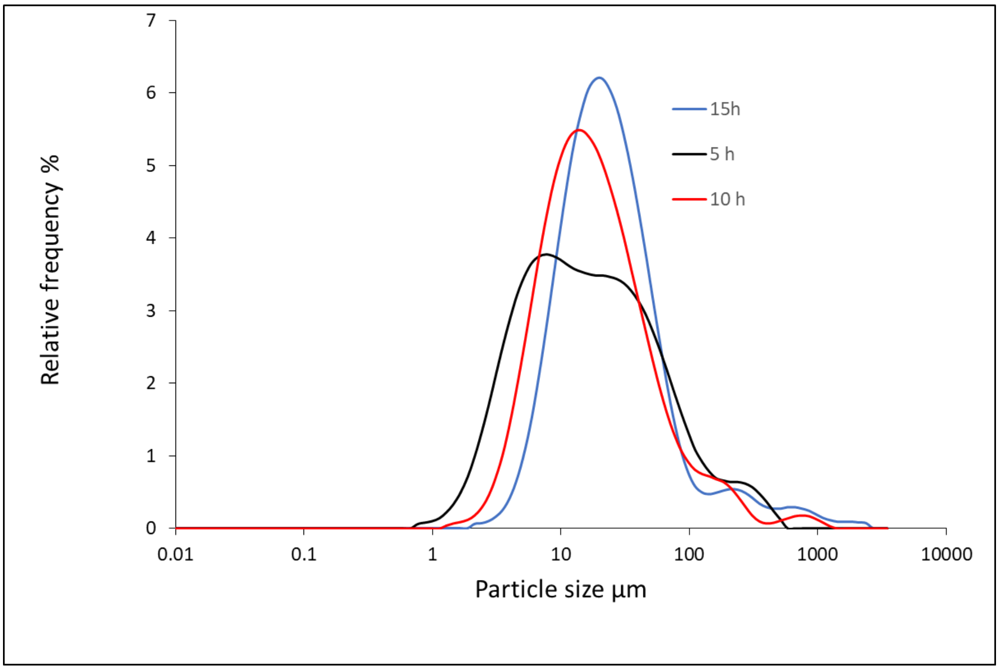

Figure 3.18 Particle size distribution of milled HEA NiMnFeCr powders as a function of milling time.

3.3.4 Effect of milling time on phase constituent/fraction , crystallite size and lattice strain of HEA NiMnFeCr

Table **3.16** summarises the values of phase composition/fraction, crystallite size and lattice strain of the milled HEA NiMnFeCr powders as a function of milling time. It is evident that the crystallite size decreases steadily as a function of milling time for both FCC and BCC phase, while the lattice strain increases as the milling time increased. The phase fraction of FCC phase increases while the phase fraction of BCC phase decreases as a function of milling time. For the FCC phase the crystallite size decreases to 6.2 nm, 5.8 nm and 4.2 nm and the phase composition increases to 40%, 67.6% and 70.3% for milling times of 5, 10 and 15 h of milling respectively. Additionally, the lattice strain increases to 1.68%, 1.79% and 2.42% for powders produced after 5, 10 and 15 h of milling respectively. For the BCC phase, the crystallite size decreases to 7.9 nm, 7.7 nm and 5.1 nm, the phase fraction decreases to 60%, 32.3% and 29.6% for milling times of 5, 10 and 15 h respectively, and the lattice strain increases to 1.28%, 1.31% and 2.08% for 5, 10 and 15 h respectively. The decrease in crystallite size and increase in lattice strain is attributed to the disintegration of crystallites and increase of dislocation density owing to the severe plastic deformation caused by the mechanical milling[54, 139]. The decrease in the volume fraction of the BCC phase as a function of milling time is attributed to further mixing of the Cr element in the alloy, through the dissolution of the Cr rich BCC phase into the FCC phase by the substitution of Cr by any other atoms of Mn, Fe, and Ni, since the atomic size of Cr is similar to that of the other elements in the studied HEA[139].

Table 3.16 Effect of milling time on phase composition, crystallite size and lattice strain of HEA NiMnFeCr powders.

Compositions	Milling time hours		Phase %	Crystallite size nm	Lattice strain %
NiMnFeCr	5	FCC	40	6.2	1.68
		BCC	60	7.9	1.28
	10	FCC	67.6	5.8	1.79
		BCC	32.3	7.7	1.31
	15	FCC	70.3	4.2	2.42
		BCC	29.6	5.1	2.08

3.3.5 Thermogravimetric analysis

Figure **3.19** (a) depicts the DSC curve of the 15 h milled HEA NiMnFeCr powders from room (25ºC) temperature to 1400ºC. The DSC curve exhibits both exothermic and endothermic trends. From 25ºC to 1000ºC the curve shows an exothermic trend with an exothermic peak at 555ºC. From 1000ºC the curve shows an endothermic trend until 1300ºC with an endothermic peak at 1283ºC. The exothermic trend between 25ºC to 1000ºC is attributed to the relieving of internal stresses caused by severe plastic deformation which results from the high energy ball milling[130]. As shown earlier the milled HEA powders possessed a major FCC phase and a minor BCC phase (Figure **3.16**).To elucidate the reason for the presence of an exothermic peak at 555ºC experimentally, XRD and phase composition analyses of the related heat-treated HEA powders were carried out over the temperature range of 250ºC to 1050ºC and depicted in Figure **3.19**(b-c) respectively. After careful examination of the XRD patterns of the HEA powder sintered at temperatures 250ºC and 350ºC (which is lower than 555ºC) the intensities of the peaks due to the BCC phase were found to remain constant. As a result, the volume fraction of the BCC phase also remained unchanged (Figure **3.19** (b-c)) in the analysed HEA powders. However, when the milled HEA powders were heat treated at temperatures of 650ºC, 950ºC and 1050ºC (which are all greater than 555ºC) respectively , the intensity of the BCC peak was observed to decrease, and consequently the amount of the BCC phase also decreases gradually as shown in Figure **3.19**(b-c). Hence it could be speculated that the exothermic peak present at 555ºC is diffusive in nature, and is attributable to an initiation of thermal diffusion of the minor BCC phase into the FCC phase with the rate of diffusion increasing significantly after 650ºC[130, 143, 144]. The endothermic trend from 1000ºC can be attributed to the absorption of energy with the endothermic peak at 1283ºC representing the melting point (the liquidus temperature) of the HEA[136].

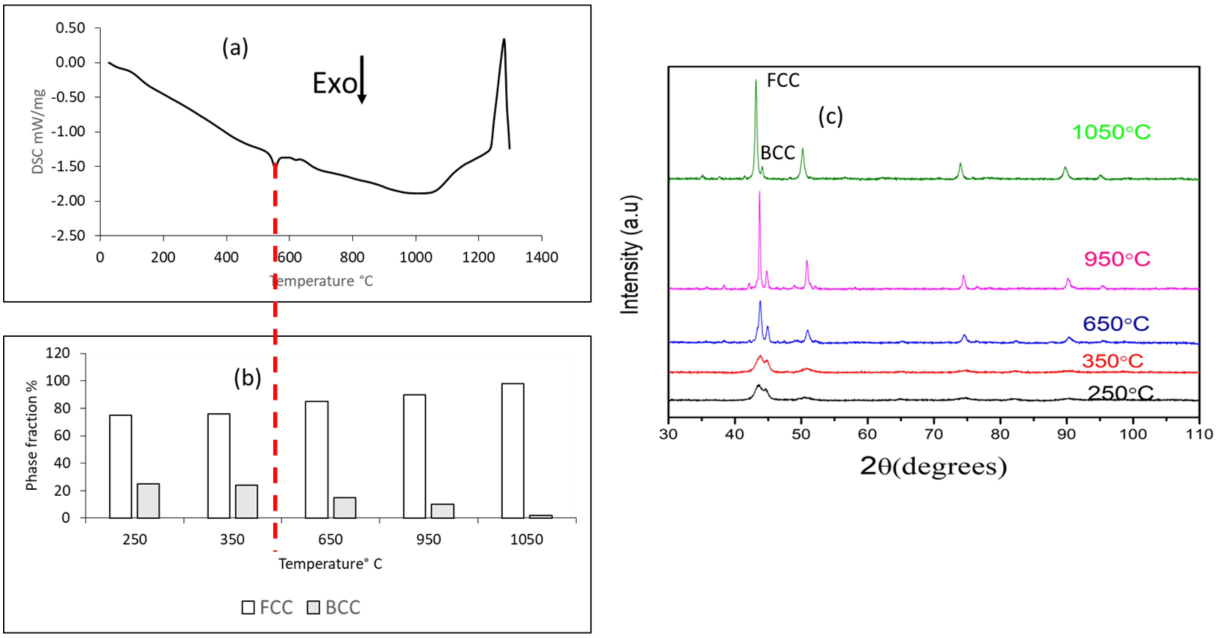

Figure 3.19 (a) DSC curve of the 15 h milled HEA NiMnFeCr (b) Phase fraction of HEA NiMnFeCr as a function of temperature (c) XRD patterns of the milled HEA NiMnFeCr powders as a function of temperature (the red partition separates regions before and after the exothermic peak at 555ºC).

The synthesised HEA powders in this research i.e NiMnFeCu , NiMnFeCrCu and NiMnFeCr all required 15 h of milling time for achieving optimum particle size for the consolidation process. The particle size for HEA NiMnFeCu increased initially up to 5 h of milling, however after 5 h of milling the particle size decreased significantly due to the single-phase FCC of NiMnFeCu powder. In contrast for HEA NiMnFeCrCu and HEA NiMnFeCr, the particle size progressively increased. This increase in particle size is due to the fact that HEA NiMnFeCrCu and NiMnFeCr possessed a dual (FCC+BCC) phase, and the minor BCC phase diffuses into the FCC phase during milling. Thermal property analyses of the HEAs NiMnFeCu, NiMnFeCrCu and NiMnFeCr powders revealed the phase transformation temperatures and melting point of the alloy powders. HEA NiMnFeCu powders exhibited both exothermic and endothermic trends, while HEA NiMnFeCrCu and NiMnFeCr powders along with the exothermic and endothermic trend, exhibited an exothermic peak at temperature (550°C for NiMnFeCrCu) and (555°C for NiMnFeCr). Existence of such an exothermic peak was also reported previously in works cited in Ref [130, 143, 144]. From these reported works it is interesting to note that the exothermic peak exists only in dual phase FCC+BCC HEAs and this exothermic peak is attributed to phase transformation or diffusion of the secondary phase (either FCC or BCC) present in the HEAs. In addition to that the amount of plastic deformation induced during milling is inversely proportional to the phase formation temperature (exothermic peak); when the milling time increases the exothermic peak shifts to lower temperature[143]. Hence for HEA NiMnFeCrCu and HEA NiMnFeCr the position of the exothermic peak is very close to each other (550°C and 555°C) due to the same milling time of 15 h.

In summary, chapter 3 systematically covered the experimental elucidation of optimized milling parameters such as milling time, ball to powder ratio, concentration of PCA and speed of milling for synthesis of HEA powders. In addition to that, the effect of milling time on particle size and powder yield was also explored. Subsequently thermal properties of the synthesised HEA powders were explored; the phase transformation temperature and melting point of the HEA powders were identified and utilized for the consolidation process via thermal analysis.

Chapter 4

Consolidation of high entropy alloys

4.1 Consolidation of HEA NiMnFeCu

The milled HEA powders should be consolidated, before being used in water electrolysis processes. The preliminary step in consolidation of the milled HEA powders is to produce cold compacted preforms which are also termed "green compacts". These green compacts are subsequently consolidated (sintered) in a vacuum furnace. Synthesis of a bulk HEA with the desired mechanical and electro catalytical properties, involves optimization of operating parameters such as compaction pressure, sintering temperature and time for each HEA composition. In this study the HEA NiMnFeCu will be utilized for optimizing the consolidation parameters such as compaction pressure, sintering temperature and time and these optimized parameters will be used for consolidating other HEAs in this study.

4.1.1 Cold compactions of the milled HEA NiMnFeCu powders

Figure **4.1** represents the change of green density as a function of compaction pressure under room temperature for HEA NiMnFeCu. It is observed clearly that the green density increases with the increase of compaction pressure. At 700 MPa the green density is about 69%. This increase in green density with increase of the compaction pressure is attributed to rearrangement and interlocking of particles under application of a uniaxial pressure[56]. Although increasing the compaction pressure beyond 700 MPa can result in high density green compacts (> 69%), which are beneficial for sintering, the compaction pressure in the present study is restricted to 700 MPa to mitigate the hazards associated with failure of the hydraulic press and the compaction die. Hence 700 MPa was considered the optimum compaction pressure and was utilized for all HEAs, namely NiMnFeCu, NiMnFeCrCu and NiMnFeCr in this study.

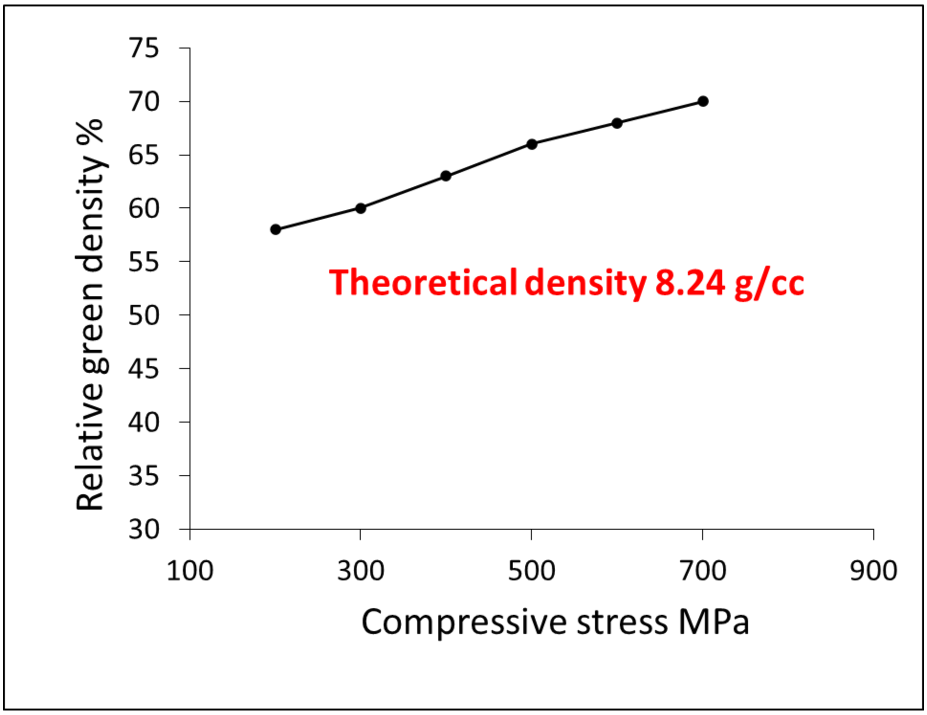

Figure 4.1 Green density as a function of compaction pressure of compacted NiMnFeCu HEA powder.

4.1.2 Densification mechanisms of HEA NiMnFeCu

Figure **4.2** depicts the schematic representation of the samples taken from the sintered HEA NiMnFeCu at three different positions. Figure **4.3** represents the OM images of the sintered HEA NiMnFeCu at 1000°C at three different positions. It is observed clearly that the porosity and the average pore size progressively increases from the centre to the periphery with the relative sintered density correspondingly decreasing steadily from the centre (80.8%) and middle (75.8%) to the periphery (73.8%) of the HEA as exhibited in Figure **4.4**. The existence of a density gradient in the sintered HEA is due to the non-uniform distribution of green density during compactions. Hence samples from the centre position were used for further microstructural, mechanical and electro catalytic investigation.

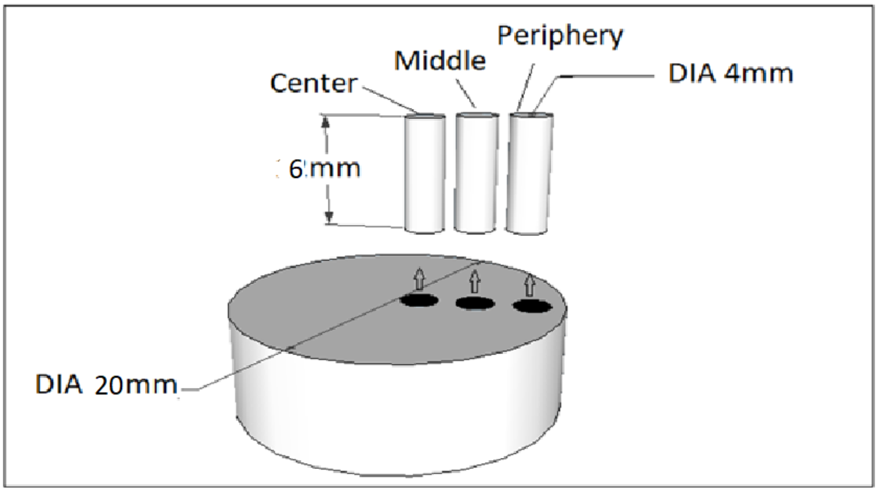

Figure 4.2 Schematic representation of the sintered HEA and sampling position for microstructural evaluation.

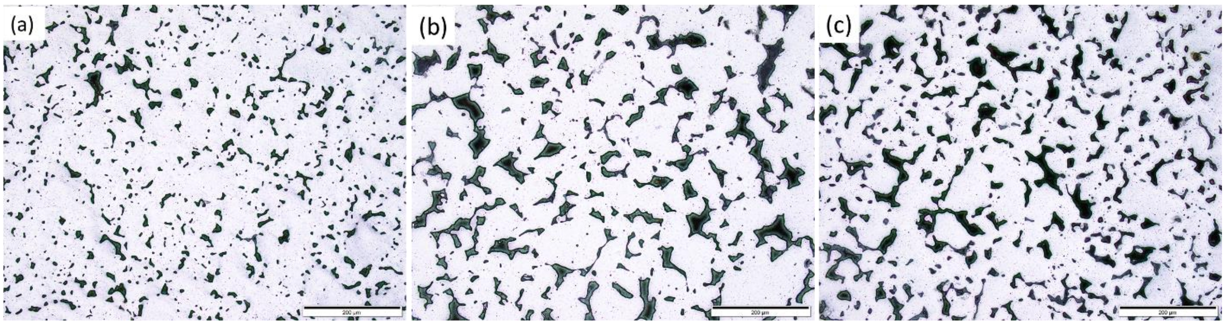

Figure 4.3 OM images of the sintered HEA NiMnFeCu at 1000°C at the three different positions.

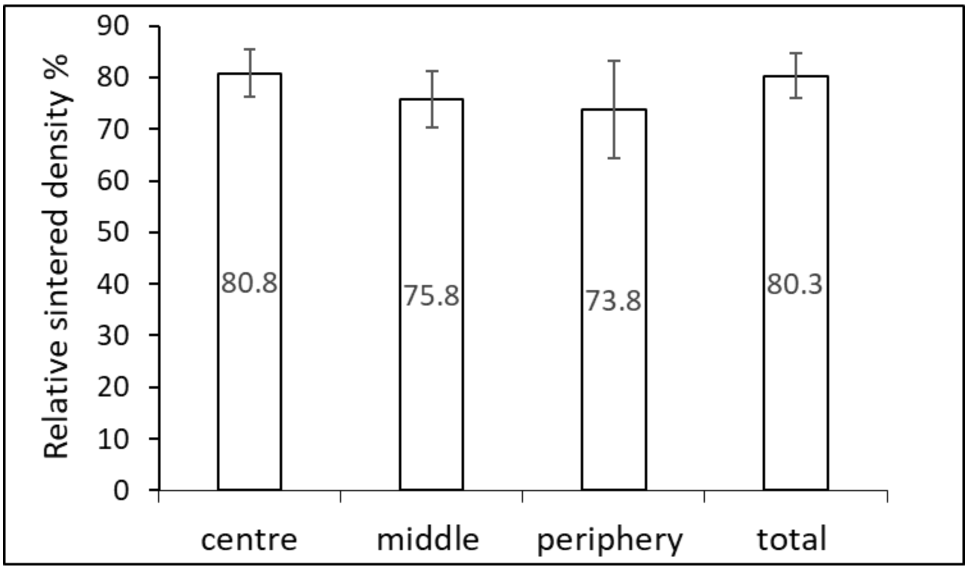

Figure 4.4 Density gradient of the sintered HEA NiMnFeCu.

4.1.3 Effect of sintering time on densification

The effect of the sintering time on densification can be studied through shrinkage of the sintered HEA. The change in diameter (radial shrinkage) and the thickness (axial shrinkage) of the cold compacted HEAs were measured before and after sintering to determine the extent of shrinkage. Shrinkage can be calculated by means of diameter reduction and thickness reduction using equations 4.1 and 4.2.

$$\%\ \text{Percentage of diameter shrinkage} \ = \frac{d_o - d_f}{d_0} \text{X}\ 100\% \qquad (4.1)$$

$$\%\ \text{Percentage of thickness hrinkage} \ = \frac{h_o - h_f}{h_0} \text{X}\ 100\% \qquad (4.2)$$

where:

d_o = Diameter before sintering in mm

d_f = Diameter after sintering in mm

h_o = Thickness before sintering in mm

h_f = Thickness after sintering in mm

Figure **4.5** depicts the axial and radial shrinkage of the sintered HEA NiMnFeCu as a function of sintering time at 1000˚C. The shrinkage parameter in radial direction increases from 4% to 9% as the holding time increased from 1-3 h; while in the axial direction, the shrinkage showed increasing trend from 3% to 5 % as the sintering time increased from 1-3 h. In addition to that, the shrinkage significantly increased both axially and radially after 2 h reaching 4.5% (axially) and 9% (radially) at the end of 3 h of sintering. It is a well-established fact, that grain growth increases significantly during the final stages of sintering (after 2 h) which is known to be detrimental to the mechanical properties of a body. As a result, sintering beyond 2 h is considered unnecessary and moreover ill-advised. 2 h of sintering was thus considered the optimum time and this is the time duration for which the other HEAs NiMnFeCrCu and NiMnFeCr in the study were sintered.

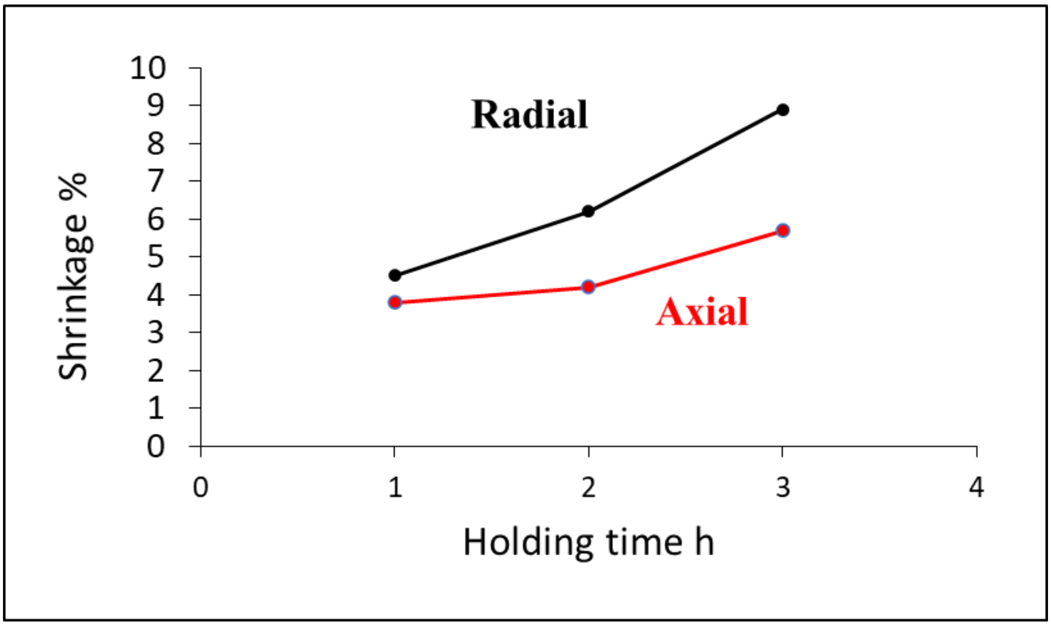

Figure 4.5 Shrinkage as a function of sintering time at 1000˚C.

4.1.4 Effect of sintering temperature and time on phase composition

Figure **4.6** shows the XRD patterns of the sintered NiMnFeCu from the various sintering conditions (S1-S4). Table **4.1** summarises the details of the sintering conditions. It is clearly seen that the sintered alloys (S1-S4) at all conditions consist of a single FCC HEA phase. This suggests that during the sintering process, no phase transformation takes place.

Table 4.1 Sintering parameters of the sintered HEA NiMnFeCu

Sample	Temperature °C	Holding time h
S1	1000	1
S2	1000	2
S3	1050	1
S4	1050	2

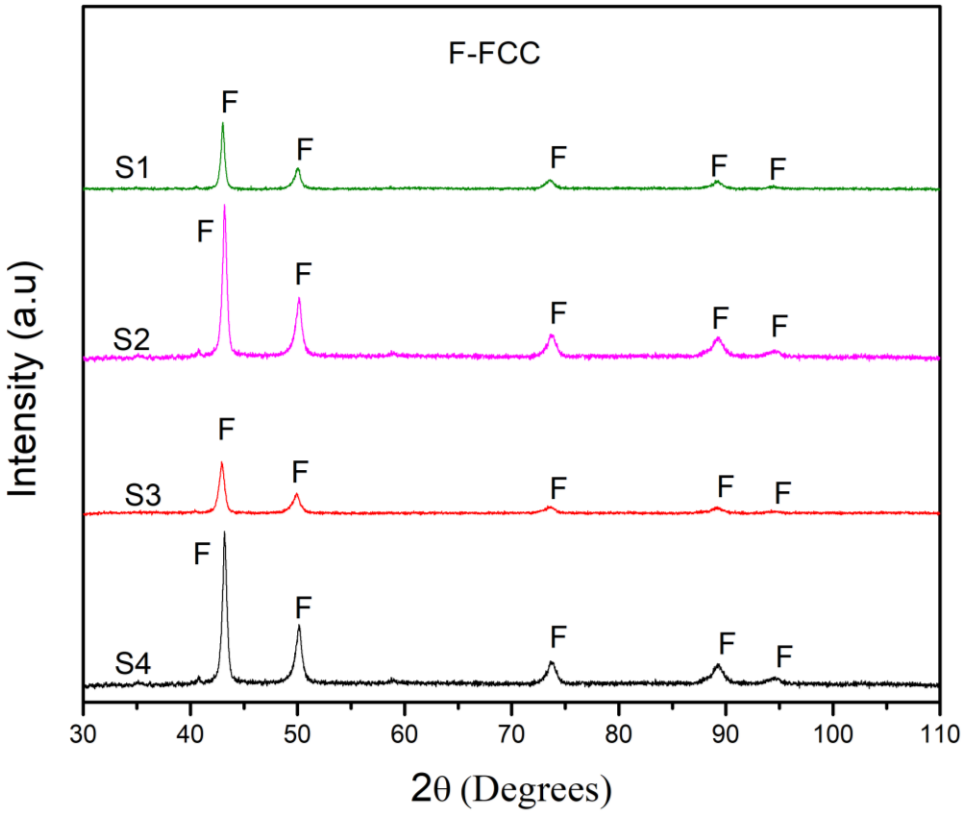

Figure 4.6 XRD patterns of the sintered HEA NiMnFeCu from the various sintering conditions.

4.1.5 Effect of sintering temperature and time on microstructure

Figure **4.7** shows the OM images of the sintered NiMnFeCu at various sintering conditions. It is seen that, the S1-S3 alloys are porous. The information regarding the pore size and the morphology for the sintered NiMnFeCu HEAs (S1-S4) are summarised in Table **4.2**. The average pore sizes of S1 and S2 are 34.7 µm and 37.3 µm respectively and the morphology of the pores of S1 and S2 remained irregular. The average pore sizes of S3 and S4 are 11.2 µm and 8.1 µm respectively. The morphology of the pores of S3 and S4 changes to spherical. The relative densities of S1 and S2 are 79% and 82%, respectively and the relative densities of S3 and S4 are 80% and 98%, respectively.

The microstructures of S1-S3 had many pores present, and the relative density for those three samples where hence much lower than that for S4. For S1 and S2, the sintering temperature was relatively low (1000°C) compared to S3 (1050°C). The sintering time was 1 h for S1 and S3, and 2 h for S2 and S4. From the microstructure observations (Figure **4.7**), limited densification takes place in the S1-S3 samples, while a relatively large densification occurred in the S4 sample. The microstructure of S4 has therefore a smaller number of pores compared to S1-S3 and S4's relative density is hence high at 98%. This enhanced densification is due to higher sintering time and optimum temperature[136].

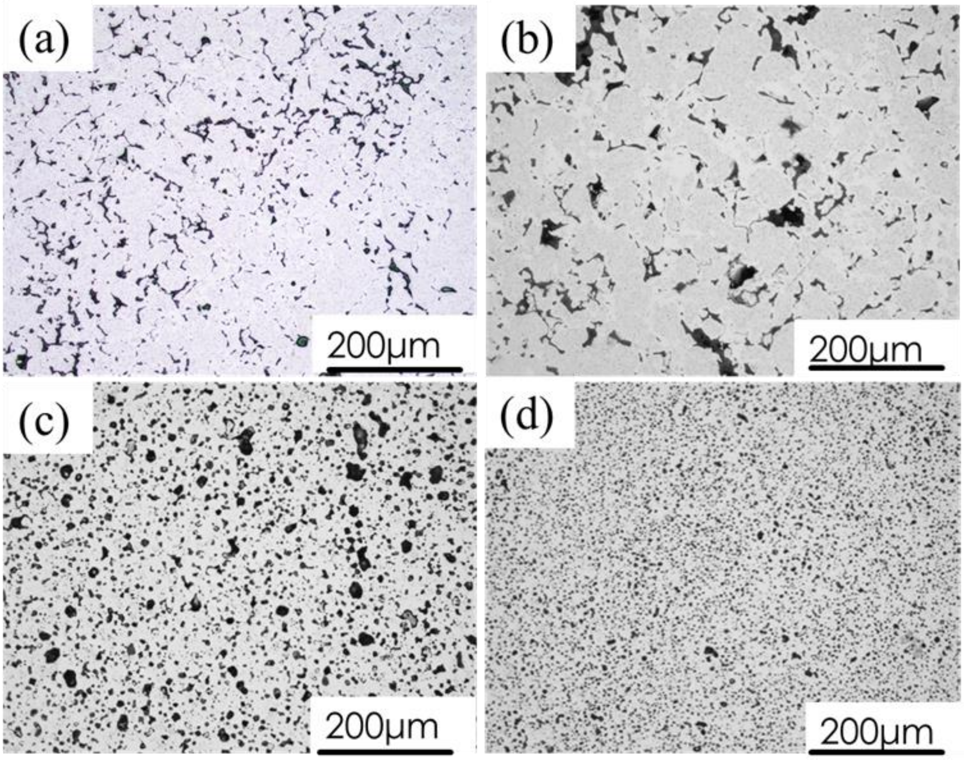

Figure 4.7 OM images of the as sintered HEA NiMnFeCu at various sintering conditions (a) at 1000°C for 1h(S1) (b) at 1000°C for 2h(S2) (c) at 1050°C for 1h(S3) (d) at 1050°C for 2h(S4).

Table 4.2 Pore size and morphology of the sintered HEA NiMnFeCu under various sintering condition.

Sample	Average pore size (µm)	Circularity of pores index	Relative sintered density(%)
S1	34.7	0.41	79
S2	37.3	0.46	82
S3	11.2	0.87	80
S4	8.1	0.89	98

Figure **4.8** and Figure **4.9** show the microstructure of the sintered HEA under low and high magnification from the various sintering conditions. It is evident that the microstructure of the S1 and S2 samples is porous. The morphology of the pores is irregular. In S1, the pores are spaced very close to each other, while in S2 the pores are clustered in a few areas of the microstructure. In the case of condition S3, a significant number of pores are seen, however the morphology of the pores is spherical. Although for condition S4 significant pores are present, the average size of the pores are relatively smaller compared to the samples (S1-S3) indicating high sintered density. Careful observation of the microstructure under high magnification (Figure **4.9**) shows that the black shades are surrounded by a grey matrix. The black shades corresponds to pores while the grey matrix represents the HEA. The grey matrix is homogenous throughout the microstructure and no secondary phases could be found as shown in the SEM/EDS map in Figure **4.10**. Hence, it can be concluded that the HEA NiMnFeCu had formed a random solid solution with FCC crystal structure evident under all sintering conditions.

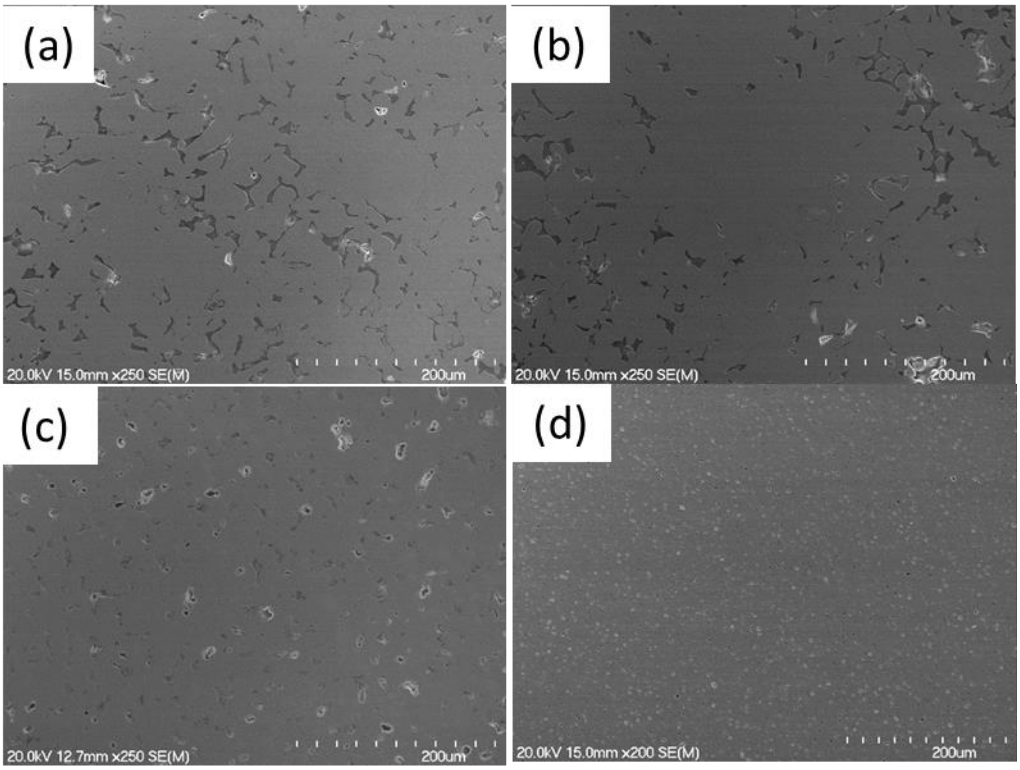

Figure 4.8 SEM images of the sintered HEA NiMnFeCu under the various sintering condition at low magnification (a) 1000°C for 1h(S1) (b) 1000°C for 2h(S2) (c) 1050°C for 1h(S3) (d) 1050°C for 2h(S4).

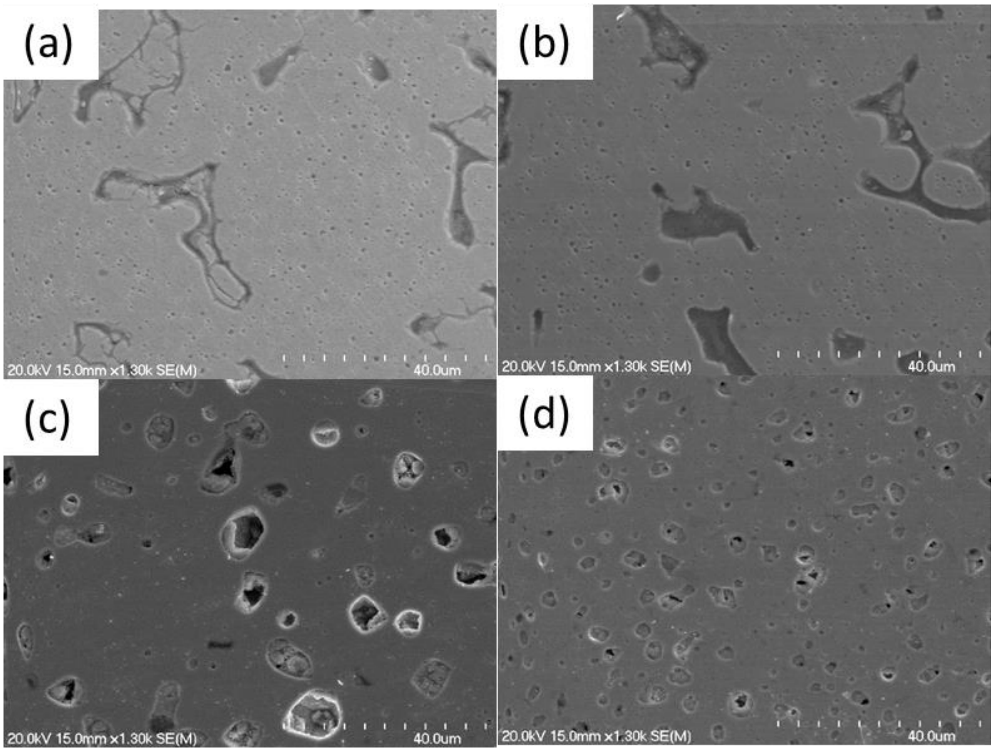

Figure 4.9 SEM images of the sintered HEA NiMnFeCu for the various sintering conditions at high magnification. (a) 1000°C for 1h (S1) (b)1000°C for 2h (S2) (c)1050°C for 1h (S3) (d) 1050°C for 2h (S4).

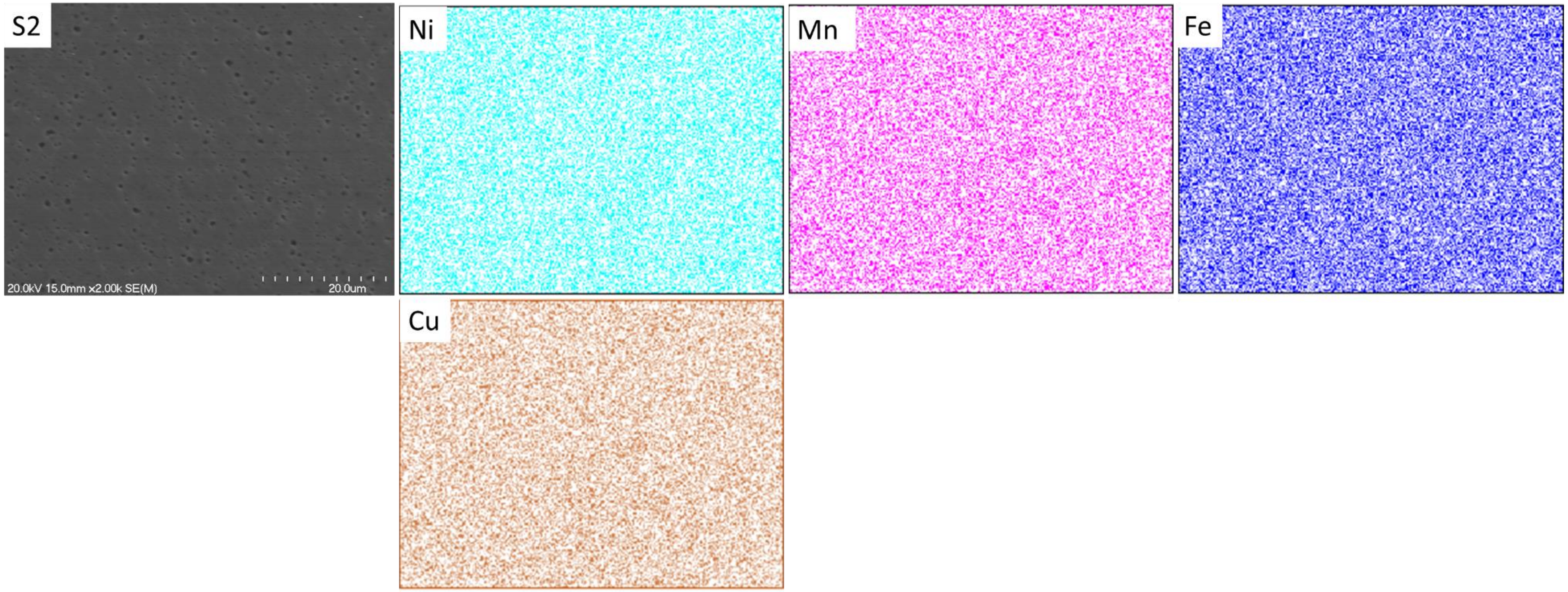

Figure 4.10 SEM/EDS map of sintered HEA NiMnFeCu for the sintering condition S2.

Figure **4.11** (a-b) represents the bright field TEM image of the sintered HEA NiMnFeCu under condition S2 and its corresponding selected area electron diffraction (SAED). The SAED pattern on the HEA matrix show the existence of a fundamental reflection of the FCC crystal structure. The d-spacings observed in the SAED pattern and from the high-resolution TEM image and the inverse fast Fourier transform (IFFT) image (Figure **4.11** (c-d)) are in accordance with the XRD results tabulated in Table **4.3**. Hence it could be concluded from SEM and TEM analyses that the HEA NiMnFeCu possessed a random solid solution as depicted in Figure **4.12** with FCC crystal structure.

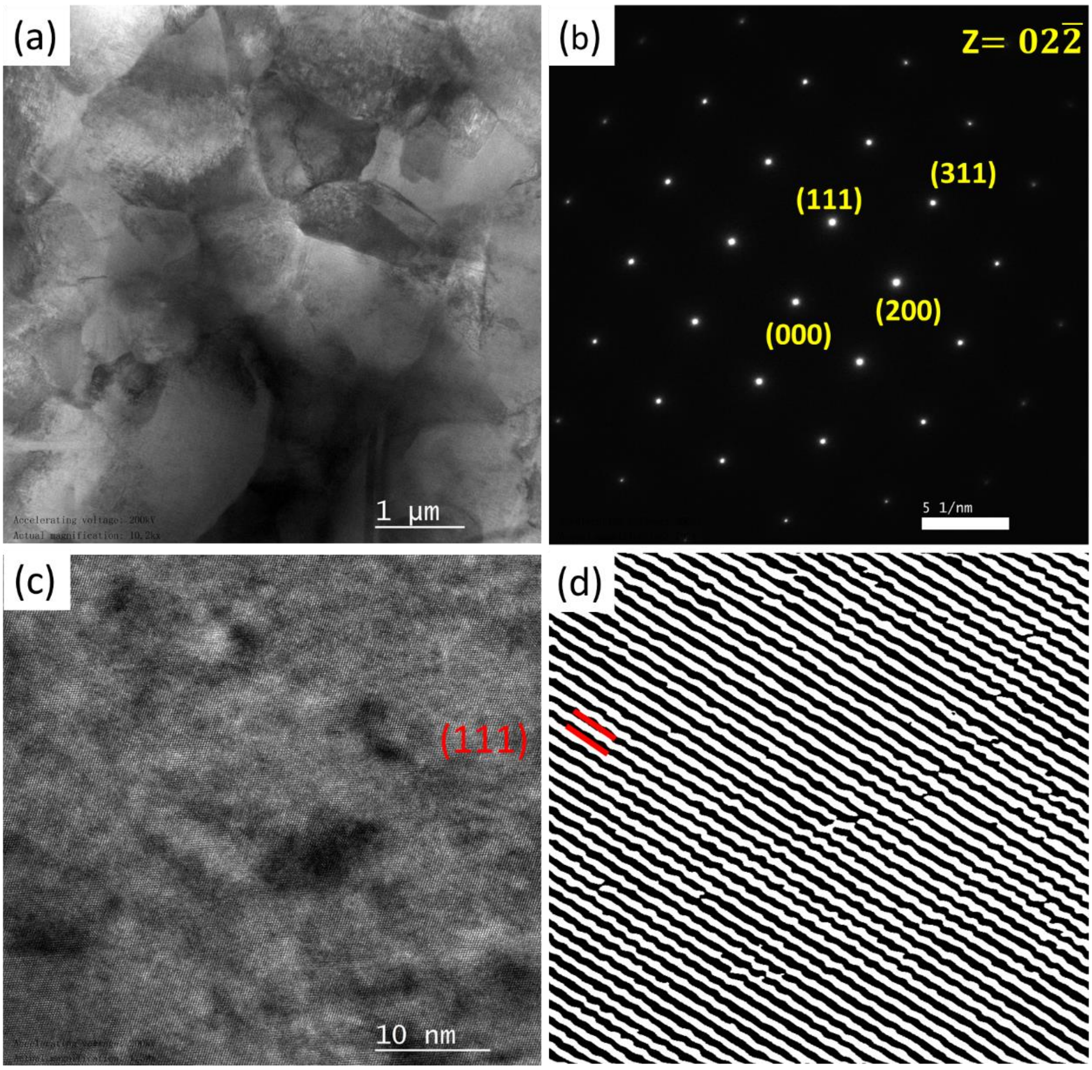

Figure 4.11 (a) Bright field TEM image of HEA NiMnFeCu under condition S2 (b) SAED pattern of the FCC2 phase zone axis [0,2,-2] (c) HRTEM image of S2 (d) Inverse FFT image of S2.

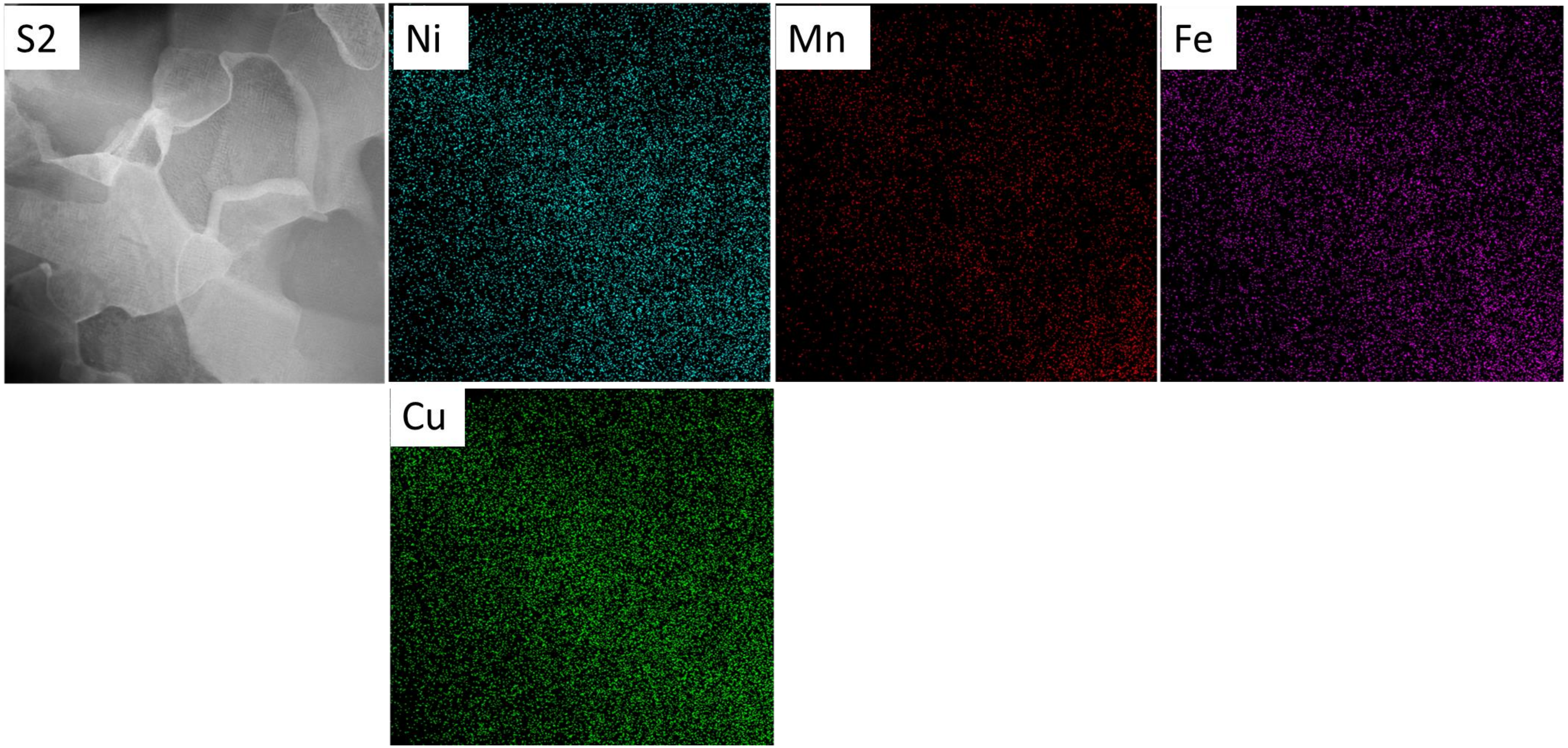

Figure 4.12 TEM/EDS map of the sintered HEA NiMnFeCu under condition S2.

Table 4.3 d spacing of the planes of the HEA NiMnFeCu measured using XRD patterns.

2θ (degrees)	Planes (hkl)	Crystal structure	d spacing nm
43.3	111	FCC	0.2081
50.3	200	FCC	0.2051
74.2	220	FCC	0.1845
89.7	311	FCC	0.1815
95.7	222	FCC	0.1491

4.1.6 Microhardness

Figure **4.13** depicts the mean and standard deviation of micro-hardness measurements of NiMnFeCu HEA under sintering conditions S1-S4. The mean and standard deviation of micro-hardness of S1and S2 are 104.88 ± 9 HV and 198.79 ± 8 HV respectively and for S3 and S4 the micro-hardness values are 115.28 ± 7 HV and 233.45 ± 9 HV respectively. It can be seen that the micro-hardness of HEA made under condition S4 is higher when compared to those HEAs made under the conditions (S1-S3)

Based on the microstructural characterization above (Figure **4.7**), S4 have high relative sintered density when compared to other sintering conditions (S1-S3). As a result, the micro-hardness of S4 is significantly higher when compared to S1-S3. The presence of a high residual porosity and low relative sintered density leads to the low micro-hardness values of samples S1-S3. For the samples S2 and S3, the relative sintered density is very close to each other, however the micro-hardness value of S2 is significantly higher than S3. It has been reported elsewhere that along with the density, the spatial and topological distribution of pores also plays a critical role in mechanical properties of the fabricated material[145, 146]. Since the depth of penetration of the micro-hardness tester (even at maximum load (9.80N)) is only a few μm , the influence of topological distribution (along the depth) of pores can be neglected, while the spatial distribution (along the length and width) of pores can be taken in account. The micro-hardness of S2 is higher compared to S3 because the microstructure of S2 had pores distributed in clusters and they are spaced wider from each other while the pores in S3 were distributed very close to each other, hence there is more probability for a pore to be present directly below the indent. As a result, the micro-hardness values of S3 are lower compared to S2[145].

NiMnFeCu retains its single-phase FCC crystal structure under all sintering conditions (S1-S4). Most reported single-phase FCC HEAs have usually possessed hardness values ranging from 100 – 200 HV [21, 147]. Hence the sintered NiMnFeCu at condition S4 possessed a micro-hardness value that was higher than those of other single-phase FCC HEAs. Although there are considerable number of HEAs having microhardness values higher than the studied NiMnFeCu HEA listed in Table **4.4**, it is important to note that those HEAs are not single phase FCC, they often have intermetallic phase which contribute to its strength.

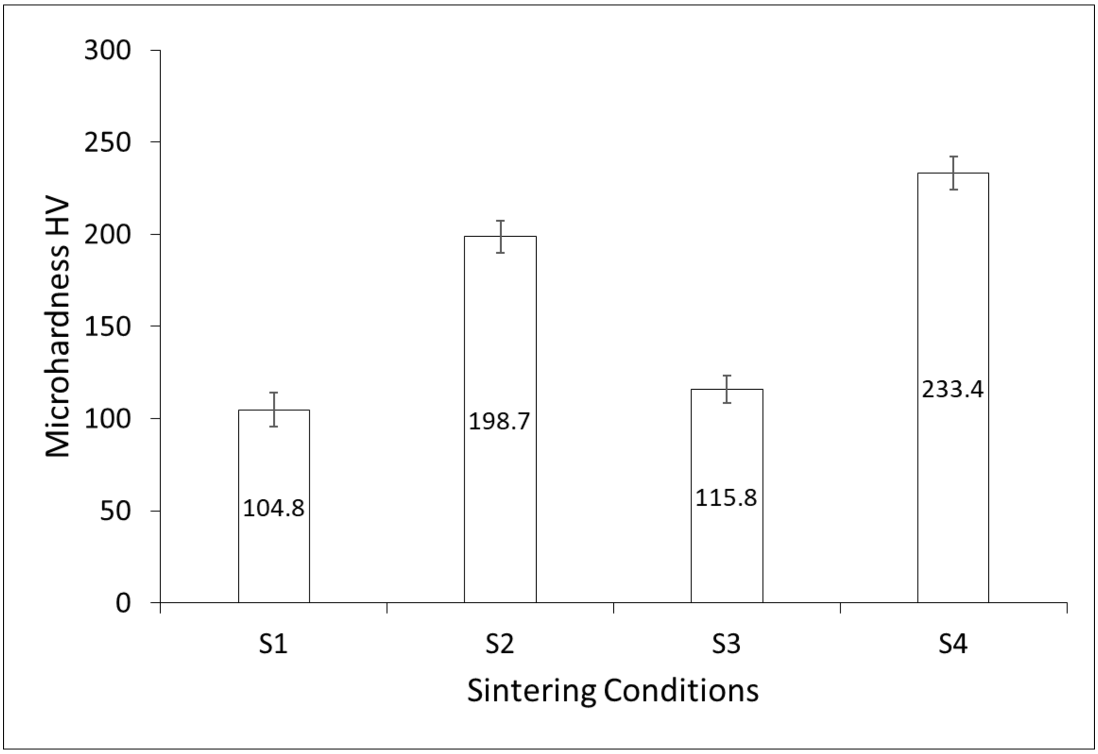

Figure 4.13 Micro-hardness test of the sintered NiMnFeCu under various sintering conditions.

Table 4.4 Micro-hardness of 3d transition metal based HEAs reported from the literature.

HEA	Micro-hardness HV	Reference
Al0.25CoFeNi	138	[147]
CoFeNiSi0.25	149	[38]
CoFeNiSi0.75	570	[147]
Al0.75CoFeNi	385	[147]
CoCrFeMo0.5Ni	210	[147]
Al0.7Co0.3CrFeNi	624	[147]
Al0.75CoCrFeNi	388	[147]

CoCrFeNi	116	[147]
NiMnFeCu	233.4	Present work

4.1.7 Compression

Figure **4.14** shows the compressive yield stress of the sintered NiMnFeCu under various sintering conditions. It appeared evident that the condition S4 possessed greater yield strength when compared to all other sintering conditions (S1-S3). For the conditions S1 and S2, the alloy yielded at 298.7 MPa and 389.8 MPa respectively and for S3 and S4 the alloys possessed a yield stress of 295.9 MPa and 516.3 MPa respectively.

S4 possessed better yield strength when compared to all other alloys (S1-S3) because of high final sintered density and less porosity. The microstructures of S1-S3 contain high porosity and this leads to reduction in yield strength. Despite the similar relative densities of the samples S2 and S3, their compressive yield strength varied significantly to each other. This could be attributed to the spatial distribution of pores[145]. The studied NiMnFeCu (S4) possessed comparable compressive yield strength when compared to other 3d transition metal based HEAs listed in Table **4.5**.

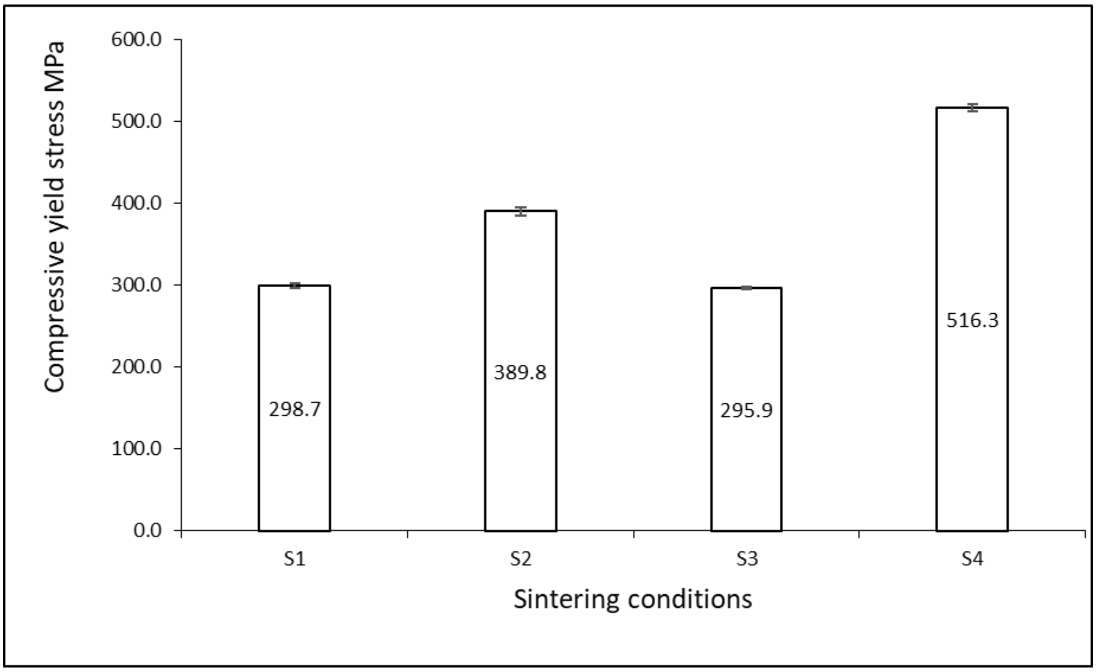

Figure 4.14 Compressive yield stress of the sintered HEA NiMnFeCu under various sintering conditions.

Table 4.5 Compressive yield stress of 3d transition metal based HEAs as reported in the literature.

HEA	Compressive yield stress MPa	Reference
Al0.25CoFeNi	158	[147]
Al0.75CoFeNi	794	[147]
CoFeNiSi0.75	1301	[147]
Al0.75CoFeNi	794	[147]
Al0.7Co0.3CrFeNi	2033	[147]
AlCoCrFeNi	1251	[147]
AlCoCrFeNi	1110	[147]
CoFeNiSi0.25	196	[38]
CoCrFeNi	148	[147]
NiMnFeCu	516.3	Present work

4.2 Consolidation of HEA NiMnFeCrCu

Table **4.6** summarises the details of the sintering conditions of the sintered HEA NiMnFeCrCu

Table 4.6 Sintering condition for HEA NiMnFeCrCu.

Sample	Temperature °C	Holding time h
R1	1000	1
R2	1000	2
R3	1050	1
R4	1050	2

4.2.1 Effect of sintering temperature on phase composition

Figure **4.15**(a) depicts the XRD patterns of the sintered HEA NiMnFeCrCu under various sintering conditions. After examination of the XRD patterns it is evident that the HEA NiMnFeCrCu exhibited two FCC phases (FCC1 & FCC2) and a BCC phase as shown Figure **4.15**(b). The HEA NiMnFeCrCu under all sintering conditions exhibited a duplex phase structure (FCC as major and BCC as minor). Despite the fact that the milled HEA NiMnFeCrCu powders after 15 h of milling possessed one FCC and one BCC, the sintered HEA under all conditions possessed two FCC phases and a BCC phase. The first FCC phase has peaks at 2θ= 42.5°, 48.3°, 72.6° .87.9° and 94.8° which correspond to (111), (200), (220), (311) and (222). The second FCC phase has peaks at 2θ= 43.3°, 50.2°, 74.0° ,89.9° and 95.2°. and they also correspond to (111), (200), (220), (311) and (222). The BCC phase has peaks at 2θ= 44.2°and 62.1°and they correspond to (110) and (200). Similar results were observed in previously reported works on similar composition[129, 138]. The presence of two FCC peak could be attributed to a phenomenon termed spinodal decomposition which will be discussed in detail in later sections[148].

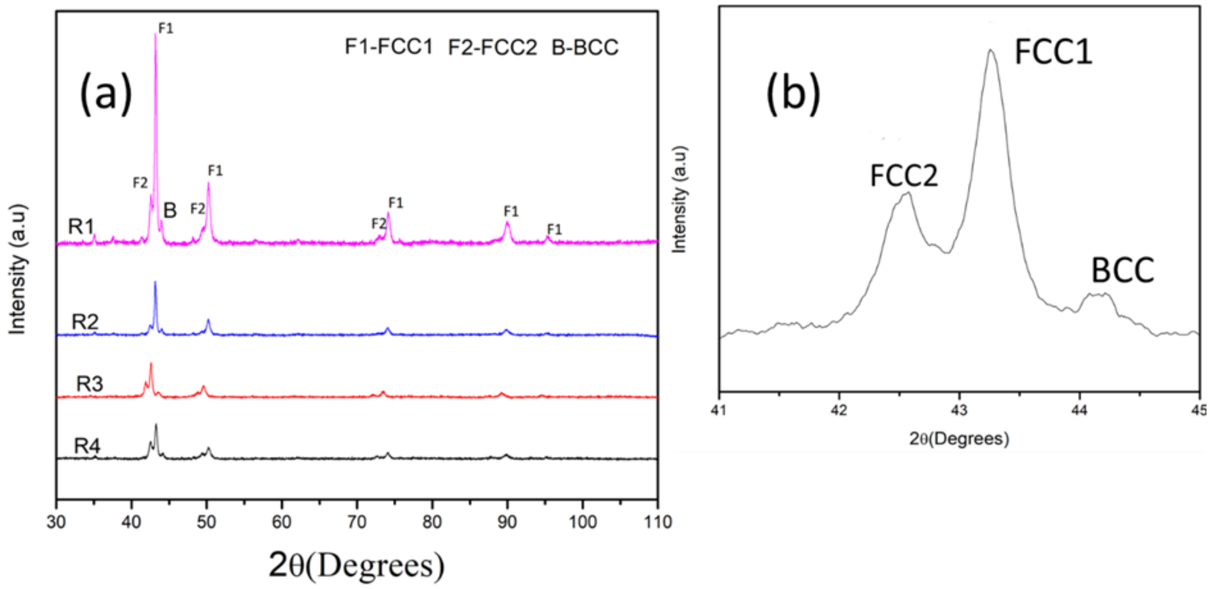

Figure 4.15 XRD patterns of the sintered HEA NiMnFeCrCu for the various sintering conditions.

4.2.2 Effect of sintering temperature and time on the microstructure of the HEA NiMnFeCrCu

Figure **4.16**(a-d) represents the OM images and Figure **4.16**(e-h) represents the SEM images of the sintered HEA NiMnFeCrCu for the various sintering conditions respectively. Table **4.7** lists the information related to porosity of the sintered HEA NiMnFeCrCu under different sintering conditions. Microstructural observation indicates that the pore size is relatively smaller for the alloys prepared under conditions R1 and R2 compared to R3 and R4. As a result, the relative sintered density of R1 and R2 are 90% and 95% and the average pore size is 3.09 µm and 2.49 µm, respectively. R3 and R4 alloys have more and larger pores than R1 and R2 and the relative density and pore size are 70% and 15.3 µm for R3 alloy and 77% and 10.7 µm for R4 alloy respectively. Usually the higher sintering temperature will produce a higher sintered density for the alloy, since the atomic diffusion is accelerated with an increase in sintering temperature[149]. However, the HEA NiMnFeCrCu showed reduced value of its final sintered density when sintering temperature was increased. To further understand the sintering kinetics of HEA NiMnFeCrCu, the HEA was sintered from 1000°C to 1150°C and the effect of phase composition as a function of sintering temperature was studied, Figure **4.17** (a and b) represents the XRD patterns of NiMnFeCrCu HEA sintered in a temperature range of 1000°C-1150°C. Figure **4.17**(c) depicts the change of phase composition of FCC1 and FCC2 as a function of increasing sintering temperature. It is observed that the phase composition of FCC2 decreased as a function of increasing sintering temperature and that the FCC1 phase composition showed the opposite trend. SEM/EDS analysis from Table **4.8** showed that the FCC2 phase was rich in Cu, with this Cu rich FCC 2 phase exhibiting a lower melting point compared to that of the other phases (FCC1,BCC) in the NiMnFeCrCu HEA[150]. Hence it can be concluded that the observed decrease in the final sintered density of the HEA with an increase in sintering temperature is due to depletion of this Cu rich secondary FCC2 owing to preferential melting as a result of its lower melting point.

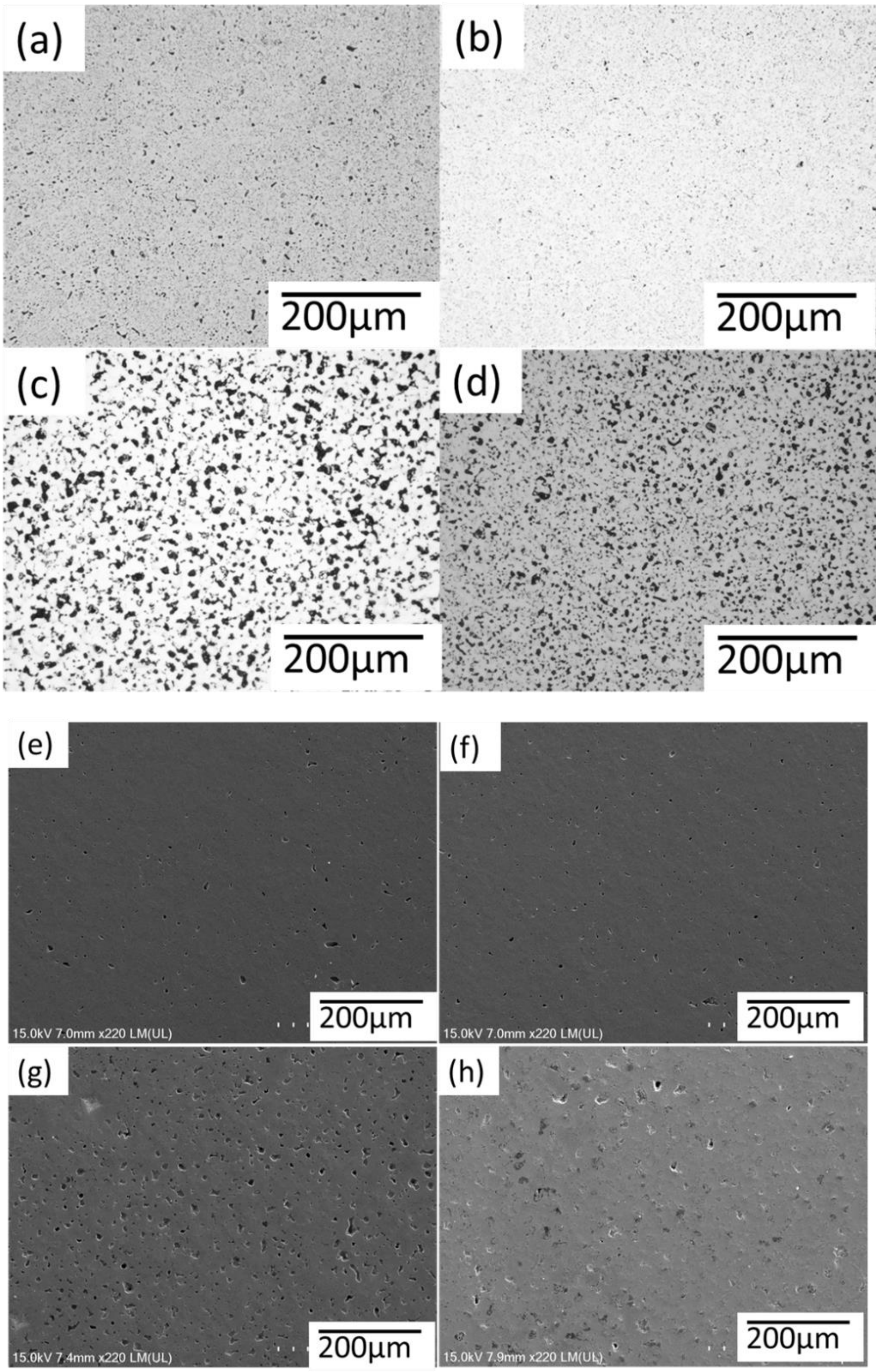

Figure 4.16 OM and SEM images of the sintered HEA NiMnFeCrCu under various sintering conditions. (a,e) at 1000°C for 1h(R1) (b,f) at 1000°C for 2h(R2) (c,g) at 1050°C for 1h(R3) (d,h) at 1050°C for 2h(R4).

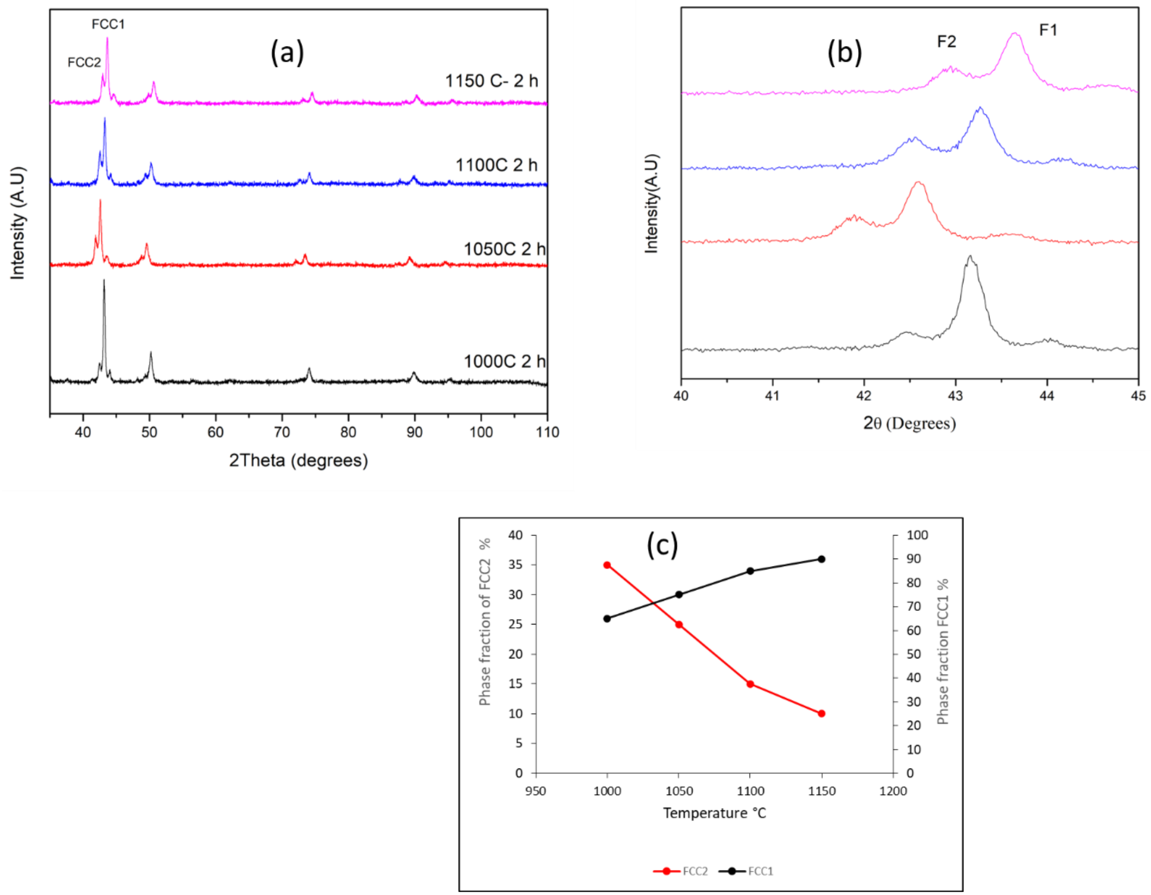

Figure 4.17 (a) XRD patterns of the sintered HEA NiMnFeCrCu at different temperatures (b) Magnified image of the most intense peak at different temperatures (c) Phase composition of FCC phases as a function of sintering temperature.

Table 4.7 Pore size and morphology of the sintered HEA NiMnFeCrCu under various sintering condition.

Sample	Average pore size (µm)	Circularity of pores index	Relative sintered density (%)
R1	3.09	0.835	90
R2	2.49	0.825	95
R3	15.31	0.787	70
R4	10.72	0.800	77

Figure **4.18**(a-b) represents the SEM image of R2 which is acquired in the secondary electrons and back scattered electrons modes, and Figure **4.19** represents the SEM/EDS mapping of the sintered HEA under the condition R2. Referring to XRD patterns depicted earlier in Figure **4.15**(a-b) and the SEM/EDS map depicted in Figure **4.19**, the following observations could be made. The dark oval shaped black band (marked in red) represents the BCC phase of the alloy. The dark grey pattern which occupies a larger area in the microstructure corresponds to FCC1(yellow) which is the main constituent of the FCC phases observed. A lighter grey band corresponds to the secondary FCC2 phase as marked in orange. The BCC phase is rich in Cr with an atomic proportion of 77.8%. In contrast, the secondary FCC2 phase is richer in Cu with an atomic proportion of 38.6% and the primary FCC1 is approximately homogenous in terms of elemental composition. The elemental compositions of each phase (full area scan of Figure **4.19**) are listed in Table **4.8**.

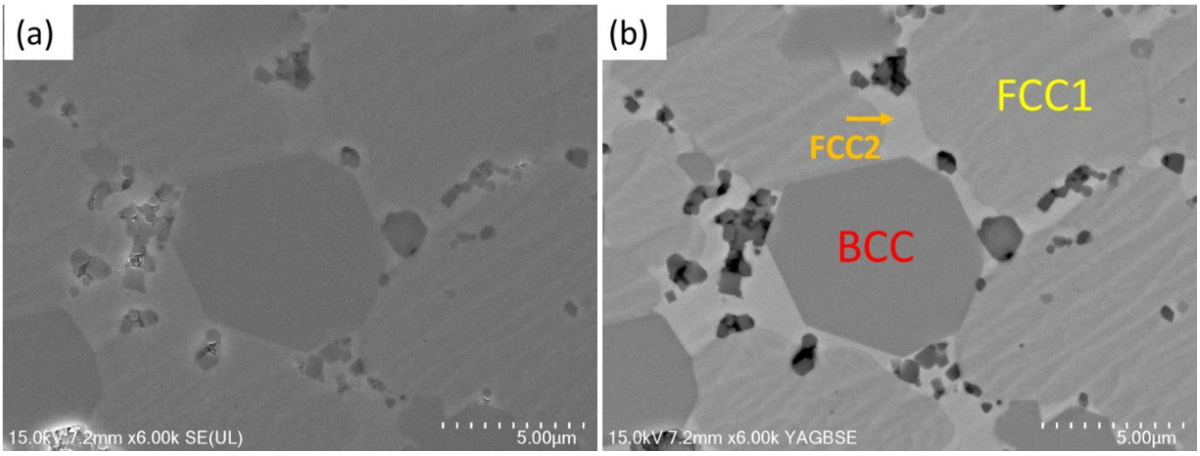

Figure 4.18 SEM images of the sintered HEA NiMnFeCrCu (a) secondary electron image (b) back scattered electron image.

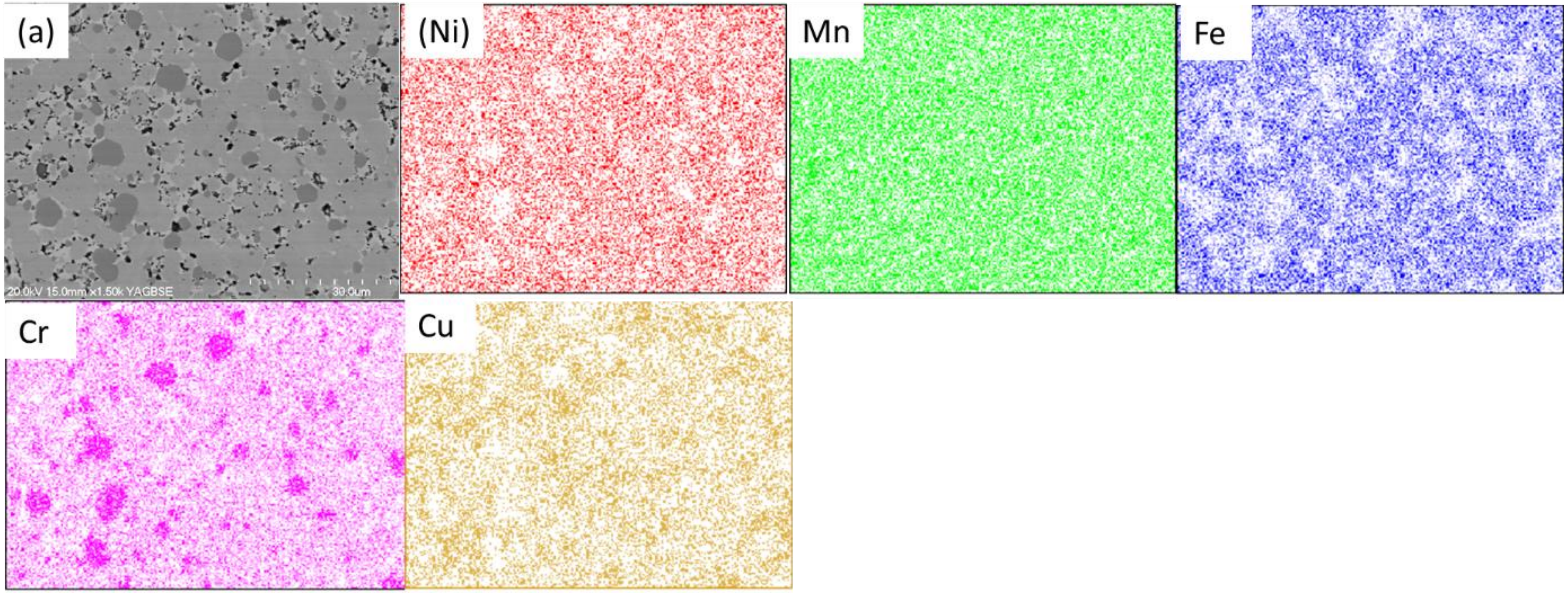

Figure 4.19 SEM/EDS maps of the sintered HEA NiMnFeCrCu under condition R2.

Table 4.8 Elemental composition in atom % of the different phases in the sintered HEA NiMnFeCrCu under condition R2.

Phases	Ni %	Mn%	Fe%	Cr%	Cu%
FCC 1	22.6	20.2	28.6	18.41	9.9
FCC 2	18.7	24.4	6.6	11.4	38.6
BCC	3.9	6.8	8.6	77.8	1.7
Total	19.6	18.8	22.1	21.3	18.04

Figure **4.20** depicts the TEM bright field image of the sintered NiMnFeCrCu HEA under condition R2. It is observed clearly that the microstructure consists of three distinct features or phases.These are: an interconnected “woven” like microstructure (Figure **4.20** (a)), a uniform homogeneous microstructure as depicted in Figure **4.21**(a) and a dark ellipsoidal shaped phase as indicated in (Figure **4.22** (a)). To further explore these microstructural features in detail, high resolution TEM (HRTEM) images and their corresponding selected area electron diffraction (SAED) patterns on the interconected “woven” like phase and on the uniform homogeneous phase were obtained. These are shown in Figure **4.20**(a-d) and Figure **4.21**(a-d) respectively. The TEM image and the corresponding SAED pattern indicate that the interconnected “woven”-like microstructure, which occupies a larger volume fraction relative to the other phases, belongs to the FCC1 phase which is the primary phase. The uniform homogenous microstructure, as shown in Figure **4.21** (a-b), belong to the FCC2 phase which represents a secondary phase. The d spacings measured from the SAED pattern from the $02\bar{2}$ FCC zone axis of the (111) planes of the FCC1 phase and FCC2 phase are 0.209nm and 0.213 nm, respectively, which are in accordance with the XRD results as shown earlier in Figure **4.17**(a-b) and Table **4.9**. The observed “woven” microstructure of FCC1 is reminiscent of a spinodal microstructure that has formed from the decomposition of a supersaturated metastable random solid soultion phase into two iso-structural phases (viz,FCC1 and FCC2) with a minor compositional fluctuation, this is caused by the fact that FCC2 is richer in Cu while FCC1 is approximately elementally homogenous as depicted in Figure **4.23**. HEAs possessing a positive enthalpy of mixing (ΔH_{mix} = 2.75 kJ mol^{-1} for NiMnFeCrCu HEA) values tend to form a spinodal microstructure which is characterized by an interconnected “woven” like microstructure[151-153]. Furthermore, the formation of a Cu rich phase is also due to the segregation that arises out of a lack of solubility of Cu with Cr and Fe owing to positive mixing enthalpy. The binary mixing enthalpy of Cu-Cr and Cu-Fe is

12 and 13 kJmol^{-1}, respectively, thus the Cu rich phase of FCC2 is expected to have lower content of Cr and Fe[150].

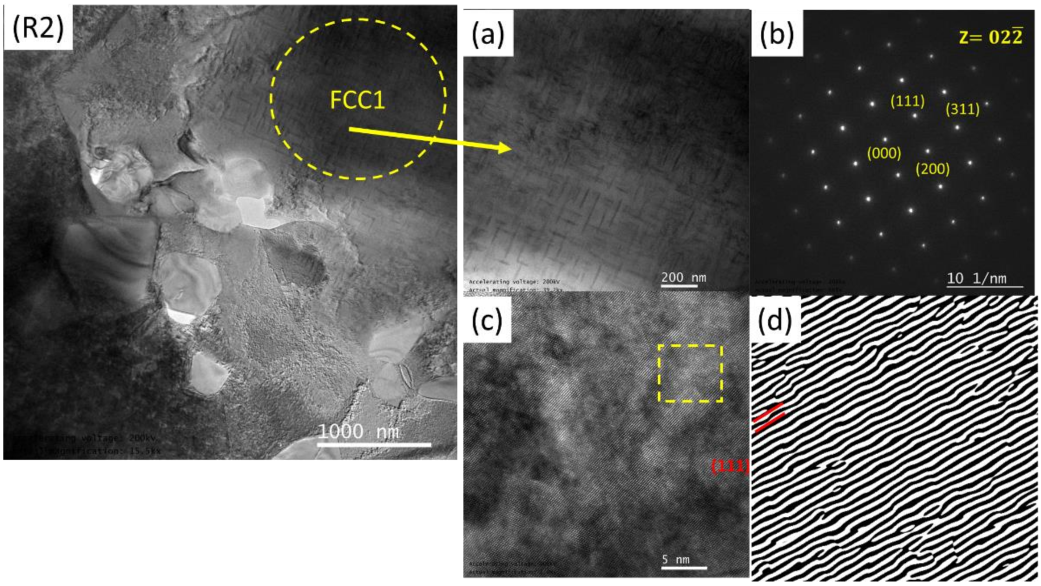

Figure 4.20 (R2) Bright field TEM image of HEA NiMnFeCrCu under condition R2 (a) Bright field TEM image of the FCC1 phase of the alloy R2 (b) SAED pattern of the FCC1 phase (c) HRTEM image of the FCC1 phase (d) Inverse FFT image of the FCC1 phase.

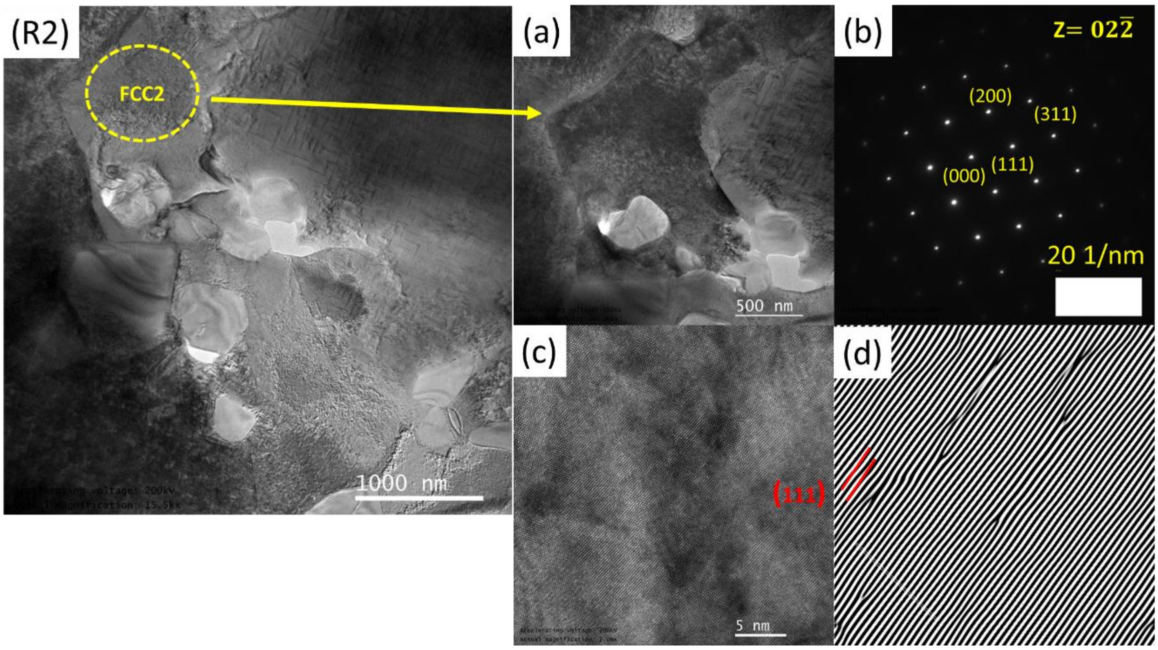

Figure 4.21 (R2) Bright field TEM image of HEA NiMnFeCrCu under condition R2 (a) Bright field TEM image of the FCC2 phase of the alloy R2 (b) SAED pattern of the FCC2 phase (c) HRTEM image of the FCC2 phase (d) Inverse FFT image of the FCC2 phase.

Figure 4.22 (a-d) represents the bright field HRTEM image and its corresponding selected area electron diffraction (SAED) pattern of the dark ellipsoidal phase. It can be clearly seen that the dark ellipsoidal shaped phase observed belongs to a BCC structure. The d spacing measured from the SAED pattern with a $00\bar{2}$ zone axis reveals that the (110) plane of the BCC phase possesses a d spacing of 0.192 nm which is in accordance with the XRD results shown earlier in Figure **4.6** (a-b) and Table **4.9**. As expected, the BCC phase is rich in Cr as depicted in Figure **4.19** and Figure **4.23** . In addition to that, remnants of oxide inclusions are observed within the BCC phase. Further analysis proves that these oxide inclusions are Cr_5O_{12}. As reported in previous works oxide inclusions are common in Cr and Mn containing HEAs with the formation of Cr_5O_{12} particles being due to the high susceptibility of Cr to form oxides[129].

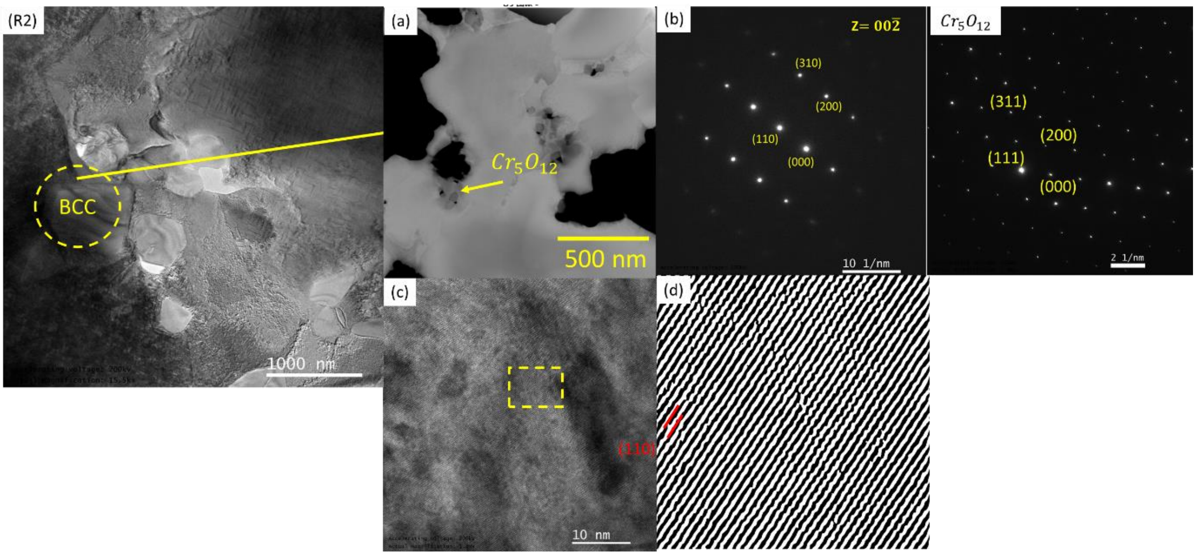

Figure 4.22 (R2) Bright field TEM image of HEA NiMnFeCrCu under condition R2 (a) Bright field TEM image of an area of the alloy containing the BCC phase of the alloy R2 (b) SAED pattern of the BCC phase (c) HRTEM image of the area of the alloy with the BCC phase (d) Inverse FFT image of the BCC phase.

Table 4.9 d spacing of the planes present in XRD patterns of the as sintered HEA NiMnFeCrCu under condition R2.

2θ (degrees)	Planes (hkl)	Crystal structure	d spacing nm
42.37	111	FCC2	0.2125
43.10	111	FCC1	0.2091
43.99	110	BCC	0.2051
49.35	200	FCC2	0.1845
50.21	200	FCC1	0.1815
62.20	200	BCC	0.1491

72.60	220	FCC2	0.1301
74.3	220	FCC1	0.1279

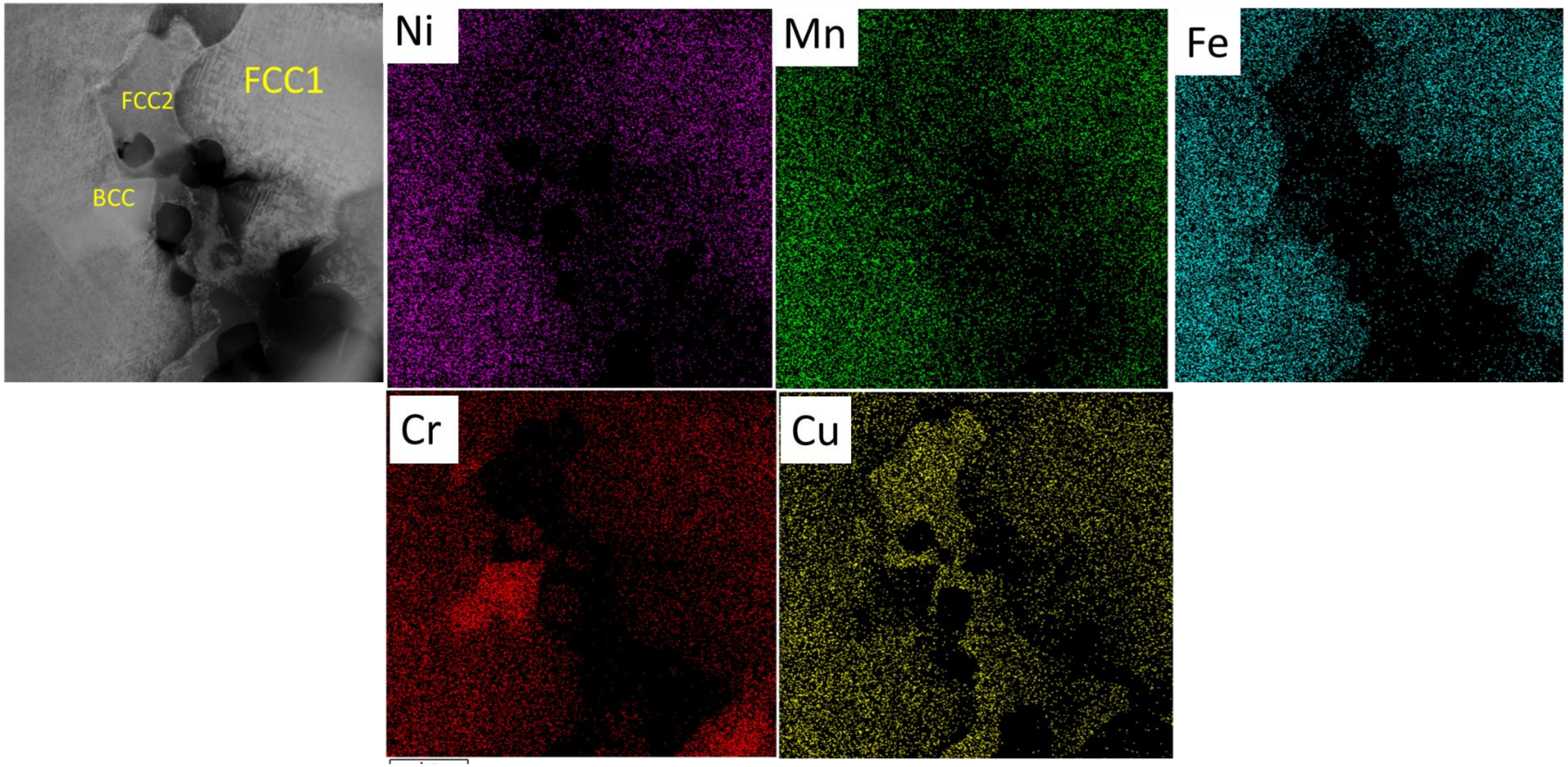

Figure 4.23 TEM/EDS of the sintered HEA NiMnFeCrCu under condition R2.

4.2.3 Microhardness

Figure 4.24 depicts the mean and standard deviation of micro-hardness measurements of NiMnFeCrCu HEA under sintering conditions R1-R4. It can be seen that the micro-hardness of HEA synthesised under condition R2 is highest followed by R1 while the microhardness of R3 and R4 were lower compared to those HEAs synthesised under conditions (R1-R2). The mean and standard deviation of the micro-hardness measurements of R1and R2 HEAs are 226.62 ± 6 HV and 250 ± 5 HV respectively and for R3 and R4 HEAs, the micro-hardness values are 104.4 ± 3 HV and 152 ± 6 HV respectively.

Based on the microstructural characterization above (Figure **4.16**), R1 and R2 have high relative sintered density when compared to HEAs made under sintering conditions (R3-R4). As a result, the micro-hardness values of R1 and R2 HEAs were similar to each other. The presence of a high residual porosity and low relative sintered density leads to the low micro-hardness values as measured for HEA samples R3 and R4. [145]. The mechanical properties in HEA stem from several factors such as grain size, phase composition and relative density. Quantification of grain size and its effect on mechanical properties are beyond the scope of this research, and it is rather the effect of phase compositions and relative density that are being considered in this research. A duplex phase structure (FCC+BCC) provides better mechanical properties when compared with single phase FCC or BCC because purely FCC HEAs lack adequate strength while pure BCC HEAs are brittle[154]. However, a duplex phase (FCC+BCC) structures provides an adequate balance between strength and plasticity because the (110) plane of BCC structure has a strong resistance towards slip so contributing to strength while the (111) plane of FCC has less resistance towards slip which contributes to plasticity [155, 156]. HEA NiMnFeCrCu is expected to have excellent mechanical properties when compared to other single-phase FCC or BCC HEAs. Hence the excellent microhardness of HEA NiMnFeCrCu manufactured under condition R2 could be attributed to its duplex structure (FCC +BCC) and its high relative density when compared to HEA sintered via the other conditions (R1, R3 and R4).

NiMnFeCrCu retained its duplex phase FCC+BCC crystal structure under all sintering conditions (R1-R4). The sintered NiMnFeCrCu at condition R2 possessed micro-hardness values comparable to that of other duplex phase FCC+BCC HEAs which are listed in Table **4.10**

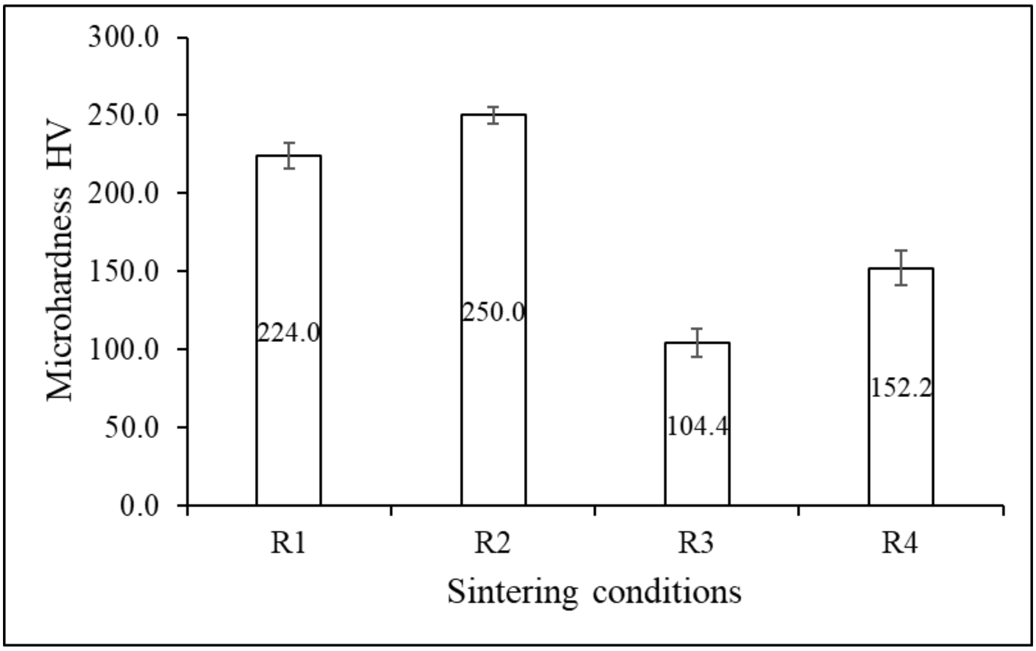

Figure 4.24 Microhardness of the sintered HEA NiMnFeCrCu under various sintering condition.

Table 4.10 Micro-hardness of 3d transition metal based HEAs reported from the literature.

HEA	Micro-hardness HV	Reference
Al0.25CoFeNi	138	[147]
CoFeNiSi0.25	149	[38]
CoFeNiSi0.75	570	[147]
Al0.75CoFeNi	385	[147]
CoCrFeMo0.5Ni	210	[147]
Al0.7Co0.3CrFeNi	624	[147]
Al0.75CoCrFeNi	388	[147]
CoCrFeNi	116	[147]
NiMnFeCrCu	250	Present work

4.2.4 Compression

Figure **4.25** shows the compressive yield stress of the sintered NiMnFeCrCu under various sintering conditions. It was evident that HEAs manufactured under the condition R2 possessed greater yield strength when compared to all other sintering conditions. R1 possessed yield stress slightly lower when compared to R2. For the conditions R1 and R2, the HEA alloy yielded at 699.5 MPa and 724 MPa respectively and for R3 and R4 the HEA alloys possessed a yield stress of 515 MPa and 563.6 MPa respectively.

R1 and R2 alloys possessed better yield strength when compared to all other alloys (R3-R4) because of the higher values of final sintered density realised in addition to the lower level of porosity observed. The microstructures of alloys R3-R4 contained higher porosity which consequently led to lower yield strength values. The studied NiMnFeCrCu (R2) possessed comparable compressive yield strength when compared to the other 3d transition metal based HEAs listed in Table **4.11**. The high yield strength could also be attributed to the presence of a duplex crystal structure as discussed previously.

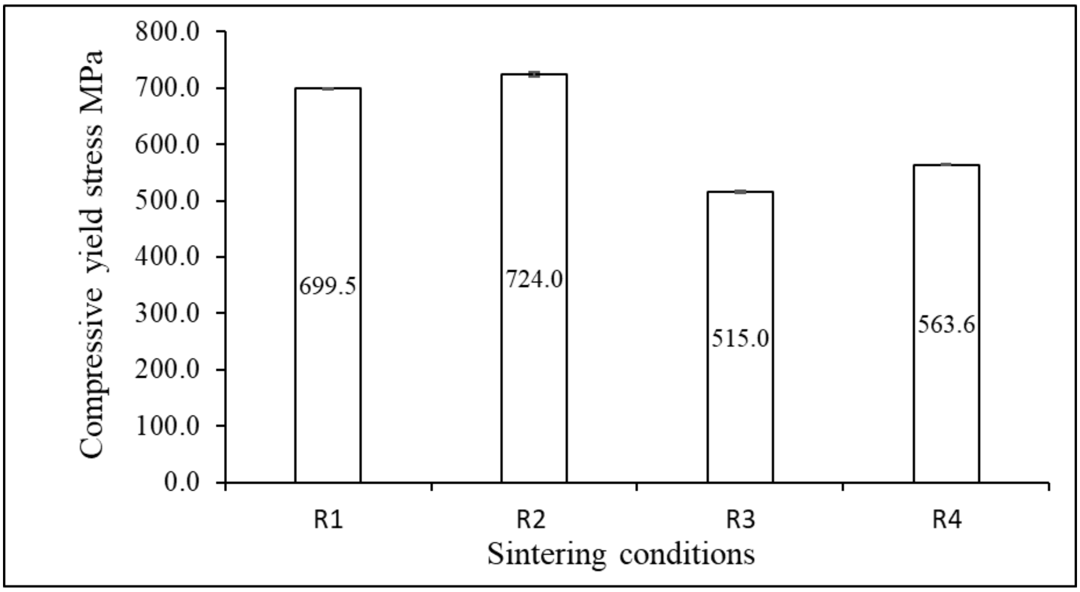

Figure 4.25 Compressive yield stress of the sintered HEA NiMnFeCrCu synthesised under various sintering conditions.

Table 4.11 Compressive yield stress of 3d transition metal based HEAs reported from the literature.

HEA	Compressive yield stress MPA	Reference
Al0.25CoFeNi	158	[147]
Al0.75CoFeNi	794	[147]
CoFeNiSi0.75	1301	[147]
Al0.75CoFeNi	794	[147]
Al0.7Co0.3CrFeNi	2033	[147]
AlCoCrFeNi	1251	[147]
AlCoCrFeNi	1110	[147]
CoFeNiSi0.25	196	[38]
CoCrFeNi	148	[147]

NiMnFeCrCu	724	Present work

4.3 Consolidation of HEA NiMnFeCr

4.3.1 Effect of sintering temperature and time on phase composition

Table 4.12 summarises the details of the sintering conditions of the sintered HEA NiMnFeCr and Figure **4.26**(a) depicts the XRD patterns of the sintered HEA NiMnFeCr synthesised under the various sintering conditions(T1-T4). Figure **4.26** (b) represents the magnified image of the most intense peaks of the sintered HEA when synthesised under a sintering condition of 1200ºC and 1 h of holding time (T1). From the patterns, it is evident that under all sintering conditions the HEA possesses a major FCC phase and a negligible BCC phase.

Table 4.12 Sintering conditions of HEA NiMnFeCr.

Sample	Temperature °C	Holding time h
T1	1150	1
T2	1150	2
T3	1200	1
T4	1200	2

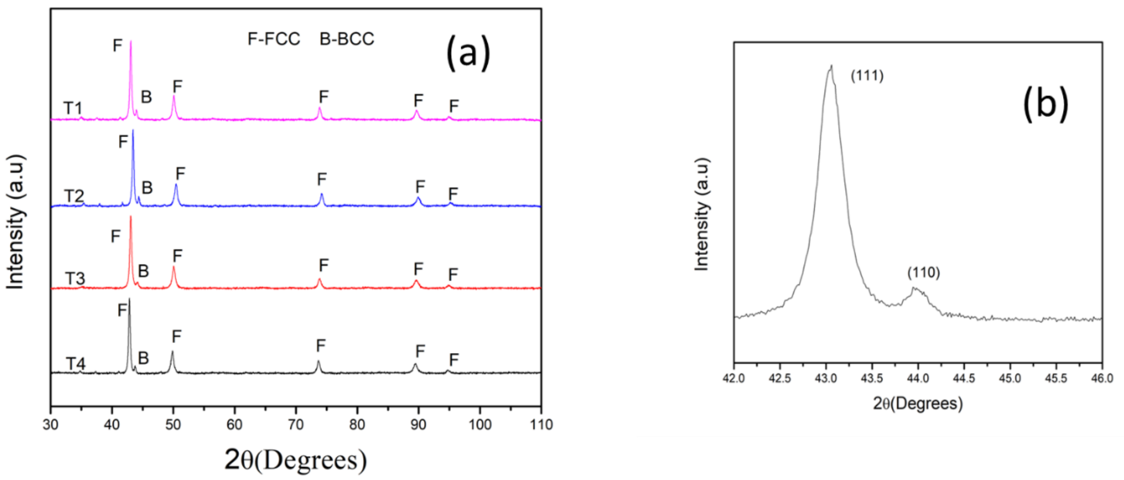

Figure 4.26 XRD patterns of the sintered HEA NiMnFeCr under various sintering conditions.

4.3.2 Effect of sintering temperature and time on microstructure

Figure **4.27**(a-d) shows the OM images of the sintered NiMnFeCr fabricated under various sintering conditions. It can be seen that, the T1-T4 HEA alloys possess a varying degree of porosity. The information regarding the pore size and the morphology for the sintered NiMnFeCr HEAs (T1-T4) can be found in Table **4.13**. The average pore sizes of T1 and T2 are 34.7 μm and 37.3 μm respectively and the morphology of the pores of the T1 and T2 samples remained irregular. The average pore sizes of T3 and T4 are 11.2 μm and 8.1 μm respectively. The sintered relative densities of T1 and T2 are 79% and 82% respectively and the sintered relative density of T3 and T4 were 83% and 94% respectively.

The sample T4 possessed the least porosity when compared to the other samples (T1-T3) and consequently the relative sintered density was the highest (94%) for the T4 sample when compared to the other samples (T1-T3). This enhanced densification of T4 could be attributed to the increased mass transport occurring at the higher sintering temperature (1200°C) over the longer sintering holding time (2 h).

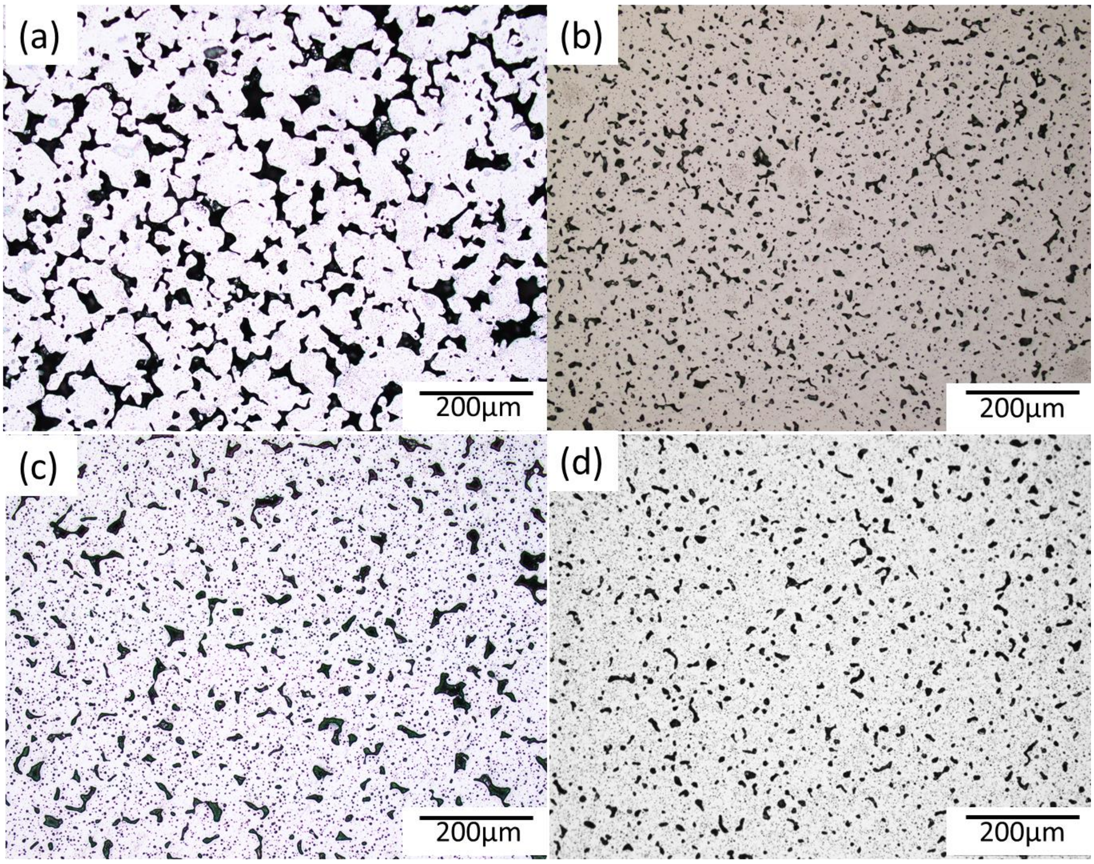

Figure 4.27 OM images of the sintered HEA NiMnFeCr prepared under various sintering conditions. (a) at 1150°C for 1h(T1) (b) at 1150°C for 2h(T2) (c) at 1200°C for 1h(T3) (d) at 1200°C for 2h(T4).

Table 4.13 Pore size and morphology of the sintered HEA NiMnFeCr under the various sintering conditions.

Sample	Average pore size (µm)	Circularity of pores index	Relative sintered density(%)
T1	34.78	0.41	79
T2	37.35	0.46	82
T3	11.2	0.87	83
T4	8.1	0.89	94

Figure **4.28** (a-d) and Figure **4.29** (a-d) shows the microstructure of the sintered HEA under low and high magnification when prepared under the various sintering conditions. The presence of excessive porosity is further confirmed in the microstructures of T1-T3. However the microstructure of T4 possessed relatively smaller size pores compared to (T1-T3). Furthermore the HEA NiMnFeCr exhibited a homogenous microstructure with a major FCC phase while the minor BCC phase could not be detected in the SEM/EDS map due to its negligible volume fraction as shown in Figure **4.30**.

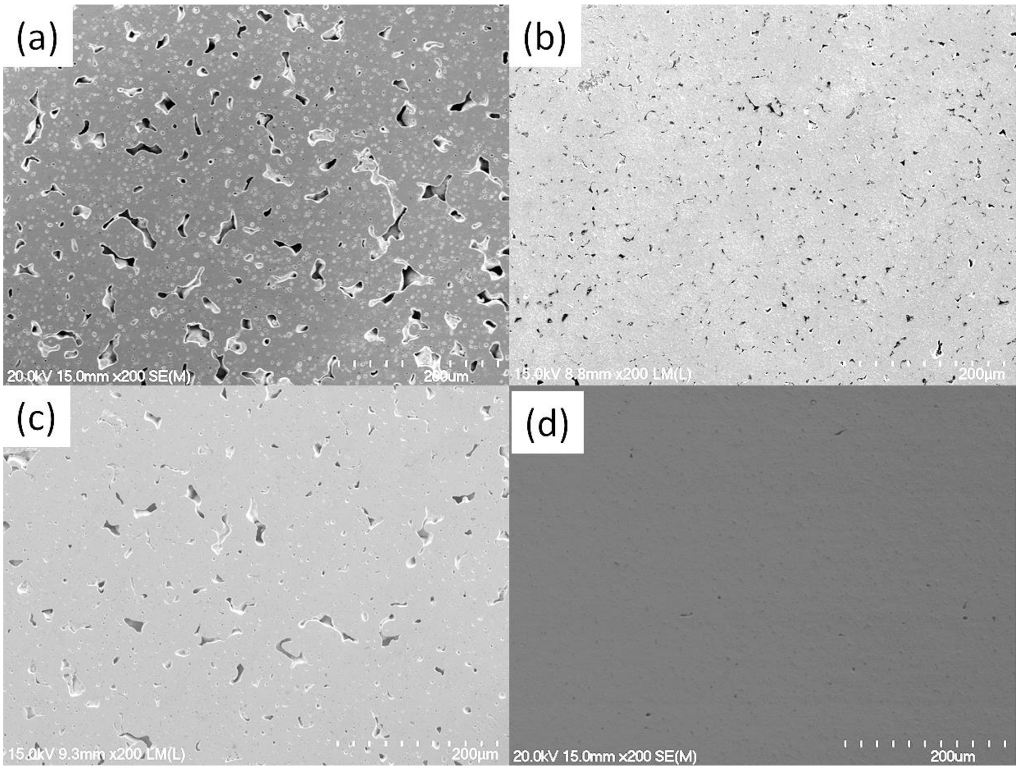

Figure 4.28 SEM images of the sintered HEA NiMnFeCr under various sintering conditions at low magnification. (a) at 1150°C for 1h(T1) (b) at 1150°C for 2h(T2) (c) at 1200°C for 1h(T3) (d) at 1200°C for 2h(T4).

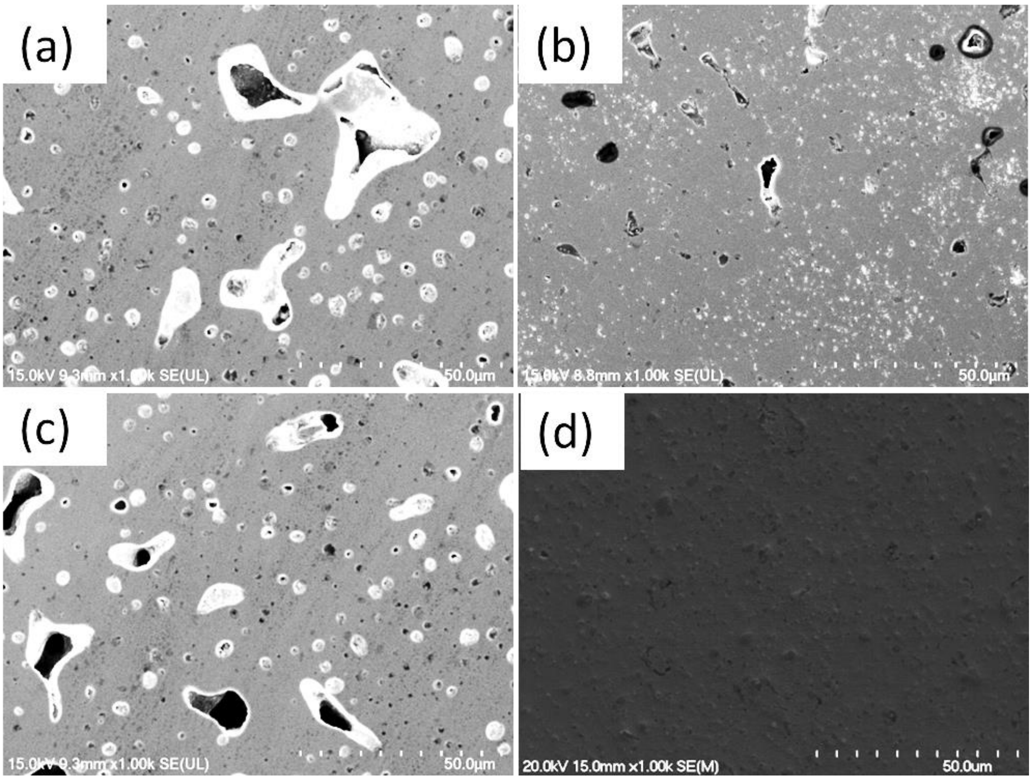

Figure 4.29 SEM images of the sintered HEA NiMnFeCr prepared under various sintering conditions at high magnification. (a) at 1150°C for 1h(T1) (b) at 1150°C for 2h(T2) (c) at 1200°C for 1h(T3) (d) at 1200°C for 2h(T4).

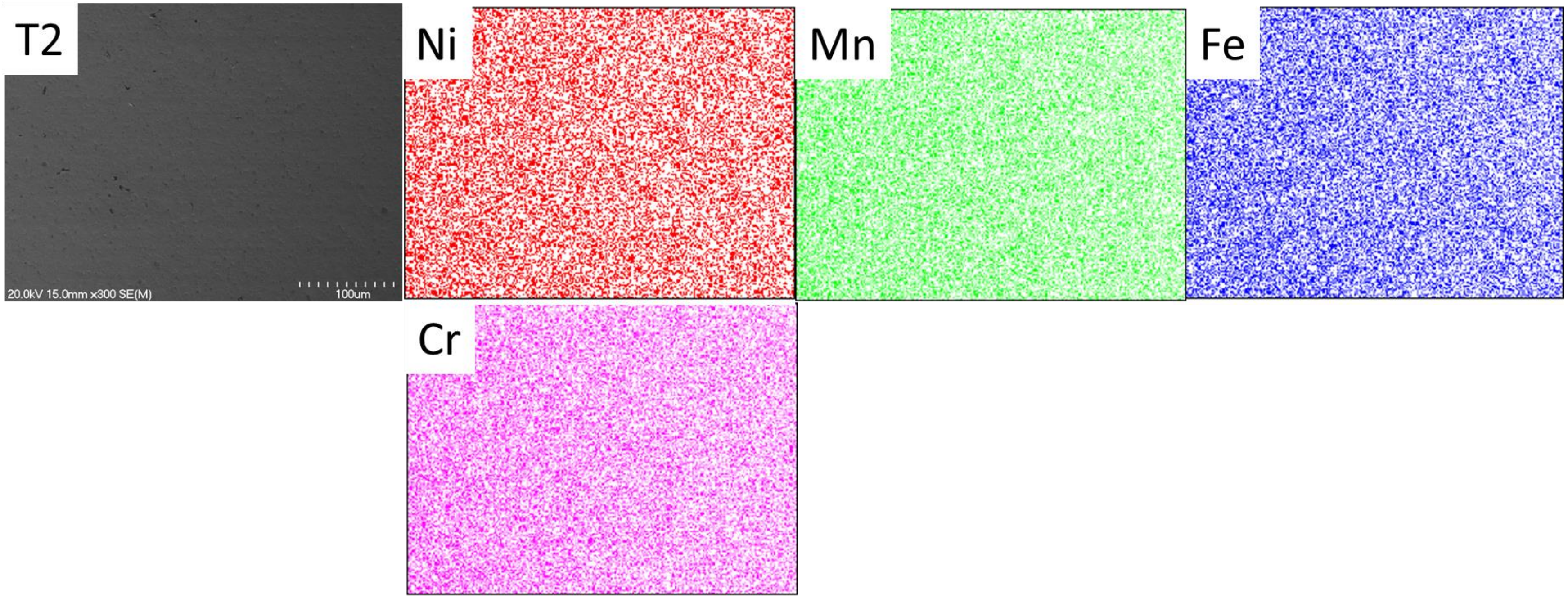

Figure 4.30 SEM/EDS maps of the sintered HEA NiMnFeCr prepared under condition T2.

Figure **4.31**(a-b) shows the high-resolution TEM image and corresponding SAED pattern of the sintered HEA NiMnFeCr (T2). The SAED pattern on the HEA matrix showed the existence of a fundamental reflection characteristic of the FCC crystal structure. The d-spacings observed in the SAED pattern were in accordance with the XRD results shown in Table **4.14**. Hence it could be concluded from SEM and TEM analyses that the HEA NiMnFeCr possessed a FCC crystal structure although the XRD pattern did reveal a small fraction of the BCC phase. This BCC phase, however, was not observed in both the SEM and TEM analyses as mentioned above.

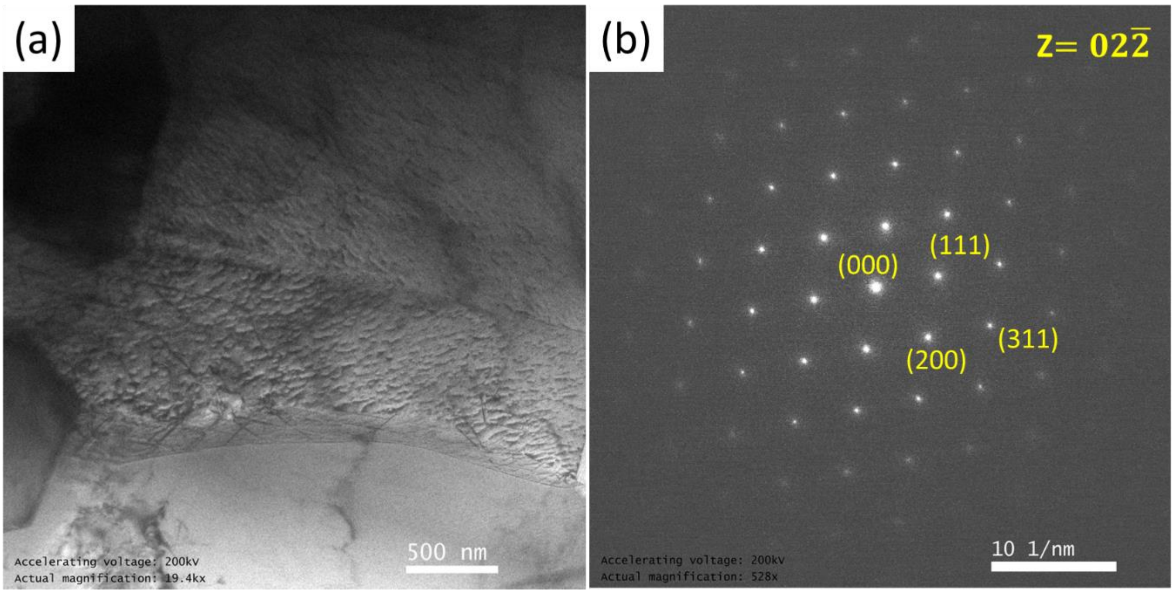

Figure 4.31 TEM image of the sintered HEA NiMnFeCr under condition T2 (a) HRTEM image (b) SAED pattern.

Table 4.14 d spacing of the planes present in XRD patterns of the sintered HEA NiMnFeCr under condition T2.

2θ (degrees)	Planes (hkl)	Crystal structure	d spacing nm
43.3	111	FCC	0.2081
44.2	110	BCC	0.1981
50.3	200	FCC	0.2051
74.2	220	FCC	0.1845
89.7	311	FCC	0.1815
95.7	222	FCC	0.1491

4.3.3 Microhardness

Figure **4.32** depicts the mean and standard deviation of the micro-hardness measurements of NiMnFeCr HEA under sintering conditions T1-T4. It is observed that the micro-hardness values of HEA alloy made under the condition T4 is higher when compared to other conditions T1-T3. The mean and standard deviation of the micro-hardness values of T1 and T2 alloy samples are 88 ± 6 HV and 134.7 ± 5 HV respectively and for T3 and T4 samples, the micro-hardness values are 96.9 ± 3 HV and 195.1 ± 6 HV respectively.

Based on the microstructural characterization above (Figure **4.27**), T4 has a higher relative sintered density when compared to sintering conditions (T1-T3). As a result, the micro-hardness of T4 was higher than for samples made under conditions T1-T3. The presence of a high residual porosity and low relative sintered density leads to the low micro-hardness of samples T1-T3 [145]. HEA NiMnFeCr under T4 possessed microhardness values comparable to other HEAs as listed in Table **4.15**.

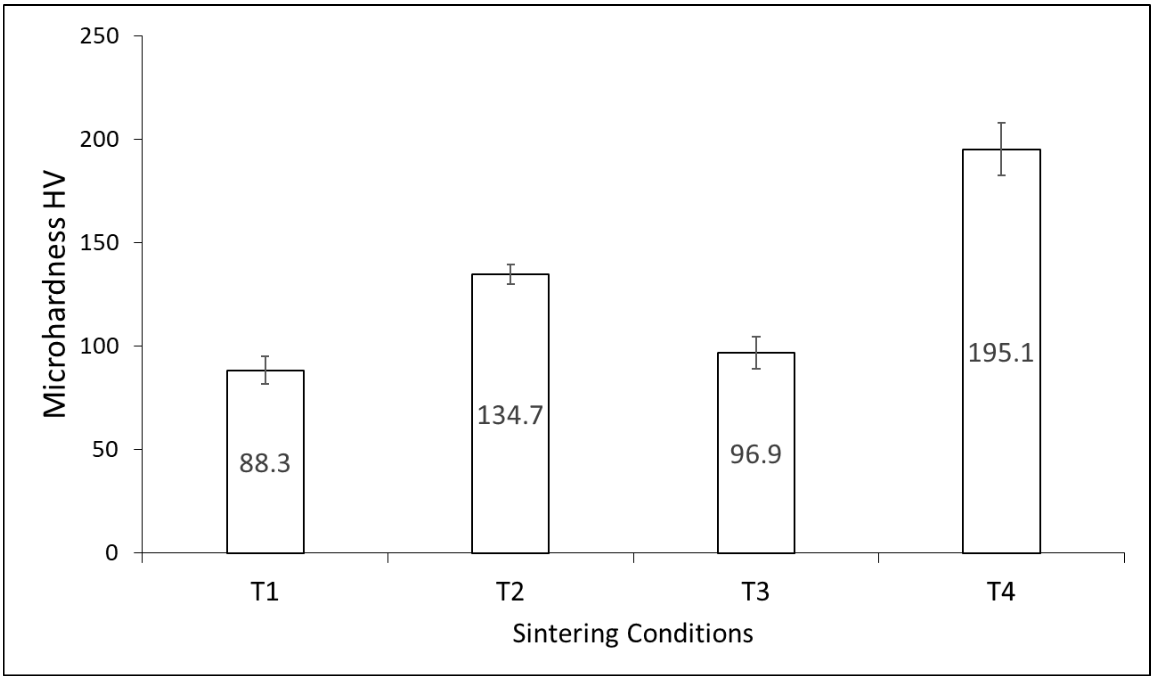

Figure 4.32 Microhardness of the sintered HEA NiMnFeCr under various sintering condition.

Table 4.15 Micro-hardness of 3d transition metal based HEAs as reported from the literature.

HEA	Micro-hardness HV	Reference
Al0.25CoFeNi	138	[147]
CoFeNiSi0.25	149	[38]
CoFeNiSi0.75	570	[147]
Al0.75CoFeNi	385	[147]
CoCrFeMo0.5Ni	210	[147]
Al0.7Co0.3CrFeNi	624	[147]
Al0.75CoCrFeNi	388	[147]
CoCrFeNi	116	[147]
NiMnFeCr	195.1	Present work

4.3.4 Compression

Figure **4.33** shows the compressive yield stress of the sintered NiMnFeCr synthesised under the various sintering conditions. It appeared evident that the alloys prepared using condition T4 possessed greater yield strength when compared to all other sintering conditions. For the conditions T1 and T2, the alloy yields at 330 MPa and 357 MPa respectively and for T3 and T4 the alloys possesses a yield stress of 306 MPa and 506 MPa respectively. T4 sample possessed better yield strength when compared to all other alloys (T1-T3) because of the higher final sintered density and the lower porosity. The studied NiMnFeCr (T4) alloy possessed a comparable compressive yield strength when compared to other 3d transition metal based HEAs as listed in Table **4.16.**

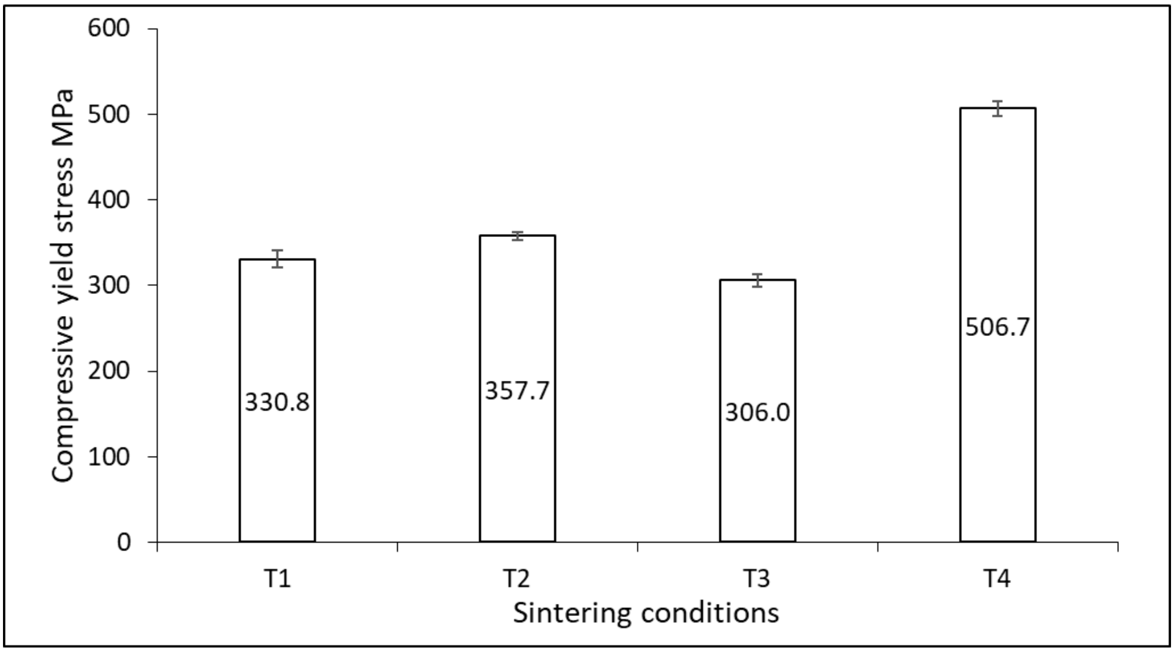

Figure 4.33 Compressive yield stress of the sintered HEA NiMnFeCr under various sintering conditions.

Table 4.16 Compressive yield stress of 3d transition metal based HEAs as reported from the literature.

HEA	Compressive yield stress MPA	Reference
Al0.25CoFeNi	158	[147]
Al0.75CoFeNi	794	[147]
CoFeNiSi0.75	1301	[147]
Al0.75CoFeNi	794	[147]
Al0.7Co0.3CrFeNi	2033	[147]
AlCoCrFeNi	1251	[147]
AlCoCrFeNi	1110	[147]
CoFeNiSi0.25	196	[38]
CoCrFeNi	148	[147]
NiMnFeCr	506	Present work

4.4 Effect of VEC on mechanical properties

The mechanical properties in HEAs stem from several factors such as grain size, phase composition and relative density between different alloys. VEC is a critical thermodynamic parameter which predicts phase formation in HEAs. The calculated VEC values for the HEAs in the present study i.e. NiMnFeCu , NiMnFeCrCu and NiMnFeCr (marked in red in Figure **4.34**) are 9 , 8.4 and 7.7 respectively. As discussed earlier in section **1.7** when VEC is > 8 , the FCC crystal structure is favoured. Although, the HEA NiMnFeCu satisfies the VEC rule, HEA NiMnFeCrCu in contrast fails to uphold the VEC rule because it exhibits FCC +BCC structure despite its VEC being 8.4 which should favour exclusively FCC. Hence it may be concluded that the thermodynamic and geometric criteria used to predict phase formation in HEAs should only be used broadly as a guideline for their design and hence cannot be considered completely accurate for predicting the phase formation in HEAs. Furthermore, the HEA NiMnFeCr exhibits FCC + BCC phase as predicted although the BCC phase is negligible in volume fraction. The crystal structure of the phases has a direct impact on the observed mechanical properties of the HEAs. HEAs with FCC solid solution phase tending to be ductile because they possess more slip directions consequently, they exhibit enhanced plasticity and low strength. Hence the HEAs exhibiting FCC crystal structure viz., NiMnFeCu and NiMnFeCr (predominantly FCC) exhibit lower yield strength as shown in Figure **4.34**. Conversely BCC HEAs exhibit higher strength and lower plasticity due to the existence of less slip. In this study HEA NiMnFeCrCu possessed a duplex structure of FCC+BCC and this duplex structure, as discussed earlier, can offer combined strength and plasticity which gives a more balanced HEA property-wise compared to single phase FCC or BCC HEAs as demonstrated in Figure **4.34** and Table **4.17**.

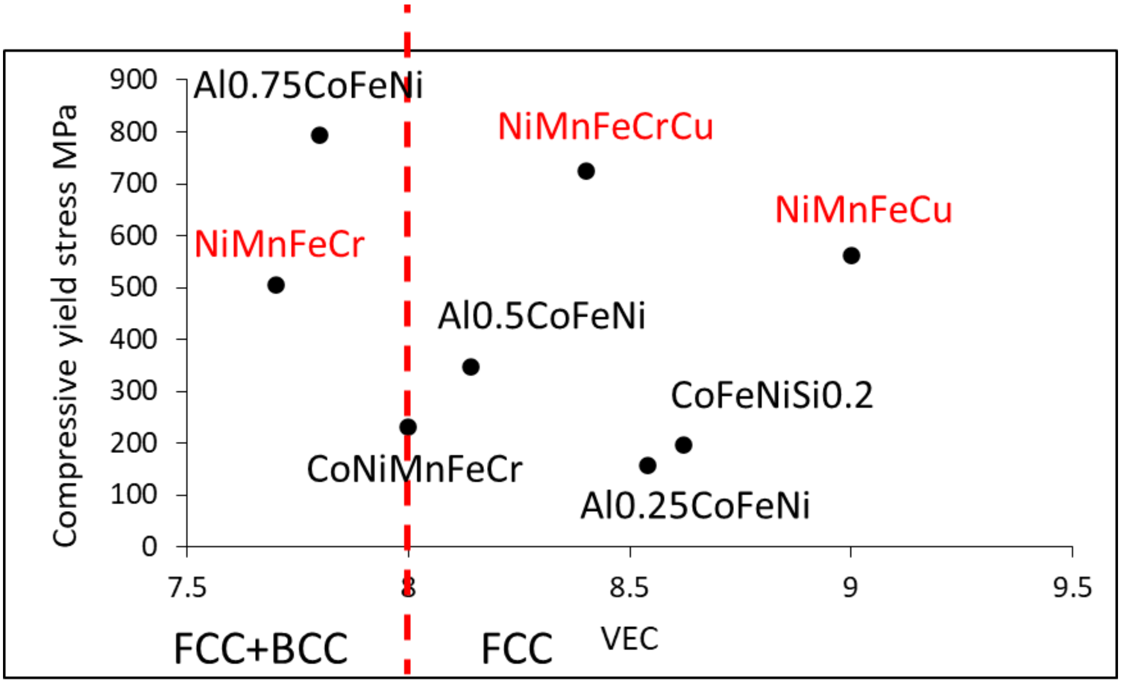

Figure 4.34 Comparison of mechanical properties of different HEAs with respect to VEC (red partition separates FCC HEAs from FCC+BCC HEAs).

Table 4.17 Comparison of mechanical properties of different HEAs with respect to VEC.

Composition	VEC	Crystal structure	Microhardness HV	Compressive stress MPa
NiMnFeCr	7.7	FCC+BCC	195	506
Al0.75CoFeNi	7.8	FCC+BCC	288	794
CoNiMnFeCr	8	FCC	144	230
Al0.5CoFeNi	8.14	FCC+BCC	212	346
NiMnFeCrCu	8.4	FCC+BCC	250	724
CoFeNiSi0.2	8.62	FCC	149	196
Al0.25CoFeNi	8.54	FCC	138	158
NiMnFeCu	9	FCC	233	563

In addition to VEC, the mechanical properties of the HEAs are influenced by several strengthening mechanisms namely the Hall Petch effect, solid solution strengthening, dispersion and ordering strengthening effects etc. Among the mentioned strengthening effects, the Hall Petch strengthening effect and sold solution strengthening effect play a predominant role in determining the mechanical properties of the HEAs. This is because the mechanical properties of the HEAs depend primarily upon the relative density of the HEAs, hence HEA alloys with the highest relative densities namely NiMnFeCu (S4), NiMnFeCrCu (R2) and NiMnFeCr (T4) were studied for grain size using the XRD peaks of the aforementioned HEAs as shown in Figure **4.35**(a). The Hall Petch relation describing the yield stress and grain size is given by 4.3.

$$\sigma_y = \sigma_o - KD^{-\frac{1}{2}} \tag{4.3}$$

Where σ_y and σ_o are the yield stress and frictional stress in MPa respectively, D is the grain diameter and K is the constant related to the material under study. Although the values of K and σ_o changes from material to material, in this comparison both K and σ_o are considered to be negligible and only the grain size D is considered. From Figure **4.35**(a-b) the grain size of HEA NiMnFeCrCu is the lowest (34 µm) and consequently its yield strength is the highest at 724 MPa. The grain size and yield strength of HEA NiMnFeCr is 78 µm and 506 MPa respectively while for HEA NiMnFeCu the grain size and yield strength is 64 µm and 516 MPa respectively. The three HEAs follow the Hall Petch relation of grain size and yield strength as shown in Figure **4.35**(b).

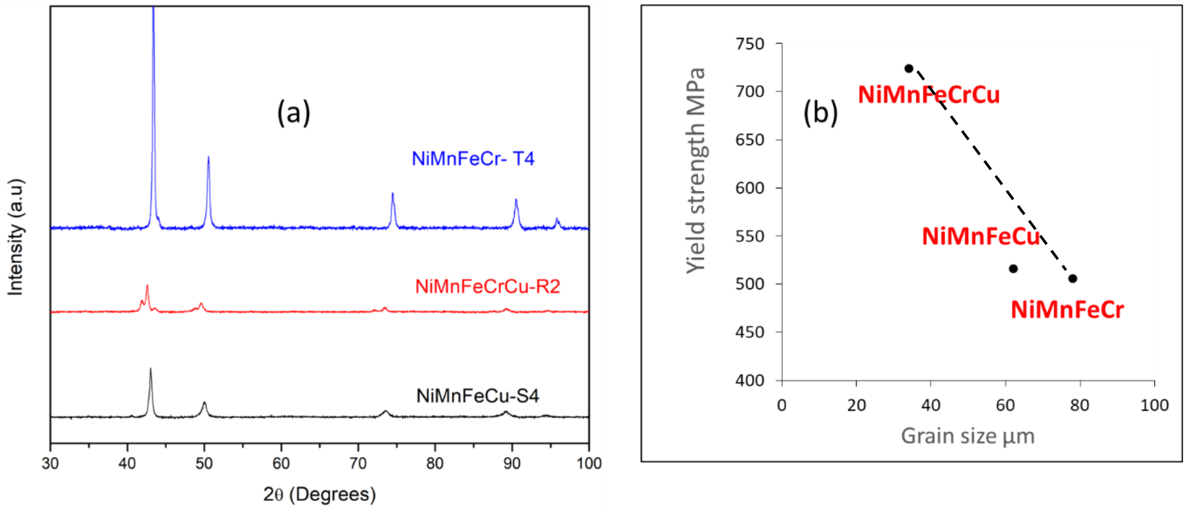

Figure 4.35 XRD patterns of the HEAs used in this study for grain size and lattice strain calculation(a) Hall Petch relation depicting the dependence of compressive yield stress on grain size(b).

Apart from grain size, the lattice strain also plays a critical role in the mechanical properties of the synthesised HEAs. It is reported elsewhere that the lattice strain is directly proportional to the atomic misfit parameter δ (equation **1.8**)[157-159]. In addition to that, lattice strain contributes significantly to the solid solution strengthening by pinning down the dislocation motions in HEAs[158]. From the Figure **4.36**(a-b) it is observed clearly that among the studied HEAs NiMnFeCu possess the highest atomic misfit parameter so that consequently it has the highest lattice strain of 1.38%, while the compressive yield stress of NiMnFeCu is 516 MPa. For HEA NiMnFeCr the atomic misfit parameter is 3.1 which is the lowest among the studied HEAs; hence as a result the HEA NiMnFeCr exhibit the lowest lattice strain of 0.78% and the lowest compressive yield stress of 506 MPa. Despite the atomic misfit parameter and lattice strain of HEA NiMnFeCrCu being lower than that for HEA NiMnFeCu; the compressive yield stress of NiMnFeCrCu HEA is the highest with a value of 724 MPa. Hence it can be concluded that the mechanical properties of HEAs may not entirely depend upon the atomic misfit parameter and a few other factors such as precipitation strengthening should also be explored to a greater degree.

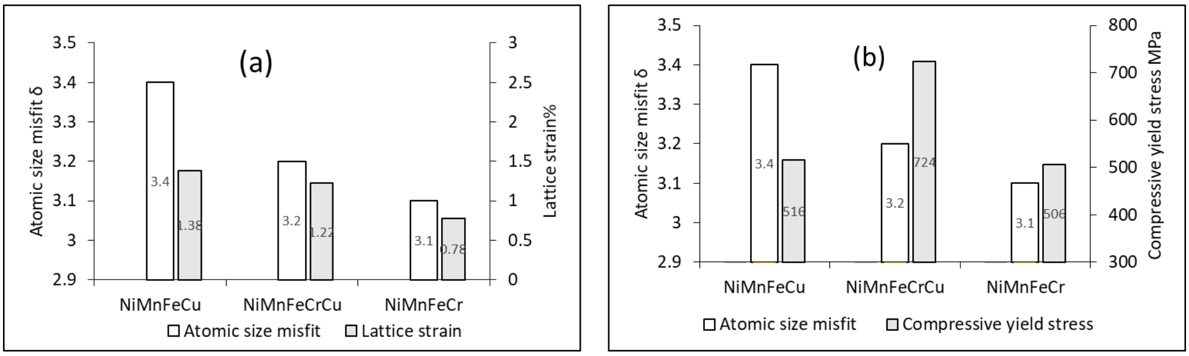

Figure 4.36 Comparison of atomic size misfit parameter with lattice strain(a) and compressive yield stress (b).

Chapter 5 Electrochemical characterization of the sintered HEAs

The sintered HEAs NiMnFeCu, NiMnFeCrCu and NiMnFeCr discussed in chapter **4** are subjected to electrochemical characterization for probing the electrocatalytic properties. Since porosity plays a critical role in deciding the catalytic activity of the electrocatalysts; as a rule of thumb, for each HEA combination two samples with density difference greater than 25% (approx.) are chosen for electrochemical characterization. Based on this notion for HEA NiMnFeCu samples S2 (relative density 82%) , S4 (relative density 98%) (refer Table **4.2**); for HEA NiMnFeCrCu samples R4 (relative density 77%) , R2 (relative density 95%)(refer Table **4.7**)and for HEA NiMnFeCr samples T3 (relative density 83%) , T4 (relative density 94%)(refer Table **4.13**) are utilized for electrochemical characterization. This chapter will discuss the experimental elucidation of OER properties of the aforementioned HEA samples in detail.

5.1 Electrochemical characterization of HEA NiMnFeCu

The details of the sintering conditions of the HEA NiMnFeCu are tabulated earlier in Table **4.1** in chapter **4** and the microstructure and mechanical properties of the sample S0 is also provided in Figure **S20** and Figure **S21** in the appendix of the thesis. The sintering condition of S0 is given by 1000ºC and 0 h. Figure **5.1**(a) shows the linear sweep voltammetry (LSV) curve of the sintered NiMnFeCu alloy under various test conditions at a scan rate of 5 $\mathrm{mV\,s^{-1}}$. The catalytic activity of the alloy is estimated through the LSV curve, as it measures the overpotential of the oxygen evolution reactions (OER). The overpotential value defines the merit of an electrocatalyst with the observation of a low overpotential being highly desirable for such materials. It is evident from Figure **5.1**(a) that the sample S2 CV 100 cycles possessed the lowest overpotential among the other tested samples. The onset overpotential is the overpotential where the current density increases sharply in the LSV spectra. The measured onset overpotential values of samples S2 CV 100 cycles, S2, S0 and S4 are 310 mV, 340 mV, 337 mV and 410 mV respectively. To reach a current density of 10 $\mathrm{mA\,cm^{-2}}$ the sintered NiMnFeCu under conditions of S2 CV 100 cycles, S2, S0 and S4 requires an overpotential of 322 mV, 362 mV, 358mV and 438mV (= E(RHE)-1.23V) respectively and their corresponding Tafel slopes are measured to be 113 mV/dec, 157 mV/dec, 116 mV/dec and 160 mV/dec respectively as depicted in Figure **5.1**(b). The double layer capacitance is calculated using the slope of the curve of $\Delta J = J_{anode} - J_{cathode}$ at 1.03 V vs RHE plotted against the voltammetric scan rate and represented in Figure **5.1**(c). The double layer capacitance C_{dl} of the sample S2 CV 100 cycles is 0.043 mF and for S2 (no cycling), S0 and S4 the C_{dl} values were 0.032 mF, 0.081 mF and 0.018 mF respectively. The charge transfer resistance (R_{ct}) (see Figure **S22** in the appendix section of the thesis) indicates the resistance to charge transfer in the OER reactions. A minimum R_{ct} value implies a minimum resistance towards charge transfer and faster OER kinetics. The Bode plot depicted in Figure **5.2**(d) represents the EIS spectra which could be fitted into the Randles equivalent circuit and the charge transfer resistance R_{ct} of the samples S2 CV 100 cycles, S2, S0 and S4 is measured to be 88 Ω, 91 Ω, 89 Ω and 98 Ω respectively. The solution resistance R_s is found to be 2 Ω for all test conditions. Table **5.1** tabulates the electrochemical characterization of the sintered HEA NiMnFeCu under the various test conditions.

Table 5.1 Electrochemical characterization of the HEA NiMnFeCu under various test conditions described in chapter 4.

Sample	Overpotential mV	Tafel slope mV/dec	R_{ct} Ω	C_{dl} mF	ECSA cm^2
S2 CV 100 cycles	322	113	88	0.043	1.07
S2	362	157	91	0.032	0.8
S4	438	160	98	0.018	0.45
S0	358	116	89	0.081	2.02

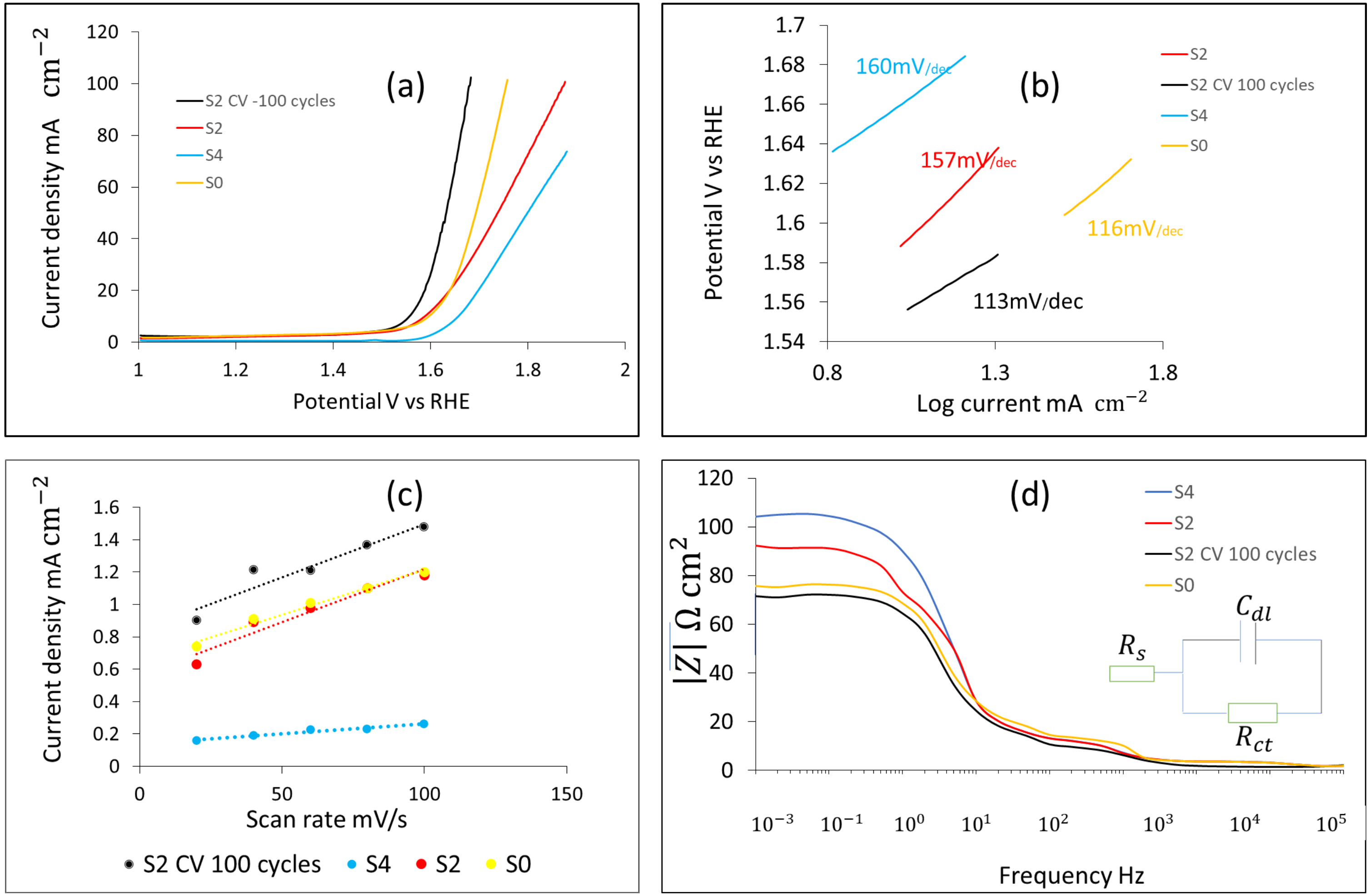

Figure 5.1 Electrochemical characterization of HEA NiMnFeCu after various testing condition treatments (a) LSV at scan rate of 5mV/s (b) Tafel slope derived from LSV curves (c) Current density difference at 1.03 V vs (RHE) at different scan rates (d) Bode plot of electrical impedance measured at AC amplitude of 1.6 V vs RHE.

The HEA NiMnFeCu under condition S2 CV 100 cycles showed a relatively lower overpotential of 322 mV for reaching a current density of 10 mA cm^{-2} when compared to HEA alloys prepared under conditions S2, S0 and S4. This lower overpotential implies a lower energy is required to initiate the surface adsorption and desorption reactions of intermediates on the electrode. Hence, the comparatively better catalytic activity of S2 with 100 cycles of CV could be due to the presence of porous microstructure (relative density 82%) and formation of nano oxide sheets during the cyclic voltammetry sweep. The combination of porosity and nano oxide layers exposed active sites and hence enhanced the catalytic activity[120, 121].

Figure **5.2**(a-b) shows the microstructure of the sintered NiMnFeCu HEA under condition S2 (unused - no electrocatalysis) and S2 CV 100 cycles respectively. The existence of the oxide sheets is confirmed in Figure **5.2**(b) with EDS data being provided in Table **5.2**. It is interesting to note that the oxide sheets are present within the vicinity of pores (marked in red in Figure **5.2**(b)) hence it could be concluded that the pores function as sites for the electrochemically active species to interact (i.e on the oxide layers) and therefore, contribute to the observed, enhanced catalytic activity. It has been reported previously that cyclic voltammetry(CV) activation also known as “electrochemical preconditioning” can be used to enhance catalytic activity[160, 161]. Dai et al. synthesised HEA MnFeCoNi for OER catalysis, where it was shown that the milled HEA after CV activation exhibited excellent catalytic properties towards OER with an overpotential of 302 mV @ 10 mA cm^{-2} being observed and a small Tafel slope of 83.7 mVdec^{-1}. This enhanced OER performance was attributed to the formation of nano oxide sheets $\mathrm{MO_x}$ (where M = Ni, Mn, Fe, Co and x is possibly 2 or 3) by CV activation which acted as the active sites. The presence of these nano oxide sheets was confirmed through ex situ characterization (of the electrodes post their use as an electrocatalyst) such as X-ray photo spectroscopy (XPS) and TEM[120]. In other reported work of a similar nature on Mn based electrocatalyst for OER process, it was found that $\mathrm{Mn(OH)_2}$ present in these systems underwent structural changes to form δ- $\mathrm{MnO_2}$ under repetitive cyclic activation (5 cycles) and that this process enhanced the OER activity[93] of the Mn-based electrocatalysts. In both of the aforementioned studies, the existence of the oxide layers by CV activation was confirmed by ex-situ analysis that it is by XPS and TEM after the materials had been used as electrocatalysts. It is important to add that, ex situ characterisation techniques like XPS are extremely surface sensitive, hence the presence of spurious surface contamination and/or other undesired compounds or exposure to the ambient atmosphere during chamber-to-chamber transportation of the electrocatalyst may complicate interpretation to deduce the active sites. Moreover, ex situ analytical techniques cannot always be relied upon to provide a meaningful level of information between what constitutes active sites and the level of catalytic activity expected[162, 163]. Taking these drawbacks into account, in the current study the presence of oxide layers in the sample S2 CV 100 cycles was affirmed only through SEM/EDS (Figure **5.4**) and advanced in-situ operando (real time electrocatalytic analysis) techniques will be utilized to prove the presence of oxide layers and the active cites on the surface of the HEAs in our future works.

Table 5.2 Elemental composition (EDS) of sintered NiMnFeCu HEA under condition S2.

Atom % / Sample	Ni	Mn	Fe	Cu	O
S2 (unused - no electrocatalysis)	23.2	22.5	23.43	20.32	0
S2 CV 100 cycles	19.84	11.14	24.67	10.50	9.71

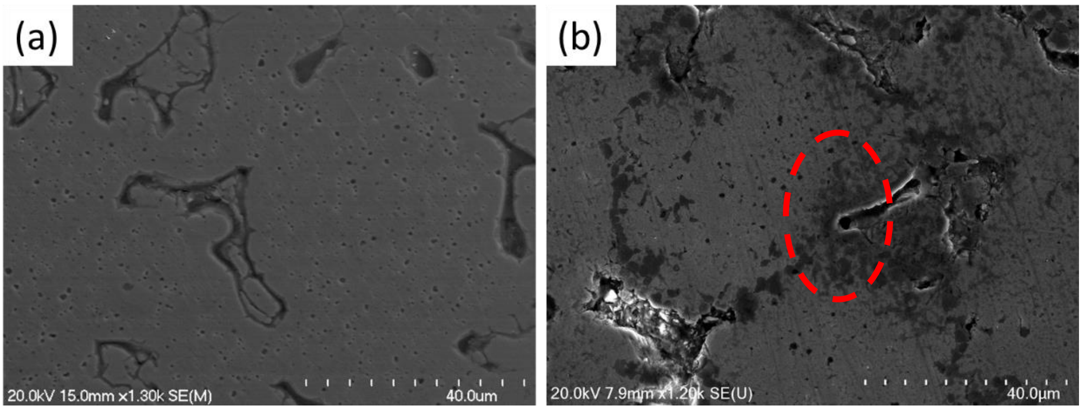

Figure 5.2 SEM image of the sintered HEA NiMnFeCu (a) S2 (unused-no electrocatalysis) (b) CV 100 cycles.

From Table **5.2** it is evident that the elemental composition of Mn in the sample S2 CV 100 cycles changed (decreased) significantly compared to what it was in the sample S2 (unused-no electrocatalysis). The elemental composition of O in the S2 CV 100 cycles sample was 9.71% with no oxygen being detected in the S2 sample (unused-no electrocatalysis). To understand the reason for the decrease in the element Mn in S2 CV 100 cycles sample an XRD was performed on the S2 (unused- no electrocatalysis) and S2 CV 100 cycles sample and depicted in Figure **5.3**. The XRD peaks revealed the existence of Mn_3O_4 oxide peaks in the S2 CV 100 cycles sample and an absence of the same peaks in the S2 (unused no electrocatalysis) sample. Hence it could be concluded that the decrease in the element Mn atom % in the sample S2 CV 100 cycles is attributed to structural transformation of FCC Mn to Mn_3O_4 oxides and that these oxide layers performed as active sites and contributed to the enhanced OER activity of the S2 CV 100 cycles sample. The role of these oxide layers and their spin correlated parameters on OER activity will be discussed in detail for the other HEA combinations NiMnFeCrCu and NiMnFeCr at a later point in this chapter.

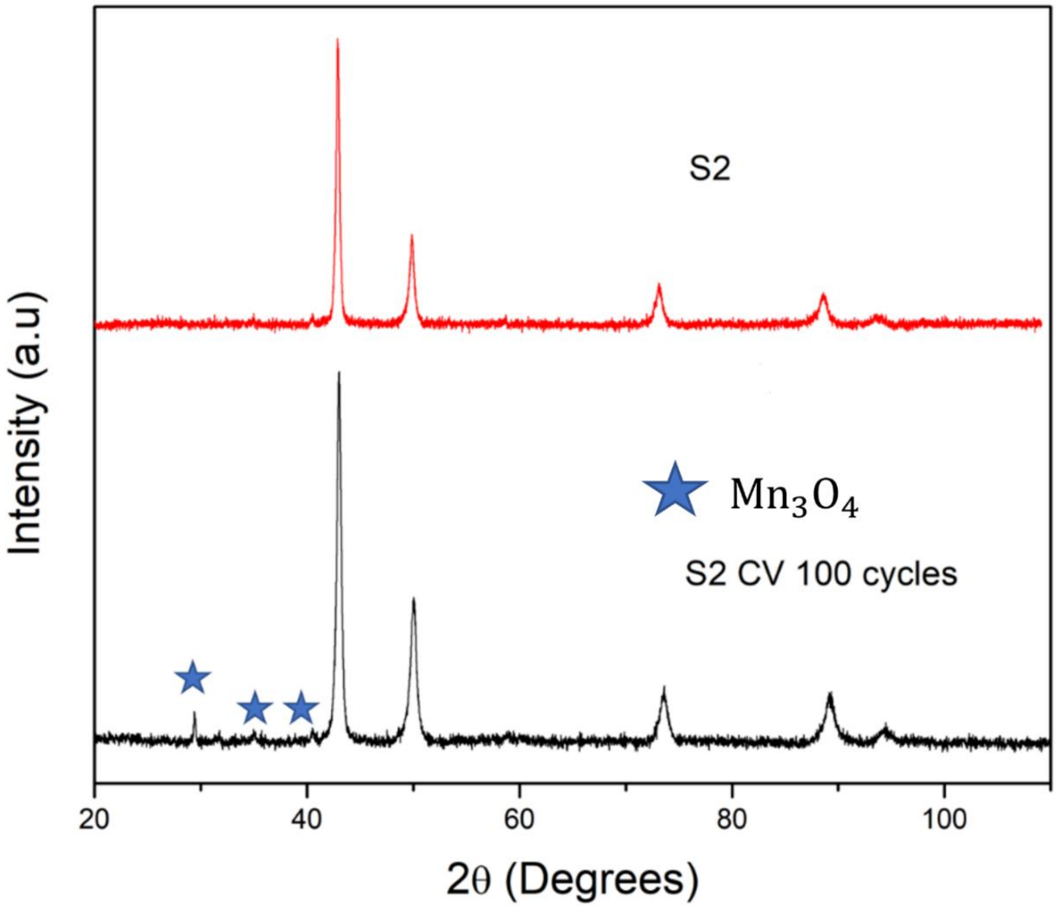

Figure 5.3 XRD patterns of the HEA NiMnFeCu under condition S2 (unused- no electrocatalysis) and S2 CV 100 cycles.

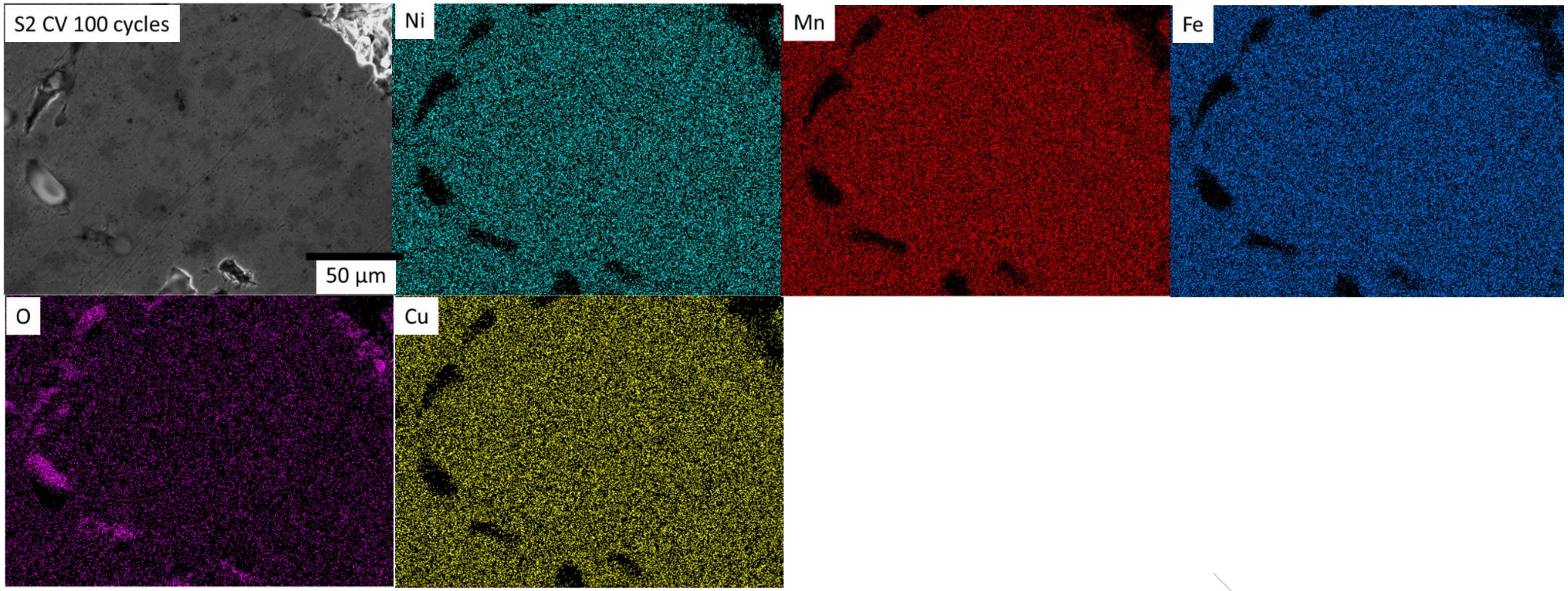

Figure 5.4 SEM/EDS map of the sintered HEA NiMnFeCu under condition S2 CV 100 cycles.

The overpotential of S2 (no cycling) is lower when compared to S4, but not as low as S2-CV 100 cycles because of the presence of porosity and the absence of nano oxide layers. The condition S4 had negligible porosity (relative density 98%) and no nano oxide layer, so its overpotential was relatively higher when compared to all the other studied conditions. In addition to that, the merit of a catalyst is also defined by a number of other parameters such as Tafel slope, charge transfer resistance $(\mathrm{R_{ct}})$ and double layer capacitance. The HEA under condition S2-CV 100 cycles possessed the lowest Tafel slope, the lowest charge transfer resistance $(\mathrm{R_{ct}})$ value and the highest double layer capacitance indicating superior catalytic performance towards OER compared to other test conditions. These faster OER kinetics are due to porosity and nano oxide layers formed on the surface of the catalyst. Most HEAs synthesised HEAs for OER such as MnFeCoNi (η= 302 mV) , CoCrFeNiMo (η= 220mV) and CoFeNiGaZn (η= 370mV)[108] are mesoporous and powder based electrocatalysts; their applicability in practical alkaline electrolysis is yet to be experimentally elucidated. These electrocatalysts undergoes microstructural degradation and lacks stability while operating under high current density in an industrial scale electrolysis (> 100 mA $\mathrm{cm^{-2}}$). Hence to develop a microstructurally stable electrocatalyst for OER intended for industrial scale hydrogen production, it is necessary to compare the catalytic activity with the mechanical strength of the synthesised HEAs.

Figure **5.5**(a-b) compares the values of the overpotential with the relative density and microhardness values of the HEA NiMnFeCu under various test conditions. It is evident that the sample S4 possessed a relative density of 98% so that its microhardness value was 233 Hv which is the highest among the tested samples. As a result of this, the overpotential of S4 is the highest measuring 438 mV which meant it showed poor catalytic property with respect to OER. On the other hand, the sample S0 possessed a relative density of 65% leading to the lowest observed microhardness value of 100 HV compared to other tested samples. However, its electrocatalytic properties with respect to the OER property were more favourable with an observed overpotential of 358 mV. In order to be utilized on an industrial scale in alkaline water electrolyses, the electrocatalyst is expected to possess a balanced property of mechanical strength and catalytic activity. The sample S2 exhibited a microhardness value of 198 HV and an overpotential of 368 mV, in addition to that the catalytic activity of the sample S2 -CV 100 cycles improved significantly to an overpotential of 322 mV under CV activation and retained high mechanical strength. Despite the better OER properties of HEA alloy S0, the alloy S2-CV 100 cycles is preferred over S0 because of the combined properties of mechanical strength and activity , furthermore it is expected to endure the rigorous operational stress of an industrial scale practical alkaline water electrolysis. The poor mechanical strength of S0 could be attributed to the low relative density (65%) compared to that of other sintered samples(S1-S4). Hence for the other HEAs studied in this research viz HEA NiMnFeCrCu and HEA NiMnFeCr the relative density is maintained at > 75% to ensure better mechanical properties compared to that of S0.

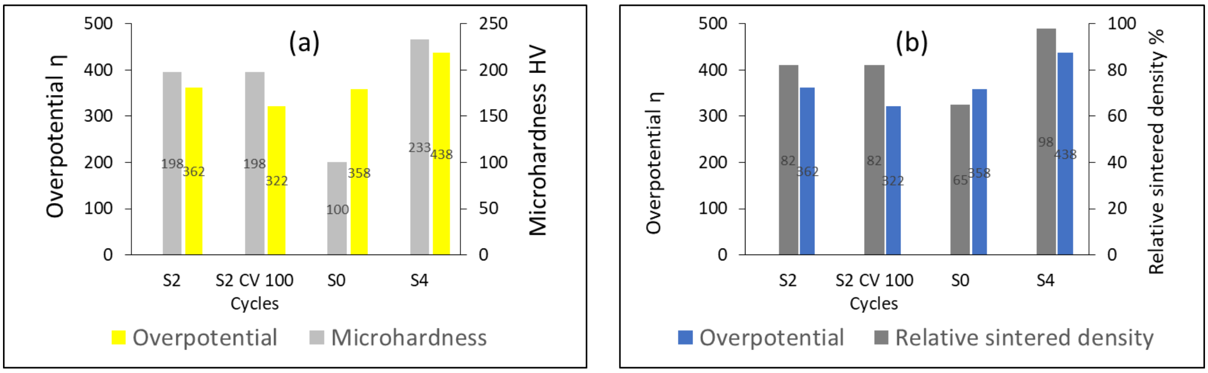

Figure 5.5 Comparison of overpotential of the sintered HEA NiMnFeCu under various test conditions with (a) relative sintered density (b) microhardness.

Figure **5.6** (a) depicts the LSV curve of the sintered NiMnFeCu (S2) at 0 and 1000 cycles of CV and Figure **5.6**(b) represents the chronoamperometry test at a constant potential of 1.6 V (vs RHE). It is clear from the data observed that the HEA exhibited negligible degradation after 1000 cycles of CV. Similarly, the stability of the sintered NiMnFeCu alloy (S2) measured a current density of 48 mA cm^{-2} initially and at the end of 10 h the current density is 39 mA cm^{-2} , hence the electrocatalyst showed only a small decrease in current density retaining 64% after 10 h of use.

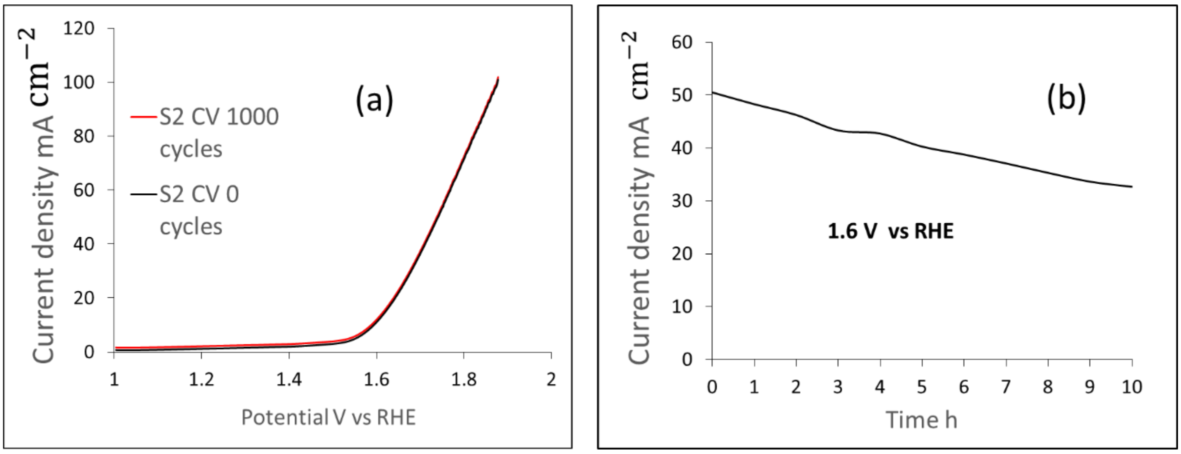

Figure 5.6 (a) Accelerated degradation test of S2 at 0 and 1000 cycles (LSV) (b) Chronoamperometry of S2 CV 100 cycles for 10 h.

The catalytic activity of the self-supported HEA electrocatalyst S2- CV 100 cycles was comparable to the existing state-of- the-art electrocatalysts IrO_2 (η= 410 mV @ 0.5 M KOH) and RuO_2 (η= 358 mV @ 0.5 M KOH)[71]. The group VIII 3d metals in either their mono-metallic form or in their corresponding phosphide , selenide and sulphide salts are widely used as electrocatalysts for OER reactions[67]. The mono-metallic form Ni (η = 444 mV @ 10mA cm^{-2})[164], Mn (η = 540 mV @ 10 mA cm^{-2})[165] , Fe (η = 420mV @ 10mA cm^{-2})[166] and Cu(η = 525 mV @ 1 mA cm^{-2}) electrocatalysts[167] showed modest catalytic activity. However, in multi-metallic form (HEA NiMnFeCu) the catalytic activity was observed to improve significantly in terms of overpotential values. The overpotential of the alloy under the conditions S2 -CV 100 cycles is comparable to most reported HEAs in the literature such as MnFeCoNi (η=302 mV) and CoCrFeNiMo (η=220 mV) [120, 138, 168]. It is worth noting that the OER activity of the sintered HEA NiMnFeCu was directly measured from the bulk alloy which would have fewer active sites when compared to a more conventional nanostructured 2D catalyst which is often grafted onto a support such as carbon fibre paper or nickel foams. Hence the observed electrocatalytic activity of these materials represents the intrinsic property of the sintered NiMnFeCu HEA which will arise due to the unique properties it has such as synergistic effects and compositional randomness. The synthesised HEA NiMnFeCu is self-supportive and highly suitable for industrial scale hydrogen production.

5.2 Electrochemical characterization of HEA NiMnFeCrCu

Figure **5.7**(a) represents the LSV curve of the sintered HEA NiMnFeCrCu tested under various conditions, which was acquired using a scan rate of 5 mV s^{-1}. It is evident that the overpotential measured for the R4 CV 100 cycles sample is the lowest of the tested samples. The overpotential of R4 CV 100 cycles, R4 (no cycling) and R2 are 310 mV, 320 mV and 420 mV for a current density of 10 mA cm^{-2} , respectively. Similarly, the Tafel slopes of R4 CV 100 cycles, R4(no cycling) and R2 are 83 mV/dec, 125 mV/dec and 138 mV/dec respectively as shown in Figure **5.7**(b). The double layer capacitance is calculated using the slope of the curve of $\Delta J = J_{anode}$- $J_{cathode}$ at 1.03 V vs RHE plotted against the voltammetric scan rate and represented in Figure **5.7**(c). The double layer capacitance C_{dl} of R4 CV 100 cycles is highest with 0.1 mF and for R4 (no cycling) and for R2 the C_{dl} was 0.03 mF and 0.01 mF respectively. The Bode plot depicted in Figure **5.7**(d) represents the EIS spectra which could be fitted into a Randles equivalent circuit. The charge transfer resistance R_{ct} of R4 CV 100 cycles, R4 and R2 was measured to be 71 Ω, 91 Ω and 100 Ω respectively. The solution resistance R_s was found to be 2 Ω for all test conditions. Table **5.3** summarises the electrochemical characterization data for the OER conducted on the HEA NiMnFeCrCu alloys.

Table 5.3 Electrochemical characterization of the HEA NiMnFeCrCu under various test conditions.

Sample	Overpotential mV	Tafel slope mV/dec	R_{ct} Ω	C_{dl} mF	ECSA cm^{-2}
R4 CV 100 cycles	310	83	71	0.1	2.5
R4	320	125	91	0.03	0.75
R2	420	138	100	0.01	0.25

From Table **5.3** it is noticeable that the HEA NiMnFeCrCu under condition R4 with CV 100 cycles exhibited the lowest overpotential value, a smaller Tafel slope and a lower charge transfer resistance when compared to HEA samples prepared under conditions R2 and R4 (no cycling). These parameter values correspond to the minimum energy required to initiate charge transfer reactions between the electrochemical reaction intermediates in solution and the electrode. This superior catalytic activity is attributed to the presence of excessive porosity in the microstructure of the sample R4 CV 100 cycles (which has a relative sintered density of 77%). The pores facilitate mass transport between the electrolyte and the electrodes thereby enhancing the OER performance[121]. Along with that, CV induced activation also results in the in-situ formation of nano oxide layers which functioned as active sites thereby increasing the catalytic activity[120, 121]. The existence of these oxide layers in R4 CV 100 cycles is confirmed by the SEM image and its corresponding EDS spectrum data depicted in Figure **5.8** and Table **5.4** while the SEM/EDS of the sample R4 (unused - no electrocatalysis) is also provided in Figure **S23** ,Table **S1** and Table **S2** in the appendix for comparison. As discussed earlier in chapter **4** the HEA NiMnFeCrCu possessed three distinct phases (FCC1, FCC2 and BCC) and from Table **5.4**, Figure **S23** and Table **S2**, it is interesting to note that the atom % of the element Mn in phases FCC1 and FCC2 of R4 CV 100 cycles decreased significantly when compared to the sample R4 (unused- no electrocatalysis) with the atom % of oxygen present in each phase FCC1,FCC2 and BCC of the R4 CV 100 cycles sample measured to be 19.8%, 18.5% and 10.1 % respectively. No oxygen was found in R4 (unused- no electrocatalysis) sample in contrast. The SEM/EDS map also confirmed the existence of oxide layers in the R4 CV 100 cycles sample as shown in Figure **5.9**.

It was desired to understand the reasons for the decrease in the Mn atom% value and for why the formation of oxide layers was observed, XRD analysis was carried out on the R4 CV 100 cycles sample and compared with that of the R4 (unused- no electrocatalysis) sample (see Figure **5.10**(a)). From the patterns it is evident that the R4 CV 100 cycles sample showed a strong peak at 2θ value 33.8 ° and this peak corresponded to an oxide of manganese namely $\mathrm{Mn_3O_4}$ (JCPDS data 04-020-3526). Hence the decrease in atom % of Mn and formation of oxides layers on R4 after 100 cycles of CV could be attributed to structural conversion of an FCC manganese into orthorhombic manganese oxide (Figure **5.10**(b)) owing to the high reactivity of manganese with respect to oxide formation due to high concentration of lone pair electrons in the d orbital compared to other elements present in the studied HEA. This orthorhombic $\mathrm{Mn_3O_4}$ possessed an average oxidation state of +2.66 as a result of manganese cations ($\mathrm{Mn^{3+}, Mn^{2+}}$) which are known to occupy an octahedral position in the unit cell of this compound resulting in an $\mathrm{e_g}$ occupancy value of 1 (for $\mathrm{Mn^{3+}}$ $\mathrm{e_g} = 1,\ \mathrm{t_{2g}} = 3)$ as depicted in Figure **5.10**(c). This leads to the enhanced OER activity because the σ* antibonding state of the e_g orbital of Mn^{3+} has stronger tendency to overlap (i.e hybridize) with an oxygen atom of the hydroxyl ion (OH^-) compared to the antibonding state of the t_{2g} orbital of the Mn^{3+} cation [169]. In addition the Mn-Mn bond length is ~3.314Å (**Table 5.5**) which is considered to be an optimal value for the enhanced OER performance according to earlier reports[170]. Despite the excessive porosity of the R4 (no cycling) sample, only a modest catalytic activity was exhibited due to their being no nano oxide layers of Mn_3O_4 as observed in the cycled systems. The sample R2 in contrast (with a relative sintered density of 95%) showed very poor catalytic activity due to the absence of both nano oxide layers and porosity.

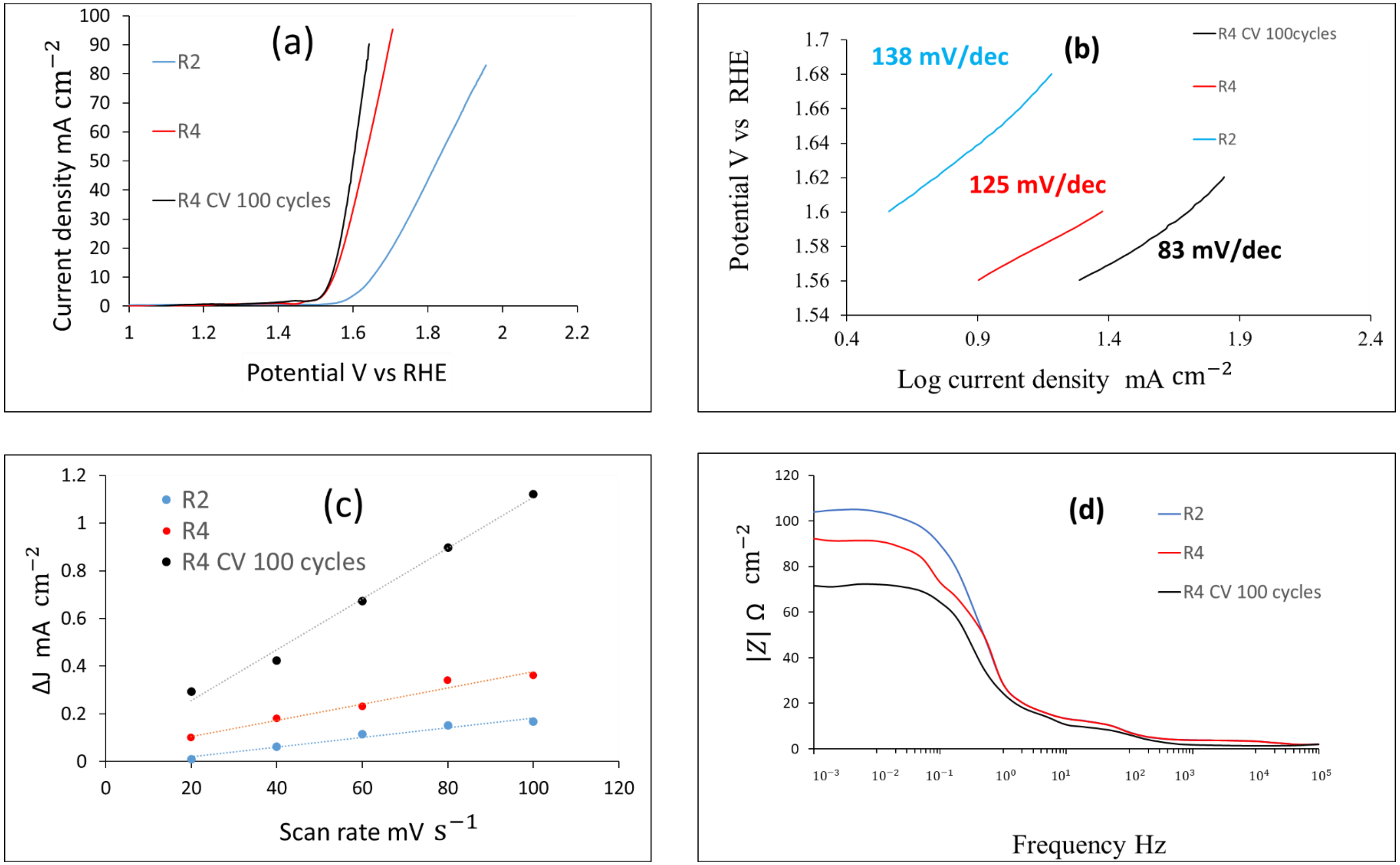

Figure 5.7 Electrochemical characterization of HEA NiMnFeCrCu at various test conditions (a) LSV at scan rate of 5mV/s (b) Tafel slope derived from LSV curves (c) Current density difference at 1.03 V vs (RHE) at different scan rates (d) Bode plot of electrical impedance measured at AC amplitude of 1.6 V vs RHE.

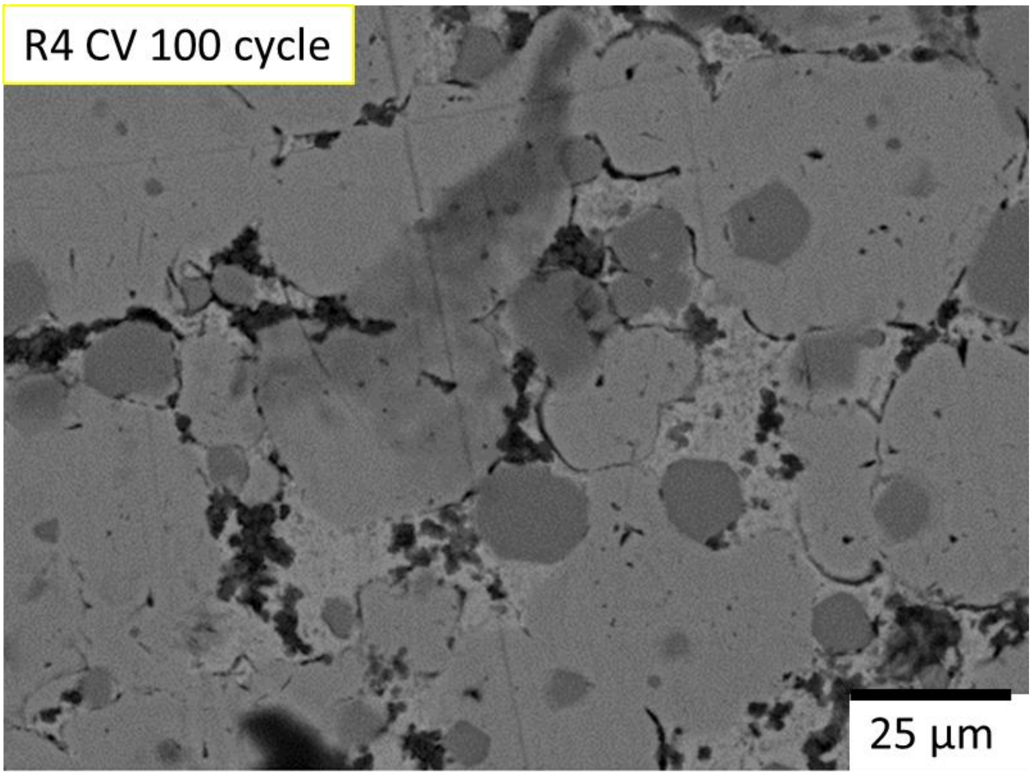

Figure 5.8 SEM image of HEA NiMnFeCrCu sample after R4 CV 100 cycle activation.

Table 5.4 Elemental atom % (EDS) of each phases present in the sample R4 CV 100 cycles.

Location \ Atom %	Ni	Mn	Fe	Cr	Cu	O
FCC1	21.2	10.8	22.1	17.3	8.8	19.8
FCC2	17.7	12.2	5.2	10.2	36.2	18.5
BCC	3.2	5.1	7.3	70	4.4	10
Total	19.4	8.8	18.6	19.8	20.2	13.2

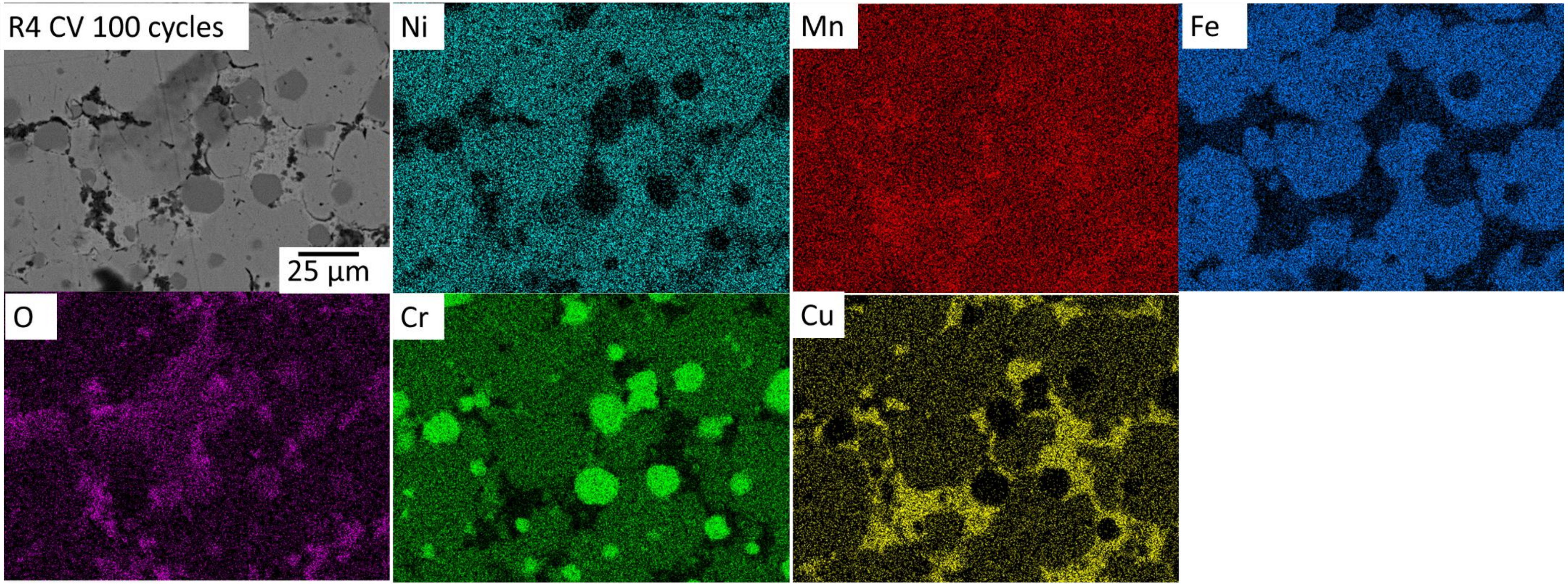

Figure 5.9 SEM/EDS map of the HEA NiMnFeCrCu sample after R4 CV 100 cycles activation.

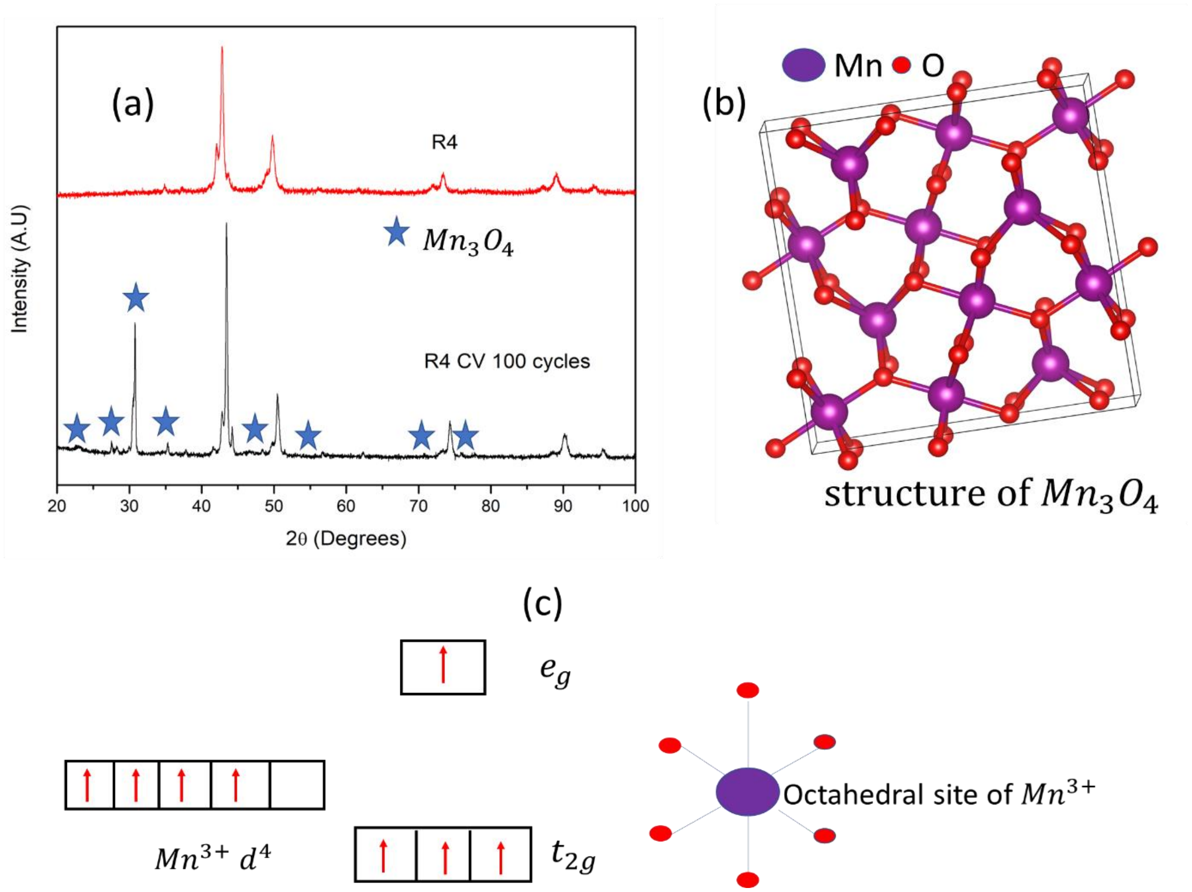

Figure 5.10 (a) XRD patterns of R4 (unused - no electrocatalysis) and R4 CV 100 cycles (b) crystal structure of Mn_3O_4 (c) Schematic representation of Mn_3O_4 depicting the filling of the e_g energy levels.

Table 5.5 Calculated descriptors for OER activity for Mn_3O_4 (calculated using the Vesta software package)[171].

Descriptors for predicting OER activity	Calculated Values
Oxidation state of the transition metal ion (M)	2.66 (average value)
M-O bond length Å	2.361
M-O-M bond angle °	34.26
M-M bond length Å	3.314

M- transition metal ion (in this case Mn)

O-Oxygen ion

Figure **5.11**(a) depicts the LSV of the HEA NiMnFeCrCu under condition R4 at 0 cycles and 1000 cycles of CV. It is observed that the HEA exhibited an onset overpotential of 228 mV (@ 1 mA cm^{-2}) and an overpotential of 328 mV at a fixed current density of 10 mA cm^{-2} under CV 0 cycles while under 1000 CV cycles the HEA exhibited an onset overpotential of 216 mV (@ 1 mA cm^{-2}) and an overpotential of 320 mV at a current density of 10 mA cm^{-2}. This suggests that the HEA showed negligible degradation under an accelerated degradation test (refer chapter **1** section **1.12.5)**. The chronoamperometry test depicted in Figure **5.11**(b) shows that initially at 0 h the current density is 42.4 mA cm^{-2} and at the end of 10 h the current density of 35.2 mA cm^{-2}(refer chapter **1** section **1.12.5**). This suggests that the HEA exhibited excellent stability with a exchange current density retention of 83%. The microstrucutre of the HEA sample under condition S2 CV 0 cycles and S2 CV 1000 cycles in provided Figure **S25** and Table **S3** in the appendix.

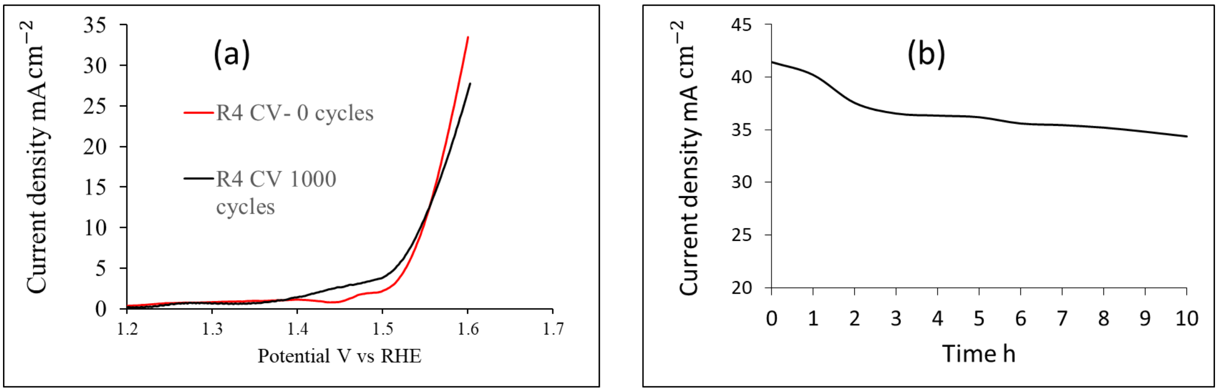

Figure 5.11(a) Accelerated degradation test of R4 at 0 cycles and 1000 cycles (LSV) (b)Chronoamperometry of the HEA NiMnFeCrCu R4 CV 100 cycles at 1.6V vs RHE.

In the studied HEA NiMnFeCrCu, the measured overpotential value is lower compared to that of Raney nickel, stainless steel and other mono-metallic catalyst such as perovskites. Furthermore, in the previously studied single-phase FCC NiMnFeCu HEA, the HEA exhibited an overpotential of 322 mV and microhardness value of 198 HV[141] while the combination, NiMnFeCrCu HEA with two FCC phases and a BCC phase exhibited an overpotential of 310 mV and microhardness value of 152 HV. Hence NiMnFeCrCu HEA exhibited excellent combined properties of strength and catalytic activity compared to the previously studied combination NiMnFeCu. This relatively lower overpotential might have stemmed from the highly distorted lattice of multi-phase NiMnFeCrCu HEA, furthermore, the presence of spinodal microstructure on the studied NiMnFeCrCu HEA also favoured enhanced electrocatalytic performance (refer to chapter **4** section **4.2.2)** [172]. Finally, the role of porosity in catalytic activity is critical in the design of an electrocatalyst. The NiMnFeCrCu HEA with a relative sintered density of 77% exhibited superior electrocatalytic activity compared to that of the 95% dense sample.

5.3 Electrochemical characterization of HEA NiMnFeCr

Figure **5.12**(a) depicts the LSV curve of the sintered NiMnFeCr HEA under various testing conditions which was acquired using a scan rate of 5 mV s^{-1}. The overpotential measured for the T3 CV using 100 cycles is the lowest of the tested samples. For T3 CV 100 cycles the overpotential is 300 mV while for T3 (no cycling) the overpotential is 334 mV and for T4 (no cycling) the overpotential is 358 mV. All the values are measured at the current density of 10 mA cm^{-2}. Similarly, the Tafel slope for T3 CV 100 cycles is the lowest at 75 mV/dec. The Tafel slopes for the T3 (no cycling) and T4 (no cycling) samples are, in contrast 97 mV/dec and 105 mV/dec respectively as shown in Figure **5.12**(b). The double layer capacitance C_{dl} of the T3 CV 100 cycles sample is the highest with 0.118 mF while for T3 the C_{dl} is 0.075 mF and for T4 the C_{dl} is 0.006 mF as displayed in Figure **5.12**(c). The Bode plot of the EIS spectra could be fitted into the Randles equivalent circuit and the charge transfer resistance R_{ct} of T3 CV 100 cycles, T3 and T4 are measured to be 77.3 Ω, 91.07 Ω and 98.34 Ω, respectively. The solution resistance R_s is found to be 2 Ω for all test conditions as illustrated in Figure **5.12**(d). Table **5.6** summarises the electrochemical characterization data for the OER process conducted on the HEA alloys described in this study.

Table 5.6 Electrochemical characterization of the HEA NiMnFeCr under various test conditions.

Sample	Overpotential mV	Tafel slope mV/dec	R_{ct} Ω	C_{dl} mF	ECSA cm^2
T4	358	105	98.34	0.006	0.15
T3	334	97	91.07	0.075	1.87
T3 CV 100 cycles	300	75	77.3	0.118	2.95

As shown in Table **5.6**, the HEA NiMnFeCr under condition T3 with CV 100 cycles exhibited a lower overpotential, lower Tafel slope, and lower charge transfer resistance, R_{ct} when compared to samples prepared under conditions of T3 and T4. This observation of low overpotential is the manifestation of excellent catalytic activity and indicates that a lower energy is necessary to start off a charge transfer reaction between the electrochemical reaction intermediates (O*, OH*, OOH*) and the surface of the electrocatalyst. This relatively superior electrocatalytic activity is attributed to the presence of excessive porosity in the microstructure of the sample T3 (which has relative sintered density of 83%). Furthermore, the CV cycling induced activation has also resulted in the in-situ formation of nano oxide layers which acted as a core shell structure and provided active sites which have also helped to enhance the catalytic activity[120, 121]. The presence of the oxide layers in the T3 CV 100 cycles sample was confirmed in the SEM/EDS spectrum data as depicted in Figure **5.13**(a-b) and in Table **5.7**. The atomic % of oxygen in the T3 CV 100 cycles samples is around 15.22% and is distributed homogeneously throughout the microstructure as shown in Figure **5.15**. It is worth noting that the oxides are clustered close to the pores in the material hence this indicates that the pores act as a preferred location for electrochemically active species such as (MO, MOH, MOOH where M = Ni,Mn,Fe,Cr) to bond through which the superior catalytic activity occurs. In addition, element Mn present in T3 CV 100 cycles (atom 10.17%) is decreased significantly compared to the sample T3 (unused- no electrocatalysis) (atom 24.2%) as shown in Table **5.7** and the element Mn is also found to be decrease in value in EDS analyses during the process of electrocatalysis for T3 CV 0 cycle (18.2%), T3 CV 100 cycles (10.17%) and T3 CV 1000 cycles(6.2%) samples compared to the sample T3 (unused - no electrocatalysis) (24.2%) as depicted in Figure **S26** and Table **S4** provided in the appendix section. To elucidate the reasons for the decrease of element Mn in

T3 CV 100 cycles sample compared to T3 (unused-no electrocatalysis) an XRD was carried out on T3 CV 100 cycles and compared with T3 (unused- no electrocatalysis) and depicted in Figure **5.14**(a). From the patterns it is evident that the T3 CV 100 cycles sample showed a strong peak at 2θ value 31.8 ° and this peak corresponded to Mn_3O_4 (JCPDS data 04-020-3526). Similar phenomena were also identified for our previously prepared HEA NiMnFeCrCu alloy[141]. Hence the decrease in atom % of Mn and formation of oxides layers on T3 after 100 cycles of CV could be attributed to structural transformation of an FCC manganese into orthorhombic manganese based oxide Mn_3O_4 (Figure **5.14** (b)). Mn containing alloys tends to oxidize easily due to the fact that Mn has high concentration of lone pairs of electrons in the valence energy levels. The in-situ formed Mn_3O_4 possessed an average oxidation state of +2.6 hence the metallic cations (Mn^{3+}, Mn^{2+}) changes the local electronic configuration resulting in an e_g occupancy value of 1 (for Mn^{3+} $e_g = 1$ $t_{2g} = 3)$. The Mn^{3+} occupying the octahedral site is electrochemically active because it exhibits low spin (LS) character and leaves a vacant space for a ligand to occupy as depicted in Figure **5.14**(c). This LS state and $(e_g = 1)$ value leads to enhanced OER activity since the σ^* antibonding state of e_g orbital of Mn^{3+} favours easy hybridization of 3d orbital of Mn^{3+} with 2p orbital of an oxygen atom of the hydroxyl ion (OH^-) compared to the Mn^{2+} cation because the high spin state (HS) of Mn^{2+} makes $e_g = 2$, which results in no vacant space for the ligand to occupy so consequently hinderings Mn-O bond formation [169]. Similarly the calculated spin corelated parameters such as oxidation states , bond angles and length are in accordance with our previously studied HEA NiMnFeCrCu work in which manganese-based oxides contributed to the OER activity of the NiMnFeCrCu HEA (refer Table **5.5**)[141]. Despite the excessive porosity of T3 (no cycling), it exhibited only a modest catalytic activity of 334 mV due to the absence of a nano oxide layers. Furthermore, larger C_{dl} value of 0.118 mF obtained for the sample T3 CV 100 cycles compared to other two samples also suggest that the existence of both porosity and oxide layers improves the electrochemical surface area. Hence it could be concluded that the increased catalytic performance is mainly attributed to the combined effect of porosity and oxide layers formed on the surface of the electrocatalyst. The sample T4(relative sintered density 94%) showed relatively poor catalytic activity due to the absence of both the oxide layers and the porosity.

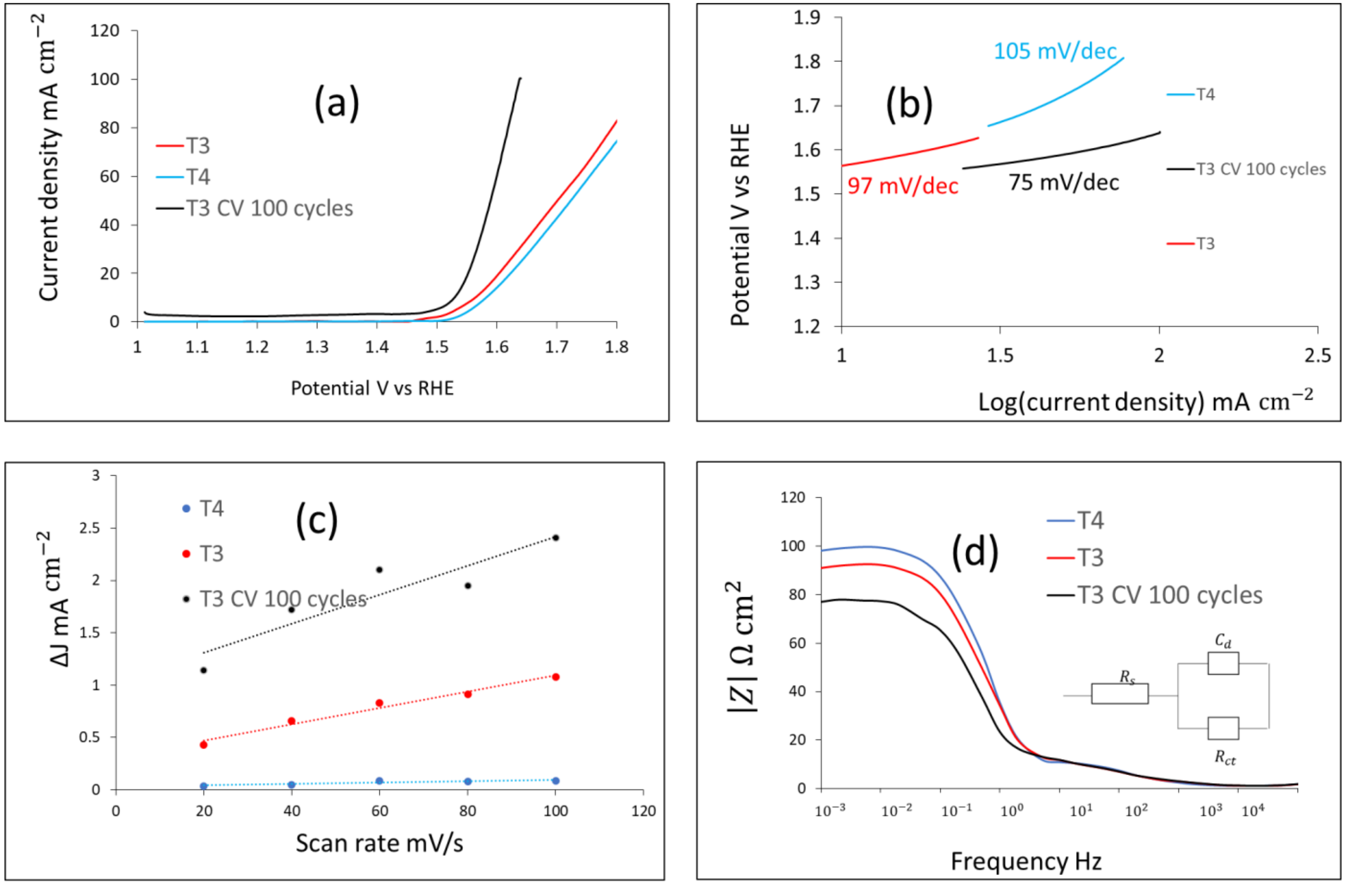

Figure 5.12 Electrochemical characterization of HEA NiMnFeCr at various test conditions (a) LSV at scan rate of 5mV/s (b) Tafel slope derived from LSV curves (c) Current density difference at 1.02 V vs (RHE) at different scan rates (d) Bode plot of electrical impedance measured at AC amplitude of 1.6 V vs RHE.

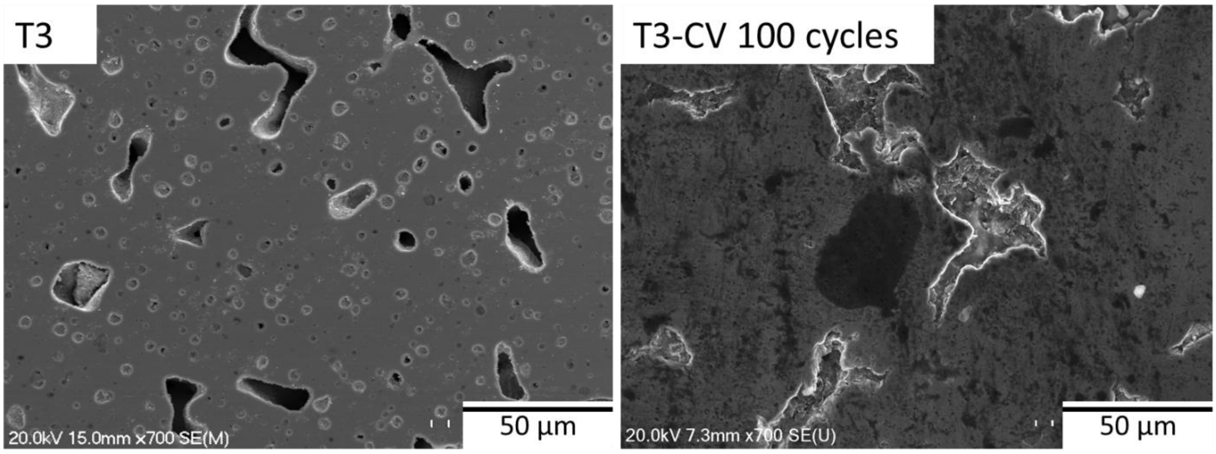

Figure 5.13 SEM image of HEA NiMnFeCr under conditions T3 (unused- no electrocatalysis) T3 CV 100 cycles.

Table 5.7 Elemental atom % composition of MEA NiMnFeCr under T3(unused-no electrocatalysis) and T3 CV 100 cycles.

Atom% / Sample	Ni	Mn	Fe	Cr	O
T3(no electrolysis)	27.2	24.2	25.4	23.2	0
T3-CV 100 cycles	25.92	10.17	20.64	29.17	15.2

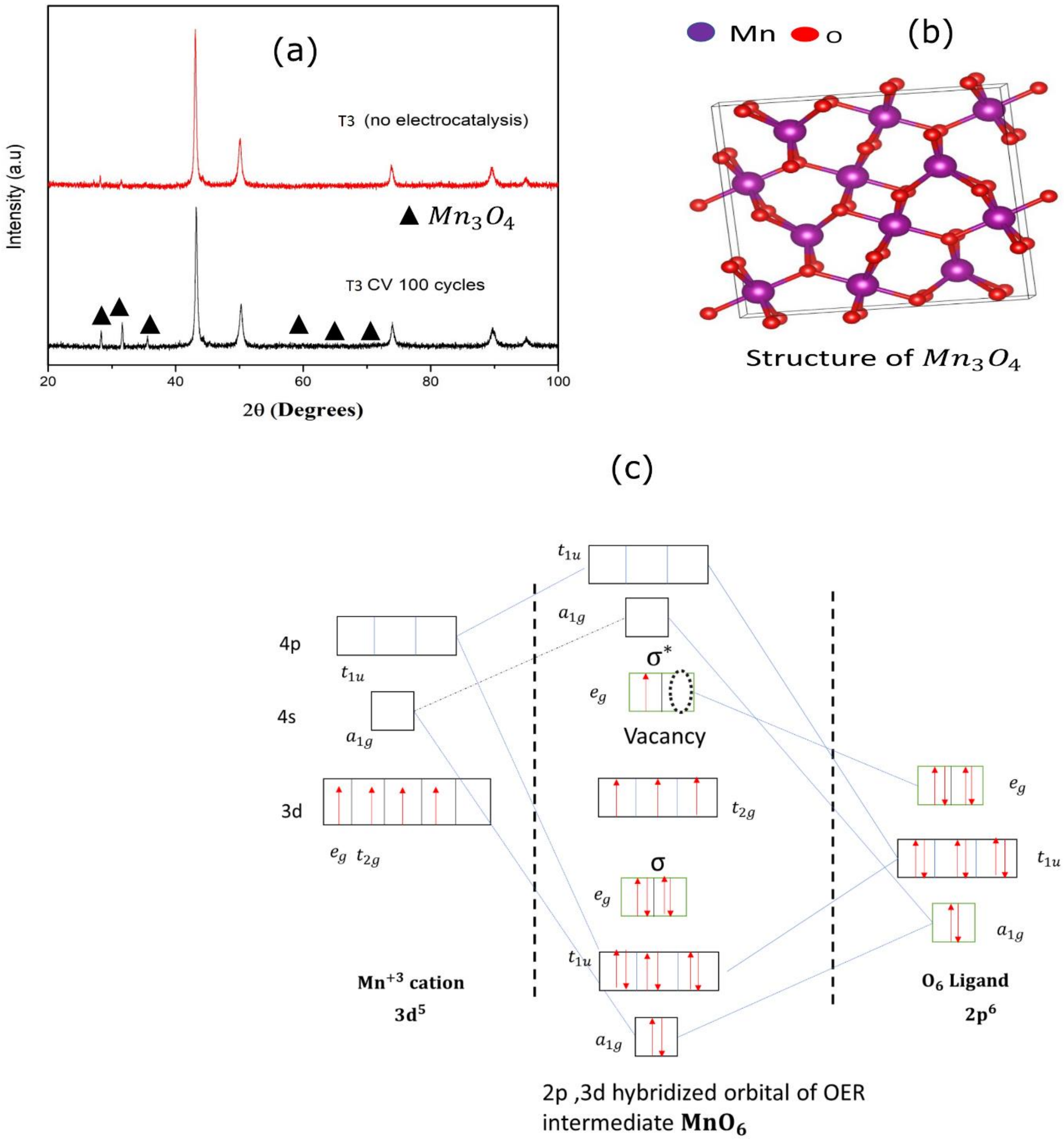

Figure 5.14 (a) XRD patterns of T3 (unused no electrocatalysis) and T3 CV 100 cycles (b) crystal structure of Mn_3O_4 (c) Schematic representation of molecular orbital of Mn_3O_4 depicting the filling of e_g energy level.

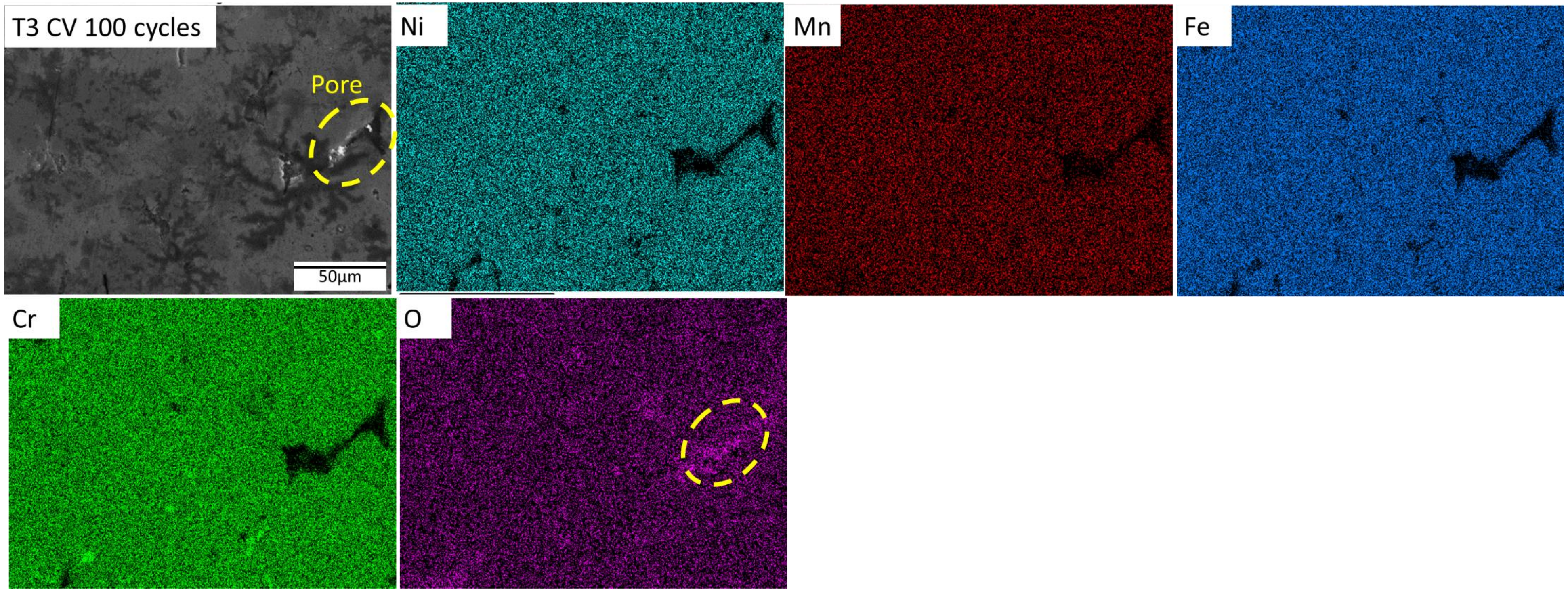

Figure 5.15 SEM EDS map of the HEA NiMnFeCr after CV 100 cycles (T3 CV100 cycles).

Figure **5.16**(a) depicts the LSV of the HEA NiMnFeCr under condition T3 at 0 cycles and 1000 cycles of CV. It is observed that the HEA exhibited an onset overpotential (@ 10 mA cm^{-2}) of 180 mV and an overpotential of 311 mV at fixed current density of 10 mA cm^{-2} under CV 0 cycles while under 1000 CV cycles the HEA exhibited an onset overpotential of 177 mV and an overpotential of 302 mV at the current density of 10 mA cm^{-2}. This suggests that the HEA shows negligible degradation under accelerated degradation test. The chronoamperometry test depicted in Figure **5.16** (b) shows that initially at 0 h the current density is 43.4 mA cm^{-2} and at the end of 10 h the current density of 35.2 mA cm^{-2}. This suggests that the HEA exhibited excellent stability with a exchange current density retention of 87%.

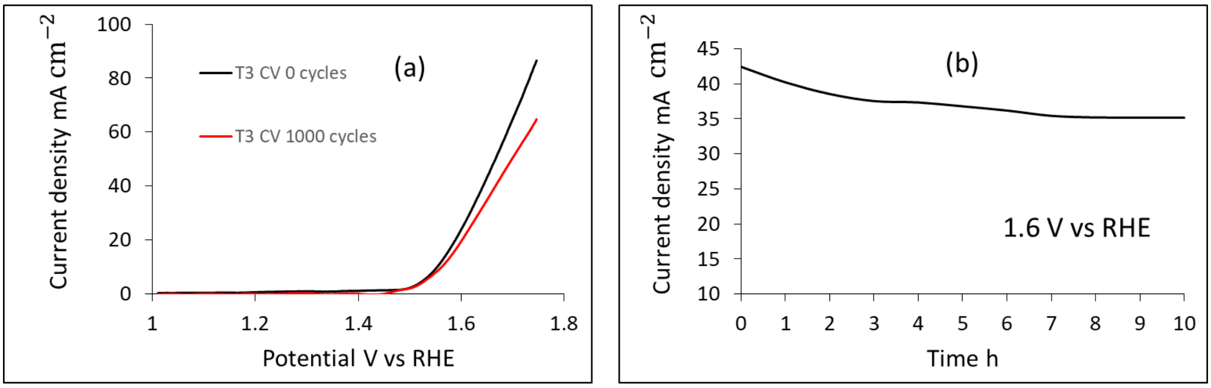

Figure 5.16 (a)Accelerated degradation of T3 CV 0 cycles and T3 CV 1000 (LSV) (b) chronoamperometry of T3 CV 100 cycles for 10 h under 1.6 V vs RHE.

5.4 Work function analysis of HEAs

The overpotential of the studied HEA NiMnFeCr is superior to that of the state-of-the-art electrocatalysts such as IrO_2 and RuO_2 and other transition metal based electrocatalysts[71]. Furthermore, the overpotential of the HEA NiMnFeCr prepared under condition T3 CV 100 cycles is comparable to several other reported HEAs such as MnFeCoNi (η= 302 mV)[120] , CoCrFeNiMo (η= 220mV)[121] and CoFeNiGaZn (η= 370mV)[108]. Along with that the catalytic activity of the NiMnFeCr HEA is better than previously studied NiMnFeCu and NiMnFeCrCu HEAs. Since the electrocatalytic OER is a process governed by an electron transfer mechanism taking place on the electrocatalyst/electrolyte interface, in order to better understand the origins of enhanced catalytic activity of the HEA NiMnFeCr, it is necessary to probe the electronic structure of the HEA NiMnFeCr and compare it with the other HEAs synthesised in this research. The electronic structure of an electrocatalyst can be easily studied through its work function measurement by valence band spectral analysis. The work function (Φ) is defined as the minimum energy required to remove an electron from the sample can be calculated using equation 5.1.

$$\Phi = \mathrm{h}\nu - \mathrm{E}_{\mathrm{cut\ off}} \tag{5.1}$$

Where $h\nu$ is the photon energy of He I, (21.2 eV).

Figure **5.17**(a) represents the valence band spectra and Figure **5.17**(b-d) depicts the enlarged view of the binding energy in the secondary electron cut off region of the three HEA combinations. The work function of the HEAs NiMnFeCr, NiMnFeCrCu and NiMnFeCu are measured to be 3.02 eV, 3.22 eV and 3.5eV respectively. It is worth noting that for HEA NiMnFeCr the work function is the lowest among the other HEAs and that also it exhibited the lowest overpotential value of 300 mV compared to HEA NiMnFeCu (η=322mV)[141] and HEA NiMnFeCrCu (η=310 mV)[138]. First row transition metals have partially filled d orbitals (exception Cu and Zn) and so they can easily hybridize with the $\mathrm{O_{2p}}$ orbital of the hydroxyl ion ($\mathrm{OH^-}$). The low work function of the electrocatalysts effectively demonstrates the ease of hybridization between the d orbital (valence band) of the transition metals and the $\mathrm{O_{2p}}$ orbital of the hydroxyl ion. Lowering of the work function hence reduces the energy barrier during the adsorption/ desorption process of the intermediates and enhances the OER kinetics[94, 173]. Similar results have also been observed in other materials system: (1) When ordered mesoporous carbon was doped with heteroatoms such as S, N and O the work function of the ordered mesoporous carbon decreased significantly, and triple doped carbon exhibited the smallest work function values leading consequently to high catalytic activity compared to that of the dual doped and mono doped carbon electrodes[174].(2) Lowering the surface work function of an Ag catalyst increased its catalytic activity towards $\mathrm{CO_2}$ reduction[175]. Hence the enhanced OER performance of the HEA NiMnFeCr that is known to have lower work function values compared to other HEAs such as NiMnFeCu and NiMnFeCrCu supports the fact that the work function of the electrocatalyst and the catalytic activity are strongly correlated properties. Furthermore, lowering of the work function of the electrocatalyst leads to improvement in the catalytic activity via reduction in the energy barrier for electron transfer through easy hybridization of the energy levels(orbitals).

As mentioned earlier in section **5.1**, the first-row transition elements are good candidates for OER electrocatalysis, (apart from Cu and Fe) because these elements are often used in monometallic form and they show modest catalytic activity e.g. Ni (η = 380 mV @ 10 mA cm^{-2}), Fe (η = 600 mV @ 10 mA cm^{-2}) [176], Mn (η = 580 mV @ 10 mA cm^{-2}) , Co (η = 420 mV @ 10 mA cm^{-2})[177], Cu ((η = 413 mV @ 10 mA cm^{-2})[178]. They tend to be used either in mono/bi/tri-metallic compositions in the form of oxides, hydroxides phosphides etc to improve the electrocatalytic activity. For instance, the synthesized bi metallic $(Ni_xFe_{1-x})_2$electrocatalyst exhibited a work function of 5.18 eV while the mono metallic Ni_2P electrocatalyst exhibited 5.20 eV, consequently the catalytic activity of $(Ni_xFe_{1-x})_2$ was better than a mono metallic Ni_2P [94]. This is because bimetallic or trimetallic electrocatalysts possess lower work function values compared to monometallic electrocatalysts which means that both bimetallic and trimetallic species offer superior catalytic activities compared to mono metallic electrocatalysts. On the other hand, HEAs are composed of at least four elements in atomic % value ranges of 5-35%, so they provide ample flexibility in fine tuning the electronic structure of the formed HEAs. For example, the measured work function of HEA NiMnFeCr is 3.02 eV, which is significantly lower than the work functions of bimetallic and monometallic electrocatalysts work function as shown in Figure **5.18**. This suggests that HEAs are expected to show far superior catalytic activities when compared to their mono/bi/tri metallic counterparts. The reason why the work functions of HEAs NiMnFeCrCu and NiMnFeCu are higher than the studied HEA NiMnFeCr (3.2 eV and 3.5 eV vs 3.02 eV) is attributed to the fact that Cu has fully occupied d orbital with an electronic configuration [Ar] $3d^{10}4s^1$, hence addition of Cu diminishes the OER activity by increasing the work function. A Cu free HEA NiMnFeCr exhibited a lower work function and consequently a higher catalytic activity towards the OER process. Table **5.8** compares the OER properties of the most common electrocatalyst with the studied HEAs.

Table 5.8 Comparison of OER properties of the most common electrocatalyst with the studied HEAs

Catalyst	Substrate	Electrolyte	Overpotential mV	Tafel slope mV/dec
NiMnFeCu	Self-supported	1M KOH	322	88
NiMnFeCrCu	Self-Supported	1M KOH	310	83
NiMnFeCr	Self-supported	1M KOH	300	75
Co_2P	GCE	1 M KOH	370 @10mA cm^{-2}	128
CoMnP	GCE	1 M KOH	330 @10mA cm^{-2}	61
Ni_2P	Nickel foam	1 M KOH	290@10mA cm^{-2}	59
CoCrNiFeMo	Self-supported	1M KOH	220@10mA cm^{-2}	59
MnFeCoNi	Carbon fibre paper	1M KOH	302@10mA cm^{-2}	83.7
$FeCoNiCuZn_{0.8}$	Self - supported	1M KOH	340@10mA cm^{-2}	48
FeCoNiCu	Self-supported	1M KOH	439 @50mA cm^{-2}	50
$Fe_{50}Mn_{30}Co_{10}Cr_{10}$	Self-supported	1M KOH	247 @10mA cm^{-2}	64
MnOOH	PtO	0.1 M KOH	470 @5 mA cm^{-2}	-
FeOOH	PtO	0.1 M KOH	525 @5mA cm^{-2}	-
NiOOH	PtO	0.1 M KOH	375 @5 mA cm^{-2}	-
CoOOH	PtO	0.1 M KOH	450 @5 mA cm^{-2}	-
$CaCu_3Fe_4O_{12}$	GCE*	0.1M KOH	400 @10mA cm^{-2}	51
$CaFeO_3$	GCE	0.1M KOH	390 @10mA cm^{-2}	47
$SrFeO_3$	GCE	0.1M KOH	410 @10mA cm^{-2}	63
$LaFeO_3$	GCE	0.1M KOH	500@10mA cm^{-2}	77
$La_{0.2}Sr_{0.8}FeO_3$	Self-supported	1M KOH	622@40mA cm^{-2}	58
$MnFe_2O_4$	GCE	0.1M KOH	470 @10mA cm^{-2}	114
$CoFe_2O_4$	GCE	0.1M KOH	370 @10mA cm^{-2}	82
$NiFe_2O_4$	GCE	0.1M KOH	440 @10mA cm^{-2}	98
$CuFe_2O_4$	GCE	0.1M KOH	410 @10mA cm^{-2}	94
Mn_3O_4	GCE	1M KOH	>600 @ 3 mA cm^{-2}	60

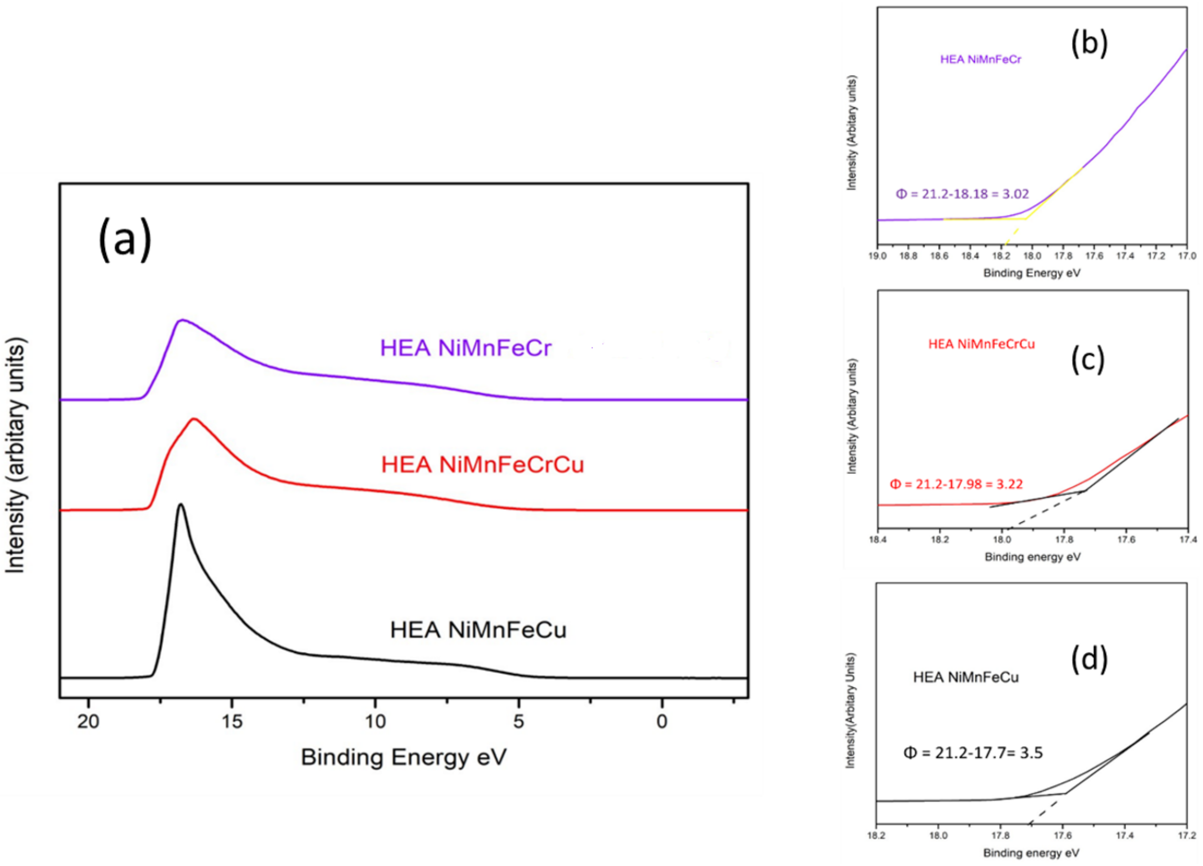

Figure 5.17 Valence band spectrum of the as sintered HEAs (a) full spectrum (b-d) secondary electron cut off energy.

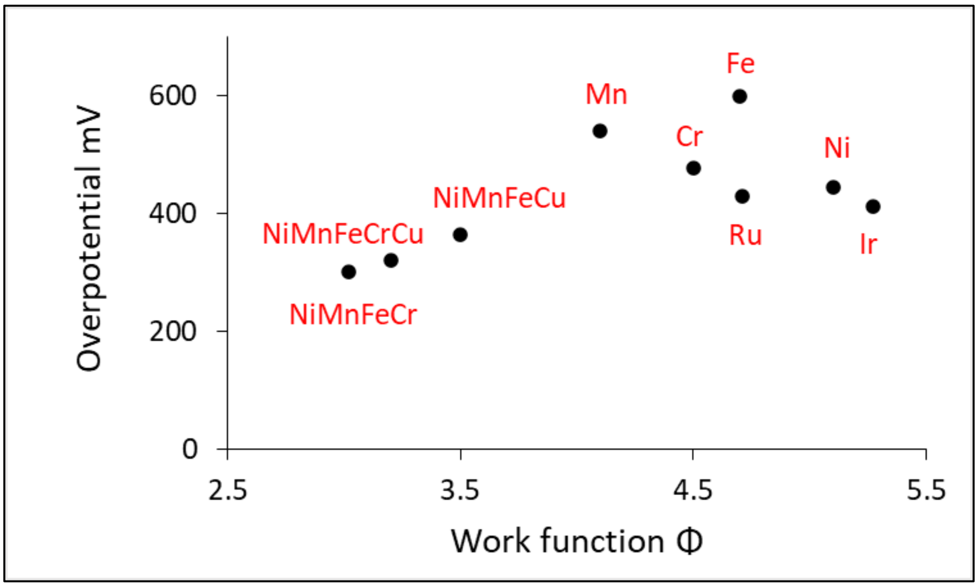

Figure 5.18 Overpotential as a function of work function for transition metals used as electrocatalyst for OER reaction[179].

5.5 Electrocatalysis of HEAs using natural sea water

Figure **5.19**(a-b) depicts the LSV curves and Tafel slopes of the HEAs studied in this Phd thesis. It is evident that the HEA NiMnFeCr (T3) exhibited better electrocatalytic properties compared to that of other HEAs studied in this research. The HEA NiMnFeCr(T3) exhibited an overpotential of 560 mV and Tafel slope of 79 mV/dec in natural seawater. Subsequently the HEA NiMnFeCrCu (R4) exhibited an overpotential of 830 mV and a Tafel slope of 119 mV/dec and the HEA NiMnFeCu(S2) showed an overpotential of 904 mV and a Tafel slope of 121mV/dec. The HEA NiMnFeCr has a better OER performance relative to that of other HEAs in natural seawater and in 1M KOH as well. The overpotential for OER in natural seawater is higher than what is observed in the 1M KOH solution. This could be due to the fact that natural seawater lacks the required concentration of hydroxyl ions which contributes to the ease of OER process. As a result, more external energy is required to perform the OER in natural sea water on this electrode. As discussed earlier the enhanced OER performance of the HEA NiMnFeCr(T3) compared in both seawater and in 1M KOH solution can be attributed to the modified electronic structure and to the large number of pores present in this material.

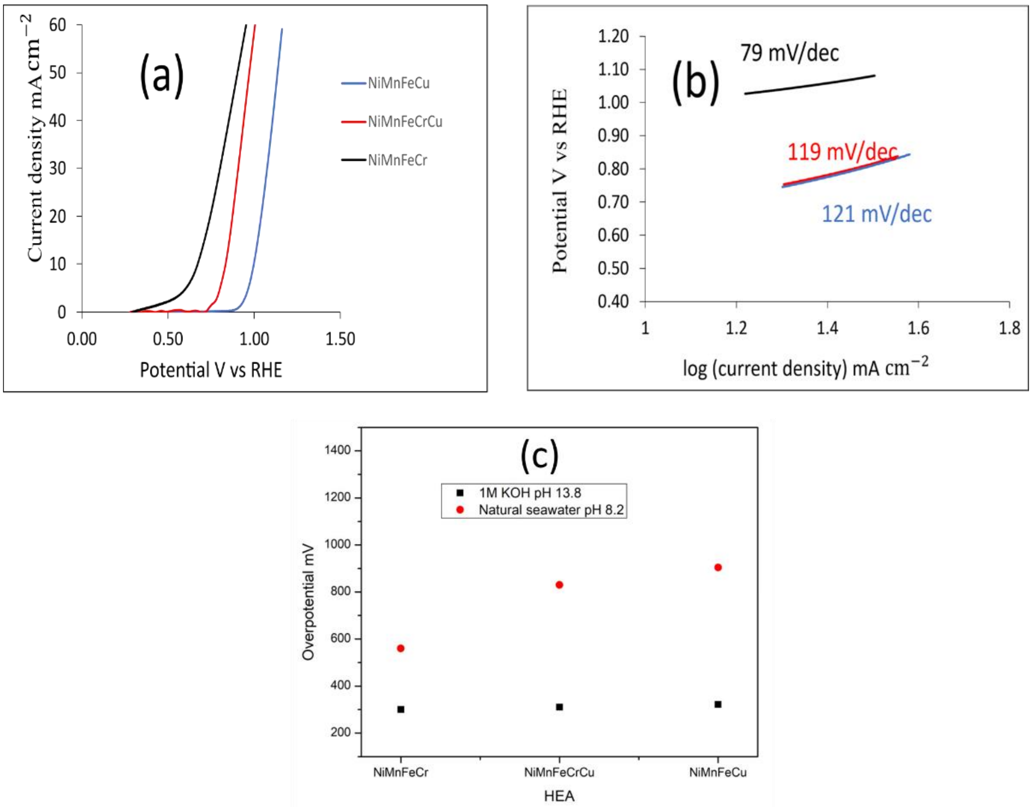

Figure 5.19 Electrochemical characterization of the studied HEAs in natural seawater (a) LSV curves (b) Tafel slopes (c) Comparison of OER performance of the HEAs in natural seawater and 1M KOH.

Chapter 6 Conclusion and future perspectives

6.1 Conclusion

The reported work demonstrates the synthesis of cost-effective transition metal based HEAs using a powder metallurgy route which involves mechanical alloying and vacuum sintering. The mechanical and electrocatalytic properties of the synthesised HEAs were evaluated and the studied HEAs could be potentially used in industrial scale practical alkaline water electrolysis. The key findings of the study are summarised briefly below:

I. Three cost effective Co free HEAs NiMnFeCu, NiMnFeCrCu and NiMnFeCr powders were successfully synthesised using a mechanical alloying technique. A milling time of 15 h was found to be sufficient for producing chemically homogeneous HEA powders for all three combinations. Furthermore 3% PCA, BPR of 10:1 and speed of 350 RPM were deemed to be the optimum condition for all three combinations.

II. The milled HEA powders of all three combinations were cold compacted at 700 MPa. The green density of HEA NiMnFeCu, NiMnFeCrCu and NiMnFeCr were 70%,67% and 65% respectively. Subsequent sintering of the HEAs resulted in the formation of bulk HEAs with FCC structure for NiMnFeCu and FCC1+FCC2+BCC structure for NiMnFeCrCu and FCC+BCC for NiMnFeCr.

III. The HEA NiMnFeCrCu possessed relatively better mechanical properties compared to other HEAs. HEA NiMnFeCrCu possessed the highest microhardness and compressive yield strength values of 250 Hv and 724 MPa respectively followed by HEA NiMnFeCu which had a microhardness value of 233 Hv and a compressive yield stress value of 516 MPa. The HEA NiMnFeCr exhibited the least mechanical strength of the three HEAs.

IV. The HEA NiMnFeCr exhibited better electrocatalytic properties for OER relative to other HEAs studied in this research. The HEA NiMnFeCr under conditions T3 (83% relative density) exhibited an overpotential of 300 mV at a current density of 10 mA/cm^2 and a Tafel slope of 75 mV/dec. The study concluded that porous HEAs (relative density (75-85) %) possessed better OER properties compared fully dense HEAs, hence porous HEAs are highly suitable for electrocatalytic applications. The HEA NiMnFeCr exhibited a combination of excellent OER and modest mechanical properties to function as an electrocatalyst for industrial scale water electrolysis. In addition, the HEA NiMnFeCr exhibited the lowest work function of 3.02 eV compared to the other HEAs which also contributed the excellent observed OER properties. Hence HEA NiMnFeCr is considered to be ideal electrocatalyst for industrial scale hydrogen production relative to the other HEAs NiMnFeCrCu and NiMnFeCu reported in this study.

6.2 Future work

The results reported in this study have also provided an opportunity to explore a few unanswered research questions related to heterogeneous catalysis. Study on this will continue focussing on the following research objectives.

I. Although preliminary investigation was carried out to explore the compatibility of the HEAs for OER studies in natural sea water, a more complex and systematic study is required for HEAs to be used in electrolytes with varying pH and naturally existing water sources.
II. Surface modification of HEAs for enhanced catalytic activity will be investigated.
III. Theoretical calculations such as DFT will be carried out to better understand the mechanisms behind heterogeneous catalysis,
IV. Advanced in situ operando techniques will be performed to probe the intermediates formed on the surface of the electrocatalyst during electrocatalysis.

Appendix

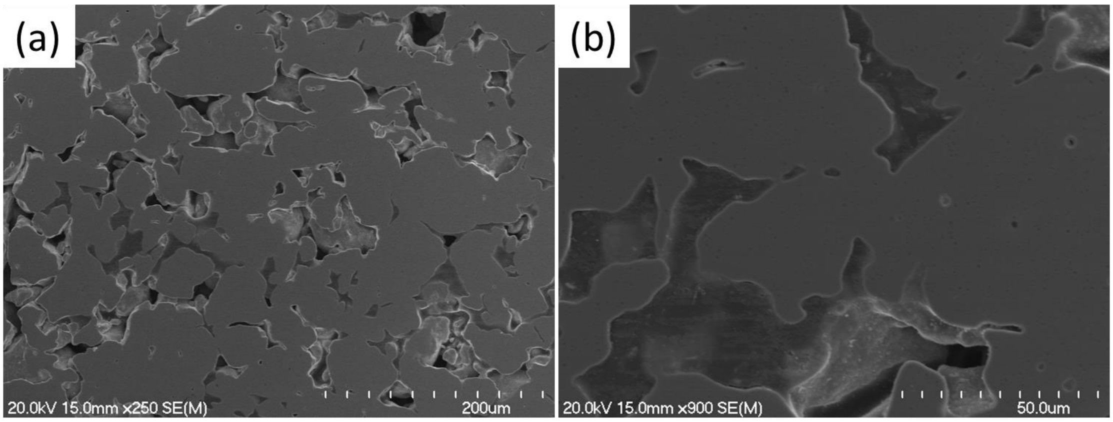

Figure S20 SEM images of the sintered HEA NiMnFeCu under condition S0 (a) low magnification (b) high magnification.

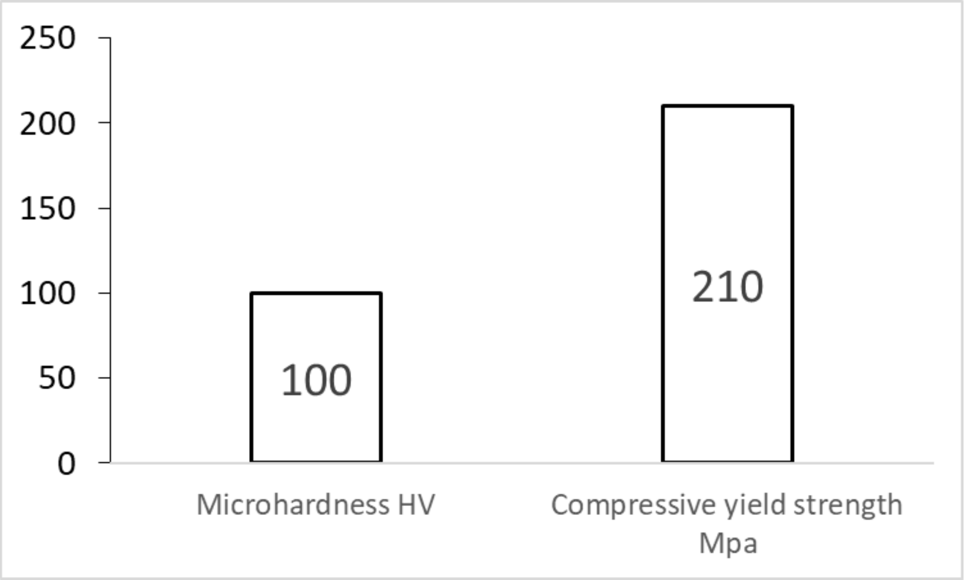

Figure S21 Mechanical properties of sintered NiMnFeCu under condition S0.

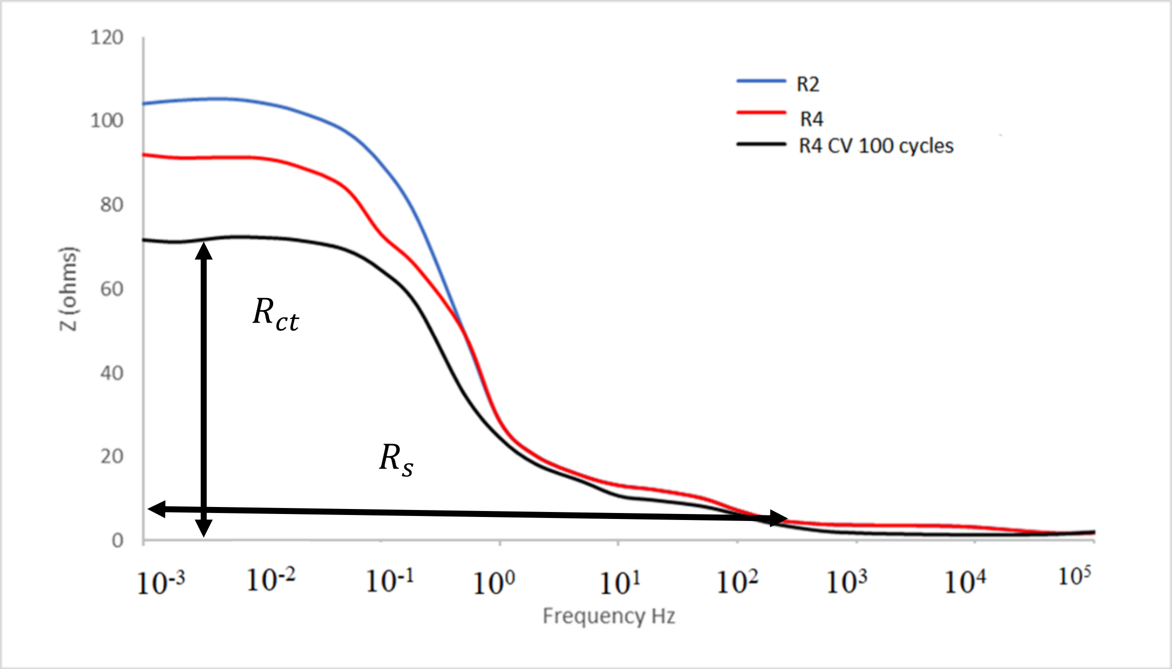

Figure S22 Electrical impedance spectroscopy (EIS) indicating charge transfer resistance R_{ct} and solution transfer R_s.

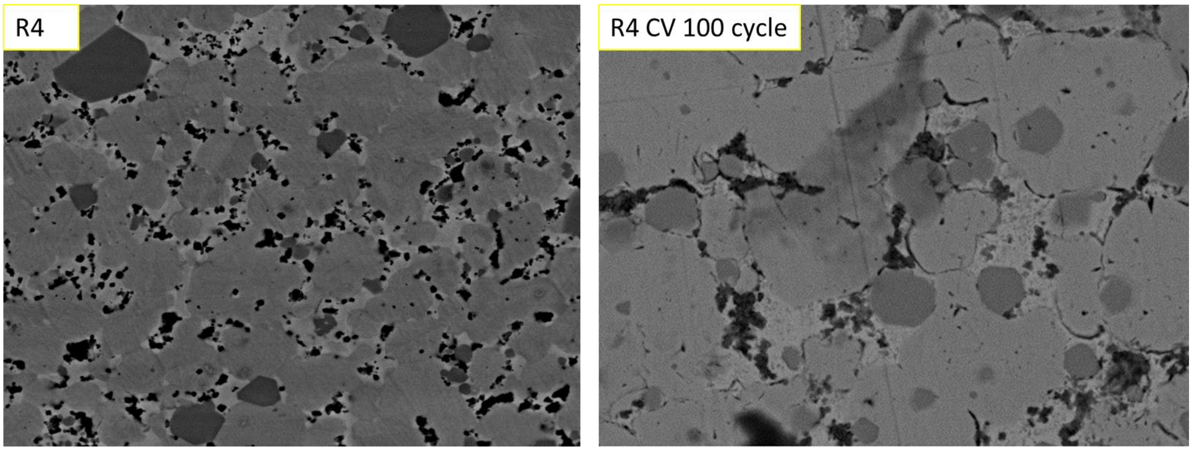

Figure S23 SEM micrographs of HEA NiMnFeCrCu under conditions R4 (no electrocatalysis) R4CV 100 cycle.

Table S1 Elemental atom % of HEA NiMnFeCrCu under conditions R4 (no electrocatalysis) R4CV 100 cycle.

Atom % Sample	Ni	Mn	Fe	Cr	Cu	O
R4 (no catalysis)	18.6	19.8	21.1	22.3	18.2	0

R4 CV 100 cycles	15.98	10.08	19.43	16.71	8.32	29.48

Table S2 Elemental atom % of HEA NiMnFeCrCu of each phase under conditions R4 (no electrocatalysis).

Phases	Ni %	Mn%	Fe%	Cr%	Cu%
FCC 1	22.4	22.2	28.1	18.41	8.9
FCC 2	16.0	22.4	5.6	11.4	44.6
BCC	4.2	6.7	8.6	77.8	2.7
Total	19.6	20.8	22.1	21.3	16.2

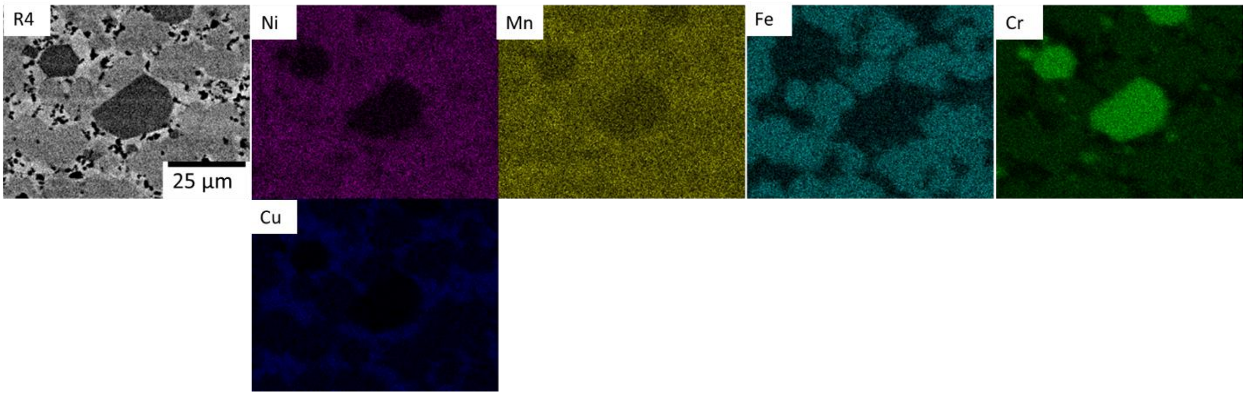

Figure S24 SEM/EDS map of the HEA NiMnFeCrCu under R4 (no electrocatalysis).

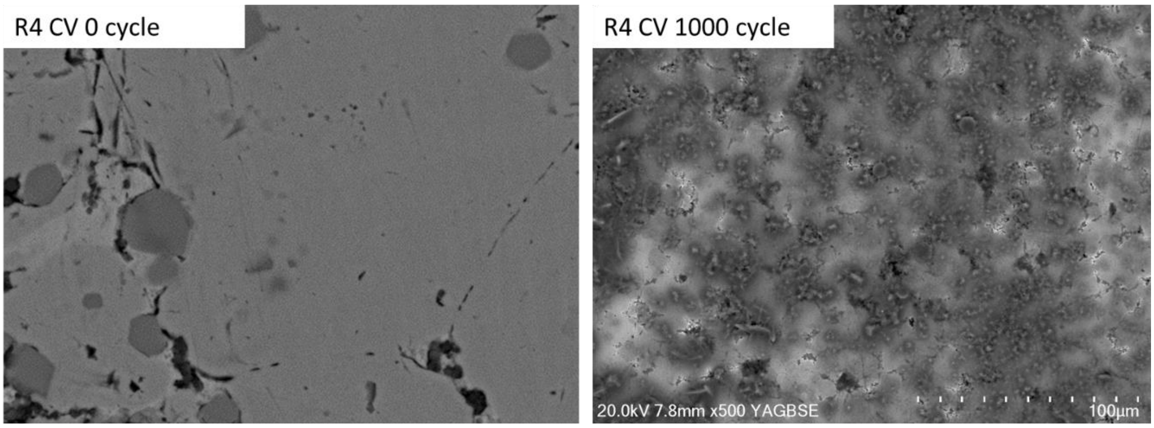

Figure S25 SEM micrographs of HEA NiMnFeCrCu under conditions R4 CV 0 cycle and R4 CV 1000 cycle.

Table S3 Elemental composition of HEA NiMnFeCrCu under various test conditions SEM/EDS.

Sample	Atom% / Phase	Ni	Mn	Fe	Cr	Cu	O
R4 CV 0 cycles	FCC1	20.2	14.8	21.1	17.3	9.8	16.8
	FCC2	16.7	15.2	9.2	11.2	36.2	11.5
	BCC	5.2	5.1	10.3	64.9	4.4	10.1
	Total	18.4	16.8	19.6	18.8	20.2	6.2
R4 CV 1000 cycles	FCC1	12.1	8.6	11.6	15.5	18.2	33.5
	FCC2	11.8	4.5	12.6	17.5	25.2	28.4
	BCC	6.8	9.5	10.6	50.5	3.1	19.5
	Total	18.8	10.4	14.4	18.5	20.1	17.9

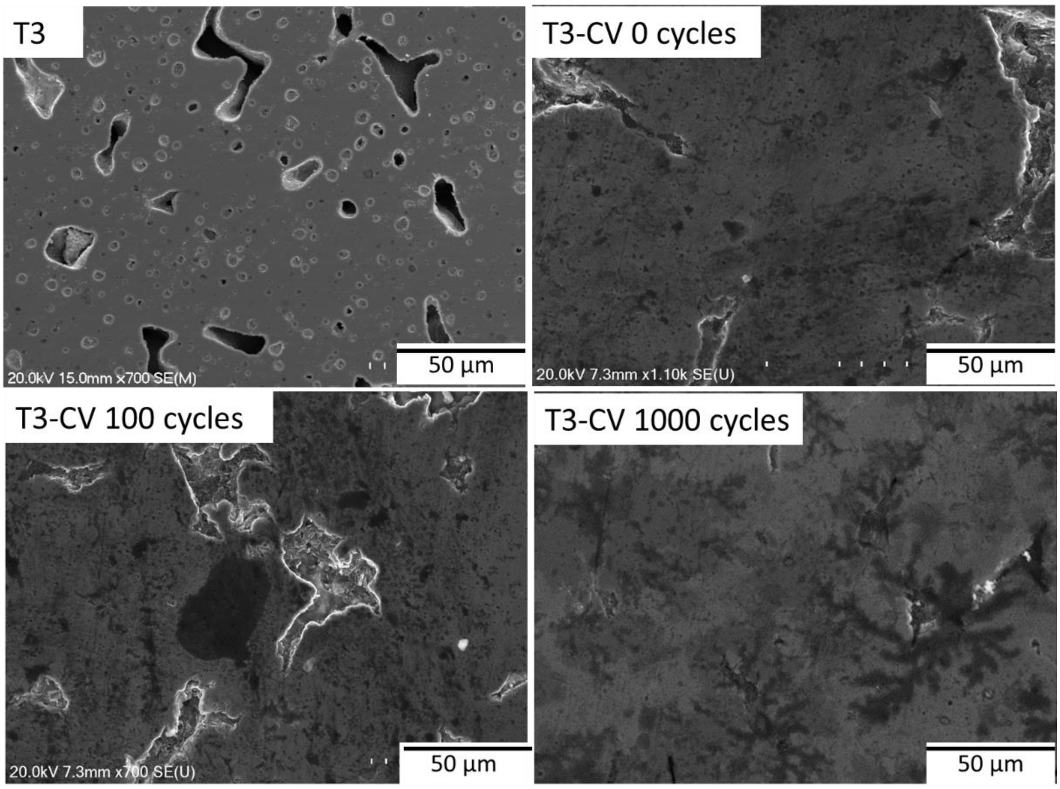

Figure S26 SEM image of the MEA NiMnFeCr under various test conditions.

Table S4 EDS elemental atom% of MEA NiMnFeCr under various test conditions.

Atom% Sample	Ni	Mn	Fe	Cr	O
T3	27.2	24.2	25.4	23.2	0
T3-CV 0 cycles	25.2	18.2	25.4	27	4.2
T3-CV 100 cycles	25.92	10.17	20.64	29.17	15.2
T3-CV 1000 cycles	25.1	6.2	26.2	23.3	19.2

References

1. Mizutani, U., *Hume-Rothery rules for structurally complex alloy phases.* MRS Bulletin, 2012. **37**(2): p. 169-169.
2. Hume-Rothery, W., *Atomic theory for students of metallurgy.* 1952.
3. Gao, M.C., et al., *High-entropy alloys*. 2016, New York, NY: Springer.
4. Gorsse, S., J.-P. Couzinié, and D.B. Miracle, *From high-entropy alloys to complex concentrated alloys.* Comptes Rendus Physique, 2018. **19**(8): p. 721-736.
5. Yeh, J.W., et al., *Nanostructured high-entropy alloys with multiple principal elements: novel alloy design concepts and outcomes.* Advanced Engineering Materials, 2004. **6**(5): p. 299-303.
6. Cantor, B., et al., *Microstructural development in equiatomic multicomponent alloys.* Materials Science Engineering: A, 2004. **375**: p. 213-218.
7. Steurer, W., *Single-phase high-entropy alloys–A critical update.* Materials Characterization, 2020. **162**: p. 110179.
8. Yeh, J.-W., *Alloy design strategies and future trends in high-entropy alloys.* Jom, 2013. **65**(12): p. 1759-1771.
9. Miracle, D., et al., *Exploration and development of high entropy alloys for structural applications.* Entropy, 2014. **16**(1): p. 494-525.
10. Otto, F., et al., *The influences of temperature and microstructure on the tensile properties of a CoCrFeMnNi high-entropy alloy.* Acta Materialia, 2013. **61**(15): p. 5743-5755.
11. Zhang, Y., et al., *Guidelines in predicting phase formation of high-entropy alloys.* Mrs Communications, 2014. **4**(2): p. 57-62.
12. Guo, S., et al., *Effect of valence electron concentration on stability of fcc or bcc phase in high entropy alloys.* Journal of applied physics, 2011. **109**(10): p. 103505.
13. Murty, B.S., et al., *High-entropy alloys*. 2019: Elsevier.
14. Yeh, J.-W., et al., *Formation of simple crystal structures in Cu-Co-Ni-Cr-Al-Fe-Ti-V alloys with multiprincipal metallic elements.* Metallurgical Materials Transactions A, 2004. **35**(8): p. 2533-2536.
15. Tsai, M.-H., *Physical properties of high entropy alloys.* Entropy, 2013. **15**(12): p. 5338-5345.
16. Cheng, K.-H., et al. *Recent progress in multi-element alloy and nitride coatings sputtered from high-entropy alloy targets*. in *Annales de chimie*. 2006. Lavoisier.
17. Tsai, M.-H. and J.-W. Yeh, *High-entropy alloys: a critical review.* Materials Research Letters, 2014. **2**(3): p. 107-123.

18. Tsai, K.-Y., M.-H. Tsai, and J.-W. Yeh, *Sluggish diffusion in Co–Cr–Fe–Mn–Ni high-entropy alloys.* Acta Materialia, 2013. **61**(13): p. 4887-4897.
19. Vaidya, M., et al., *Radioactive isotopes reveal a non sluggish kinetics of grain boundary diffusion in high entropy alloys.* Scientific reports, 2017. **7**(1): p. 1-11.
20. Ranganathan, S., *Alloyed pleasures: multimetallic cocktails.* Current science, 2003. **85**(5): p. 1404-1406.
21. Miracle, D.B. and O.N. Senkov, *A critical review of high entropy alloys and related concepts.* Acta Materialia, 2017. **122**: p. 448-511.
22. Takeuchi, A., et al., *Pd20Pt20Cu20Ni20P20 high-entropy alloy as a bulk metallic glass in the centimeter.* Intermetallics, 2011. **19**(10): p. 1546-1554.
23. Turnbull, D., *On the Gram-Atomic Volumes of Metal-Metalloid Glass Forming Alloys*. 1977, HARVARD UNIV CAMBRIDGE MA DIV OF APPLIED SCIENCES.
24. Greer, A.L., *Confusion by design.* Nature, 1993. **366**(6453): p. 303-304.
25. Inoue, A., *Stabilization of metallic supercooled liquid and bulk amorphous alloys.* Acta materialia, 2000. **48**(1): p. 279-306.
26. Murty, B.S., J.-W. Yeh, and S. Ranganathan, *High-entropy alloys*. 2014: Butterworth-Heinemann.
27. Smith, W.F. and J. Hashemi, *Foundations of materials science and engineering*. 2006: Mcgraw-Hill Publishing.
28. Tong, C.-J., et al., *Microstructure characterization of Al x CoCrCuFeNi high-entropy alloy system with multiprincipal elements.* Metallurgical Materials Transactions A, 2005. **36**(4): p. 881-893.
29. Zhang, Y., et al., *Solid-solution phase formation rules for multi-component alloys.* Advanced Engineering Materials, 2008. **10**(6): p. 534-538.
30. Takeuchi, A. and A. Inoue, *Classification of bulk metallic glasses by atomic size difference, heat of mixing and period of constituent elements and its application to characterization of the main alloying element.* Materials Transactions, 2005. **46**(12): p. 2817-2829.
31. Massalski, T.B., *Comments concerning some features of phase diagrams and phase transformations.* Materials transactions, 2010. **51**(4): p. 583-596.
32. Yang, X. and Y. Zhang, *Prediction of high-entropy stabilized solid-solution in multi-component alloys.* Materials Chemistry and Physics 2012. **132**(2-3): p. 233-238.
33. Chen, S.-T., et al., *Microstructure and properties of age-hardenable AlxCrFe1. 5MnNi0. 5 alloys.* Materials Science Engineering: A, 2010. **527**(21-22): p. 5818-5825.
34. Tsai, M.-H., et al., *Criterion for sigma phase formation in Cr-and V-containing high-entropy alloys.* Materials Research Letters, 2013. **1**(4): p. 207-212.
35. Joubert, J.-M., *Crystal chemistry and Calphad modeling of the σ phase.* Progress in Materials Science, 2008. **53**(3): p. 528-583.
36. Boesch, W.J. and J.S. Slaney, *Preventing sigma phase embrittlement in nickel base superalloys.* Metal Progress, 1964. **86**(1): p. 109-111.
37. Sims, C.T., N.S. Stoloff, and W.C. Hagel, *superalloys II*. 1987: Wiley New York.
38. Zhang, Y., et al., *High-entropy alloys with high saturation magnetization, electrical resistivity, and malleability.* Scientific reports, 2013. **3**: p. 1455.
39. Li, P., A. Wang, and C. Liu, *A ductile high entropy alloy with attractive magnetic properties.* Journal of Alloys and Compounds, 2017. **694**: p. 55-60.
40. Yao, C.-Z., et al., *Electrochemical preparation and magnetic study of Bi–Fe–Co–Ni–Mn high entropy alloy.* Electrochimica Acta, 2008. **53**(28): p. 8359-8365.
41. Guo, W., et al., *Microstructures and mechanical properties of ductile NbTaTiV refractory high entropy alloy prepared by powder metallurgy.* Journal of Alloys and Compounds, 2019. **776**: p. 428-436.

42. Varalakshmi, S., M. Kamaraj, and B. Murty, *Processing and properties of nanocrystalline CuNiCoZnAlTi high entropy alloys by mechanical alloying.* Journal of Materials Science and Engineering, 2010. **527**(4-5): p. 1027-1030.
43. Sekhar, R.A., et al., *Microstructure and mechanical properties of Ti-Al-Ni-Co-Fe based high entropy alloys prepared by powder metallurgy route.* Journal of Alloys and Compounds, 2019.
44. Dolique, V., A.-L. Thomann, and P. Brault, *High-entropy alloys deposited by magnetron sputtering.* IEEE Transactions on Plasma Science, 2011. **39**(11): p. 2478-2479.
45. Chang, S.-Y., et al., *Mechanical properties, deformation behaviors and interface adhesion of (AlCrTaTiZr) Nx multi-component coatings.* Surface Coatings Technology, 2010. **204**(20): p. 3307-3314.
46. He, F., et al., *Stability of lamellar structures in CoCrFeNiNbx eutectic high entropy alloys at elevated temperatures.* Materials & Design, 2016. **104**: p. 259-264.
47. Zuo, T., et al., *Novel high entropy alloys of Fe x Co 1-x NiMnGa with excellent soft magnetic properties.* Intermetallics, 2018. **100**: p. 1-8.
48. Zhou, Y., et al., *Solid solution alloys of Al Co Cr Fe Ni Ti x with excellent room-temperature mechanical properties.* Applied physics letters, 2007. **90**(18): p. 181904.
49. Wang, F., et al., *Cooling rate and size effect on the microstructure and mechanical properties of AlCoCrFeNi high entropy alloy.* Journal of engineering materials technology, 2009. **131**(3).
50. Yu, F., et al., *Recent developments in earth-abundant and non-noble electrocatalysts for water electrolysis.* Materials Today Physics, 2018. **7**: p. 121-138.
51. Pradeep, K., et al., *Atomic-scale compositional characterization of a nanocrystalline AlCrCuFeNiZn high-entropy alloy using atom probe tomography.* Acta Materialia, 2013. **61**(12): p. 4696-4706.
52. Kang, B., et al., *Ultra-high strength WNbMoTaV high-entropy alloys with fine grain structure fabricated by powder metallurgical process.* Materials Science Engineering: A, 2018. **712**: p. 616-624.
53. Raza, A., et al., *Transition in microstructural and mechanical behavior by reduction of sigma-forming element content in a novel high entropy alloy.* Materials & Design, 2018. **145**: p. 11-19.
54. Suryanarayana, *Mechanical alloying and milling.* Progress in materials science, 2001. **46**(1-2): p. 1-184.
55. Suryanarayana, C., *Does a disordered γ-TiAl phase exist in mechanically alloyed TiAl powders?* Intermetallics, 1995. **3**(2): p. 153-160.
56. Upadhyaya, G.S., *Powder metallurgy technology*. 1997: Cambridge Int Science Publishing.
57. Thummler, F. and R. Oberacker, *Introduction to powder metallurgy*. 1993: Oxford Science Publications
58. Liu, P. and G.-F. Chen, *Porous materials: processing and applications*. 2014: Elsevier.
59. Dincer, I. and C. Acar, *Review and evaluation of hydrogen production methods for better sustainability.* International journal of hydrogen energy, 2015. **40**(34): p. 11094-11111.
60. Secretariat, R., *Renewables 2020 global status report.* Rep. Paris: REN12, 2020.
61. Heubaum, H. and F. Biermann, *Integrating global energy and climate governance: The changing role of the International Energy Agency.* Energy Policy, 2015. **87**: p. 229-239.

62. Krieger, E.M. and C.B. Arnold, *Effects of undercharge and internal loss on the rate dependence of battery charge storage efficiency.* Journal of Power Sources, 2012. **210**: p. 286-291.
63. Astaneh, M., et al., *A novel lifetime prediction method for lithium-ion batteries in the case of stand-alone renewable energy systems.* International Journal of Electrical Power Energy Systems, 2018. **103**: p. 115-126.
64. Ji, M. and J. Wang, *Review and comparison of various hydrogen production methods based on costs and life cycle impact assessment indicators.* International Journal of Hydrogen Energy, 2021. **46**(78): p. 38612-38635.
65. Wang, J., et al., *Non-noble metal-based carbon composites in hydrogen evolution reaction: fundamentals to applications.* Advanced materials, 2017. **29**(14): p. 1605838.
66. Lee, H., et al., *Outlook of industrial-scale green hydrogen production via a hybrid system of alkaline water electrolysis and energy storage system based on seasonal solar radiation.* Journal of Cleaner Production, 2022: p. 134210.
67. Anantharaj, S., et al., *Recent trends and perspectives in electrochemical water splitting with an emphasis on sulfide, selenide, and phosphide catalysts of Fe, Co, and Ni: a review.* Acs Catalysis, 2016. **6**(12): p. 8069-8097.
68. Khzouz, M. and E.I. Gkanas, *Hydrogen technologies for mobility and stationary applications: hydrogen production, storage and infrastructure development*, in *Renewable Energy-Resources, Challenges and Applications*. 2020, IntechOpen.
69. Jayabal, S., et al., *Understanding the high-electrocatalytic performance of two-dimensional MoS 2 nanosheets and their composite materials.* Journal of Materials Chemistry A, 2017. **5**(47): p. 24540-24563.
70. Anwar, S., et al., *Recent development in electrocatalysts for hydrogen production through water electrolysis.* International Journal of Hydrogen Energy, 2021. **46**(63): p. 32284-32317.
71. Suen, N.-T., et al., *Electrocatalysis for the oxygen evolution reaction: recent development and future perspectives.* Chemical Society Reviews, 2017. **46**(2): p. 337-365.
72. Faber, M.S., et al., *High-performance electrocatalysis using metallic cobalt pyrite (CoS2) micro-and nanostructures.* Journal of the American Chemical Society, 2014. **136**(28): p. 10053-10061.
73. Sharaf, O.Z. and M.F. Orhan, *An overview of fuel cell technology: Fundamentals and applications.* Renewable and sustainable energy reviews, 2014. **32**: p. 810-853.
74. Elgrishi, N., et al., *A practical beginner's guide to cyclic voltammetry.* Journal of chemical education, 2018. **95**(2): p. 197-206.
75. Song, F., et al., *Transition metal oxides as electrocatalysts for the oxygen evolution reaction in alkaline solutions: an application-inspired renaissance.* Journal of the American Chemical Society, 2018. **140**(25): p. 7748-7759.
76. Wang, Q., K. Dastafkan, and C. Zhao, *Design strategies for non-precious metal oxide electrocatalysts for oxygen evolution reactions.* Current Opinion in Electrochemistry, 2018. **10**: p. 16-23.
77. Reier, T., M. Oezaslan, and P. Strasser, *Electrocatalytic oxygen evolution reaction (OER) on Ru, Ir, and Pt catalysts: a comparative study of nanoparticles and bulk materials.* Acs Catalysis, 2012. **2**(8): p. 1765-1772.
78. Tahir, M., et al., *Electrocatalytic oxygen evolution reaction for energy conversion and storage: a comprehensive review.* Nano Energy, 2017. **37**: p. 136-157.

79. Audichon, T., et al., *Electroactivity of RuO2–IrO2 mixed nanocatalysts toward the oxygen evolution reaction in a water electrolyzer supplied by a solar profile.* International journal of hydrogen energy, 2014. **39**(30): p. 16785-16796.
80. Dai, Y., et al., *Mini-review of perovskite oxides as oxygen electrocatalysts for rechargeable zinc–air batteries.* Chemical Engineering Journal, 2020. **397**: p. 125516.
81. Matsumoto, Y., et al., *Oxygen Evolution on La1− x Sr x Fe1− y Co y O 3 Series Oxides.* Journal of Magnetism Magnetic Materials, 1980. **127**(11): p. 2360-2364.
82. Hong, W.T., R.E. Welsch, and Y. Shao-Horn, *Descriptors of oxygen-evolution activity for oxides: a statistical evaluation.* The Journal of Physical Chemistry C, 2015. **120**(1): p. 78-86.
83. Subbaraman, R., et al., *Trends in activity for the water electrolyser reactions on 3 d M (Ni, Co, Fe, Mn) hydr (oxy) oxide catalysts.* Nature materials, 2012. **11**(6): p. 550-557.
84. Corrigan, D.A., *The catalysis of the oxygen evolution reaction by iron impurities in thin film nickel oxide electrodes.* Journal of The Electrochemical Society, 1987. **134**(2): p. 377.
85. Trotochaud, L., et al., *Nickel–iron oxyhydroxide oxygen-evolution electrocatalysts: the role of intentional and incidental iron incorporation.* Journal of the American Chemical Society, 2014. **136**(18): p. 6744-6753.
86. Stern, L.-A., et al., *Ni 2 P as a Janus catalyst for water splitting: the oxygen evolution activity of Ni 2 P nanoparticles.* Energy Environmental Science, 2015. **8**(8): p. 2347-2351.
87. Colli, A.N., H.H. Girault, and A. Battistel, *Non-precious electrodes for practical alkaline water electrolysis.* Materials, 2019. **12**(8): p. 1336.
88. Zayat, B., D. Mitra, and Narayanan, *Inexpensive and efficient alkaline water electrolyzer with robust steel-based electrodes.* Journal of The Electrochemical Society, 2020. **167**(11): p. 114513.
89. Lee, H.I., et al., *The Structural Effect of Electrode Mesh on Hydrogen Evolution Reaction Performance for Alkaline Water Electrolysis.* Frontiers in Chemistry, 2021. **9**.
90. Yang, H., M. Driess, and P.W. Menezes, *Self-supported electrocatalysts for practical water electrolysis.* Advanced Energy Materials, 2021. **11**(39): p. 2102074.
91. Scholz, J., et al., *Tailoring the Oxygen Evolution Activity and Stability Using Defect Chemistry.* Catalysts, 2017. **7**(5): p. 139.
92. Zhang, R., et al., *Electrochemical activation of atomic layer-deposited cobalt phosphate electrocatalysts for water oxidation.* ACS catalysis, 2021. **11**(5): p. 2774-2785.
93. Ham, K., et al., *Boosting the oxygen evolution reaction performance of wrinkled Mn (OH) 2 via conductive activation with a carbon binder.* Journal of Energy Chemistry, 2022. **71**: p. 580-587.
94. Sun, S., et al., *Tailoring the d-Band Centers Endows (Ni x Fe1–x) 2P Nanosheets with Efficient Oxygen Evolution Catalysis.* ACS Catalysis, 2020. **10**(16): p. 9086-9097.
95. Zhang, P., et al., *Nitrogen-doped carbon wrapped Co-Mo2C dual Mott–Schottky nanosheets with large porosity for efficient water electrolysis.* Applied Catalysis B: Environmental, 2021. **284**: p. 119738.
96. Seh, Z.W., et al., *Combining theory and experiment in electrocatalysis: Insights into materials design.* Science, 2017. **355**(6321): p. eaad4998.
97. Zhang, J., M.-R. Gao, and J.-L. Luo, *In situ exsolved metal nanoparticles: a smart approach for optimization of catalysts.* Chemistry of Materials, 2020. **32**(13): p. 5424-5441.

98. Fabbri, E., et al., *Dynamic surface self-reconstruction is the key of highly active perovskite nano-electrocatalysts for water splitting.* Nature materials, 2017. **16**(9): p. 925-931.
99. Garlyyev, B., et al., *Theoretical and experimental identification of active electrocatalytic surface sites.* Current Opinion in Electrochemistry, 2019. **14**: p. 206-213.
100. Suntivich, J., et al., *A perovskite oxide optimized for oxygen evolution catalysis from molecular orbital principles.* Science, 2011. **334**(6061): p. 1383-1385.
101. Nørskov, J.K., et al., *Origin of the overpotential for oxygen reduction at a fuel-cell cathode.* The Journal of Physical Chemistry B, 2004. **108**(46): p. 17886-17892.
102. Bhattacharjee, S., U.V. Waghmare, and S.-C. Lee, *An improved d-band model of the catalytic activity of magnetic transition metal surfaces.* Scientific reports, 2016. **6**(1): p. 1-10.
103. Jiao, S., X. Fu, and H. Huang, *Descriptors for the Evaluation of Electrocatalytic Reactions: d-Band Theory and Beyond.* Advanced Functional Materials, 2022. **32**(4): p. 2107651.
104. Häusler, J., et al., *Elucidating the Influence of the d-Band Center on the Synthesis of Isobutanol.* Catalysts, 2021. **11**(3): p. 406.
105. Pettersson, L.G.M. and A. Nilsson, *A molecular perspective on the d-band model: synergy between experiment and theory.* Topics in catalysis, 2014. **57**(1): p. 2-13.
106. Chen, Q., et al., *Surface Phase Engineering Modulated Iron-Nickel Nitrides/Alloy Nanospheres with Tailored d-Band Center for Efficient Oxygen Evolution Reaction.* Small, 2022. **18**(4): p. 2105696.
107. He, C., et al., *Synergistic tuning of oxygen vacancies and d-band centers of ultrathin cobaltous dihydroxycarbonate nanowires for enhanced electrocatalytic oxygen evolution.* Nanoscale, 2020. **12**(21): p. 11735-11745.
108. Sharma, L., et al., *Low-cost high entropy alloy (HEA) for high-efficiency oxygen evolution reaction (OER).* Nano Research, 2021: p. 1-8.
109. Wang, X., et al., *Carbonaceous-assisted confinement synthesis of refractory high-entropy alloy nanocomposites and their application for seawater electrolysis.* Journal of Colloid and Interface Science, 2022. **607**: p. 1580-1588.
110. Cheon, J.Y., et al., *Intrinsic relationship between enhanced oxygen reduction reaction activity and nanoscale work function of doped carbons.* Journal of the American Chemical Society, 2014. **136**(25): p. 8875-8878.
111. Schlaf, R., *Tutorial on work function.* Tampa: USF Surface Science Laboratory, Dept of Electrical Engineering at University of South Florida, 2007.
112. Qi, J., W. Zhang, and R. Cao, *Porous materials as highly efficient electrocatalysts for the oxygen evolution reaction.* ChemCatChem, 2018. **10**(6): p. 1206-1220.
113. Chen, P., et al., *Nitrogen-doped nanoporous carbon nanosheets derived from plant biomass: an efficient catalyst for oxygen reduction reaction.* Energy & Environmental Science, 2014. **7**(12): p. 4095-4103.
114. Wang, J., *H. x. Zhong, Y. l. Qin and X. b. Zhang.* Angew. Chem., Int. Ed, 2013. **52**: p. 5248-5253.
115. Qi, J., et al., *Water Splitting: Porous Nickel–Iron Oxide as a Highly Efficient Electrocatalyst for Oxygen Evolution Reaction (Adv. Sci. 10/2015).* 2015. **2**(10).
116. Qi, J., W. Zhang, and R. Cao, *Aligned cobalt-based Co@ CoO x nanostructures for efficient electrocatalytic water oxidation.* Chemical Communications, 2017. **53**(66): p. 9277-9280.

117. Luo, P., et al., *Targeted synthesis of unique nickel sulfide (NiS, NiS2) microarchitectures and the applications for the enhanced water splitting system.* ACS applied materials & interfaces, 2017. **9**(3): p. 2500-2508.
118. Amores, E., M. Sánchez-Molina, and M. Sánchez, *Effects of the marine atmosphere on the components of an alkaline water electrolysis cell for hydrogen production.* Results in Engineering, 2021: p. 100235.
119. Carrette, L., K. Friedrich, and U. Stimming, *Fuel cells–fundamentals and applications*. 2001: Springer.
120. Dai, W., T. Lu, and Y. Pan, *Novel and promising electrocatalyst for oxygen evolution reaction based on MnFeCoNi high entropy alloy.* Journal of Power Sources, 2019. **430**: p. 104-111.
121. Tang, J., et al., *Microwave sintered porous CoCrFeNiMo high entropy alloy as an efficient electrocatalyst for alkaline oxygen evolution reaction.* Journal of Materials Science & Technology, 2021. **79**: p. 171-177.
122. Huang, J., et al., *Regulating electrolytic Fe0. 5CoNiCuZnx high entropy alloy electrodes for oxygen evolution reactions in alkaline solution.* Journal of Materials Science and Technology, 2021. **93**: p. 110-118.
123. Zhou, P., et al., *Corrosion engineering boosting bulk Fe50Mn30Co10Cr10 high-entropy alloy as high-efficient alkaline oxygen evolution reaction electrocatalyst.* Journal of Materials Science & Technology, 2022. **109**: p. 267-275.
124. Liu, G., *Oxygen evolution reaction electrocatalysts for seawater splitting: A review.* Journal of Electroanalytical Chemistry, 2022: p. 116805.
125. Maril, M., et al., *Critical aspects in the development of anodes for use in seawater electrolysis.* International Journal of Hydrogen Energy, 2021.
126. Zhang, F., et al., *Rational design of oxygen evolution reaction catalysts for seawater electrolysis.* Trends in Chemistry, 2021. **3**(6): p. 485-498.
127. Cullity, B.D. and S.R. Stock, *Elements of X-ray Diffraction*. Vol. 3. 2001: Prentice hall New Jersey.
128. Muralikrishna, G.M., et al., *Influence of Al content on thermal stability of nanocrystalline AlxCoCrFeNi high entropy alloys at low and intermediate temperatures.* Advanced Powder Technology, 2020.
129. Ren, B., et al., *Effect of elemental interaction on microstructure of CuCrFeNiMn high entropy alloy system.* Journal of Alloys and Compounds, 2010. **493**(1-2): p. 148-153.
130. Cheng, H., et al., *Microstructure and mechanical properties of FeCoCrNiMn high-entropy alloy produced by mechanical alloying and vacuum hot pressing sintering.* Transactions of Nonferrous Metals Society of China, 2018. **28**(7): p. 1360-1367.
131. Wang, G., et al., *Synthesis and thermal stability of a nanocrystalline MoNbTaTiV refractory high-entropy alloy via mechanical alloying.* International Journal of Refractory Metals and Hard Materials, 2019. **84**: p. 104988.
132. Yim, D., et al., *Compaction behavior of water-atomized CoCrFeMnNi high-entropy alloy powders.* Materials Chemistry Physics, 2018. **210**: p. 95-102.
133. Nouri, A., P. Hodgson, and C. Wen, *Effect of process control agent on the porous structure and mechanical properties of a biomedical Ti–Sn–Nb alloy produced by powder metallurgy.* Acta biomaterialia, 2010. **6**(4): p. 1630-1639.
134. Nouri, A. and C. Wen, *Surfactants in mechanical alloying/milling: a catch-22 situation.* Critical reviews in solid state and material sciences, 2014. **39**(2): p. 81-108.
135. Ji, W., et al., *Mechanical alloying synthesis and spark plasma sintering consolidation of CoCrFeNiAl high-entropy alloy.* Journal of Alloys and Compounds, 2014. **589**: p. 61-66.

136. Rohila, S., et al., *Nearly full-density pressureless sintering of AlCoCrFeNi-based high-entropy alloy powders.* Journal of Materials Research, 2019. **34**(5): p. 777-786.
137. Jadhav, M., et al., *An investigation on high entropy alloy for bond coat application in thermal barrier coating system.* Journal of Alloys and Compounds, 2019. **783**: p. 662-673.
138. Cui, X., et al., *Electrocatalytic activity of high-entropy alloys toward oxygen evolution reaction.* MRS Communications, 2018. **8**(3): p. 1230-1235.
139. Zhang, K., et al., *Nanocrystalline CoCrFeNiCuAl high-entropy solid solution synthesized by mechanical alloying.* Journal of Alloys and Compounds, 2009. **485**(1-2): p. L31-L34.
140. Yurkova, A.I., et al., *Structure formation and mechanical properties of the high-entropy AlCuNiFeCr alloy prepared by mechanical alloying and spark plasma sintering.* Journal of Alloys and Compounds, 2019. **786**: p. 139-148.
141. Kumar, A., et al., *Fabrication, Microstructure, Mechanical, and Electrochemical Properties of NiMnFeCu High Entropy Alloy from Elemental Powders.* Metals, 2022. **12**(1): p. 167.
142. Tian, L., M. Fu, and W. Xiong, *Microstructural evolution of AlCoCrFeNiSi high-entropy alloy powder during mechanical alloying and its coating performance.* Materials, 2018. **11**(2): p. 320.
143. Koundinya, N., et al., *Phase evolution and thermal analysis of nanocrystalline AlCrCuFeNiZn high entropy alloy produced by mechanical alloying.* Journal of materials engineering and performance, 2013. **22**(10): p. 3077-3084.
144. Mishra, R.K., P. Sahay, and R. Shahi, *Alloying, magnetic and corrosion behavior of AlCrFeMnNiTi high entropy alloy.* Journal of Materials Science, 2019. **54**(5): p. 4433-4443.
145. Venkataraman, R., et al., *Study on influence of porosity, pore size, spatial and topological distribution of pores on microhardness of as plasma sprayed ceramic coatings.* Materials Science and Engineering, 2007. **445**: p. 269-274.
146. Bilger, N., et al., *Effect of a nonuniform distribution of voids on the plastic response of voided materials: a computational and statistical analysis.* International Journal of Solid Structures, 2005. **42**(2): p. 517-538.
147. Gorsse, S., et al., *Database on the mechanical properties of high entropy alloys and complex concentrated alloys.* Data in brief, 2018. **21**: p. 2664-2678.
148. Zhang, K., et al., *Microstructure and mechanical properties of CoCrFeNiTiAlx high-entropy alloys.* Materials Science and Engineering: A, 2009. **508**(1-2): p. 214-219.
149. Kang, S.-J.L., *Sintering: densification, grain growth and microstructure*. 2004: Elsevier.
150. Campo, K.N., et al., *CrCuFeMnNi high-entropy alloys for semisolid processing: The effect of copper on phase formation, melting behavior, and semisolid microstructure.* Materials Characterization, 2021. **178**: p. 111260.
151. Cheng, W.-C., et al., *Phase transformation of the L12 phase to kappa-carbide after spinodal decomposition and ordering in an Fe–C–Mn–Al austenitic steel.* Materials Science and Engineering: A, 2015. **642**: p. 128-135.
152. Palisaitis, J., et al., *Direct observation of spinodal decomposition phenomena in InAlN alloys during in-situ STEM heating.* Scientific reports, 2017. **7**(1): p. 1-8.
153. Zhang, Y., et al., *Concurrence of spinodal decomposition and nano-phase precipitation in a multi-component AlCoCrCuFeNi high-entropy alloy.* Journal of Materials Research and Technology 2019. **8**(1): p. 726-736.

154. Sharma, A., M.C. Oh, and B. Ahn, *Microstructural evolution and mechanical properties of non-Cantor AlCuSiZnFe lightweight high entropy alloy processed by advanced powder metallurgy.* Materials Science Engineering :A, 2020: p. 140066.
155. Toda-Caraballo, I. and P.E. Rivera-Díaz-del-Castillo, *Modelling solid solution hardening in high entropy alloys.* Acta Materialia, 2015. **85**: p. 14-23.
156. Fan, Q., B. Li, and Y. Zhang, *Influence of Al and Cu elements on the microstructure and properties of (FeCrNiCo) AlxCuy high-entropy alloys.* Journal of Alloys and Compounds, 2014. **614**: p. 203-210.
157. Song, H., et al., *Local lattice distortion in high-entropy alloys.* Physical Review Materials, 2017. **1**(2): p. 023404.
158. Thirathipviwat, P., et al., *A role of atomic size misfit in lattice distortion and solid solution strengthening of TiNbHfTaZr high entropy alloy system.* Scripta Materialia, 2022. **210**: p. 114470.
159. Ding, Q., et al., *Tuning element distribution, structure and properties by composition in high-entropy alloys.* Nature, 2019. **574**(7777): p. 223-227.
160. Huynh, M., et al., *Nature of activated manganese oxide for oxygen evolution.* Journal of the American Chemical Society, 2015. **137**(47): p. 14887-14904.
161. Zhao, S., et al., *Calculating the electrochemically active surface area of iridium oxide in operating proton exchange membrane electrolyzers.* Journal of The Electrochemical Society, 2015. **162**(12): p. F1292.
162. Li, X., et al., *In situ/operando characterization techniques to probe the electrochemical reactions for energy conversion.* Small Methods, 2018. **2**(6): p. 1700395.
163. Zhu, Y., et al., *In situ/operando studies for designing next-generation electrocatalysts.* ACS Energy Letters, 2020. **5**(4): p. 1281-1291.
164. Liang, H., M. Xu, and E. Asselin, *Corrosion of monometallic iron-and nickel-based electrocatalysts for the alkaline oxygen evolution reaction: A review.* Journal of Power Sources, 2021. **510**: p. 230387.
165. Gorlin, Y. and T.F. Jaramillo, *A bifunctional nonprecious metal catalyst for oxygen reduction and water oxidation.* Journal of the American Chemical Society, 2010. **132**(39): p. 13612-13614.
166. Liu, Q., A.M. Asiri, and X. Sun, *Hematite nanorods array on carbon cloth as an efficient 3D oxygen evolution anode.* Electrochemistry communications, 2014. **49**: p. 21-24.
167. Putra, R.P., H. Horino, and I. Rzeznicka, *An efficient electrocatalyst for oxygen evolution reaction in alkaline solutions derived from a copper chelate polymer via in situ electrochemical transformation.* Catalysts, 2020. **10**(2): p. 233.
168. Jia, Z., et al., *A novel multinary intermetallic as an active electrocatalyst for hydrogen evolution.* Advanced Materials, 2020. **32**(21): p. 2000385.
169. Hirai, S., et al., *Enhancement of the oxygen evolution reaction in Mn 3+-based electrocatalysts: correlation between Jahn–Teller distortion and catalytic activity.* RSC advances, 2016. **6**(3): p. 2019-2023.
170. Yamada, I., et al., *Bifunctional oxygen reaction catalysis of quadruple manganese perovskites.* Advanced Materials, 2017. **29**(4): p. 1603004.
171. Momma, K. and F. Izumi, *VESTA 3 for three-dimensional visualization of crystal, volumetric and morphology data.* Journal of applied crystallography, 2011. **44**(6): p. 1272-1276.
172. Xiang, W., et al., *3D atomic-scale imaging of mixed Co-Fe spinel oxide nanoparticles during oxygen evolution reaction.* Nature Communications, 2022. **13**(1): p. 1-14.

173. Sharma, M., et al., *Work function-tailored graphene via transition metal encapsulation as a highly active and durable catalyst for the oxygen reduction reaction.* Energy & Environmental Science, 2019. **12**(7): p. 2200-2211.
174. Xu, X., et al., *Elemental core level shift in high entropy alloy nanoparticles via X-ray photoelectron spectroscopy analysis and first-principles calculation.* ACS nano, 2020. **14**(12): p. 17704-17712.
175. Luo, X., et al., *Regulating the work function of silver catalysts via surface engineering for enhanced CO 2 electroreduction.* Physical Chemistry Chemical Physics, 2022. **24**(16): p. 9188-9195.
176. Xie, M., et al., *An Fe (TCNQ) 2 nanowire array on Fe foil: an efficient non-noble-metal catalyst for the oxygen evolution reaction in alkaline media.* Chemical Communications, 2018. **54**(18): p. 2300-2303.
177. Zhu, W., et al., *Porous amorphous FeCo alloys as pre-catalysts for promoting the oxygen evolution reaction.* Journal of Alloys and Compounds, 2020. **828**: p. 154465.
178. Jiang, S., et al., *Alloying strategy for constructing multi-component nano-catalysts towards efficient and durable oxygen evolution in alkaline electrolyte.* Electrochimica Acta, 2021. **391**: p. 138933.
179. Hölzl, J. and F.K. Schulte, *Work function of metals.* Solid surface physics, 1979: p. 1-150.